AD-A230 189

DTIC FILE COPY

(2)

WRDC-TR-90-9003
Volume I

UNIFORM THEORY OF DIFFRACTION (UTD) SCATTERING FROM STRUCTURES, INCLUDING HIGHER ORDER TERMS

Volume I: Far-Zone Bistatic Scattering From Flat Plates

DTIC
ELECTE
DEC 20 1990
S D
D

ElectroScience Laboratory
The Ohio State University
1320 Kinnear Road
Columbus, OH 43212

November 1990
Final Report for Period April 1986 - December 1989

Approved for Public Release; Distribution is Unlimited

Signature Technology Directorate
Wright Research and Development Center
Air Force Systems Command
Wright Patterson Air Force Base, OH 45433-6523

NOTICE

When Government drawings, specifications, or other data are used for any purpose other than in connection with a definitely Government-related procurement, the United States Government incurs no responsibility or any obligation whatsoever. The fact that the government may have formulated or in any way supplied the said drawings, specifications, or other data, is not to be regarded by implication, or otherwise in any manner construed, as licensing the holder, or any other person or corporation; or as conveying any rights or permission to manufacture, use, or sell any patented invention that may in any way be related thereto.

This report is releasable to the National Technical Information Service (NTIS). At NTIS, it will be available to the general public, including foreign nations.

This technical report has been reviewed and is approved for publication.

J. EARL JONES, Project Engineer
Defensive Avionics Division
Signature Technology Directorate

JOSEPH C. FAISON, Chief
Defensive Avionics Division
Signature Technology Directorate

FOR THE COMMANDER

FRANKLIN D. CHERRY, Director
Signature Technology Directorate

If your address has changed, if you wish to be removed from our mailing list, or if the addressee is no longer employed by your organization please notify WRDC/SNA , WPAFB, OH 45433- 6523 to help us maintain a current mailing list.

Copies of this report should not be returned unless return is required by security considerations, contractual obligations, or notice on a specific document.

UNCLASSIFIED
SECURITY CLASSIFICATION OF THIS PAGE

REPORT DOCUMENTATION PAGE

Form Approved
OMB No. 0704-0188

1a. REPORT SECURITY CLASSIFICATION UNCLASSIFIED	1b. RESTRICTIVE MARKINGS NONE
2a. SECURITY CLASSIFICATION AUTHORITY N/A	3. DISTRIBUTION/AVAILABILITY OF REPORT Approved for Public Release; Distribution is Unlimited
2b. DECLASSIFICATION/DOWNGRADING SCHEDULE N/A	
4. PERFORMING ORGANIZATION REPORT NUMBER(S) 718295-8	5. MONITORING ORGANIZATION REPORT NUMBER(S) WRDC-TR-90-9003, Vol. 1
6a. NAME OF PERFORMING ORGANIZATION Ohio State University ElectroScience Laboratory 6b. OFFICE SYMBOL (If applicable)	7a. NAME OF MONITORING ORGANIZATION Wright Research and Development Center Signature Technology Directorate (WRDC/SNA)
6c. ADDRESS (City, State, and ZIP Code) 1320 Kinnear Road Columbus, OH 43212	7b. ADDRESS (City, State, and ZIP Code) Wright-Patterson AFB, OH 45433-6523
8a. NAME OF FUNDING/SPONSORING ORGANIZATION 8b. OFFICE SYMBOL (If applicable)	9. PROCUREMENT INSTRUMENT IDENTIFICATION NUMBER F33615-86-K-1023
8c. ADDRESS (City, State, and ZIP Code)	10. SOURCE OF FUNDING NUMBERS PROGRAM ELEMENT NO. 61101F; PROJECT NO. ILIR; TASK NO A6; WORK UNIT ACCESSION NO 03

11. TITLE (Include Security Classification)
UNIFORM THEORY OF DIFFRACTION (UTD) SCATTERING FROM STRUCTURES, INCLUDING HIGHER ORDER TERMS ; VOLUME I: Far-Zone Bistatic Scattering from Flat Plates

12. PERSONAL AUTHOR(S)
Brinkley, Timothy J.; and Marhefka, Ronald J.

13a. TYPE OF REPORT	13b. TIME COVERED	14. DATE OF REPORT (Year, Month, Day)	15. PAGE COUNT
Final	FROM APR 86 TO DEC 89	November 1990	195

16. SUPPLEMENTARY NOTATION
This report volume is Volume I of six volumes. This report was submitted as a M. Sc. thesis by T. Brinkley, Spring 1988.

17. COSATI CODES			18. SUBJECT TERMS (Continue on reverse if necessary and identify by block number)
FIELD	GROUP	SUB-GROUP	Uniform Theory of Diffraction (UTD), Geometric Theory of Diffraction (GTD), Ray Theory, Electromagnetic Scattering, Radar Cross Section (RCS)

19. ABSTRACT (Continue on reverse if necessary and identify by block number)

New equivalent edge currents and corner diffraction coefficients are obtained for the case of far zone bistatic scattering from flat plates. It is shown that the new solution does not contain the so-called false shadow boundaries found in previous high frequency solutions. The results illustrate that this solution gives good first-order results when compared with measurements, moment method calculations, and previous high frequency solutions.

20. DISTRIBUTION/AVAILABILITY OF ABSTRACT ☒ UNCLASSIFIED/UNLIMITED ☐ SAME AS RPT. ☐ DTIC USERS	21. ABSTRACT SECURITY CLASSIFICATION Unclassified
22a. NAME OF RESPONSIBLE INDIVIDUAL J. Earl Jones	22b. TELEPHONE (Include Area Code) (513)-255-9335 22c. OFFICE SYMBOL WRDC/SNA

DD Form 1473, JUN 86 Previous editions are obsolete.

SECURITY CLASSIFICATION OF THIS PAGE
UNCLASSIFIED

This volume of the Final Technical Report for Contract No. F33615-86-K-1023 was originally submitted as a Master of Science Thesis to The Ohio State University Department of Electrical Engineering by Timothy J. Brinkley in 1988.

DTIC
COPY
INSPECTED
6

Accesion For
NTIS CRA&I
By
Availability Codes
A-1

TABLE OF CONTENTS

LIST OF FIGURES v

LIST OF TABLES xii

I. INTRODUCTION 1
- 1.1 Objective 1
- 1.2 Motivation 1
- 1.3 Problem History 2
- 1.4 Outline of Solution 2
- 1.5 Notation, Abbreviations and Symbols 3
  - 1.5.1 Symbols 3
  - 1.5.2 Abbreviations 5
  - 1.5.3 Edge Fixed Coordinate System 6
  - 1.5.4 Radar Cross Section 7
- 1.6 Pattern Coordinate System 9

II. THEORETICAL BACKGROUND 11
- 2.1 Introduction 11
- 2.2 Geometrical Optics 11
- 2.3 Geometrical Theory of Diffraction 14
- 2.4 Physical Optics 16
- 2.5 Physical Theory of Diffraction 18
- 2.6 Method of Equivalent Currents 19
- 2.7 Previous Corner Diffraction Coefficient 26
- 2.8 Stationary Phase Method 27

III. THEORY 33
- 3.1 Introduction 33
- 3.2 Physical Optics Surface Integral 33
- 3.3 Fringe Equivalent Currents 37
- 3.4 Equivalent Currents Written in the Form of Diffraction Coefficients 44

3.5 New Corner Diffraction Coefficient 46
3.6 Conclusion 50

IV. PROPERTIES OF THE NEW CORNER DIFFRACTION SOLUTION 53
4.1 Introduction 53
4.2 Singularities 53
4.3 Boundary Conditions 66
4.4 Reciprocity 70
4.5 RCS of a Rectangular Plate at Broadside 88
4.6 Equivalent Currents on the Keller Cone 89
4.7 Physical Significance of Parameters α and γ 90

V. RESULTS 95
5.1 Introduction 95
5.2 Brief Description of Program 95
5.3 Examples 96
5.3.1 Ross 96
5.3.2 Northrop Fin 96
5.3.3 Sikta's triangle 102
5.3.4 Cube 130
5.3.5 6" Cube 130
5.3.6 Swept Frequency Results 136
5.3.7 Bistatic Scattering from a 2λ plate illuminated by a fixed source 141
5.3.8 Bistatic scattering from a 2λ plate illuminated by a fixed source in a second position 151
5.4 Conclusion 160

VI. CONCLUSION 161

A. NEW CORNER DIFFRACTION COEFFICIENTS 163

B. EQUIVALENT CURRENTS FOR EDGE ON INCIDENCE 166

C. RCS FOR NORMAL INCIDENCE ON A RECTANGULAR FLAT PLATE 169

D. AN EQUIVALENT EXPRESSION FOR THE EQUIVALENT CURRENTS 177

REFERENCES 181

LIST OF FIGURES

1 Edge Fixed Coordinates. 6
2 Definition of Distances r_1 and r_2. 8
3 Astigmatic ray tube. 12
4 Projection of rays on to b-n plane. 14
5 Keller's cone of diffracted rays. 15
6 PO Currents on an arbitrary scatterer. 17
7 Strips used in Ryan and Peters Equivalent Currents by Sikta [2]. . 21
8 False Shadow Boundary example geometry (2λ square plate in the x-y plane). 23
9 Co-polarized RCS in the $\phi = 60°$ plane of a 2λ square plate with a $\hat{\theta}^i$ polarized fixed source at $\theta^i = 45°$, $\phi^i = 0°$. 24
10 Co-polarized RCS in the $\phi = 60°$ plane of a 2λ square plate with a $\hat{\phi}^i$ polarized fixed source at $\theta^i = 45°$, $\phi^i = 0°$. 24
11 Cross-polarized RCS in the $\phi = 60°$ plane of a 2λ square plate with a $\hat{\theta}^i$ polarized fixed source at $\theta^i = 45°$, $\phi^i = 0°$. 25
12 Cross-polarized RCS in the $\phi = 60°$ plane of a 2λ square plate with a $\hat{\phi}^i$ polarized fixed source at $\theta^i = 45°$, $\phi^i = 0°$. 25
13 Definition of angles for the Corner Diffraction Coefficients. 28
14 Co-polarized RCS in the $\phi = 60°$ plane of a 2λ square plate with a $\hat{\theta}^i$ polarized fixed source at $\theta^i = 45°$, $\phi^i = 0°$. 29
15 Co-polarized RCS in the $\phi = 60°$ plane of a 2λ square plate with a $\hat{\phi}^i$ polarized fixed source at $\theta^i = 45°$, $\phi^i = 0°$. 29
16 Cross-polarized RCS in the $\phi = 60°$ plane of a 2λ square plate with a $\hat{\theta}^i$ polarized fixed source at $\theta^i = 45°$, $\phi^i = 0°$. 30
17 Cross-polarized RCS in the $\phi = 60°$ plane of a 2λ square plate with a $\hat{\phi}^i$ polarized fixed source at $\theta^i = 45°$, $\phi^i = 0°$. 30
18 Integration direction (or strip orientation) used in finding the equivalent fringe currents. 40
19 Branch for α. 42
20 Edge Fixed coordinates for a straight edge. 48

21 Definition of the Angles used in the New Corner Diffraction Coefficients. 51
22 Direction of Integration for one face. 52
23 Plate Geometry for the Illustration of Ufiimtsev's Singularity. . . . 54
24 H-plane pattern for $\phi = 0°$ cut of a 2λ square plate with a fixed source at $\theta_i = 90°, \phi_i = 0°$. 55
25 H-plane pattern for $\phi = 0°$ cut of a 2λ square plate with a fixed source at $\theta_i = 90°, \phi_i = 0°$. 55
26 H-plane pattern for $\phi = 45°$ cut of a 2λ square plate with a fixed source at $\theta_i = 90°, \phi_i = 45°$. 56
27 H-plane pattern for $\phi = 45°$ cut of a 2λ square plate with a fixed source at $\theta_i = 90°, \phi_i = 45°$. 57
28 2λ square plate in the x-y plane illuminated by a fixed source located in the $\theta^i = 45°$, $\phi^i = 0°$ direction. 58
29 RCS for the $\theta = 89°$ cut of a 2λ square plate with a $\hat{\phi}^i$ polarized fixed source at $\theta^i = 45°$, $\phi^i = 0°$. 59
30 RCS for the $\theta = 89°$ cut of a 2λ square plate with a $\hat{\phi}^i$ polarized fixed source at $\theta^i = 45°$, $\phi^i = 0°$. 59
31 $F_{im}, \beta' = 135°$ 60
32 $F_m, \beta' = 135°$ 62
33 $F_{im}, \beta' = 135°$ 63
34 $F_m, \beta' = 135°$ 63
35 Backscatter ($\sigma_{\theta\theta}$ and $\sigma_{\theta\phi}$) from a 2λ square plate for $\theta = 89°$ . . . 64
36 Backscatter ($\sigma_{\phi\phi}$ and $\sigma_{\phi\theta}$) from a 2λ square plate for $\theta = 89°$ . . . 64
37 Boundary Conditions Example. 67
38 Reciprocity example. 71
39 Relative positions of the two antennas for the first two patterns. . 73
40 RCS of 2λ square plate for $\hat{\theta}$ polarized antennas (which are positioned as indicated in Figure 39) in the $\phi = 0°$ plane. 74
41 RCS of 2λ square plate for $\hat{\phi}$ polarized antennas (which are positioned as indicated in Figure 39) in the $\phi = 0°$ plane. 74
42 Relative positions of the two antennas for the next two patterns. . 75
43 RCS of 2λ square plate for $\hat{\theta}$ polarized antennas (which are positioned as indicated in Figure 42) in the $\phi = 45°$ plane. 76
44 RCS of 2λ square plate for $\hat{\phi}$ polarized antennas (which are positioned as indicated in Figure 42) in the $\phi = 45°$ plane. 76
45 Relative positions of the two antennas for the next three patterns. 77

46 RCS of 2λ square plate for $\hat{\theta}$ polarized antennas (which are positioned as indicated in Figure 45) in the $\phi = 30°$ plane. 78
47 RCS of 2λ square plate for $\hat{\phi}$ polarized antennas (which are positioned as indicated in Figure 45) in the $\phi = 30°$ plane. 79
48 RCS of 2λ square plate for cross polarized antennas (which are positioned as indicated in Figure 45) in the $\phi = 30°$ plane. 79
49 Relative positions of the two antennas for the next four patterns. . 80
50 RCS of 2λ square plate for horizontally polarized antennas (which are positioned as indicated in Figure 49). 81
51 RCS of 2λ square plate for vertically polarized antennas (which are positioned as indicated in Figure 49). 82
52 RCS of 2λ square plate for antenna one horizontally polarized and antenna two vertically polarized (which are positioned as indicated in Figure 49). 82
53 RCS of 2λ square plate for antenna one vertically polarized and antenna two horizontally polarized (which are positioned as indicated in Figure 49). 83
54 RCS of 2λ cube for $\hat{\theta}$ polarized antennas (which are positioned as indicated in Figure 39) in the $\phi = 0°$ plane. 84
55 RCS of 2λ cube for $\hat{\phi}$ polarized antennas (which are positioned as indicated in Figure 39) in the $\phi = 0°$ plane. 84
56 RCS of 2λ cube for $\hat{\theta}$ polarized antennas (which are positioned as indicated in Figure 42) in the $\phi = 45°$ plane. 85
57 RCS of 2λ cube for $\hat{\phi}$ polarized antennas (which are positioned as indicated in Figure 42) in the $\phi = 45°$ plane. 86
58 RCS of 2λ cube for $\hat{\theta}$ polarized antennas (which are positioned as indicated in Figure 45) in the $\phi = 30°$ plane. 87
59 RCS of 2λ cube for $\hat{\phi}$ polarized antennas (which are positioned as indicated in Figure 45) in the $\phi = 30°$ plane. 87
60 RCS of 2λ cube for cross polarized antennas (which are positioned as indicated in Figure 45) in the $\phi = 30°$ plane. 88
61 Integration direction (strip orientation) used to find the LPO components of the equivalent currents. 91

62 Ross 4" x 4" plate. 97
63 E-plane pattern in x-z plane of Ross plate. 98
64 E-plane pattern in x-z plane of Ross plate. 99
65 Northrop Fin. 100

66 E-plane pattern in x-y plane at 17.76 GHz of Northrop Fin. 101
67 E-plane pattern in x-y plane at 17.76 GHz of Northrop Fin. 102
68 Sikta's Triangle. 103
69 The E-plane pattern ($\phi = 0°$) for Sikta's triangle with $a = 2\lambda$ and $\alpha = 30°$. 104
70 The H-plane pattern ($\phi = 0°$) for Sikta's triangle with $a = 2\lambda$ and $\alpha = 30°$. 105
71 The E-plane pattern ($\phi = 0°$) for Sikta's triangle with $a = 3\lambda$ and $\alpha = 30°$. 107
72 The H-plane pattern ($\phi = 0°$) for Sikta's triangle with $a = 3\lambda$ and $\alpha = 30°$. 108
73 The E-plane pattern ($\phi = 0°$) for Sikta's triangle with $a = 9\lambda$ and $\alpha = 30°$. 109
74 The H-plane pattern ($\phi = 0°$) for Sikta's triangle with $a = 9\lambda$ and $\alpha = 30°$. 110
75 The E-plane pattern ($\phi = 0°$) for Sikta's triangle with $a = 2\lambda$ and $\alpha = 30°$. 111
76 The H-plane pattern ($\phi = 0°$) for Sikta's triangle with $a = 2\lambda$ and $\alpha = 30°$. 112
77 The E-plane pattern ($\phi = 0°$) for Sikta's triangle with $a = 3\lambda$ and $\alpha = 30°$. 113
78 The H-plane pattern ($\phi = 0°$) for Sikta's triangle with $a = 3\lambda$ and $\alpha = 30°$. 114
79 The E-plane pattern ($\phi = 0°$) for Sikta's triangle with $a = 9\lambda$ and $\alpha = 30°$. 115
80 The H-plane pattern ($\phi = 0°$) for Sikta's triangle with $a = 9\lambda$ and $\alpha = 30°$. 116
81 The E-plane pattern ($\phi = 0°$) for Sikta's triangle with $a = 4\lambda$ and $\alpha = 45°$. 117
82 The H-plane pattern ($\phi = 0°$) for Sikta's triangle with $a = 4\lambda$ and $\alpha = 45°$. 118
83 The E-plane pattern ($\phi = 0°$) for Sikta's triangle with $a = 4\lambda$ and $\alpha = 60°$. 119
84 The H-plane pattern ($\phi = 0°$) for Sikta's triangle with $a = 4\lambda$ and $\alpha = 60°$. 120
85 The E-plane pattern ($\phi = 0°$) for Sikta's triangle with $a = 4\lambda$ and $\alpha = 90°$. 121

86 The H-plane pattern ($\phi = 0°$) for Sikta's triangle with $a = 4\lambda$ and $\alpha = 90°$. 122
87 The E-plane pattern ($\phi = 0°$) for Sikta's triangle with $a = 4\lambda$ and $\alpha = 45°$. 124
88 The H-plane pattern ($\phi = 0°$) for Sikta's triangle with $a = 4\lambda$ and $\alpha = 45°$. 125
89 The E-plane pattern ($\phi = 0°$) for Sikta's triangle with $a = 4\lambda$ and $\alpha = 60°$. 126
90 The H-plane pattern ($\phi = 0°$) for Sikta's triangle with $a = 4\lambda$ and $\alpha = 60°$. 127
91 The E-plane pattern ($\phi = 0°$) for Sikta's triangle with $a = 4\lambda$ and $\alpha = 90°$. 128
92 The H-plane pattern ($\phi = 0°$) for Sikta's triangle with $a = 4\lambda$ and $\alpha = 90°$. 129
93 H-plane pattern for Cube (with $\theta = 90°$). 131
94 E-plane pattern for Cube (with $\phi = 90°$). 132
95 Cube geometry with the illuminated corners labeled. 133
96 H-plane pattern for 6" cube. 134
97 E-plane pattern for 6" cube. 134
98 6" Cube tilted 45° in the x-z plane. 135
99 H-plane pattern for 6" cube tilted 45° in the x-z plane. 135
100 E-plane pattern for 6" cube tilted 45° in the x-z plane. 136
101 6" Cube tilted 45° in the x-z plane, then 35.2° in the y-z plane. . . 137
102 H-plane pattern for a 6" Cube tilted 45° in the x-z plane, then 35.2° in the y-z plane. 138
103 E-plane pattern for a 6" Cube tilted 45° in the x-z plane, then 35.2° in the y-z plane. 138
104 Impulse response for 6" cube and a $\hat{\theta}$ polarized source at $\theta = 35.2°$, $\phi = 45°$. 141
105 Impulse response for 6" cube and a $\hat{\phi}$ polarized source at $\theta = 35.2°$, $\phi = 45°$. 142
106 2λ square plate in the x-y plane with a fixed source at $\theta^i = 45°$ and $\phi^i = 0$. 143
107 Co-polarized RCS in the $\phi = 0°$ plane of a 2λ square plate with a $\hat{\theta}^i$ polarized fixed source at $\theta^i = 45°$, $\phi^i = 0°$. 144
108 Co-polarized RCS in the $\phi = 0°$ plane of a 2λ square plate with a $\hat{\phi}^i$ polarized fixed source at $\theta^i = 45°$, $\phi^i = 0°$. 144

109 Co-polarized RCS in the $\phi = 30°$ plane of a 2λ square plate with a $\hat{\theta}^i$ polarized fixed source at $\theta^i = 45°$, $\phi^i = 0°$. 145
110 Co-polarized RCS in the $\phi = 30°$ plane of a 2λ square plate with a $\hat{\phi}^i$ polarized fixed source at $\theta^i = 45°$, $\phi^i = 0°$. 145
111 Cross-polarized RCS in the $\phi = 30°$ plane of a 2λ square plate with a $\hat{\theta}^i$ polarized fixed source at $\theta^i = 45°$, $\phi^i = 0°$. 146
112 Cross-polarized RCS in the $\phi = 30°$ plane of a 2λ square plate with a $\hat{\phi}^i$ polarized fixed source at $\theta^i = 45°$, $\phi^i = 0°$. 146
113 Co-polarized RCS in the $\phi = 60°$ plane of a 2λ square plate with a $\hat{\theta}^i$ polarized fixed source at $\theta^i = 45°$, $\phi^i = 0°$. 147
114 Co-polarized RCS in the $\phi = 60°$ plane of a 2λ square plate with a $\hat{\phi}^i$ polarized fixed source at $\theta^i = 45°$, $\phi^i = 0°$. 147
115 Cross-polarized RCS in the $\phi = 60°$ plane of a 2λ square plate with a $\hat{\theta}^i$ polarized fixed source at $\theta^i = 45°$, $\phi^i = 0°$. 148
116 Cross-polarized RCS in the $\phi = 60°$ plane of a 2λ square plate with a $\hat{\phi}^i$ polarized fixed source at $\theta^i = 45°$, $\phi^i = 0°$. 149
117 Co-polarized RCS in the $\phi = 90°$ plane of a 2λ square plate with a $\hat{\theta}^i$ polarized fixed source at $\theta^i = 45°$, $\phi^i = 0°$. 149
118 Co-polarized RCS in the $\phi = 90°$ plane of a 2λ square plate with a $\hat{\phi}^i$ polarized fixed source at $\theta^i = 45°$, $\phi^i = 0°$. 150
119 Cross-polarized RCS in the $\phi = 90°$ plane of a 2λ square plate with a $\hat{\theta}^i$ polarized fixed source at $\theta^i = 45°$, $\phi^i = 0°$. 150
120 Cross-polarized RCS in the $\phi = 90°$ plane of a 2λ square plate with a $\hat{\phi}^i$ polarized fixed source at $\theta^i = 45°$, $\phi^i = 0°$. 151
121 2λ square plate in the x-y plane with a fixed source located at $\theta^i = 45°$, $\phi^i = 45°$. 152
122 Co-polarized RCS in the $\phi = 45°$ plane of a 2λ square plate with a $\hat{\theta}^i$ polarized fixed source at $\theta^i = 45°$, $\phi^i = 45°$. 153
123 Co-polarized RCS in the $\phi = 45°$ plane of a 2λ square plate with a $\hat{\phi}^i$ polarized fixed source at $\theta^i = 45°$, $\phi^i = 45°$. 153
124 Co-polarized RCS in the $\phi = 75°$ plane of a 2λ square plate with a $\hat{\theta}^i$ polarized fixed source at $\theta^i = 45°$, $\phi^i = 45°$. 154
125 Co-polarized RCS in the $\phi = 75°$ plane of a 2λ square plate with a $\hat{\phi}^i$ polarized fixed source at $\theta^i = 45°$, $\phi^i = 45°$. 155
126 Cross-polarized RCS in the $\phi = 75°$ plane of a 2λ square plate with a $\hat{\theta}^i$ polarized fixed source at $\theta^i = 45°$, $\phi^i = 45°$. 155
127 Cross-polarized RCS in the $\phi = 75°$ plane of a 2λ square plate with a $\hat{\phi}^i$ polarized fixed source at $\theta^i = 45°$, $\phi^i = 45°$. 156

128 Co-polarized RCS in the $\phi = 105°$ plane of a 2λ square plate with a $\hat{\theta}^i$ polarized fixed source at $\theta^i = 45°$, $\phi^i = 45°$. 156
129 Co-polarized RCS in the $\phi = 105°$ plane of a 2λ square plate with a $\hat{\phi}^i$ polarized fixed source at $\theta^i = 45°$, $\phi^i = 45°$. 157
130 Cross-polarized RCS in the $\phi = 105°$ plane of a 2λ square plate with a $\hat{\theta}^i$ polarized fixed source at $\theta^i = 45°$, $\phi^i = 45°$. 157
131 Cross-polarized RCS in the $\phi = 105°$ plane of a 2λ square plate with a $\hat{\phi}^i$ polarized fixed source at $\theta^i = 45°$, $\phi^i = 45°$. 158
132 Co-polarized RCS in the $\phi = 135°$ plane of a 2λ square plate with a $\hat{\theta}^i$ polarized fixed source at $\theta^i = 45°$, $\phi^i = 45°$. 158
133 Co-polarized RCS in the $\phi = 135°$ plane of a 2λ square plate with a $\hat{\phi}^i$ polarized fixed source at $\theta^i = 45°$, $\phi^i = 45°$. 159
134 Cross-polarized RCS in the $\phi = 135°$ plane of a 2λ square plate with a $\hat{\theta}^i$ polarized fixed source at $\theta^i = 45°$, $\phi^i = 45°$. 159
135 Cross-polarized RCS in the $\phi = 135°$ plane of a 2λ square plate with a $\hat{\phi}^i$ polarized fixed source at $\theta^i = 45°$, $\phi^i = 45°$. 160

136 Flat plate for RCS calculation with normal incidence. 170
137 Equivalent currents on a finite straight edge. 171
138 Relationship between the edge fixed coordinates and the pattern coordinates. 172

LIST OF TABLES

1 Delay times from different corners of the 6" cube. 140

CHAPTER I

INTRODUCTION

1.1 Objective

An approximate expression for the far zone field scattered by the vertex of a finite perfectly conducting wedge is obtained. The solution is cast in the form of the UTD and is based on asymptotic equivalent currents found using modified PTD concepts. The faces of the wedge must be flat (the normal to each individual face is a constant everywhere on the face except at the edge) and the edges must be straight. For plane wave incidence from an arbitrary direction the first order contribution from each vertex to the far zone scattered field is obtained.

1.2 Motivation

Since diffraction is a local phenomena at high frequencies the results obtained for a finite wedge may be applied to much more complex bodies made up of simple shapes. The field scattered by a three-dimensional shape constructed from flat plates may be approximated to first order as the sum of the contributions from each individual corner. The first order solution should be reasonably accurate in or near the specular regions as long as the object is convex. A convex body is defined here as a closed surface made up of flat plates such that all of the exterior wedge angles, taken between faces and exterior to the surface, are greater than 180 degrees. A simple example of an object that does not meet this requirement is a

corner reflector. The effect of shadowing of the faces by other parts of the object, however, must be taken into account. A brief description of how this is done is given in Section 5.2.

1.3 Problem History

There are many approximate solutions to the scattered field from a finite perfectly conducting wedge. Some of these include the Physical Optics approximation, the Method of Equivalent Currents [1], the previous Corner Diffraction coefficients [2], the Uniform Geometrical Theory of Diffraction [3],and the Physical Theory of Diffraction [4]. The Physical Optics, Method of Equivalent Currents, and Physical Theory of Diffraction will be described briefly in the next chapter. The previous Corner Diffraction Coefficient was heuristically derived from the equivalent currents of Ryan and Peters [1] and the Uniform Geometrical Theory of Diffraction [3]. Although it gives good results in the backscatter region, it has been found to give unsatisfactory results for certain bistatic cases. Specifically, it has problems at the so-called false shadow boundaries which will be illustrated in Chapter II.

1.4 Outline of Solution

It is assumed that the incident field, and therefore the scattered field, is a time harmonic field with time dependence given by $e^{j\omega t}$, which will be suppressed throughout this report. The solution will be based on the PTD and cast into the form of the method of equivalent currents and then into diffraction coefficients. This will be done as follows. The actual currents on each face of the plate will be approximated by the PTD currents. The resulting double integral over the surface is then reduced to a line integral along the edge by doing the integration over

one coordinate in closed form. This is done by taking the asymptotic endpoint contribution in one case and by the application of some algebraic manipulation followed by the use of Stoke's theorem in the other case. The remaining integral along the edge is written in the form of a radiation integral so that the equivalent currents may be identified. Then this integral is evaluated using the method of stationary phase to obtain the contribution from each corner.

1.5 Notation, Abbreviations and Symbols

This section contains some information on the notation, abbreviations, and symbols that are used in this report. Normally the term equivalent currents refers to the surface currents used in the equivalence theorem. In this report, however, the terms equivalent edge currents and equivalent currents will be used interchangeably to refer to equivalent edge currents.

1.5.1 Symbols

These are some of the symbols used. Most of them are also defined as they first appear in the text.

β = diffracted ray elevation angle in edge fixed coordinates

$\hat{\beta}$ = diffracted ray elevation unit vector in edge fixed coordinates

β' = incident ray elevation angle in edge fixed coordinates

$\hat{\beta}'$ = incident ray elevation unit vector in edge fixed coordinates

λ = free space wavelength of the time harmonic fields

ϕ = diffracted ray azimuth angle in edge fixed coordinates or in pattern coordinates (depending on context)

$\hat{\phi}$ = diffracted ray azimuth unit vector in edge fixed

coordinates or in pattern coordinates (depending on context)

ϕ' = incident ray azimuth angle in edge fixed coordinates or in pattern coordinates (depending on context)

$\hat{\phi}'$ = incident ray azimuth unit vector in edge fixed coordinates or in pattern coordinates (depending on context)

σ = Radar Cross Section

θ = diffracted ray elevation angle in pattern coordinates

$\hat{\theta}$ = diffracted ray elevation unit vector in pattern coordinates

θ' = incident ray elevation angle in pattern coordinates

$\hat{\theta}'$ = incident ray elevation vector in pattern coordinates

ω = angular frequency

$\hat{b}$ = bi-normal unit vector

$D_{s,h}$ = soft, hard diffraction coefficients

$D^c_{s,h}$ = soft, hard corner diffraction coefficients

D^c_2 = cross polarized corner diffraction coefficient (hard incidence, soft diffracted)

$\vec{E}^c$ = corner diffracted field

$\vec{E}^d$ = diffracted field

$\vec{E}^i, \vec{H}^i$ = incident field

E^i_t, H^i_t = components of the incident field tangent to the edge

F = transition function

j = $\sqrt{-1}$

$I_{e,m}$ = electric equivalent currents

k = $2\pi/\lambda$

M = magnetic equivalent current

n = wedge angle parameter

$\hat{n}$ = unit vector normal to the face of the wedge

$\hat{t}$ = unit vector tangent to the edge

$\hat{s}'$ = incident ray direction

$\hat{s}$ = diffracted ray direction

Y_0 = admittance of free space

Z_0 = impedance of free space

Components of the equivalent currents will be designated by placing appropriate superscripts on the symbols I_e, I_m, and M.

1.5.2 Abbreviations

GO = Geometrical Optics

GTD = Geometrical Theory of Diffraction

MM = Moment Method

PEC = Perfect Electrical Conductor

PO = Physical Optics

PTD = Physical Theory of Diffraction

RCS = Radar Cross Section

UTD = Uniform Geometrical Theory of Diffraction

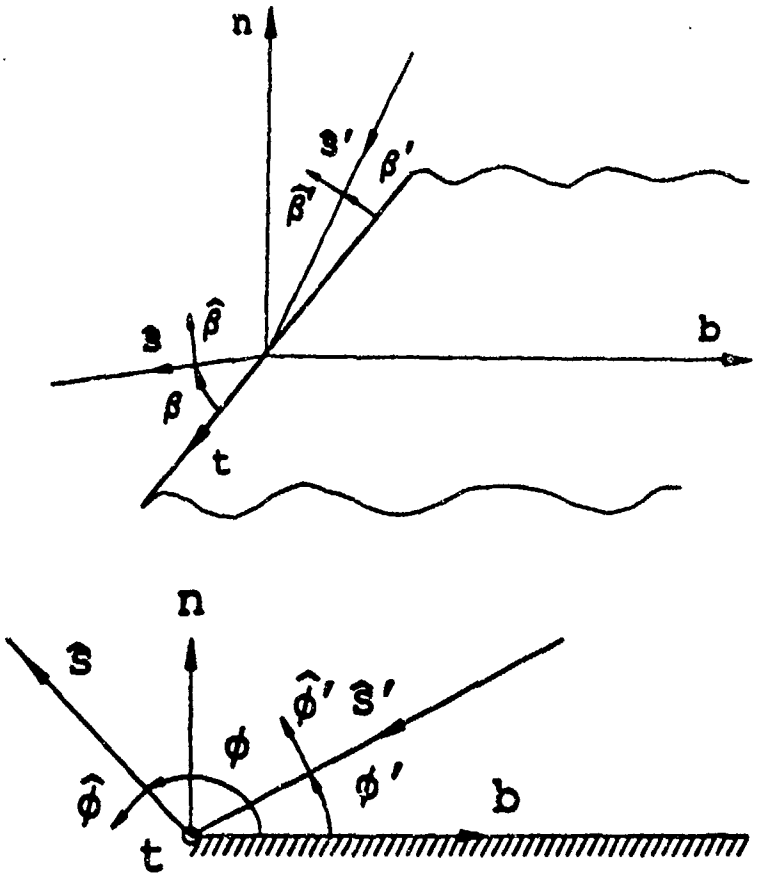

Figure 1: Edge Fixed Coordinates.

1.5.3 Edge Fixed Coordinate System

An edge fixed coordinate system will be used throughout the discussion of the equivalent currents and the corner diffraction coefficient. As shown in Figure 1, the origin of the right hand system (b,n,t) is placed on the edge. The point on the edge where the origin is placed will depend on the problem being considered and will be specified. The $\hat{n}$ direction is chosen so $\hat{n}$ is normal to the face under consideration and directed outward from the interior of the body. In the case of a flat plate the outward normal is ambiguous, and the positive $\hat{n}$ direction may be arbitrarily chosen in either of the two directions. The $\hat{t}$ axis is chosen tangent to

the edge. The positive $\hat{t}$ direction is chosen such that the positive $\hat{b}$ axis ($\hat{b} = \hat{n} \times \hat{t}$) will lie on the wedge face under consideration. Since only one face is considered at a time this results in a convenient and unambiguous coordinate system for all of the problems considered here.

The incident ray is described by the spherical coordinate system (s', β', ϕ') based on an axis in the $-\hat{t}$ direction. The incident field may, therefore, be described as a sum of its components in the $\hat{\beta}'$ and $\hat{\phi}'$ directions since it is always assumed to be a plane wave in this report. Similarly the diffracted rays are described by the spherical coordinate system (s, β, ϕ) based on an axis in the positive $\hat{t}$ direction. The radial component of the diffracted field will be zero in the far zone, resulting in a field which may be expressed in terms of its $\hat{\beta}$ and $\hat{\phi}$ components. The angles and unit vectors are shown in Figure 1.

1.5.4 Radar Cross Section

The numerical results are expressed in terms of Radar Cross Section throughout this report. Radar Cross Section is the mathematical area that intercepts the power from the incident wave on the target, which if scattered in an isotropic manner would produce the same scattered power density as produced by the actual target assuming that both the transmitter and the receiver are in the far zone of the target; i.e. $r_1, r_2 > 2D^2/\lambda$, where D is the maximum dimension of the target and r_1, r_2 are defined in Figure 2. Letting S^i= power density incident on the target from the transmitter (constant over the target for plane wave incidence); S^{sc}= power density scattered from the target toward the receiver (constant, see S^i) results in

$$\lim_{r_2 \to \infty} \left[\frac{\sigma S^i(\theta_t, \phi_t)}{4\pi r_2^2} \right] = S^{sc}(\theta_r, \phi_r). \tag{1.1}$$

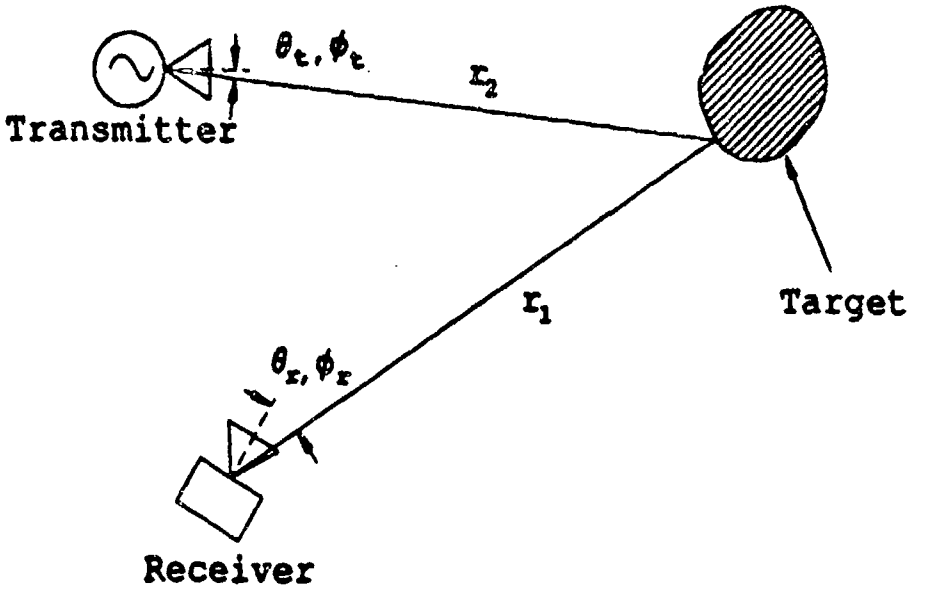

Figure 2: Definition of Distances r_1 and r_2.

Solving for σ gives

$$\sigma = \lim_{r_2 \to \infty} 4\pi r_2^2 \frac{S^{sc}(\theta_r, \phi_r)}{S^i(\theta_t, \phi_t)} \tag{1.2}$$

Since for most problems of practical importance and all of the problems done here the medium is free space the power densities are simply related to the fields by

$$S = \frac{|E|^2}{Z_0} = |H|^2 Z_0 \tag{1.3}$$

where $|E|$ and $|H|$ are the rms values of the electric and magnetic fields, respectively, at the point of interest, and Z_0 is the impedance of free space. Therefore the RCS reduces to

$$\sigma = \lim_{r_2 \to \infty} 4\pi r_2^2 \frac{|E^{sc}|^2}{|E^i|^2} = \lim_{r_2 \to \infty} 4\pi r_2^2 \frac{|H^{sc}|^2}{|H^i|^2} \tag{1.4}$$

where $|E^{sc}|$ and $|H^{sc}|$ are the magnitude of the scattered electric and magnetic fields, respectively, at the receiver and $|E^i|$ and $|H^i|$ are the magnitude of the incident electric and magnetic fields at the target.

1.6 Pattern Coordinate System

The usual spherical coordinate system is used for all of the results. The source is located in the far zone direction specified by the spherical angles θ' and ϕ' (or sometimes by θ^i and ϕ^i). Similarly the observation point is located in the far zone direction specified by the spherical angles θ and ϕ. In the special case of backscatter both the source and receiver locations will be indicated by θ and ϕ. Notice that ϕ and ϕ' are also used in defining the observation and source directions, respectively, in edge fixed coordinates, but it should be obvious from the context which angle is being identified. The RCS is given in terms of the polarization of the transmitted and received fields. The following definitions will be used throughout this report

$$\sigma_{\theta\theta} = 4\pi r_2^2 \frac{\left|E_\theta^{sc}\right|^2}{\left|E_{\theta'}^i\right|^2} \tag{1.5}$$

$$\sigma_{\phi\theta} = 4\pi r_2^2 \frac{\left|E_\phi^{sc}\right|^2}{\left|E_{\theta'}^i\right|^2} \tag{1.6}$$

$$\sigma_{\phi\phi} = 4\pi r_2^2 \frac{\left|E_\phi^{sc}\right|^2}{\left|E_{\phi'}^i\right|^2} \tag{1.7}$$

$$\sigma_{\theta\phi} = 4\pi r_2^2 \frac{\left|E_\theta^{sc}\right|^2}{\left|E_{\phi'}^i\right|^2} \tag{1.8}$$

where $\left|E_{\phi'}^i\right|$ and $\left|E_{\theta'}^i\right|$ are the magnitude of the $\hat{\phi}'$ and $\hat{\theta}'$ components, respectively, of the incident field at the target. Similarly $\left|E_\phi^{sc}\right|$ and $\left|E_\theta^{sc}\right|$ are the $\hat{\phi}$ and $\hat{\theta}$ components of the scattered field at the receiver. The first subscript on σ refers to the polarization of the received field; whereas, the second one refers to the polarization of the incident field, both in pattern coordinates. For the general case of bistatic scattering, the notation will remain the same even though $\hat{\theta}$ and $\hat{\theta}'$ (and

$\hat{\phi}$ and $\hat{\phi}'$) are in different directions. All results shown are given in terms of either dB relative to a square meter or dB relative to a square wavelength depending on the specific problem. They are simply related to the above expressions by

$$\sigma(in\ dB) = 10\log_{10}\sigma \tag{1.9}$$

or

$$\sigma(in\ dB) = 20\log_{10}\left(r_2\frac{|E^{sc}|}{|E^i|}\right) + 10\log_{10}(4\pi) \tag{1.10}$$

for each of the combinations of transmitting and receiving polarizations.

CHAPTER II

THEORETICAL BACKGROUND

2.1 Introduction

The high frequency methods used to derive the new far zone corner diffraction coefficients are described briefly here. Geometrical Optics (GO) and Physical Optics (PO) are discussed first since both of these are important in the implementation of the new solution. The basic concepts of the Physical Theory of Diffraction (PTD) are then given. Following this is a description of the differences between the Method of Equivalent Currents as proposed by Ryan and Peters [1] and the method used to derive the new equivalent currents. A corner diffraction coefficient based on the old equivalent currents is also given. The results from the method of stationary phase are then described briefly.

2.2 Geometrical Optics

A brief summary of Geometrical Optics (GO) is given here. Further information on the subject may be found in references [5] - [8], and the basic principles are covered in many antennas textbooks, such as [9]. The propagation of electromagnetic energy through isotropic, lossless media can be described using GO. It has long been known that at high frequencies electromagnetic energy can be viewed as traveling along well defined paths known as rays. The ray paths, in any continuous medium, may be determined using Fermat's principle which states

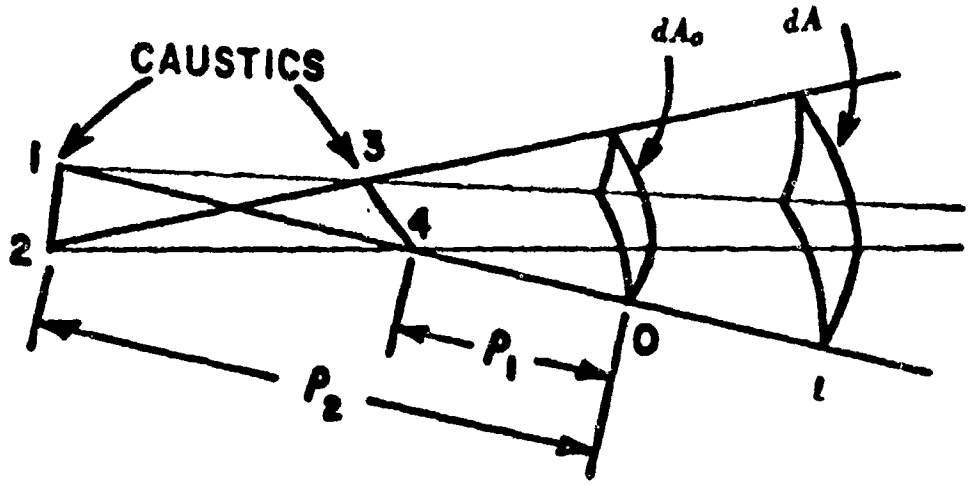

Figure 3: Astigmatic ray tube.

the energy will flow along the path of shortest electrical length between any two points in the medium. The shortest electrical path is the path which results in the shortest propagation time between the two points. Furthermore, these rays are orthogonal to surfaces of constant phase. If the media is also homogeneous, which is true in this case, the ray paths are straight lines. Assuming the field is known at some constant phase reference surface, it can be calculated at any point away from caustics using conservation of energy. Referring to Figure 3, if the field is known at some constant phase surface dA_0 along with the principle radii of curvature, ρ_1 and ρ_2, of the surface dA_0 then the field at dA may be calculated using the conservation of energy and the above assumption that the electromagnetic energy travels in straight lines. Since the energy flux at both of the surfaces is proportional to the square of the field, it follows from the conservation of energy that

$$\left|\vec{E}(0)\right|^2 dA_0 = \left|\vec{E}(\ell)\right|^2 dA \,. \tag{2.1}$$

From geometric considerations it can be shown that

$$\frac{dA}{dA_0} = \left|\frac{(\rho_1+\ell)(\rho_2+\ell)}{\rho_1\rho_2}\right| \tag{2.2}$$

Combining these two equations gives

$$\left|\vec{E}(\ell)\right| = \left|\vec{E}(0)\right| \sqrt{\left|\frac{\rho_1\rho_2}{(\rho_1+\ell)(\rho_2+\ell)}\right|} \tag{2.3}$$

where it is assumed that the positive ℓ direction is in the direction of propagation and the principle radii of curvature ρ_1 and ρ_2 may be both positive (concave wave front), both negative (convex wave front), or opposite in sign (saddle wave front). The complete expression for the field, one that includes the phase as well as the magnitude of the field, must be obtained from the asymptotic solution of Maxwell's equations and is given by

$$\vec{E}(\ell) = \vec{E}(0)\sqrt{\left|\frac{\rho_1\rho_2}{(\rho_1+\ell)(\rho_2+\ell)}\right|}e^{-j(k\ell-m\frac{\pi}{2})} \tag{2.4}$$

where m is the number of caustics the ray passes through going from O to ℓ. For example, m=0 for points to the right of the caustic labeled 3-4 as shown in Figure 3, m=1 for points between 1-2 and 3-4, and m=2 for points to the left of 1-2. It has been assumed that the wave is traveling from left to right so ℓ is positive to the right of O and negative to the left of O. GO obviously fails at the caustics where it predicts that the field becomes infinite.

Only two special cases are of interest here. Letting $\rho_1, \rho_2 \rightarrow \infty$ and replacing ℓ with s gives: $\vec{E}(s) = \vec{E}(0)e^{-jks}$ which is the well known result for a plane wave propagating in the positive s direction where E(0) is the field at any convenient constant phase plane, and s is the distance from the reference plane to the point of interest. The spherical wave is the second case of interest here. In this case, $\rho_1 = \rho_2 = \rho$ giving

$$\vec{E}(s) = \vec{E}(0)\left|\frac{\rho}{\rho+s}\right| e^{-j(ks-m\frac{\pi}{2})} \tag{2.5}$$

letting the reference point approach the caustic and assuming $\rho\vec{E}(0) \rightarrow \vec{A}_s$ as

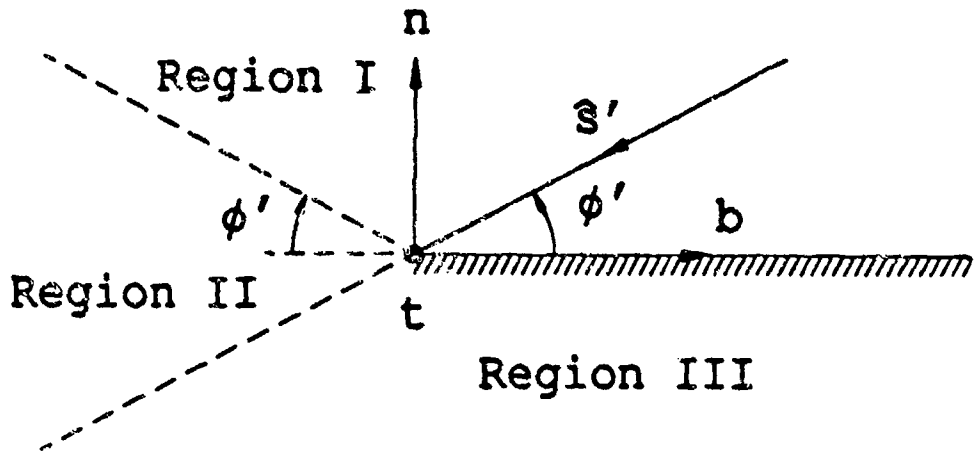

Figure 4: Projection of rays on to b-n plane.

$\rho \to 0$ gives

$$\vec{E}(s) = \vec{A}_s \frac{e^{-jks}}{s} \tag{2.6}$$

which is the familiar spherical wave result. Notice that m=0 in both cases since no caustics are crossed.

2.3 Geometrical Theory of Diffraction

If Fermat's principle is extended to include refraction, reflection, and diffraction points then GO may be extended to media with discontinuities in electrical characteristics. This means that not only is the field from the direct or line-of-sight path included, but also paths which include points on the surface where the media is discontinuous. In this case the discontinuity is a wedge with perfectly conducting flat faces. The edge-fixed coordinate system described earlier is used. The projection of the rays onto the b-n plane is shown in Figure 4. For a fixed source, the observation point may be in one of three regions around the wedge. In region I ($0 < \phi < \pi - \phi'$), all three rays contribute to the total field. In region II ($\pi - \phi' < \phi < \pi + \phi'$), only the direct and diffracted fields contribute to the

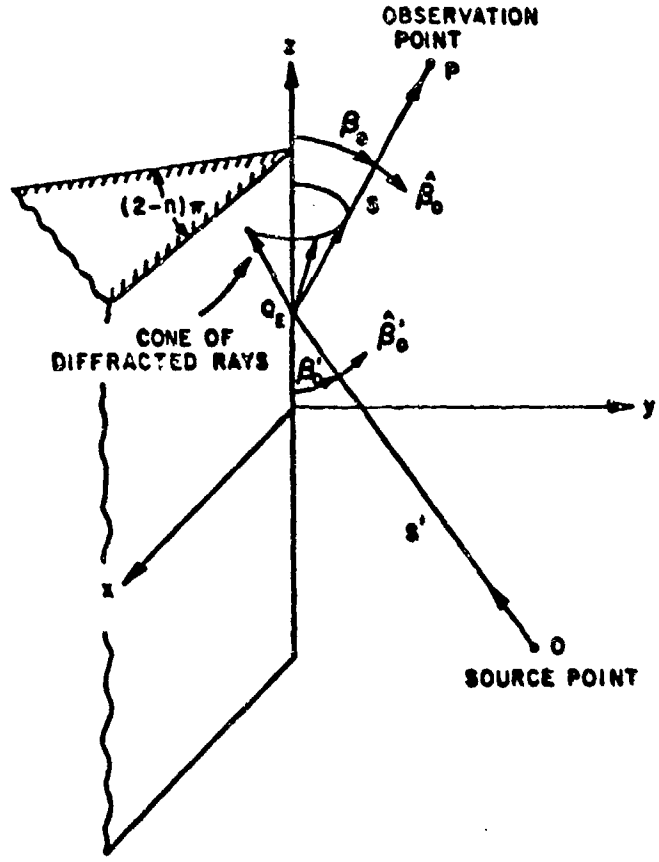

Figure 5: Keller's cone of diffracted rays.

total field since no point on the wedge satisfies the law of reflection. In region III ($\pi + \phi' < \phi < n\pi$), only the diffracted field contributes to the total field. Notice that, in general, the reflected field is discontinuous at the reflection shadow boundary ($\phi + \phi' = \pi$), and the direct field is discontinuous at the incident shadow boundary ($\phi - \phi' = \pi$). Keller [10] derived an expression for the diffracted field in terms of the field incident on the edge and showed that the major contribution comes from a single point (the diffraction point). The condition $\beta = \beta'$ is met at the diffraction point. The cone of rays that satisfy this condition for a given point along the edge is known as the Keller cone (see Figure 5). Keller's results for the diffracted field were only for observation points away from the shadow boundaries.

Kouyoumjian and Pathak [3] later formulated the Uniform Geometrical Theory of Diffraction (UTD) which extended the solution to all regions of space. The results, in terms of the edge fixed coordinates shown earlier in Figure 1, for a plane wave incident from the direction (β',ϕ') and a far field observation direction at (β,ϕ) are given by

$$\begin{bmatrix} E^d_\beta \\ E^d_\phi \end{bmatrix} = -\begin{bmatrix} D_s & 0 \\ 0 & D_h \end{bmatrix} \begin{bmatrix} E^i_{\beta'}(Q_e) \\ E^i_{\phi'}(Q_e) \end{bmatrix} \frac{e^{-jks}}{s} \tag{2.7}$$

where

$$\begin{aligned} D_{s,h} &= \frac{-e^{-j\frac{\pi}{4}}}{2n\sqrt{2\pi k}\sin\beta'} \left\{ \left[\cot\left(\frac{\pi-(\phi-\phi')}{2n}\right) + \cot\left(\frac{\pi+(\phi-\phi')}{2n}\right) \right] \right. \\ &\quad \left. \mp \left[\cot\left(\frac{\pi-(\phi+\phi')}{2n}\right) + \cot\left(\frac{\pi+(\phi+\phi')}{2n}\right) \right] \right\} . \end{aligned}$$

Q_e is the point on the wedge which satisfies the condition $\beta = \beta'$, $E^i_{\beta'}(Q_e)$ is the component of the incident field in the $\hat{\beta}'$ direction at Q_e and $E^i_{\phi'}(Q_e)$ is the component of the incident field in the $\hat{\phi}'$ direction at Q_e (see Figure 5). The diffracted field is described in terms of transverse components, $\hat{\beta}$ and $\hat{\phi}$, at a far zone distance s. The first and third cotangent terms have been associated with the O-face incident and reflection boundaries, respectively. Similarly the second and fourth cotangent terms are associated with the N-face incident and reflection boundaries.

2.4 Physical Optics

Physical Optics is a widely used technique for finding the field scattered by a perfectly conducting body of arbitrary shape. The physical optics approximation to the surface current is given in [11] by:

$$\vec{J}_{PO} = \begin{cases} 2\hat{n} \times \vec{H}^i \text{ ; } \textit{in lit regions} \\ 0 \text{ ; } \textit{in shadow regions} \end{cases} \tag{2.8}$$

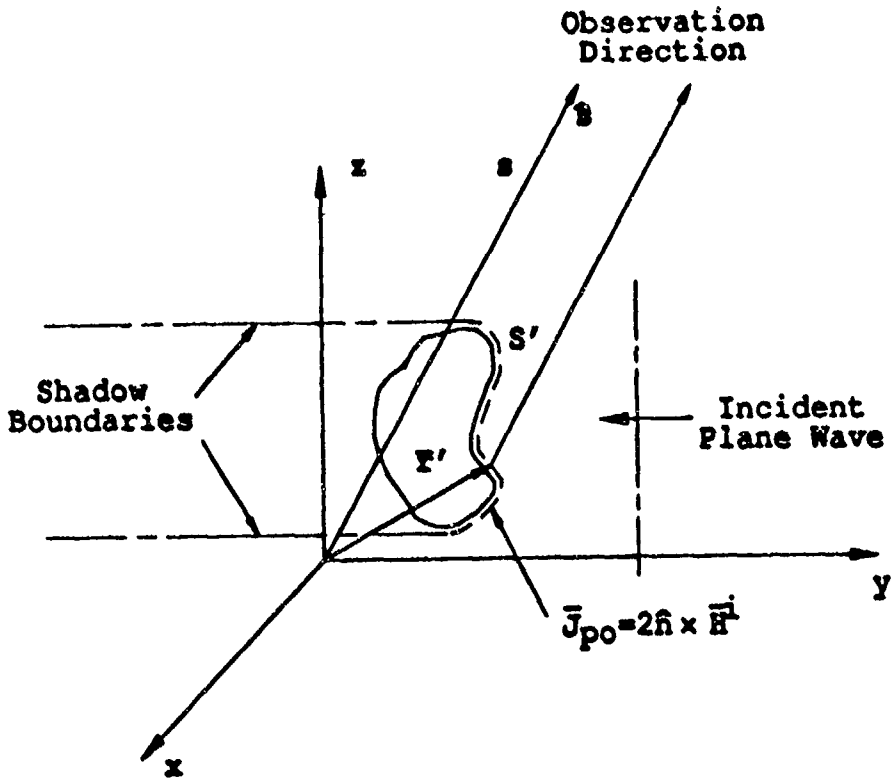

Figure 6: PO Currents on an arbitrary scatterer.

where the illuminated and shadowed regions are determined using ray optics, and $\vec{H}^i$ is the incident magnetic field on the surface of the perfectly conducting body and is approximated by the GO incident field in this case. Since only far zone sources are considered here the incident field will always be locally plane and the rays will be parallel. A simple 2-D example illustrating the lit and shadowed regions is given in Figure 6.

The scattered field is found using the far zone radiation integral which is defined by

$$\vec{E}^s(s) = \frac{jkZ_0}{4\pi}\frac{e^{-jks}}{s}\int_{S'}\vec{J}(\vec{r}')e^{jk\hat{s}\cdot\vec{r}'}dS' \ . \tag{2.9}$$

Plugging in the PO approximation to the surface current gives:

$$\vec{E}^s(s) = \frac{jkZ_0}{4\pi}\frac{e^{-jks}}{s}\int_{S'}2\hat{n}\times\vec{H}^i(\vec{r}')e^{jk\hat{s}\cdot\vec{r}'}dS' \tag{2.10}$$

where S' is the illuminated region on the scattering surface and $s, \hat{s}$, and $\vec{r'}$ are defined in Figure 6.

2.5 Physical Theory of Diffraction

The Physical Theory of Diffraction was first widely used for scattering problems by Ufimtsev [4]. Additional currents are added to the Physical Optics currents so that the solution is valid for larger regions of space and for smaller scatterers than is possible with either GO or PO. Letting the total surface current be $\vec{J} = \vec{J}_{PO} + \vec{J}_f$ where $\vec{J}_f$ is the correction to the PO current which when added to the PO current would approximate the actual current on the scatterer. Since the PO current is derived from the assumption that the surface may be locally approximated as an infinite plane tangent to the surface, it is expected that $\vec{J}_f$ could be described as the current due to the deviation of the surface from an infinite plane. The sharp edge or wedge is the only deviation from a planar surface considered here. Ufimtsev speculated that this correction to the PO current would only be important near the edges of the scatterer in this case.

Assuming plane wave incidence, the magnitude of the PO component of the current is constant on the illuminated region of a planar scatterer so Ufimtsev named this the uniform component of the current. The magnitude of the correction current is obviously not constant on the surface and is thus called the nonuniform component of the current. In the case of a wedge, Ufimtsev refers to the field radiated by the nonuniform part of the current as an elementary edge wave or simply an edge wave since it is produced by the nonuniform part of the current which is concentrated along the edge and rapidly decreases away from the edge. In his latest paper [12], however, it seems as though he refers to the scattered field as the total edge wave and the field due to the correction current, $\vec{J}_f$, on an

infinitesimal strip of the wedge as the elementary edge wave. In this case the only contribution to the nonuniform current $\vec{J}_f$ is due to the edge discontinuities. If the edges are long in terms of the wavelength and have radii of curvature which are also long in terms of the wavelength the total current may be approximated by the current on an infinite wedge tangent to the scatterer at the point of interest. The nonuniform component of the current may then be found by subtracting the GO current from this approximation to the total current. Ufimtsev calls the approximation to the nonuniform current given by the infinite wedge the fringe current, and the field produced by this current the fringing field. Ufimtsev never actually found the fringe current, instead he found the fringing field by indirect considerations. In recent years both Michaeli [13,14] and Ufimtsev [12,15] have derived expressions for the fringing field involving expressions for the fringe current on the wedge. Michaeli's expressions for the fringe current will be used in the later development of the corner diffraction coefficient.

2.6 Method of Equivalent Currents

The method of equivalent currents was originally used by Millar in [16] - [18]. Ryan and Peters [1] used the method of equivalent currents to find the diffracted field in the region of caustics of the UTD diffracted field. Ryan and Peters equivalent currents have been used to find the original corner diffraction solution shown in the next section. Ryan and Peters equivalent currents are discussed here since they may be used to illustrate some important points about the use of equivalent currents in general. A brief description of the methods of finding the new equivalent currents used in the corner diffraction coefficient will be given.

Ryan and Peters compared the asymptotic approximation to the far zone diffracted fields from an infinite wedge illuminated by a plane wave to the expres-

sions for the far zone fields radiated by infinite magnetic and electric line sources. Equating the two fields, they obtained expressions for the equivalent edge currents which depend on the direction of incidence and the direction of observation. The field scattered by an arbitrary three-dimensional body made up of smoothly curved faces terminated in sharp edges is found by numerically evaluating the usual radiation integral along the edges of the scatterer using the equivalent currents. These equivalent edge currents are obviously not physical currents since they are functions of the observation point. They are a means of mathematically simplifying the problem of finding the diffracted field.

It was shown later by Northrop [19] and Sikta, *et al.* [2] that if the surfaces were represented by very thin strips oriented in the proper direction, the solution was more accurate for three-dimensional problems. The strips are oriented in a direction such that the angle between the vector tangent to the edge ($\hat{t}$) and the strip is given by

$$\tan\theta_s = -\tan\beta' \cos\phi' \quad 0 \leq \theta_s \leq \pi \tag{2.11}$$

as shown in Figure 7. This orients the strips so that the incident ray is normal to the infinitesimal edge on each strip.

Later, it was found by Marhefka [20] that for the case of bistatic scattering changing the orientation of the strips, in general improved the results. The modification used is simply to replace $\vec{e}_*$ given in [2] by:

$$\vec{e}_* = \frac{(\hat{I} - \hat{s}) \times \hat{n}}{\left|(\hat{I} - \hat{s}) \times \hat{n}\right|} \left\{ \frac{(\hat{I} - \hat{s}) \times \hat{n}}{\left|(\hat{I} - \hat{s}) \times \hat{n}\right|} \cdot \hat{e}_p \right\} \tag{2.12}$$

where $\hat{s}$ is the diffraction direction, $\hat{I}$ is the incident ray direction, $\hat{n}$ is the normal to the face, and $\hat{e}_p$ is the edge vector. This expression reduces to the expression for $\hat{e}_*$ given in [2] for the special case of backscatter. This replacement is equivalent

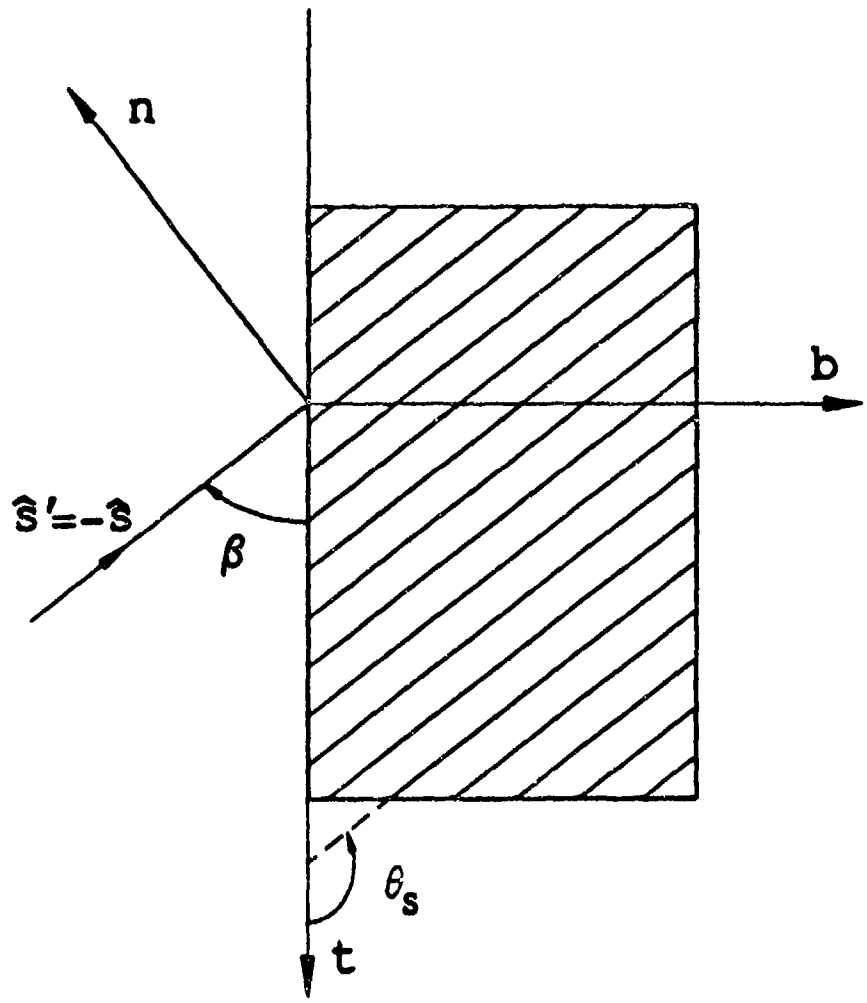

Figure 7: Strips used in Ryan and Peters Equivalent Currents by Sikta [2].

to placing the strips such that:

$$\cot\theta_s = \frac{\cos\beta - \cos\beta'}{\sin\beta\cos\phi + \sin\beta'\cos\phi'} \quad 0 \le \theta_s \le \pi \tag{2.13}$$

where θ_s is measured as illustrated in Figure 7. It is interesting to note that this is the strip orientation associated with the PO surface integral (see Section 4.7).

As a result of the two-dimensional nature of the solution and the orientation of the strips, the scattered field predicted by the equivalent currents is singular at the so-called false shadow boundaries. The false shadow boundaries are the regions of space where the two-dimensional problem goes through a shadow boundary ($\phi \pm \phi' = \pi$), but the three-dimensional problem does not ($\beta \neq \beta'$). The major reason for this problem is the two-dimensional nature of the solution. A simple example is given next illustrating this property.

The bistatic scattering from a flat plate two wavelengths on a side is calculated using the equivalent currents given in [2] with the replacement of $\hat{e}_*$ as described above. A fixed source is placed at $\theta^i = 45°$ and $\phi^i = 0°$ as shown in Figure 8. The pattern is taken in the $\phi = 60°$ plane and the results are illustrated for the entire scattering matrix. The results using the previous equivalent currents are compared with Method of Moments results in Figures 9 to 12 for the four different combinations of incident field and diffracted field polarizations. In all four cases, the previous equivalent current solution is singular at the false shadow boundaries ($\theta \approx 240°$ and $\theta \approx 300°$ in this case). The spikes are due to singularities in the contributions from both the front and back edges which have false shadow boundaries at both $\theta \approx 240°$ and $\theta \approx 300°$.

The idea of using infinitesimal strips to represent a flat face is used again in deriving the new equivalent currents; however, the strips are oriented in a different direction in finding the new equivalent currents. A different approach is used to

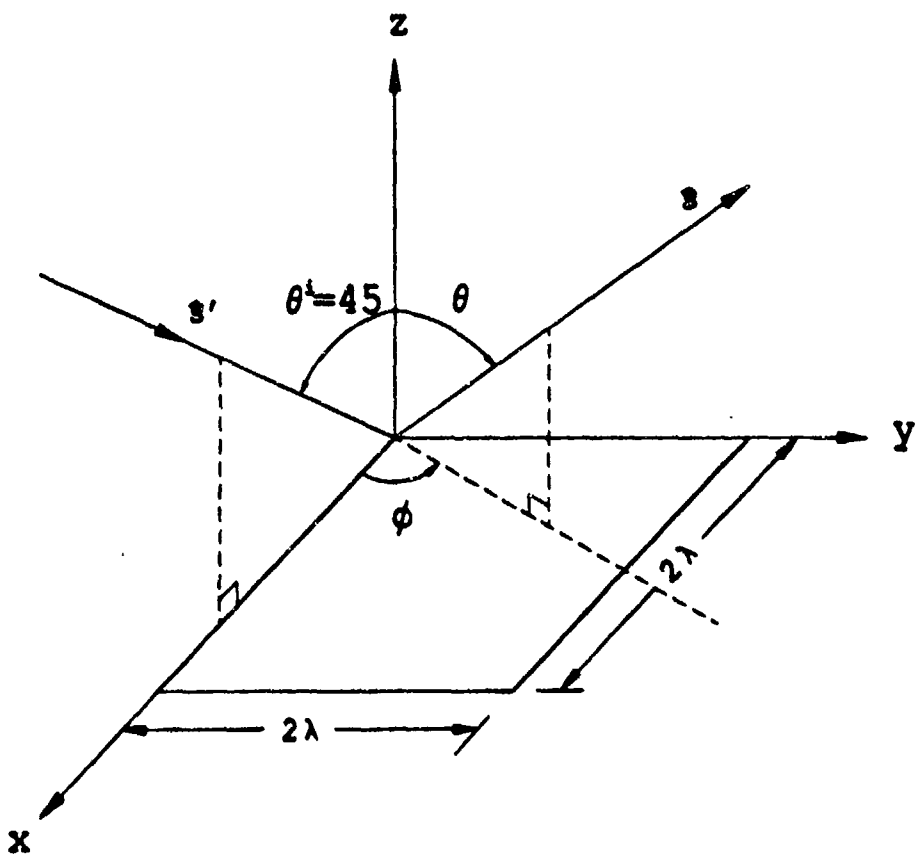

Figure 8: False Shadow Boundary example geometry (2λ square plate in the x-y plane).

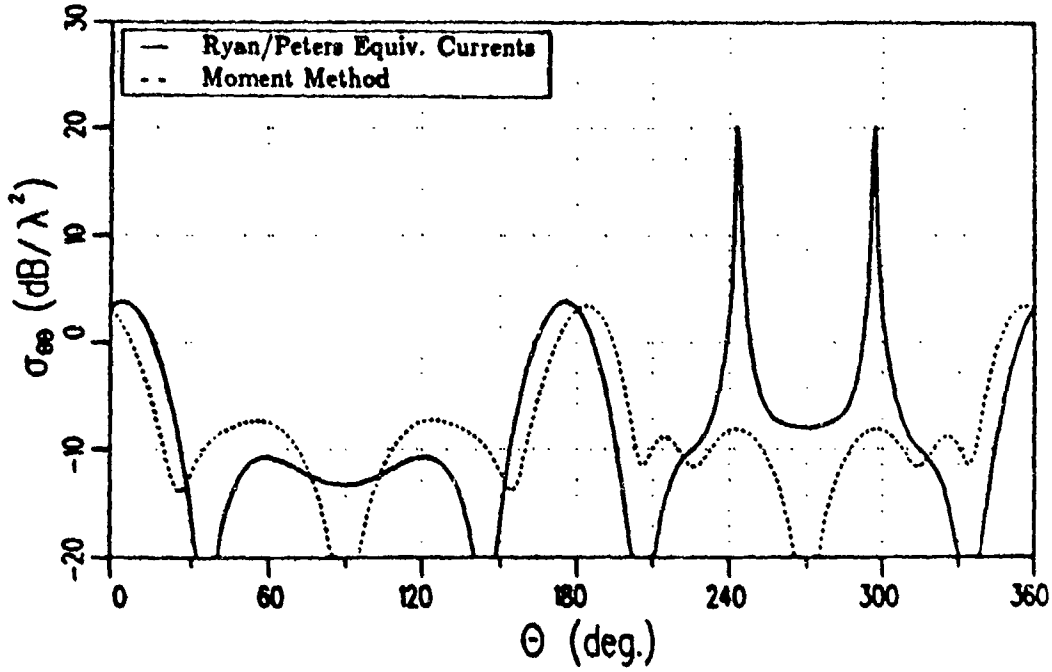

Figure 9: Co-polarized RCS in the $\phi = 60°$ plane of a 2λ square plate with a $\hat{\theta}^i$ polarized fixed source at $\theta^i = 45°$, $\phi^i = 0°$.

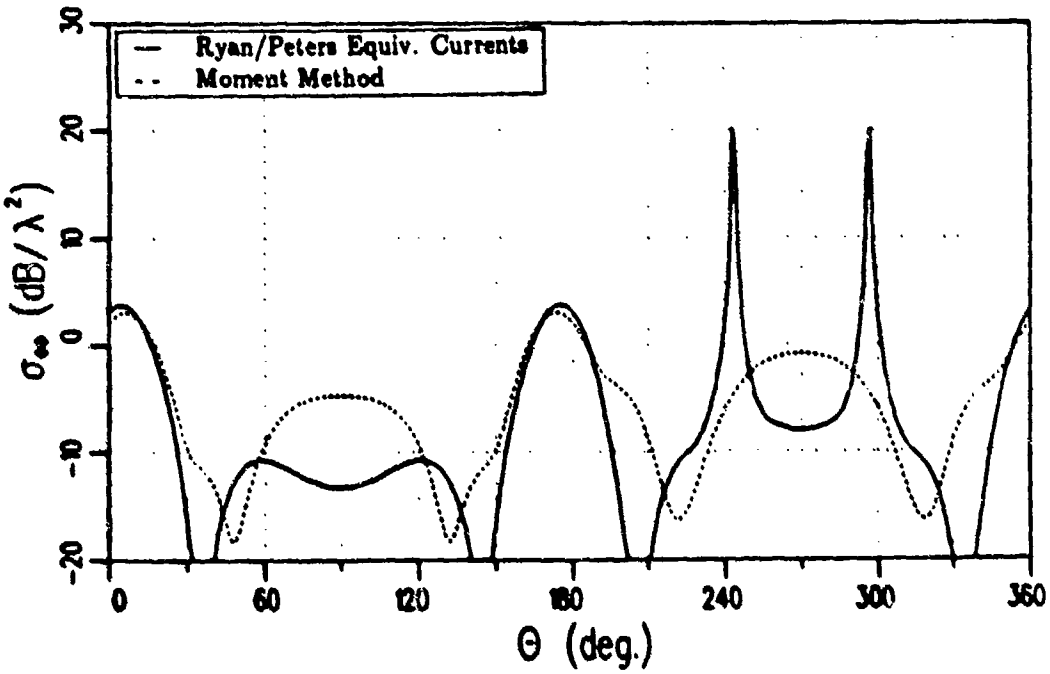

Figure 10: Co-polarized RCS in the $\phi = 60°$ plane of a 2λ square plate with a $\hat{\phi}^i$ polarized fixed source at $\theta^i = 45°$, $\phi^i = 0°$.

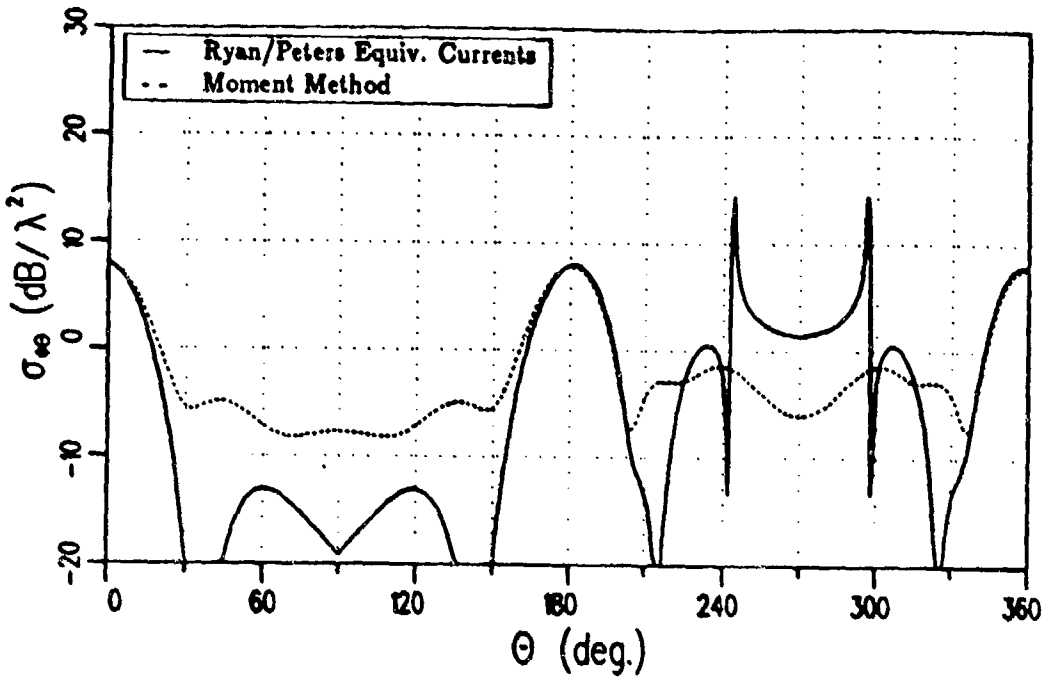

Figure 11: Cross-polarized RCS in the $\phi = 60°$ plane of a 2λ square plate with a $\hat{\theta}^i$ polarized fixed source at $\theta^i = 45°$, $\phi^i = 0°$.

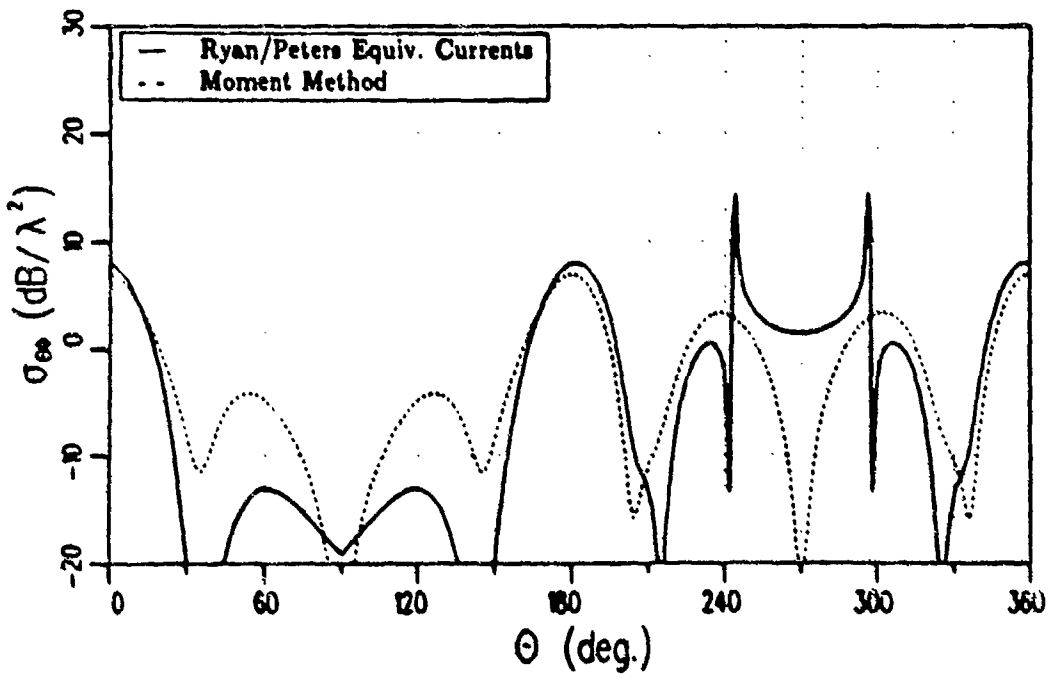

Figure 12: Cross-polarized RCS in the $\phi = 60°$ plane of a 2λ square plate with a $\hat{\phi}^i$ polarized fixed source at $\theta^i = 45°$, $\phi^i = 0°$.

find the new equivalent edge currents, and different expressions are obtained. The scattered field is found from the new equivalent edge currents in the same way as it is found from Ryan and Peters previous expressions. The new equivalent currents, however, predict smooth fields at the false shadow boundaries. This is illustrated in Section 5.3.7 where the above example is repeated for the new equivalent currents.

2.7 Previous Corner Diffraction Coefficient

A diffraction coefficient for a corner formed by the intersection of two straight edges was derived by Burnside and Pathak [2]. It is based on the asymptotic evaluation of the radiation integral containing the equivalent currents of Ryan and Peters [1] The result was then empirically modified so that the diffraction coefficient would not change sign abruptly as it passes through the false shadow boundaries. It was derived for spherical wave incidence and remains valid for cases when the diffraction point is near the corner since the integral was evaluated for a saddle point near an end point; however, only the far zone result is shown here. The corner diffracted field due to one corner and one edge in the case of plane wave incidence and a far zone receiver is given by

$$\begin{bmatrix} E^c_{\beta_o} \\ E^c_{\phi} \end{bmatrix} = -\begin{bmatrix} E^i_{\beta'_o}(Q_c)\, D^c_s\left(\phi,\phi',\beta_o,\beta_{oc}\right) \\ E^i_{\phi'}(Q_c)\, D^c_h\left(\phi,\phi',\beta_o,\beta_{oc}\right) \end{bmatrix} \frac{e^{-jks}}{s} \tag{2.14}$$

$$\begin{bmatrix} D^c_s \\ D^c_h \end{bmatrix} = \mp \begin{bmatrix} C_s(Q_e) \\ C_h(Q_e) \end{bmatrix} \frac{\sqrt{\sin\beta_o \sin\beta_{oc}}}{(\cos\beta_{oc} + \cos\beta_o)} \frac{e^{-j\frac{\pi}{4}}}{\sqrt{2\pi k}} \tag{2.15}$$

$$\begin{aligned} C_{s,h}(Q_e) &= \frac{-e^{-j\frac{\pi}{4}}}{2n\sqrt{2\pi k}\sin\beta_o} \Big\{ \left[D^c_o(\phi-\phi') + D^c_n(\phi-\phi') \right] \\ &\mp \left[D^c_o(\phi+\phi') + D^c_n(\phi+\phi') \right] \Big\} \\ D^c_{o,n}(\psi) &= D_{o,n}(\psi) \left| F\left[\frac{\sin^2\beta_o a^{\mp}(\psi)}{2\pi a(\beta_{oc}+\beta_o)} \right] \right| \end{aligned}$$

$$a(\beta) = 2\cos^2\left(\frac{\beta}{2}\right), \quad a^{\mp}(\psi) = 2\cos^2\left(\frac{2n\pi N^{\mp} - \psi}{2}\right)$$

where $N^{\mp}$ is the integer which most nearly satisfies $2n\pi N^{\mp} - \psi = \mp\pi$, and

$$\begin{aligned} D_{o,n}(\psi) &= \cot\left[\frac{\pi \mp \psi}{2n}\right] \\ \beta_a &= \frac{\pi + \beta_o - \beta oc}{2} \\ F(x) &= 2j\left|\sqrt{x}\right| e^{jx} \int_{|\sqrt{x}|}^{\infty} e^{-j\tau^2} d\tau \end{aligned} \tag{2.16}$$

where the angles are shown in Figure 13. The sign on the diffraction coefficient may be plus or minus depending on which endpoint of the edge is being considered. Choosing the correct sign is discussed in Section 3.5.

The heuristic factor added to the corner diffraction coefficients changes the behavior of the solution at the false shadow boundaries, as illustrated in the next example. The bistatic scattering example from Section 2.6 (2λ square plate, source fixed at $\theta^i = 45°$ and $\phi^i = 0°$, and $\phi = 60°$ pattern) is repeated here using the corner diffraction coefficients. The results for the four different combinations of incident and diffracted polarizations are shown in Figures 14 to 17. As the figures show, the previous corner diffraction solution is discontinuous at the false shadow boundaries ($\theta \approx 240°$ and $\theta \approx 300°$) of the front and back edges.

2.8 Stationary Phase Method

The stationary phase method is a widely used method for asymptotically evaluating a certain class of integrals described below. The results are stated. Further information on the stationary phase method and asymptotic series is given in [21] for the following

$$I(\kappa) = \int_a^b F(x) e^{j\kappa\phi(x)} dx \tag{2.17}$$

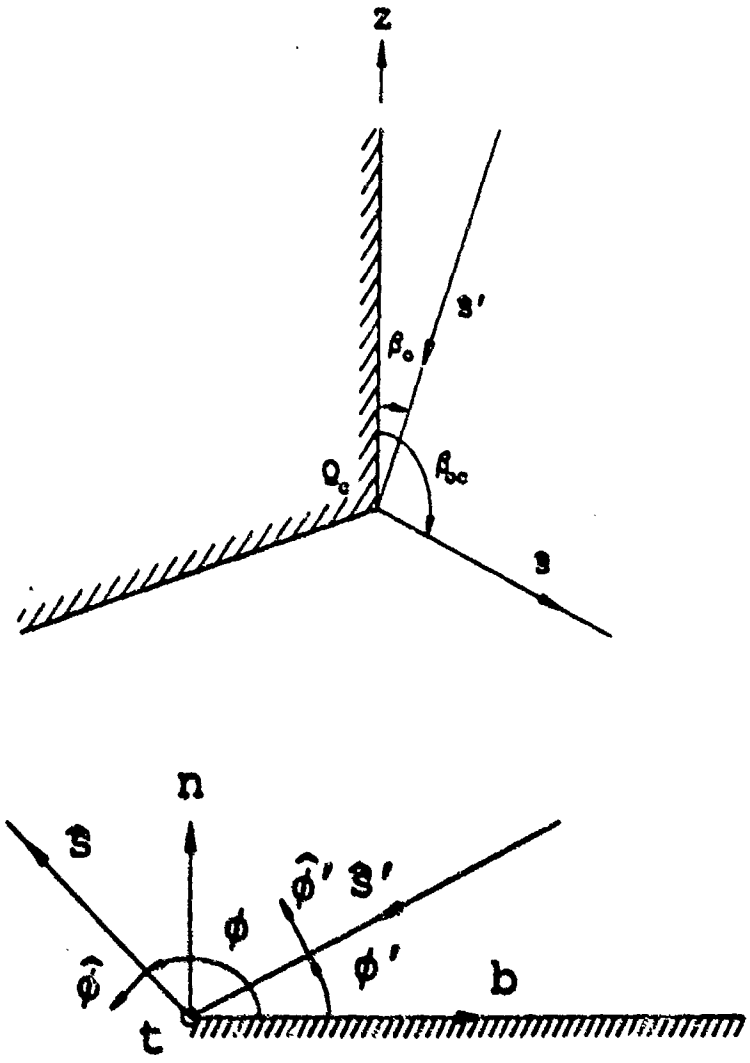

Figure 13: Definition of angles for the Corner Diffraction Coefficients.

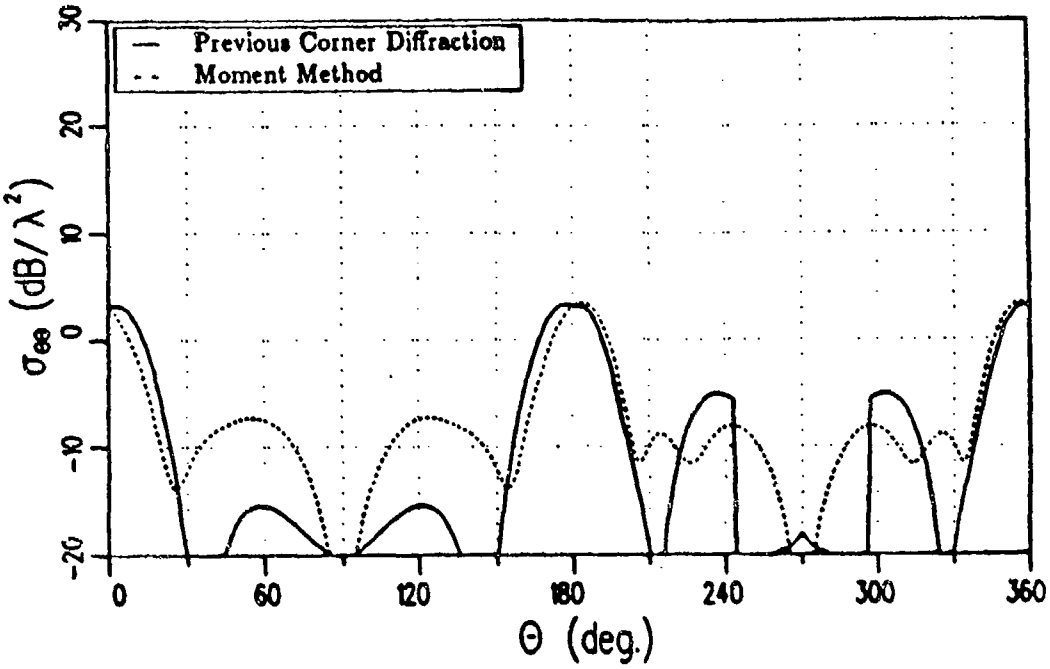

Figure 14: Co-polarized RCS in the $\phi = 60°$ plane of a 2λ square plate with a $\hat{\theta}^i$ polarized fixed source at $\theta^i = 45°$, $\phi^i = 0°$.

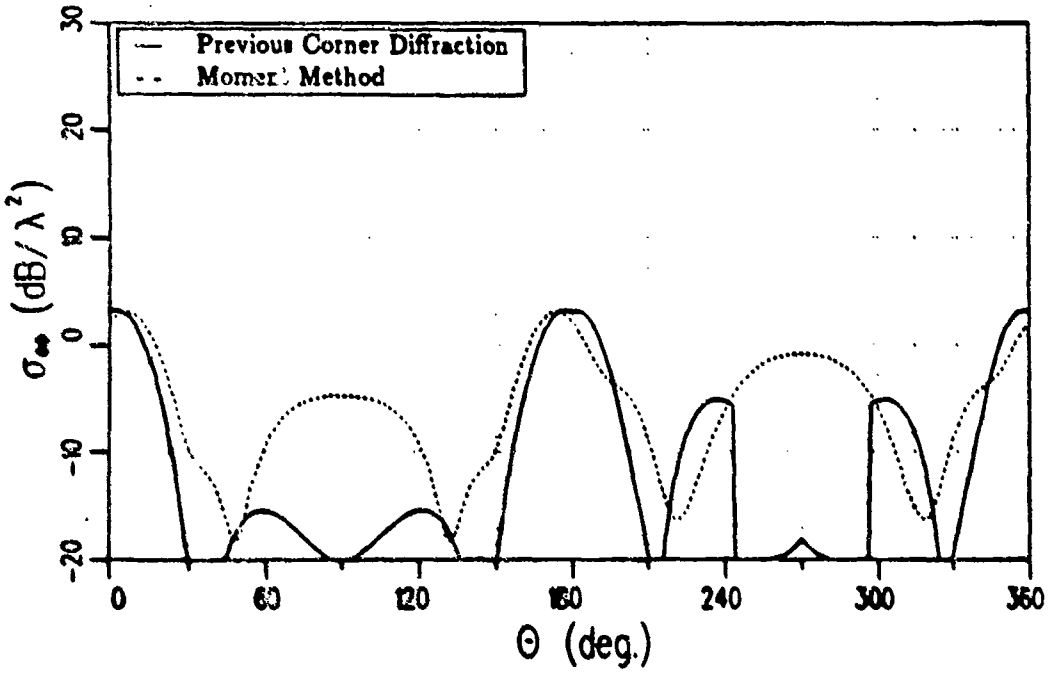

Figure 15: Co-polarized RCS in the $\phi = 60°$ plane of a 2λ square plate with a $\hat{\phi}^i$ polarized fixed source at $\theta^i = 45°$, $\phi^i = 0°$.

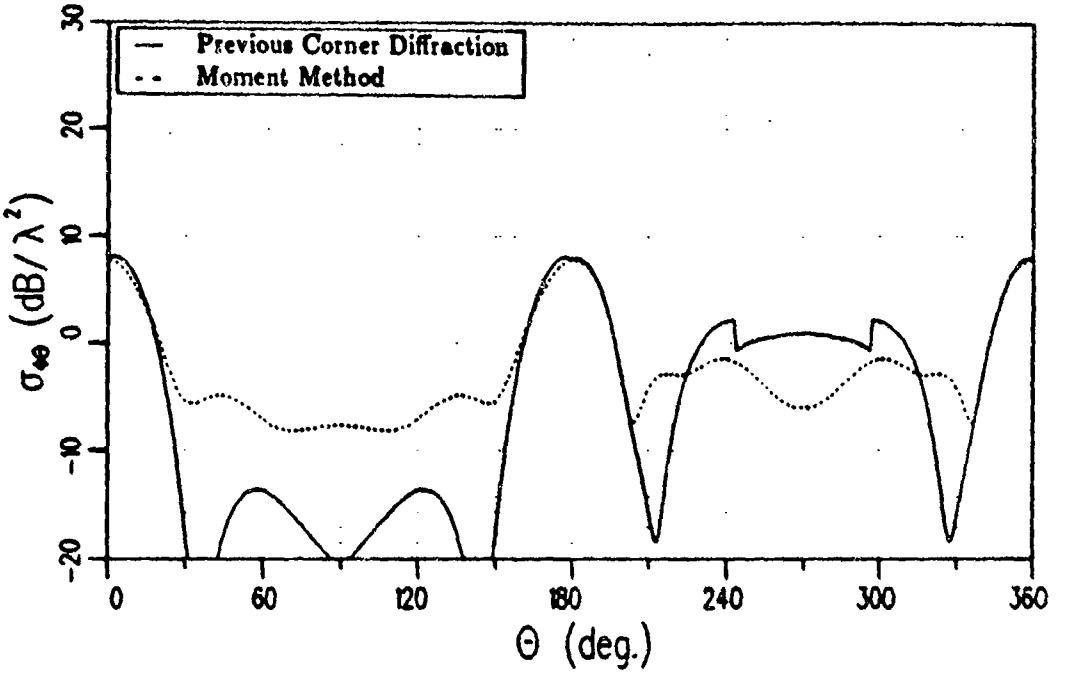

Figure 16: Cross-polarized RCS in the $\phi = 60°$ plane of a 2λ square plate with a $\hat{\theta}^i$ polarized fixed source at $\theta^i = 45°$, $\phi^i = 0°$.

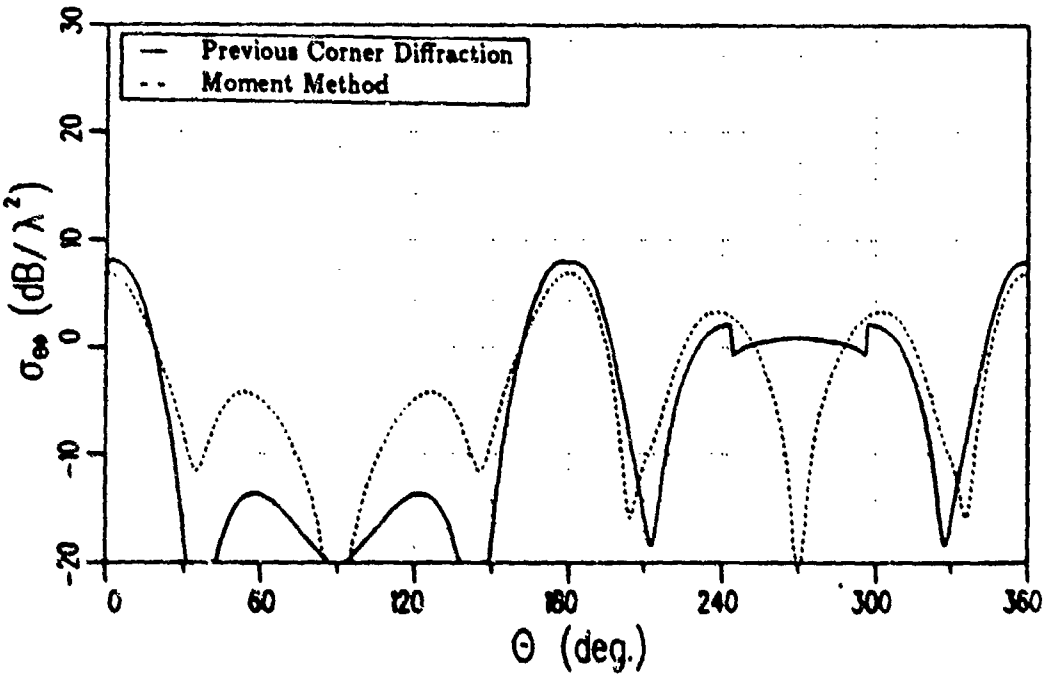

Figure 17: Cross-polarized RCS in the $\phi = 60°$ plane of a 2λ square plate with a $\hat{\phi}^i$ polarized fixed source at $\theta^i = 45°$, $\phi^i = 0°$.

where x is a real variable; κ is real, positive and large; $\phi(x)$ is a real, continuous function with continuous derivatives for $a \leq x \leq b$; $\phi'(x_s) = 0$,for $a < x_s < b$ and x_s is not close to a or b. Note that F(x) is a complex function which is slowly varying and well-behaved on [a,b] then $I(\kappa)$ is asymptotically approximated by

$$\begin{aligned} I(\kappa) &\sim F(x_s)\sqrt{\frac{2\pi}{\kappa\left|\phi''(x_s)\right|}}e^{j\left[\kappa\phi(x_s)+\frac{\pi}{4}sgn(\phi''(x_s))\right]} \\ &+ \frac{1}{\kappa}\frac{F(b)}{\phi'(b)}e^{j\left[\kappa\phi(b)-\frac{\pi}{2}\right]} - \frac{1}{\kappa}\frac{F(a)}{\phi'(a)}e^{j\left[\kappa\phi(a)-\frac{\pi}{2}\right]} + O\left(\kappa^{-\frac{3}{2}}\right) . \end{aligned} \tag{2.18}$$

The first term is the contribution from the stationary point while the second and third terms are the contributions from the end points b and a, respectively. If there is no stationary point in the interval [a,b] and there are not any stationary points x_s near the end points a and b, the integral is asymptotically equal to the sum of the end point such that

$$I(\kappa) \sim \frac{1}{\kappa}\frac{F(b)}{\phi'(b)}e^{j\left[\kappa\phi(b)-\frac{\pi}{2}\right]} - \frac{1}{\kappa}\frac{F(a)}{\phi'(a)}e^{j\left[\kappa\phi(a)-\frac{\pi}{2}\right]} + O\left(\kappa^{-\frac{3}{2}}\right) . \tag{2.19}$$

This result will be used to reduce the equivalent edge currents to corner diffraction coefficients. It is also easily seen that the terms of order $1/\kappa$ in the stationary phase approximation give the exact integral in the special case where $F(x)$ is a constant, such that $F(a) = F(b) = F$. Then, $\phi(x) = cx$ such that $\phi'(x) = c$ which is a constant. This obviously indicates that no stationary points are in the interval or near the end points. Plugging into the above equation and retaining only terms of order $1/\kappa$, one obtains that

$$I(\kappa) \sim \frac{1}{\kappa}\frac{F}{c}e^{j\left[\kappa bc-\frac{\pi}{2}\right]} - \frac{1}{\kappa}\frac{F}{c}e^{j\left[\kappa ac-\frac{\pi}{2}\right]} \tag{2.20}$$

$$I(\kappa) \sim \frac{1}{\kappa}\frac{F}{jc}e^{j\kappa bc} - \frac{1}{\kappa}\frac{F}{jc}e^{j\kappa ac} \tag{2.21}$$

which is the same as the result one obtains by integrating the following expression

$$I(\kappa) = \int_a^b F e^{j\kappa c x} dx \, . \tag{2.22}$$

CHAPTER III

THEORY

3.1 Introduction

This chapter outlines the derivation of the new equivalent currents for finding the far zone scattered fields from a perfectly conducting wedge illuminated by a plane wave. This is a combination of the work done by Michaeli [13,14] and Buyukdura [22]. The contribution from a single face of the wedge is written in the form of an equivalent edge current. The equivalent currents are then reduced to corner diffraction coefficients. Then the corner diffraction coefficients are written in a form that is consistent with previous forms for diffraction coefficients.

3.2 Physical Optics Surface Integral

Gordon [23] showed that the far zone radiation integral over the PO currents for a plane wave incident on a flat plate may be converted from a surface integral to a line integral around the edge of the scatterer. Later Buyukdura [22] arrived at the same result using a different method. The steps he used to find the PO equivalent edge currents are repeated here. The PO equivalent edge current is found for a plate with the O-face illuminated. The results may be easily used for a general wedge since the PO contribution from each illuminated face may be calculated separately and summed to give the total PO contribution. If a face of the wedge is not illuminated then that face makes no contribution to the scattered field and

does not interact with the other face of the wedge in the PO approximation. Using the edge fixed coordinates given in Figure 1 and choosing the normal direction so that $\phi' \leq \pi$ it is assumed that the contribution from the O-face to the far zone scattered field may be written as

$$\vec{E}^s = \frac{jkZ_0}{4\pi}\frac{e^{-jkR}}{R}\hat{s} \times \hat{s} \times \int_c \vec{K}(t)e^{jkx(t)}e^{jkz(t)}dt \tag{3.1}$$

where c is the curve along the edge or edges of the scatterer and $\vec{K}(t)$ is an unknown function of the source and observation directions which is to be found. The field produced by electric and magnetic line currents placed along the edge are given by

$$\vec{E}^s = \frac{jk}{4\pi}\frac{e^{-jkR}}{R}\int_c \left[Z_0\, \hat{s} \times \hat{s} \times \hat{t}\, I + \hat{s} \times \hat{t}\, M\right] e^{jk_x x}e^{jk_z z}dt \tag{3.2}$$

where

$$k_x = k\hat{s} \cdot \hat{x}, \quad k_z = k\hat{s} \cdot \hat{z}\ . \tag{3.3}$$

Equating this result with Equation (3.1) one finds that

$$I = K_t - K_b \cot\beta \cos\phi \tag{3.4}$$

and

$$M = -K_b Z_0 \frac{\sin\phi}{\sin\beta} \tag{3.5}$$

where

$$\vec{K}(t) = \hat{t}K_t + \hat{b}K_b\ . \tag{3.6}$$

Placing the PO currents in the radiation integral over the surface of the plate gives

$$\vec{E}^s = \frac{jkZ_0}{4\pi}\frac{e^{-jkR}}{R}\hat{s} \times \hat{s} \times \int\int_s (2\hat{n} \times \vec{H}_0^i)e^{j(k_x - k_x^i)x}e^{j(k_z - k_z^i)z}dxdz \tag{3.7}$$

where

$$\vec{J}^{GO}(x,z) = 2\hat{n} \times \vec{H}^i(x,0,z) \tag{3.8}$$

$$\vec{H}^i(x,0,z) = \vec{H}_0^i e^{-jk_x^i x} e^{-jk_z^i z} \tag{3.9}$$

$$k_x^i = k\hat{s}' \cdot \hat{x}, \quad k_z^i = k\hat{s}' \cdot \hat{z} \tag{3.10}$$

and $\vec{H}^i$ is the GO incident field. Using the following vector identity

$$e^{j(k_x-k_x^i)x} e^{j(k_z-k_z^i)z} = \hat{y} \cdot \nabla \times \left\{ \left[(k_z - k_z^i)\hat{x} - (k_x - k_x^i)\hat{z} \right] \frac{e^{j(k_x-k_x^i)x} e^{j(k_z-k_z^i)z}}{jk^2h^2} \right\} \tag{3.11}$$

with

$$h^2 = \frac{(k_x - k_x^i)^2 + (k_z - k_z^i)^2}{k^2} \tag{3.12}$$

gives

$$\begin{aligned} \vec{E}^s &= \frac{jkZ_0}{4\pi} \frac{e^{-jkR}}{R} \hat{s} \times \hat{s} \times \int\int_s (2\hat{n} \times \vec{H}_0^i)\hat{y} \cdot \nabla \times \\ &\quad \left\{ \left[(k_z - k_z^i)\hat{x} - (k_x - k_x^i)z \right] \frac{e^{j(k_x-k_x^i)x} e^{j(k_z-k_z^i)z}}{jk^2h^2} \right\} dx dz \ . \end{aligned} \tag{3.13}$$

Then applying Stokes' theorem, one obtains that

$$\vec{E}^s = \frac{jkZ_0}{4\pi} \frac{e^{-jkR}}{R} \hat{s} \times \hat{s} \times \int_c (2\hat{n} \times \vec{H}_0^i) \left\{ \frac{-(k_x - k_x^i) e^{j(k_x-k_x^i)x} e^{j(k_z-k_z^i)z}}{jk^2h^2} \right\} dz \tag{3.14}$$

where the line integral is around the edge of the plate. Comparing this integral with the integral in Equation (3.1) results in the following:

$$K_t = \frac{2}{jk} H_b^i \frac{\sin\beta\cos\phi + \sin\beta'\cos\phi'}{h^2} \tag{3.15}$$

$$K_b = -\frac{2}{jk} H_t^i \frac{\sin\beta\cos\phi + \sin\beta'\cos\phi'}{h^2} \tag{3.16}$$

where

$$\vec{H}^i = \hat{b}\vec{H}_b^i + \hat{n}\vec{H}_n^i + \hat{t}\vec{H}_t^i \tag{3.17}$$

using

$$\vec{H}^i = \frac{1}{Z_0} \hat{k}^i \times \vec{E}^i \tag{3.18}$$

gives

$$H_b^i = -\frac{E_t^i}{Z_0}\frac{\sin\phi'}{\sin\beta'} + H_t^i \cot\beta' \cos\phi' \,. \tag{3.19}$$

Using Equations (3.15), (3.16), and (3.19) in Equations (3.4) and (3.5) gives

$$M = \frac{2Z_0}{jk} H_t^i \frac{\sin\phi}{\sin\beta} \frac{U(\pi-\phi')\sin\beta\cos\phi + \sin\beta'\cos\phi'}{\left[(\cos\beta-\cos\beta')^2 + (\sin\beta\cos\phi + \sin\beta'\cos\phi')^2\right]} \tag{3.20}$$

and

$$\begin{aligned} I &= U(\pi-\phi') \\ &\times \left\{ -\frac{2Y_0}{jk} E_t^i \frac{\sin\phi'}{\sin\beta'} \frac{\sin\beta\cos\phi + \sin\beta'\cos\phi'}{\left[(\cos\beta-\cos\beta')^2 + (\sin\beta\cos\phi + \sin\beta'\cos\phi')^2\right]} \right. \\ &+ \left. \frac{2}{jk} H_t^i \frac{(\sin\beta\cos\phi + \sin\beta'\cos\phi')(\cot\beta\cos\phi + \cot\beta'\cos\phi')}{(\cos\beta-\cos\beta')^2 + (\sin\beta\cos\phi + \sin\beta'\cos\phi')^2} \right\} \end{aligned} \tag{3.21}$$

where the unit step function $U(\pi-\phi')$ has been included to stress the fact that the equivalent currents are zero if the face is not illuminated by the incident field. Letting

$$\cos\gamma = \frac{\sin\beta\cos\phi}{\sin\beta'} + \frac{(\cos\beta-\cos\beta')^2}{\sin\beta'(\sin\beta\cos\phi + \sin\beta'\cos\phi')} \tag{3.22}$$

results in

$$M = \frac{2Z_0}{jk} H_t^i \frac{\sin\phi}{\sin\beta\sin\beta'} \frac{U(\pi-\phi')}{(\cos\gamma + \cos\phi')} \tag{3.23}$$

$$\begin{aligned} I &= -\frac{2Y_0}{jk} E_t^i \frac{\sin\phi'}{\sin^2\beta'} \frac{U(\pi-\phi')}{(\cos\gamma+\cos\phi')} \\ &+ \frac{2}{jk} H_t^i \frac{U(\pi-\phi')}{\sin\beta'} \frac{(\cot\beta\cos\phi + \cot\beta'\cos\phi')}{\cos\gamma+\cos\phi'} \,. \end{aligned} \tag{3.24}$$

Since the above equivalent currents (referred to later as the LPO component of the equivalent currents since they result from the reduction of the PO surface to a line integral) were derived from a surface integral over a finite surface and integrand,

it might be expected that they would remain finite for all aspects of incidence and observation. Even though the currents themselves become infinite for certain directions of incidence and observation, the fields radiated by the currents remain finite, as explained below. The magnetic current becomes infinite as $\sin\beta \to 0$. This is not a problem however, since it will always be cancelled by a factor of $\sin\beta$ in the radiation integral due to the $\hat{s} \times \hat{t}$ term. It appears that the electric current becomes infinite for edge on incidence ($\sin\beta' = 0$), but the current remains finite here since the factor of $\sin\beta'$ in the denominator is cancelled by a factor of $\sin\beta'$ in E_t^i. Both of the currents become infinite at the GTD shadow boundaries ($\beta = \beta'$ and $\phi \pm \phi' = \pm\pi$). This is only an artifact of the conversion of the surface integral to the line integral. When the complete integration is done around the edges of a finite scatterer, the infinite contributions from the different edges combine to yield a finite result. This is illustrated analytically for the special case of backscatter at broadside of a rectangular flat plate in Section 4.5 and in other cases by many numerical examples in Chapter V.

3.3 Fringe Equivalent Currents

Many people have worked on the problem of finding equivalent edge currents for a perfectly conducting wedge that are valid away from the Keller cone. Mitzner [24] derived Incremental Length Diffraction Coefficients (ILDC) using some symmetry arguments. Knott [25] later showed that Mitzner's ILDC could be written as equivalent edge currents. Michaeli [13] later derived equivalent edge currents for the wedge problem using a more mathematically rigorous method. Knott [25] also showed that Mitzner's ILDC and Michaeli's equivalent edge currents are the same except that Mitzner's ILDC give expressions for the fringe field only, while Michaeli's equivalent edge currents are for the total field. In this first

attempt at the equivalent currents, the plate is modeled as a series of infinitesimal strips oriented normal to the edge (i.e. the strips are parallel to the $\hat{b}$ direction).

In a later paper Michaeli [14] points out many singularities in the original expressions for the equivalent fringe currents and derives new expressions which have fewer singularities. This is accomplished by changing the direction of asymptotic evaluation of the integral from normal to the edge to a direction skewed from the edge normal. Not only does the new orientation of the strips reduce the number of singularities in the fringe equivalent currents, it is, as will be explained later, also more consistent with the physics of the problem. The original expressions for the equivalent fringe currents had many singularities. Michaeli points out that there are so many singularities that it is probably impossible to remove all of them. Going back to the radiation integral over one face of the wedge he points out the cause of two of the singularities. The equivalent fringe currents become infinite when $\hat{s}\cdot\hat{b} = \hat{s}'\cdot\hat{b}$ where $\hat{s}$ is the observation direction, $\hat{s}'$ is the incident ray direction, and $\hat{b}$ is the edge fixed coordinate direction defined previously in Figure 1. The current becomes infinite here because the phase of the PO component of the surface current cancels the phase of the outgoing wave. The fringe equivalent currents also become infinite when $\hat{s}\cdot\hat{b} = \hat{\sigma}\cdot\hat{b}$ where $\hat{\sigma} = \hat{t}\cos\beta' + \hat{b}\sin\beta'$. The fringe currents are infinite here because the phase of the UTD surface current cancels the phase of the outgoing wave. The cone of rays where the equivalent currents become infinite ($\hat{s}\cdot\hat{b} = \hat{\sigma}\cdot\hat{b}$) in the second case may be reduced to a single direction by a change of variables. This is included in the summary below. A summary of the procedure Michaeli [14] used to derive the fringe equivalent edge currents is given below:

1. The wedge is replaced at each point along its edge by an infinite tangent wedge with flat faces.

2. The currents on one face of the infinite wedge are expressed as a spectral integral using the solution to the two-dimensional infinite wedge problem.

3. The field due to these currents is expressed as a triple integral (one over the spectrum and a double integral over the surface of the tangent wedge).

4. The order of integration is changed. The integration over the spectrum and the integration over one of the spatial variables (b) are interchanged.

5. The integral over b is replaced by an integration along the $\hat{\sigma}$ direction (see Figure 18), and the integration variable b is replaced by $\sigma \sin \beta'$ in the integral.

6. The asymptotic end point contribution from the integral over the first spatial coordinate, σ, is determined.

7. The integration over the spectrum is done, after the path has been distorted, using the method of steepest descent. The contributions from the poles (PO contribution) are removed leaving the fringe contribution only.

8. The remaining integral is an integration along the edge of the wedge.

9. The radiation integral for electric and magnetic line sources along the edge is compared to the integral remaining in 8 and the equivalent edge currents are identified as:

$$M^f = M^{UTD} - M^{PO} \tag{3.25}$$

$$I^f = I^{UTD} - I^{PO} \tag{3.26}$$

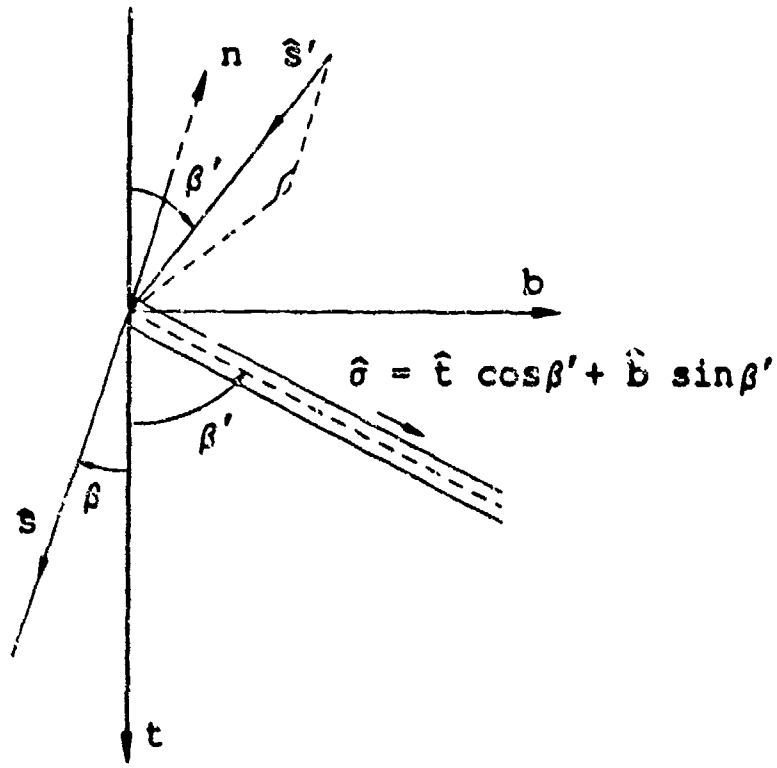

Figure 18: Integration direction (or strip orientation) used in finding the equivalent fringe currents.

where:

$$M^{UTD} = \frac{2jZ\sin\phi}{k\sin\beta\sin\beta'}\frac{(1/n)\sin[(\pi-\alpha)/n]\csc\alpha}{\cos[(\pi-\alpha)/n]-\cos(\phi'/n)}H_t^i \tag{3.27}$$

$$\begin{aligned} I^{UTD} &= \frac{2j}{k\sin\beta'}\frac{1/n}{\cos(\phi'/n)-\cos[(\pi-\alpha)/n]}\left\{\frac{\sin(\phi'/n)}{Z\sin\beta'}E_t^i\right. \\ &+ \left.\frac{\sin[(\pi-\alpha)/n]}{\sin\alpha}(\cos\alpha\cot\beta'-\cot\beta\cos\phi)H_t^i\right\} \\ &- \frac{2j\cot\beta'}{kn\sin\beta'}H_t^i \end{aligned} \tag{3.28}$$

$$M^{PO} = \frac{-2jZ\sin\phi U(\pi-\phi')}{k\sin\beta\sin\beta'(\cos\phi'+\cos\alpha)}H_t^i \tag{3.29}$$

$$\begin{aligned} I^{PO} &= \frac{2jU(\pi-\phi')}{k\sin\beta'(\cos\phi'+\cos\alpha)}\left[\frac{\sin\phi'}{Z\sin\beta'}E_t^i\right. \\ &- \left.(\cot\beta'\cos\phi'+\cot\beta\cos\phi)H_t^i\right] \end{aligned} \tag{3.30}$$

$$\alpha = \cos^{-1}\mu = -j\ln\left(\mu+\sqrt{\mu^2-1}\right) \tag{3.31}$$

$$\mu = \frac{\sin\beta\cos\phi}{\sin\beta'}+\frac{(\cos\beta-\cos\beta')\cos\beta'}{\sin^2\beta'} \tag{3.32}$$

and the branch cut chosen is assumed to be the same as previously obtained by Michaeli [13]

$$\sqrt{\mu^2-1} = \begin{cases} -\left|\sqrt{\mu^2-1}\right| & \mu<-1 \\ j\left|\sqrt{1-\mu^2}\right| & -1\le\mu\le 1 \\ \left|\sqrt{\mu^2-1}\right| & \mu>1 \end{cases} . \tag{3.33}$$

Although Michaeli does not specify the branch for the $\ln z$ in Equation (3.31), it seems reasonable to take the principal branch of the natural log. Specifically $\ln z = \ln|z| + jarg(z)$ where $0 \le arg(z) \le \pi$. From the equations for the equivalent currents, it is obvious that the $arg(z)$ may also be taken between π and 2π, since the equations remain unchanged if α is replaced by $2\pi-\alpha$. An equivalent method of finding α is to choose the branch of $\cos^{-1}\mu$ so that α is continuous for $\mu = \pm 1$ and the two branches are chosen to run from $\alpha = \pi$ to $\alpha = \pi - j\infty$ and $\alpha = 0$

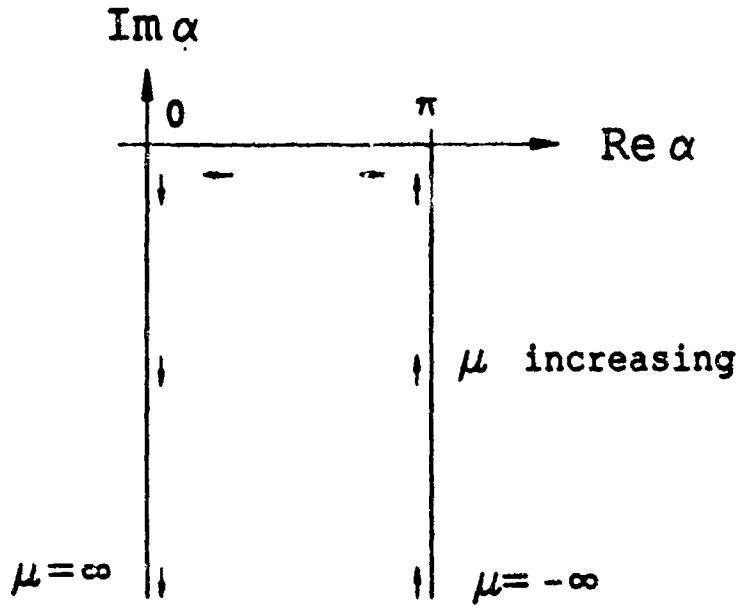

Figure 19: Branch for α.

to $\alpha = 0 - j\infty$ respectively, as shown in Figure 19. Notice that the last term on the right hand side of the expression for I^{UTD} in Equation (3.28) will be dropped since it will be cancelled by a term of opposite sign due to the other face. Since each edge is made up of two faces and the term does not depend on which face is being illuminated this term will always be cancelled by the corresponding term from the other face for a perfectly conducting wedge.

The only difference between the procedure Michaeli used to find these equivalent currents and the procedure he used to find his previous equivalent currents [13] is in step 5 listed previously. This change in variables not only results in fewer singularities in the equivalent currents, but also makes more sense physically as Ufimtsev points out in [12]. The field on one of the plates of the infinite tangent wedge should only depend on the contribution from the strip on which the field point is lying. The only strip orientation which meets this condition is the orientation described step 5, where the first spatial integration is taken in the $\hat{\sigma}$ direction.

In this case, all points along the strip lie on the Keller cone so that when the line integral along the edge is evaluated the major contribution to any field point on the strip will be due to the strip itself. All other directions of integration result in equivalent currents which "contaminate" the field along their strips with contributions from the other strips. The singularities remaining in the new equivalent fringe currents are listed below :

1. The currents become infinite when the direction of observation is the same as the direction of a glancing incident ray, that is the forward scattering direction in the plane of the plate where $\beta = \beta'$,$\phi = 0$, and $\phi' = \pi$. Michaeli refers to this as the Ufimtsev singularity.

2. I^f and M^f do not tend to a definite limit, but remain bounded as $\hat{s} \rightarrow \hat{\sigma}$.

3. Both I^f and M^f approach finite limits for edge on incidence ($\beta' \rightarrow 0$ or $\beta' \rightarrow \pi$), except of course when $\hat{s} = \hat{s}'$ which corresponds to the Ufimtsev singularity described in item 1.

4. Both I^f and M^f are discontinuous for $\phi' = \pi$.

5. I^f and M^f are finite for $\hat{s} \cdot \hat{\sigma} = -\hat{s}' \cdot \hat{\sigma}$ or $\alpha \pm \phi' = \pi$, although the components of the currents become infinite here.

Michaeli points out that all of these singularities except for the first one are integrable so the fringe fields found using these currents are finite for all aspects of incidence and observation except in a single forward scatter direction. Since the Ufimtsev singularity is in the forward scattering direction, it will probably not cause any trouble in solutions of practical importance. These singularities may cause spikes and discontinuities in the pattern when the equivalent currents are used as the bases for the new corner diffraction coefficient. This behavior will be illustrated in Chapter IV.

3.4 Equivalent Currents Written in the Form of Diffraction Coefficients

The equivalent edge currents may be written in a diffraction coefficient form closer to that used by Kouyoumjian and Pathak [3]. Using the following trigonometric identities:

$$\begin{aligned}
\frac{1}{\cos a + \cos b} &= \frac{1}{4}\frac{1}{\sin b}\left\{\left[\cot\left(\frac{\pi-(a-b)}{4}\right) - \cot\left(\frac{\pi+(a-b)}{4}\right)\right]\right. \\
&\quad \left. - \left[\cot\left(\frac{\pi-(a+b)}{4}\right) - \cot\left(\frac{\pi+(a+b)}{4}\right)\right]\right\} \qquad (3.34) \\
\frac{1}{\cos a + \cos b} &= -\frac{1}{4}\frac{1}{\sin a}\left\{\left[\cot\left(\frac{\pi-(a-b)}{4}\right) - \cot\left(\frac{\pi+(a-b)}{4}\right)\right]\right. \\
&\quad \left. + \left[\cot\left(\frac{\pi-(a+b)}{4}\right) - \cot\left(\frac{\pi+(a+b)}{4}\right)\right]\right\} \qquad (3.35) \\
\frac{\sin a}{\cos a - \cos b} &= -\frac{1}{2}\left[\cot\left(\frac{a-b}{2}\right) + \cot\left(\frac{a+b}{2}\right)\right] \qquad (3.36) \\
\frac{\sin b}{\cos a - \cos b} &= -\frac{1}{2}\left[\cot\left(\frac{a-b}{2}\right) - \cot\left(\frac{a+b}{2}\right)\right] \qquad (3.37)
\end{aligned}$$

and a little algebra, one obtains the equivalent edge currents (O-face contribution only) given by

$$M = M^{LPO} + M^{UTD} - M^{PO} \qquad (3.38)$$

$$I = I_e + I_m \qquad (3.39)$$

$$I_{e,m} = I_{e,m}^{LPO} + I_{e,m}^{UTD} - I_{e,m}^{PO} \qquad (3.40)$$

where:

$$\begin{aligned}
\begin{bmatrix} M^{LPO}, I_m^{LPO} \\ I_e^{LPO} \end{bmatrix} &= -\frac{1}{2}U^i \begin{bmatrix} C_h(\gamma), C_2(\gamma,\phi') \\ C_s \end{bmatrix} \\
&\quad \left\{\left[\cot\left(\frac{\pi-(\gamma-\phi')}{4}\right) - \cot\left(\frac{\pi+(\gamma-\phi')}{4}\right)\right]\right.
\end{aligned}$$

$$
\begin{aligned}
& \left\{\left[\cot\left(\frac{\pi-(\gamma-\phi')}{4}\right)-\cot\left(\frac{\pi+(\gamma-\phi')}{4}\right)\right]\right. \\
\pm & \left.\left[\cot\left(\frac{\pi-(\gamma+\phi')}{4}\right)-\cot\left(\frac{\pi+(\gamma+\phi')}{4}\right)\right]\right\}
\end{aligned}
$$

$$
\begin{bmatrix} M^{UTD}, I_m^{UTD} \\ I_e^{UTD} \end{bmatrix} = -\frac{1}{n}\begin{bmatrix} C_h(\alpha), C_2(\alpha,\pi-\alpha) \\ C_s \end{bmatrix}
$$

$$
\left[\cot\left(\frac{\pi-(\alpha-\phi')}{2n}\right)\pm\cot\left(\frac{\pi-(\alpha+\phi')}{2n}\right)\right]
$$

$$
\begin{bmatrix} M^{PO}, I_m^{PO} \\ I_e^{PO} \end{bmatrix} = \begin{bmatrix} M^{LPO}, I_m^{LPO} \\ I_e^{LPO} \end{bmatrix} \text{(with } \gamma \text{ replaced by } \alpha) \tag{3.41}
$$

$$
C_h(\delta) = \frac{jH_t^i}{Y_0 k}\frac{\sin\phi}{\sin\beta\sin\beta'\sin\delta} \quad ; \quad C_s = \frac{jE_t^i}{Z_0 k}\frac{1}{\sin^2\beta'} \tag{3.42}
$$

$$
C_2(\delta,\epsilon) = \frac{jH_t^i}{k}\frac{\cot\beta\cos\phi+\cot\beta'\cos\epsilon}{\sin\delta\sin\beta'} \tag{3.43}
$$

$$
\cos\gamma = \frac{\sin\beta\cos\phi}{\sin\beta'}+\frac{(\cos\beta-\cos\beta')^2}{\sin\beta'(\sin\beta\cos\phi+\sin\beta'\cos\phi')} \tag{3.44}
$$

$$
\cos\alpha = \frac{\sin\beta\cos\phi}{\sin\beta'}+\frac{(\cos\beta-\cos\beta')\cos\beta'}{\sin^2\beta'} \tag{3.45}
$$

$$
U^i = \begin{cases} 0 & ,\pi-\phi'<0 \\ 1 & ,\pi-\phi'>0 \end{cases} \tag{3.46}
$$

The branch of $\cos^{-1}$ is described in Section 3.3. For the special case of a flat plate (n=2), it is much easier to consider the contribution from each edge due to both faces than to consider the contribution from the edge due to each face separately. For the case of a flat plate the total contribution from each edge is given by (note: the normal may be taken in either direction perpendicular to the plane of the plate.):

$$
M = M^{LPO}+M^{UTD}-M^{PO} \tag{3.47}
$$

$$
I = I_e+I_m \tag{3.48}
$$

$$
I_{e,m} = I_{e,m}^{LPO}+I_{e,m}^{UTD}-I_{e,m}^{PO} \tag{3.49}
$$

where:

$$
\begin{aligned}
\begin{bmatrix} M^{LPO}, I_m^{LPO} \\ I_e^{LPO} \end{bmatrix} &= -\frac{1}{2} S^i \begin{bmatrix} C_h(\gamma), C_2(\gamma, \phi') \\ C_s \end{bmatrix} \\
&\quad \left\{ \left[\cot\left(\frac{\pi - (\gamma - \phi')}{4}\right) - \cot\left(\frac{\pi + (\gamma - \phi')}{4}\right) \right] \right. \\
&\pm \left. \left[\cot\left(\frac{\pi - (\gamma + \phi')}{4}\right) - \cot\left(\frac{\pi + (\gamma + \phi')}{4}\right) \right] \right\} \\
\begin{bmatrix} M^{UTD}, I_m^{UTD} \\ I_e^{UTD} \end{bmatrix} &= -\frac{1}{2} \begin{bmatrix} C_h(\alpha), C_2(\alpha, \pi - \alpha) \\ C_s \end{bmatrix} \\
&\quad \left\{ \left[\cot\left(\frac{\pi - (\alpha - \phi')}{4}\right) + \cot\left(\frac{\pi + (\alpha - \phi')}{4}\right) \right] \right. \\
&\pm \left. \left[\cot\left(\frac{\pi - (\alpha + \phi')}{4}\right) + \cot\left(\frac{\pi + (\alpha + \phi')}{4}\right) \right] \right\} \\
\begin{bmatrix} M^{PO}, I_m^{PO} \\ I_e^{PO} \end{bmatrix} &= \begin{bmatrix} M^{LPO}, I_m^{LPO} \\ I_e^{LPO} \end{bmatrix} (\textit{with } \gamma \textit{ replaced by } \alpha) \\
S^i &= \begin{cases} -1 & , \pi - \phi' < 0 \\ 1 & , \pi - \phi' > 0 \end{cases}
\end{aligned}
\tag{3.50}
$$

where C_h, C_2, C_s, γ, and α are the same as the expressions given earlier in Equations (3.42) to (3.45). The terms may be associated with the O-face incident and reflection shadow boundaries and the N-face incident and reflection shadow boundaries, as indicated previously for the UTD diffraction coefficients.

3.5 New Corner Diffraction Coefficient

Buyukdura [22] has derived the corner diffraction coefficients from the equivalent currents using the stationary phase approximation. If the object is made up of flat faces with straight edges then all of the edges are terminated in sharp vertices. It is assumed that the current near each edge, even very near the vertex, is unperturbed by the other edge making up the vertex. The same assumption

was made in the derivation of the previous corner diffraction coefficient given in Section 2.7. Despite this shortcoming the corner diffraction solution gives fairly accurate results (see the next chapter for numerical results). Since it is assumed that the two edges forming the vertex do not interact near the vertex (to first order) the scattered field may be expressed as a line integral along the edges of the object. The line integral along the edges may obviously be expressed as the sum of integrals along each individual edge such that

$$\vec{E}^s = \sum_i \sum_n \frac{jk}{4\pi} \frac{e^{-jkR}}{R} \int_{a_{in}}^{b_{in}} \left[Z_0 \, \hat{s} \times \hat{s} \times \hat{t} \, I + \hat{s} \times \hat{t} \, M \right] e^{-j(k_b b + k_t t)} dt \tag{3.51}$$

where the first sum is over the faces of the object, the second sum is over the edges of each face, and the edge fixed coordinates $\hat{t}$ and $\hat{b}$ along with the limits on the integrals obviously depend on which face and edge are being considered. Looking only at the contribution due to one face and one edge at a time, one finds that

$$\vec{E}^s(i,n) = \frac{jk}{4\pi} \frac{e^{-jkR}}{R} \int_{a_{in}}^{b_{in}} \left[Z_0 \, \hat{s} \times \hat{s} \times \hat{t} \, I + \hat{s} \times \hat{t} \, M \right] e^{-j(k_x x + k_z z)} dz \tag{3.52}$$

where the coordinates are defined in Figure 20. Notice that along the straight edge the edge fixed coordinate directions $(\hat{b}, \hat{n}, \hat{t})$, and the angular directions $(\beta', \phi', \beta, \phi)$ are constant. The only factors in the equivalent currents which vary along the edge, therefore, are E_t^i and H_t^i. To simplify the integration, these factors will be separated out using the following definitions:

$$I = \frac{2jY_0 G_{ie} E_t^i}{k \sin\beta \sin\beta'} + \frac{2jG_{im} H_t^i}{k \sin\beta \sin\beta'} \tag{3.53}$$

$$M = \frac{2jZ_0 G_m H_t^i}{k \sin\beta \sin\beta'} \tag{3.54}$$

From which it is easily seen that G_{ie}, G_{im}, and G_m are all constant along the straight edge. Taking the phase reference at some arbitrary point O along the t-axis and using:

$$E_t^i(z) = E_t^i(0) e^{-jk\cos\beta'} \tag{3.55}$$

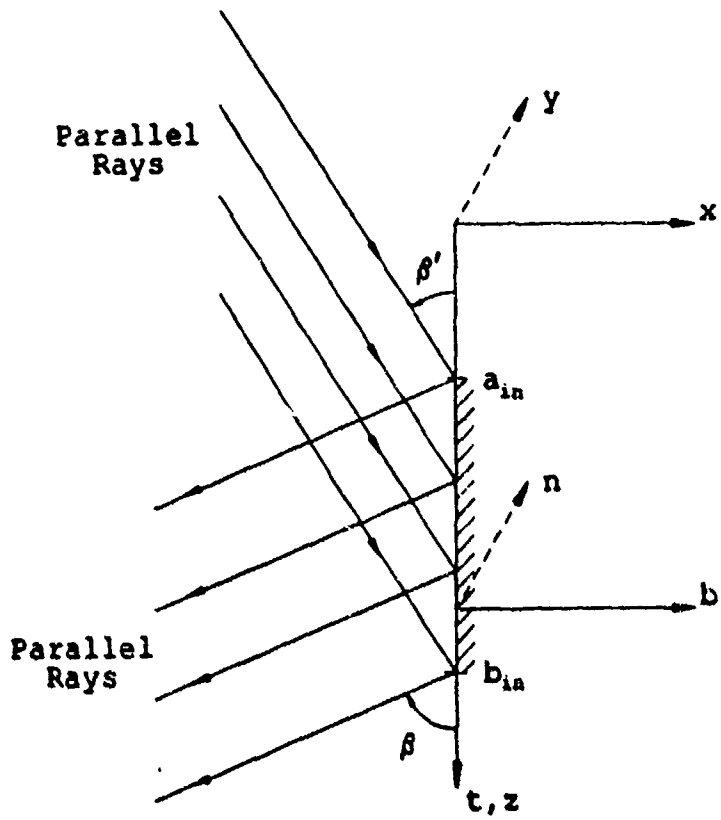

Figure 20: Edge Fixed coordinates for a straight edge.

$$H_t^i(z) = H_t^i(0)e^{-jk\cos\beta'} \tag{3.56}$$

$$x = 0 \tag{3.57}$$

$$k_z = k\cos\beta' \tag{3.58}$$

gives

$$\begin{aligned}\vec{E}^s = & - \frac{1}{2\pi}\frac{e^{-jkR}}{R}\int_a^b \left\{ \hat{s}\times\hat{s}\times\hat{t}\left[\frac{G_{ie}E_t^i(0)}{\sin\beta\sin\beta'} + \frac{G_{im}Z_0H_t^i(0)}{\sin\beta\sin\beta'}\right]\right. \\ & + \left.\hat{s}\times\hat{t}\,\frac{Z_0G_mH_t^i(0)}{\sin\beta\sin\beta'}\right\} e^{jkz(\cos\beta-\cos\beta')}dz \end{aligned} \tag{3.59}$$

Since the term in brackets is constant, using either the method of stationary phase or regular integration (see Chapter II) and only including the contribution from the end point at b along with the following relations:

$$E_t^i = E_{\beta'}^i\sin\beta' \tag{3.60}$$

$$H_t^i = -\frac{1}{Z_0}E_{\phi'}^i\sin\beta' \tag{3.61}$$

$$\hat{s}\times\hat{t} = -\hat{\phi}\sin\beta \tag{3.62}$$

$$\hat{s}\times\hat{s}\times\hat{t} = \hat{\beta}\sin\beta \tag{3.63}$$

results in the following expressions for the new diffraction coefficients in terms of the new equivalent currents:

$$\begin{bmatrix} E^c_\beta \\ E^c_\phi \end{bmatrix} = \begin{bmatrix} D^c_s & D^c_2 \\ 0 & D^c_h \end{bmatrix} \begin{bmatrix} E^i_{\beta'} \\ E^i_{\phi'} \end{bmatrix} \frac{e^{-jks}}{s} \tag{3.64}$$

$$\begin{bmatrix} D^c_s \\ D^c_h \\ D^c_2 \end{bmatrix} = \pm \begin{bmatrix} + \\ - \\ + \end{bmatrix} \frac{1}{4\pi} \frac{\sin\beta \sin\beta'}{\cos\beta - \cos\beta'} \begin{bmatrix} I_e/Y_0 E^i_t \\ M/Z_0 H^i_t \\ I_m/H^i_t \end{bmatrix} \tag{3.65}$$

where E^c_β and E^c_ϕ are the $\hat{\beta}$ and $\hat{\phi}$ components of the corner diffraction contribution from one corner, one edge, and one face. The phase is referenced to the corner. $E^i_{\beta'}$ and $E^i_{\phi'}$ are the $\hat{\beta}'$ and $\hat{\phi}'$ components of the incident field at the corner. The angles are the edge fixed angles with the origin located at the corner as illustrated in Figure 21. The equivalent currents I_e, I_m, and M are given by Equations (3.41) and (3.39), respectively, or by Equations (3.49) and (3.47) for the case of a flat plate. The sign used depends on which end point the particular contribution is coming from and the direction of integration. The direction of integration is always chosen to be in the counterclockwise direction when the face is viewed from the positive n-direction. The negative sign is used for the first corner contribution of each corner (as the direction of integration is traced out) and the positive sign is used for the second corner contribution of the edge as indicated in Figure 22. Equations for the corner diffraction coefficients with the expressions given in Equations (3.41) and (3.39) substituted into Equation (3.65) are given in Appendix A.

3.6 Conclusion

Expressions for new equivalent currents based on the PTD are given in Equations (3.39) and (3.41). The new equivalent currents are used to derive a new corner diffraction coefficient. Both the new equivalent currents and the new cor-

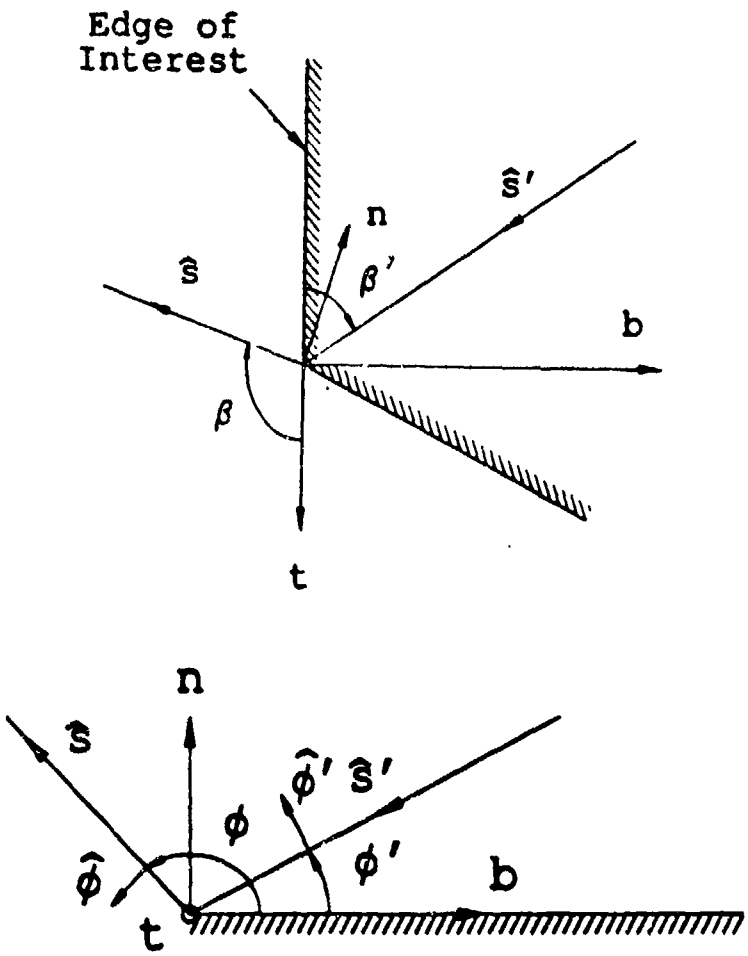

Figure 21: Definition of the Angles used in the New Corner Diffraction Coefficients.

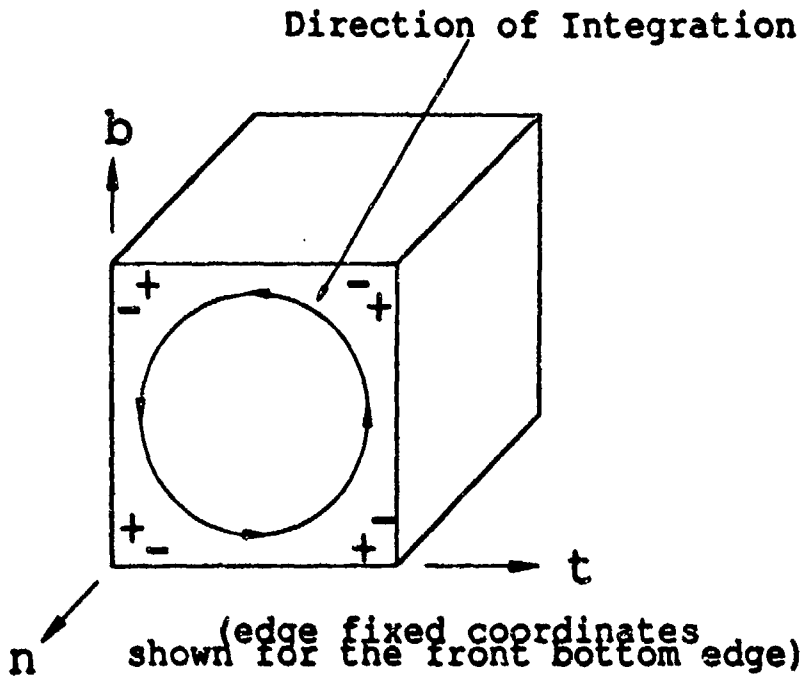

Figure 22: Direction of Integration for one face.

ner diffraction give the same results for the first order scattering from a convex body made up of perfectly conducting flat plates. Even though the equivalent currents are not valid in the region of a vertex (corner), it will be shown in Chapter V that the equivalent currents (and the corner diffraction coefficients) give reasonable results for many directions of incidence and observation. Several important properties of this solution are discussed in Chapter IV followed by several examples in Chapter V.

CHAPTER IV

PROPERTIES OF THE NEW CORNER DIFFRACTION SOLUTION

4.1 Introduction

The behavior of the new corner diffraction coefficient will be discussed for various situations. The significance of its various properties will be outlined to give insight into how the solution may be expected to behave in certain special cases. Several more examples given in Chapter V illustrate that the solution agrees closely with either the Method of Moments or previous first order solutions in most cases.

4.2 Singularities

First the singularities in the solution will be discussed. The singularities in the new corner diffraction coefficients are simply the combination of the singularities in the line PO component and in the fringe component of the new equivalent currents. The singularities and some examples illustrating how they may effect a pattern are given below.

1. Ufimtsev's singularity in the forward scattering direction in the half plane of the face ($\beta = \beta'$,$\phi = 0$, and $\phi' = \pi$). This singularity was previously discussed in item 1 of Section 3.3. To illustrate how this may affect the results, the bistatic RCS of a two wavelength square plate is calculated. In the

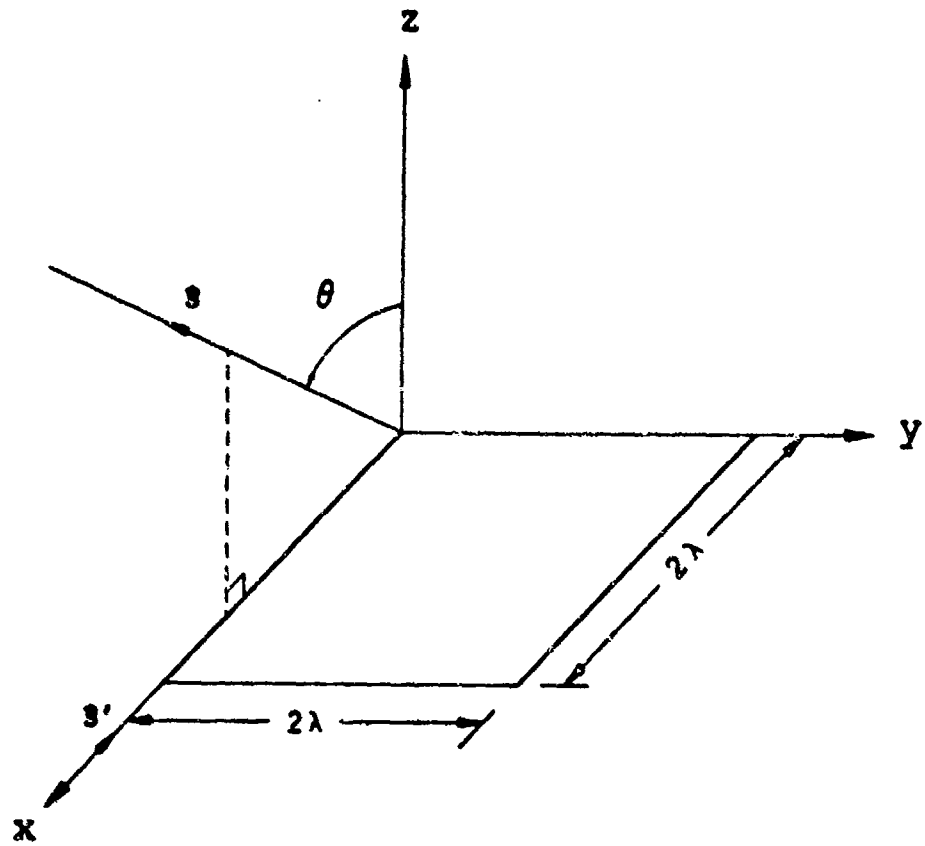

Figure 23: Plate Geometry for the Illustration of Ufiimtsev's Singularity.

first example the source remains fixed at $\theta^i = 90°$ and $\phi^i = 0°$ (see Figure 23) while the pattern is taken in the $\phi = 0°$ plane. The results for the H-plane pattern in the x-z plane are shown compared with a Method of Moments solution in Figure 24. This result shows that the new corner diffraction solution is fairly accurate for directions greater than 15° to 20° away from the forward direction for cases of grazing incidence. The previous corner diffraction solution and equivalent current solution also become infinite in the forward direction for grazing incidence. The previous solutions are compared with the new solution in Figure 25 for the H-plane pattern and the geometry given above. The new and old solutions are actually so close that they

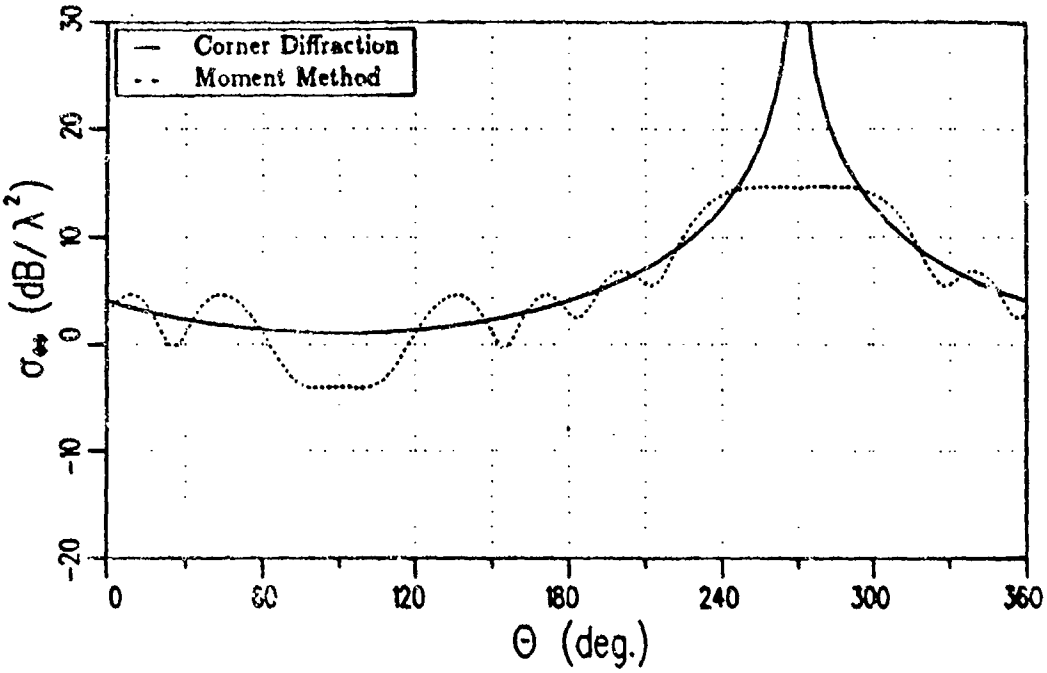

Figure 24: H-plane pattern for $\phi = 0°$ cut of a 2λ square plate with a fixed source at $\theta_i = 90°, \phi_i = 0°$.

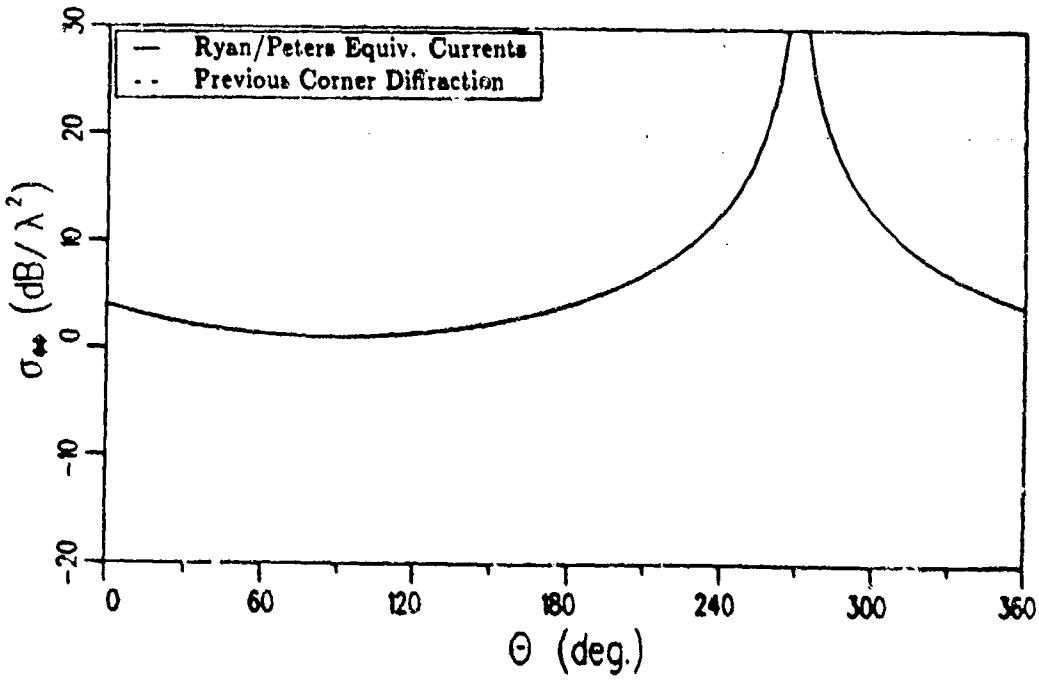

Figure 25: H-plane pattern for $\phi = 0°$ cut of a 2λ square plate with a fixed source at $\theta_i = 90°, \phi_i = 0°$.

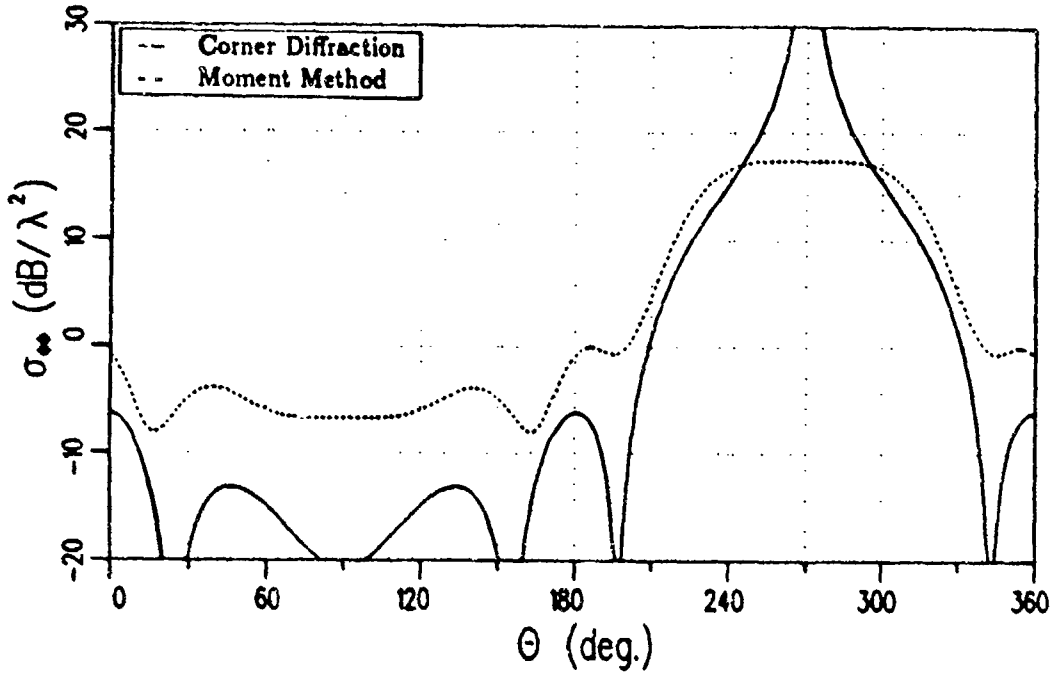

Figure 26: H-plane pattern for $\phi = 45°$ cut of a 2λ square plate with a fixed source at $\theta_i = 90°, \phi_i = 45°$.

are indistinguishable in the plot in Figure 25. To see how moving off the Keller cone affects the behavior of the solution, the bistatic RCS of the two wavelength plate is plotted for a pattern in the $\phi = 45°$ plane while the source is held fixed at $\theta_i = 90°$ and $\phi_i = 45°$. The results for the H-plane pattern are plotted along with Moment Method calculations in Figure 26. In this example the new corner diffraction solution is fairly accurate in the major lobe region away from the forward direction ($\theta = 90°$). The previous corner diffraction solution and previous equivalent current solution are compared with the new solution for this example in Figure 27. Although the pattern is taken away from the Keller cone, all three solutions are fairly close.

2. I_m^f (and D_2^c) and M^f (and D_h^c) do not tend to definite limits as $\hat{s} \to \hat{\sigma}$, where $\hat{\sigma} = \hat{t}\sin\beta' + \hat{b}\cos\beta'$ and is shown in Figure 18, but they remain bounded. In practice this means that both D_2^c and D_h^c, and therefore E_β^c and E_ϕ^c, are

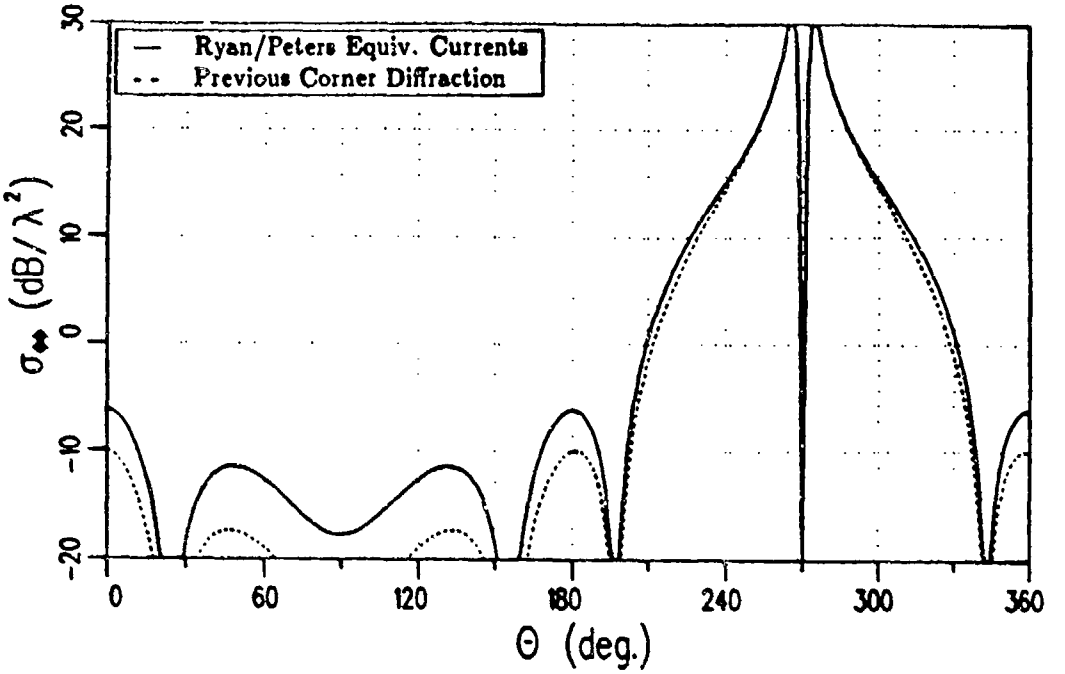

Figure 27: H-plane pattern for $\phi = 45°$ cut of a 2λ square plate with a fixed source at $\theta_i = 90°, \phi_i = 45°$.

discontinuous at this point in the pattern. A simple example illustrates how this discontinuity can affect a pattern. The bistatic RCS from a flat plate, two wavelengths on a side, in the x-y plane is considered. The source, linearly polarized in the $\hat{\phi}^i$ direction, remains fixed at $\theta^i = 45°$ and $\phi^i = 0°$ while the pattern is taken near the x-y plane ($\theta = 89°$). The source geometry is shown in Figure 28. The bistatic RCS is given in Figures 29 and 30 for the co-polarized and cross polarized fields, respectively. The abrupt null at $\phi \approx 135°$ in the co-polarized pattern and the spike at the same location in the cross-polarized pattern are due to discontinuities in the contribution from edge 4 (indicated in Figure 28). The point $\phi \approx 135°$ coincides with $\beta_4 = \beta_4'$ and $\phi_4 \approx 0$ where β_4, β_4', and ϕ_4 are the edge fixed coordinates for edge 4. Due to the geometry $\hat{\beta}_4 \approx \hat{\phi}$ and $\hat{\phi}_4 \approx \hat{\theta}$ so the discontinuity in $\sigma_{\phi\phi}$ is due to the discontinuity in D_2^c and, likewise, the discontinuity in $\sigma_{\phi\theta}$ is due to the discontinuity in D_h^c.

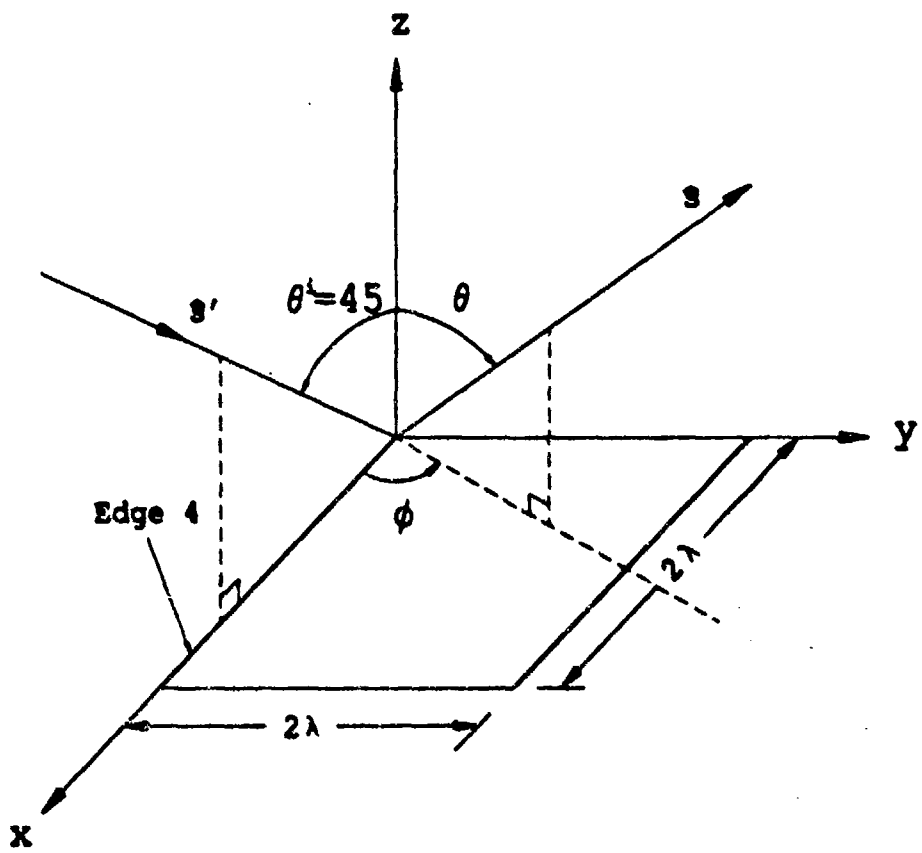

Figure 28: 2λ square plate in the x-y plane illuminated by a fixed source located in the $\theta^i = 45°$, $\phi^i = 0°$ direction.

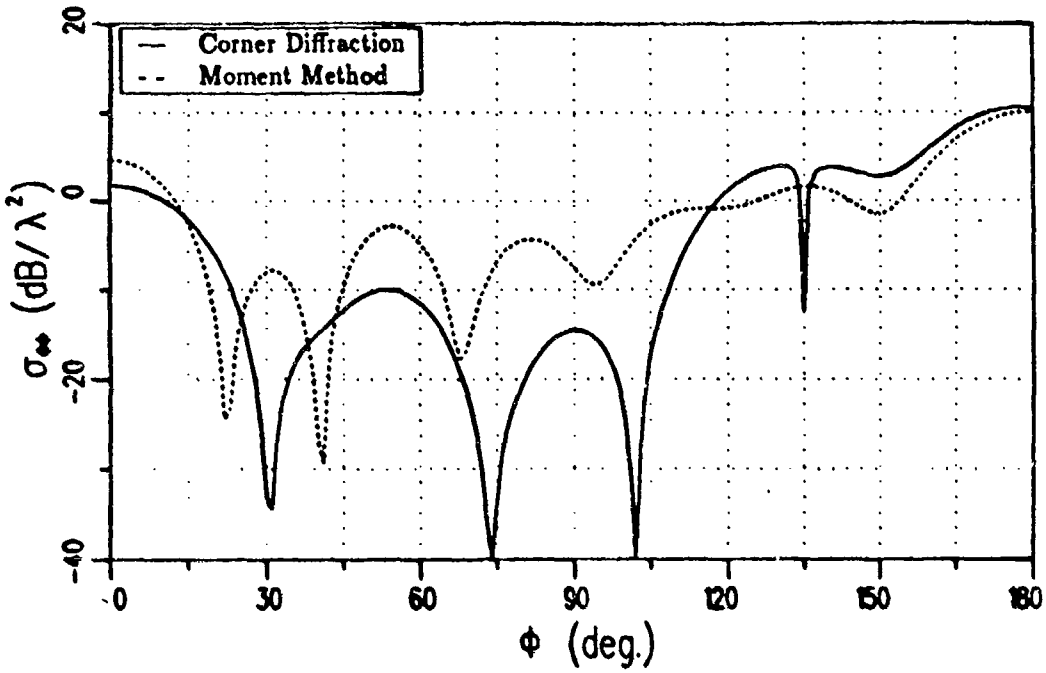

Figure 29: RCS for the $\theta = 89°$ cut of a 2λ square plate with a $\hat{\phi}^i$ polarized fixed source at $\theta^i = 45°$, $\phi^i = 0°$.

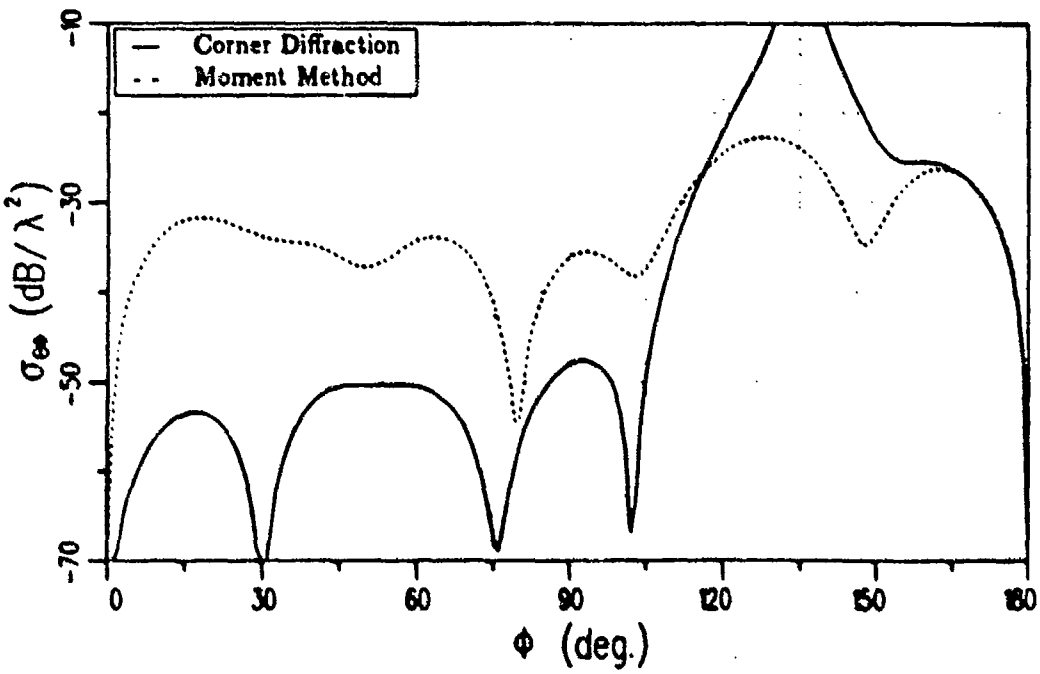

Figure 30: RCS for the $\theta = 89°$ cut of a 2λ square plate with a $\hat{\phi}^i$ polarized fixed source at $\theta^i = 45°$, $\phi^i = 0°$.

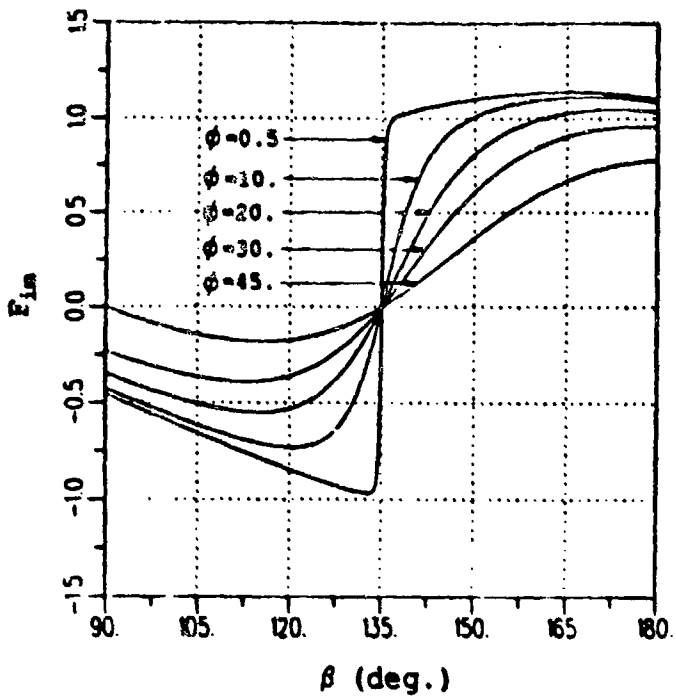

Figure 31: F_{im}, $\beta' = 135°$

The specific terms which are discontinuous in D_2^c and D_h^c are examined further here. The discontinuity in D_2^c at this point is due to the discontinuity in I_m^{UTD}. Specifically, it is due to the following factor:

$$F_{im}(\beta, \beta', \phi) = \frac{\cos\alpha \cot\beta' - \cot\beta \cos\phi}{\sin\alpha} . \tag{4.1}$$

F_{im} is plotted as a function of β with ϕ as a parameter and $\beta' = 135°$ in Figure 31. For ϕ on the order of a few degrees, F_{im} changes sign abruptly at $\beta = \beta'$. This is exactly what happens to the contribution to the $\hat{\phi}$ polarized field from edge 4 in the above example. The same conclusion may be reached analytically by realizing that

$$F_{im}(\beta, \beta', \phi) = \frac{\cos\alpha \cot\beta' - \cot\beta \cos\phi}{\sin\alpha} \approx \frac{\Delta\beta}{\sqrt{(\Delta\phi \sin\beta')^2 + (\Delta\beta)^2}} \tag{4.2}$$

where

$$\Delta\phi = \phi \tag{4.3}$$

$$\Delta\beta = \beta - \beta' \tag{4.4}$$

for $\Delta\phi$ and $\Delta\beta$ small. Which will further reduce to the following signum function if $\Delta\phi << \Delta\beta$:

$$F_{im}(\beta, \beta', \phi) = \frac{\cos\alpha \cot\beta' - \cot\beta \cos\phi}{\sin\alpha} \rightarrow sgn(\Delta\beta) \tag{4.5}$$

as $\phi \rightarrow 0$.

The discontinuity in D_h^c is examined next. The only factor in D_h^c that is discontinuous at the intersection of the Keller cone and the half plane associated with the edge ($\beta = \beta'$ and $\phi = 0$) is

$$F_m = \frac{\sin\phi}{\sin\alpha}\,. \tag{4.6}$$

This factor only causes a discontinuity in the M^{UTD} term since another factor in the M^{PO} causes M^{PO} to go to zero here. F_m is plotted as a function of β with ϕ as a parameter and $\beta' = 135°$ in Figure 32. For ϕ on the order of a few degrees, F_m becomes a very narrow spike at $\beta = \beta'$. This also occurs to the contribution for the $\hat{\theta}$ polarized field from edge 4 in the above example. The same conclusion may be reached analytically by realizing that:

$$F_m(\beta, \beta', \phi) = \frac{\sin\phi}{\sin\alpha} \approx \frac{\Delta\phi}{\sqrt{(\Delta\phi)^2 + \left(\frac{\Delta\beta}{\sin\beta'}\right)^2}} \tag{4.7}$$

where:

$$\Delta\phi = \phi \tag{4.8}$$

$$\Delta\beta = \beta - \beta' \tag{4.9}$$

for $\Delta\phi$ and $\Delta\beta$ small. Equations (4.2) and (4.7) show that F_{im} and F_m are very similar with the major difference being that the roles of $\Delta\beta$ and $\Delta\phi$

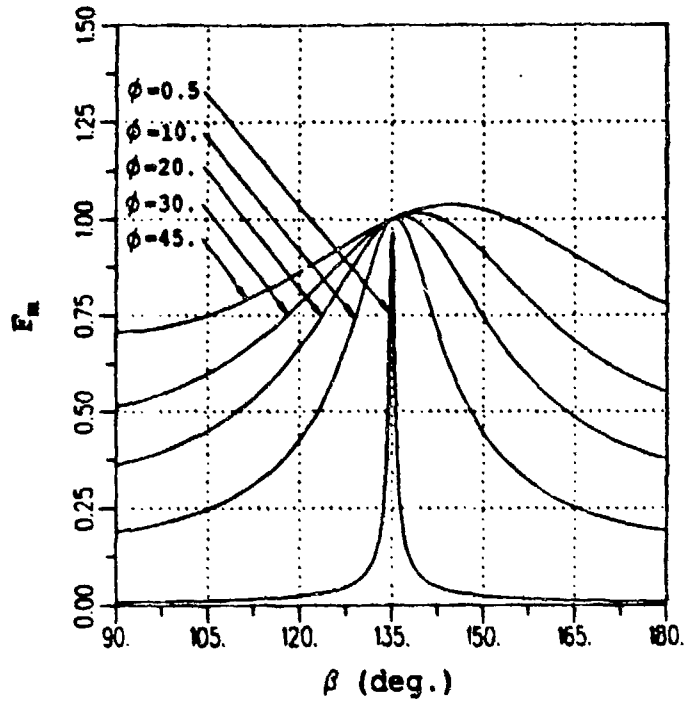

Figure 32: F_m, $\beta' = 135°$

are interchanged. F_{im} and F_m are plotted again in Figure 33 and Figure 34, respectively, this time as a function of ϕ with β as a parameter and $\beta' = 135°$.

These discontinuities are not restricted to the case of bistatic scattering and may also appear for backscatter examples. The backscattered field (co- and cross-polarized), for a $\hat{\theta}$ polarized field incident upon the plate shown in Figure 28 and calculated close to the x-y plane ($\theta = 89°$), is shown in Figure 35. In both cases the patterns have a glitch, due to the contributions from the far edge at $\phi = 90°$, similar to those in the previous bistatic results. It should be noted that the fields for a $\hat{\phi}$ polarized incident field (shown in Figure 36) are smooth for this pattern. The cross polarized field, $\sigma_{\phi\theta}$, is not visible on this plot since it is below $-50\ dB/\lambda^2$ through the entire pattern.

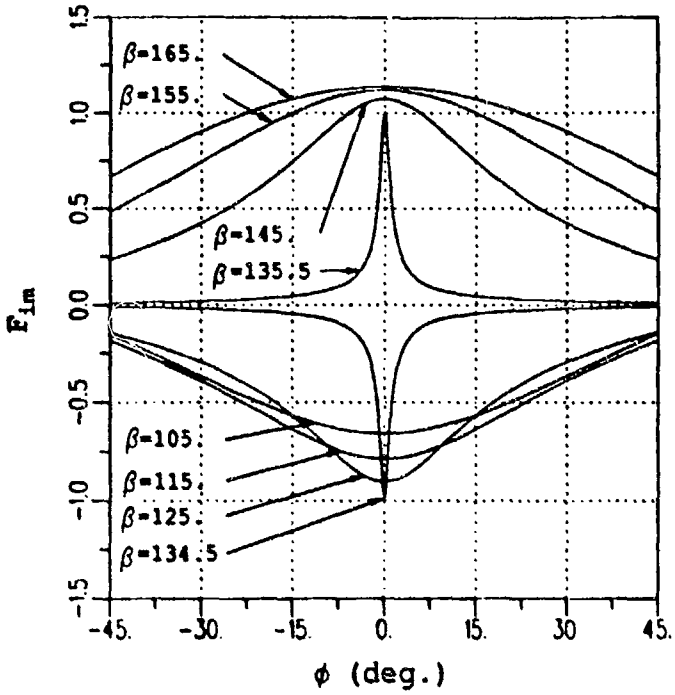

Figure 33: $F_{im}, \beta' = 135°$

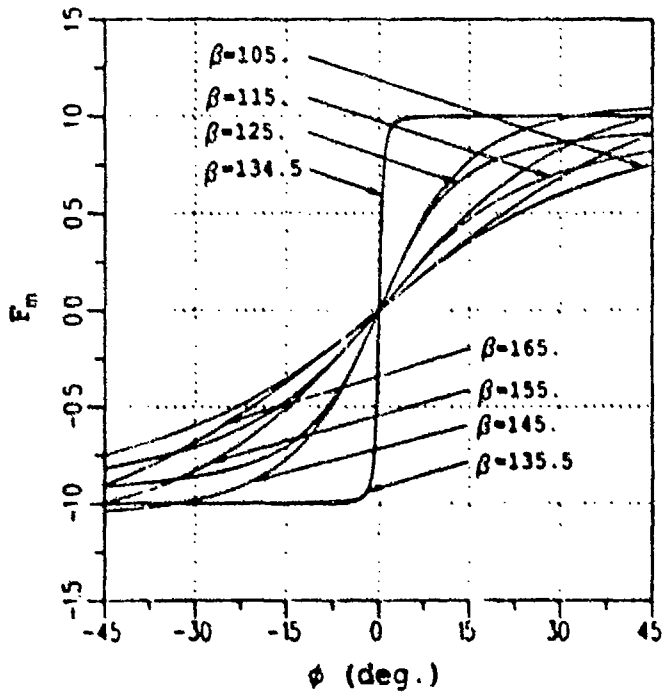

Figure 34: $F_m, \beta' = 135°$

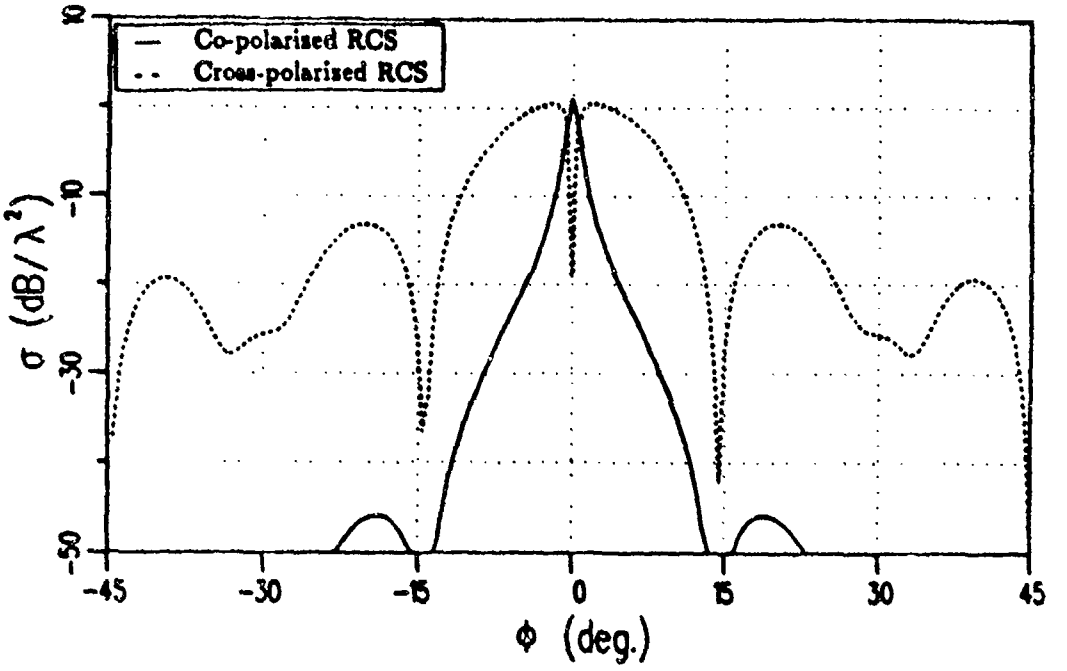

Figure 35: Backscatter ($\sigma_{\theta\theta}$ and $\sigma_{\theta\phi}$) from a 2λ square plate for $\theta = 89°$

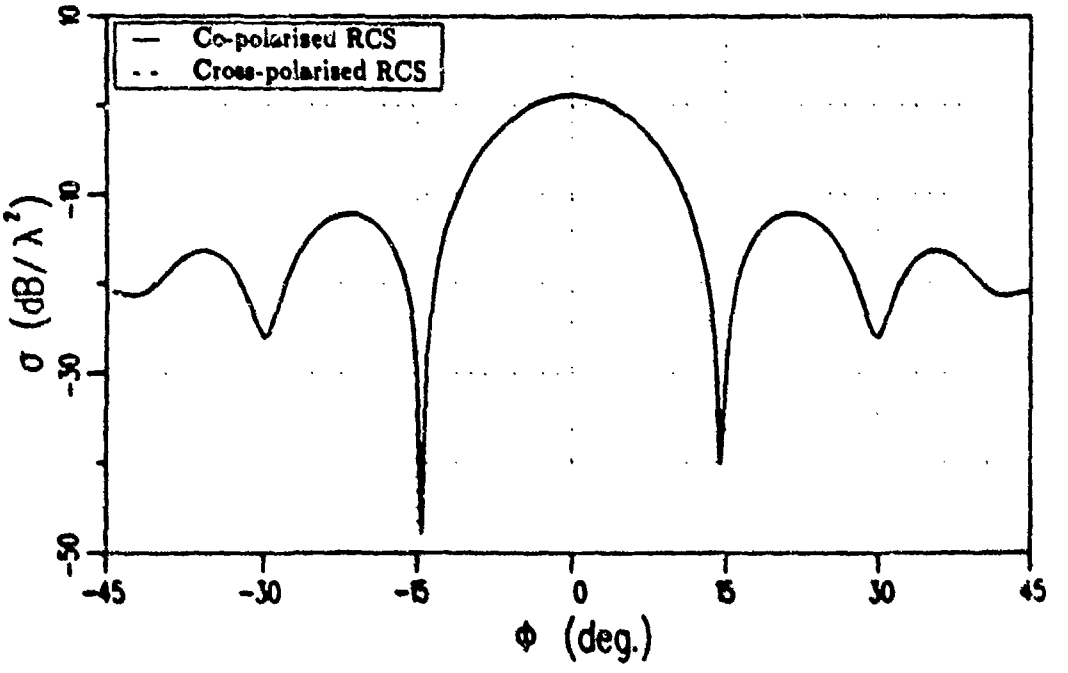

Figure 36: Backscatter ($\sigma_{\phi\phi}$ and $\sigma_{\phi\theta}$) from a 2λ square plate for $\theta = 89°$

The discontinuity in the new equivalent currents (and the diffraction coefficients) at the intersection of the Keller cone and the infinite half plane associated with the edge ($\beta = \beta'$ and $\phi = 0$) may be expected to cause discontinuities or narrow spikes depending on the polarization and the pattern cut. As the examples illustrate these disturbances only affect a typical pattern cut for around 5° to 10°. Further information on how the solution behaves in this region is discussed in Section 4.3.

3. Excluding the case when the diffracted ray is in the same direction as the incident ray (see item 1), the currents are all finite for both edge on incidence ($\beta' \rightarrow 0, \pi$) and edge on observation ($\beta \rightarrow 0, \pi$). This is shown for edge on incidence in Appendix B. For edge on observation it is easily seen by noting that the factors of $1/\sin\beta$ in the equivalent currents are cancelled by a factor of $\sin\beta$ in the numerator of the radiation integral due to either $\hat{s} \times \hat{t}$ or $\hat{s} \times \hat{s} \times \hat{t}$ depending on whether it is an equivalent electric current or an equivalent magnetic current.

4. D_2^c and D_h^c are discontinuous for $\phi' = \pi$, since I_m^{PO}, I_m^{LPO}, M^{PO}, M^{LPO} are discontinuous for $\phi' = \pi$, except for two important special cases. In the case of backscatter $\phi = \phi' = \pi$ and all of the components with the factor containing the step function are zero for $\phi' = \pi$, so that the resulting corner diffraction coefficient is continuous. When the observation point is on the Keller cone $I_m^{LPO} = I_m^{PO}$ and $M^{LPO} = M^{PO}$ so that the discontinuous components in the corner diffraction coefficients cancel leaving the corner diffraction coefficients continuous. It is pointed out how this discontinuity may affect some typical patterns in Section 4.4.

5. D_s^c, D_2^c, and D_h^c are all infinite at the shadow boundaries because the LPO components are infinite. The LPO components are infinite because the vector identity used to derive them is not valid at the shadow boundaries (see the end of Section 3.2). This is not a problem in practice since the corner diffraction coefficients will remain finite a small distance away from the shadow boundaries.

6. All of the diffraction coefficients become infinite on the Keller cone. This is not a problem however, since for straight edges the contribution from the other corner of the edge will also be infinite and their sum will combine to form the familiar $\sin x/x$ pattern associated with a constant current element.

7. The contribution to the scattered field from the individual corner happens to be infinite when $\beta = \beta'$. This is not the case for the finite plate, however, since the individual contributions from all of the edges balance each other to give a bounded result. This is shown analytically in Section 4.5 for the special case of backscatter from a rectangular plat at normal incidence. It is also illustrated many times in Chapter V since $\beta = \beta'$ for at least one edge in all of the patterns taken in the principle plane.

4.3 Boundary Conditions

Since the new solution is only valid in the far zone it does not need to meet the boundary conditions on the scattering structure, except for the special case of a half plane (semi-infinite). Actually the scattered field in the plane of a given face must meet different conditions. The conditions on the scattered field may be easily found using the far zone radiation integral combined with the fact that the faces of the structure are flat. Given an arbitrary perfectly conducting flat face

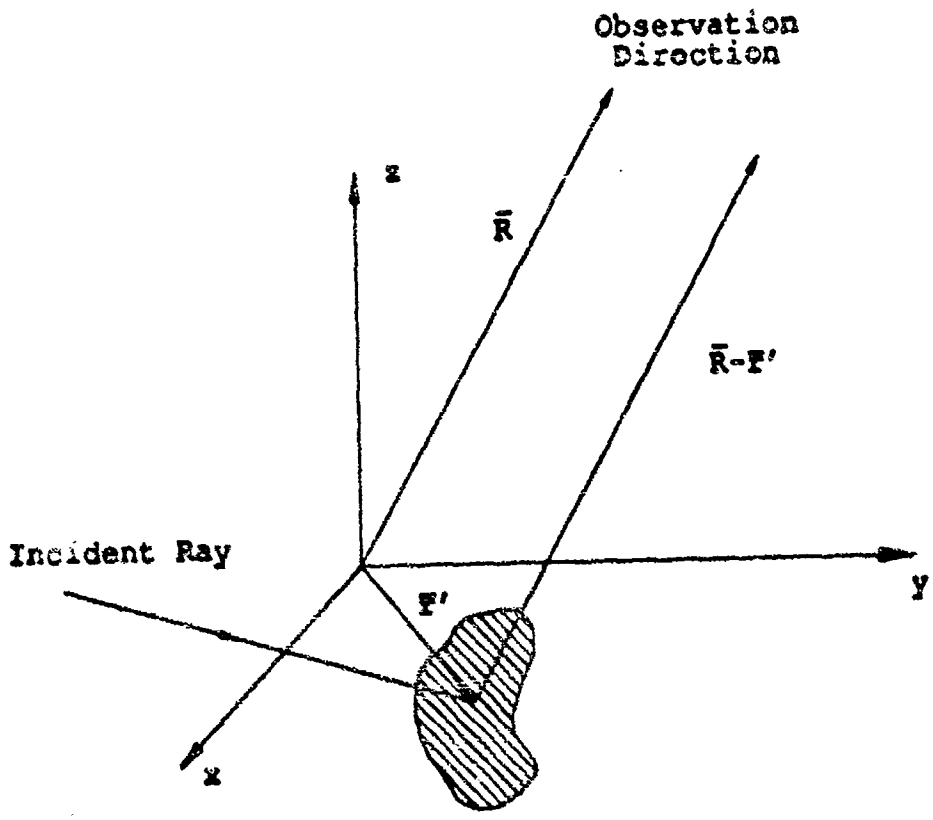

Figure 37: Boundary Conditions Example.

shown in Figure 37 and illuminated from some arbitrary direction, the far zone scattered field is given by

$$\vec{E}^s = \frac{jkZ_0}{4\pi}\frac{e^{-jkR}}{R}\hat{s}\times\hat{s}\times\int\int_{S'}\vec{J}_s(r')e^{jk\hat{s}\cdot\vec{r}'}dxdy \tag{4.10}$$

where the important coordinates are defined in Figure 37 and $\vec{J}_s$ is the actual current on the surface of the face. Obviously $\vec{J}_s$ only has nonzero components in the $\hat{x}$ and $\hat{y}$ directions. As a result when the observation point is in the plane of the face (the x-y plane) the z component of the total scattered electric field must be zero. This also implies, by reciprocity, that the total scattered field in the special case when the face shown is the only scattering object (n=2) should be zero everywhere for a $\hat{z}$ directed source placed in the x-y plane. These conditions only apply to the total scattered field and do not necessarily apply to a first order solution as is given here.

It is assumed that the first order fields radiated by the equivalent currents must meet these conditions in the plane of the face. (Why this assumption is not correct will be discussed later in this section.) This assumption combined with the radiation integral for the equivalent edge currents given by

$$\vec{E}^s = \frac{jk}{4\pi}\frac{e^{-jkR}}{R}\int_c\left[Z_0\,\hat{s}\times\hat{s}\times\hat{t}\,I+\hat{s}\times\hat{t}\,M\right]e^{jk\hat{s}\cdot\vec{t}}dt \tag{4.11}$$

or the corner diffraction coefficients lead to the following properties:

1. M=0 and $D_h^c = 0$ when $\phi = 0$ or $\phi = \pi$,

2. $I_m = M = 0$ and $D_h^c = D_2^c = 0$ when $\phi' = 0$ and $n = 2$ or $\phi' = \pi$ and $n = 2$ ($I_e = 0$ and D_s^c contributes zero to the scattered field since $E_{\phi'}^i = E_t^i = 0$).

Plugging $\phi = 0, \pi$ into the new solution it is seen that the first property is met everywhere in the plane of the face with the exception of two directions. One

is in the forward scatter direction which corresponds to the Ufimtsev singularity discussed in item 1 of Section 4.2. The other direction where this property is not met is the direction where the Keller cone and the infinite half plane associated with the edge meet. It is interesting to note that this direction lies along the infinite strip used in deriving the equivalent fringe currents. Two of the equivalent currents associated with the solution to the infinite wedge (I_m^{UTD} and M^{UTD}) are discontinuous here, as illustrated in item 2 of Section 4.2. It appears that the solution meets the first far zone condition given above everywhere except on this strip where it meets the boundary conditions on a PEC. Plugging in $\phi' = 0, \pi$ and $n = 2$ into Equations (3.47) and (3.49) it is easily seen that the second condition given above is not met in general.

Both the previous equivalent currents given in Section 2.6 and the previous corner diffraction solution given in Section 2.7 meet the boundary conditions on the infinite half plane associated with the edge. That is $I = 0$ (and $D_s^c = 0$) for $\phi = 0$ and $I = 0$ (and $D_s^c = 0$) for $\phi' = 0$.

It has been shown that, in general, the first order solution should not meet the far zone conditions described here. Specifically, both Sikta [26] (for the special case of backscatter) and Tiberio [27] have shown that for the two-dimensional problem of an infinite strip of finite width the double diffraction term cancels the first order term so that the far zone conditions in the plane of the face are met. The new solution is still consistent with this requirement since it reduces to the previous equivalent currents for observation points on the Keller cone (see Section 4.6). Since the solution to the infinite quarter plane has not been reduced to a ray optical form, the conditions that the first order field must meet in the plane of the face when the observation point is not on the Keller cone are not clear. In this case the new solution and the previous solutions behave much differently.

Therefore, when the observation point is not on the Keller cone the higher order terms for the new solution may be significantly different than those developed for previous solutions. Some results for three-dimensional problems including higher order terms have been published by Sikta, *et al.* [2] and [26] and Michaeli [28] using the previous equivalent currents and the new equivalent currents, respectively.

4.4 Reciprocity

Although only the total scattered field must satisfy reciprocity, once again it would seem desirable for the first order scattered field given by the new equivalent currents or corner diffraction coefficients to also satisfy reciprocity. Both the reflected GO field and the edge diffracted field satisfy reciprocity even though they only make up a partial contribution to the total scattered field. Even though the new solution is not reciprocal, several examples are given that show it is probably close enough, in most cases, for engineering purposes.

A simple example is used to illustrate that the new solution is not reciprocal. This is shown by considering where the singularities of the fringe occur. Neither $I_m^f = I_m^{UTD} - I_m^{PO}$ nor $M^f = M^{UTD} - M^{PO}$ approach definite limits as the observation point approaches the intersection of the Keller cone and the infinite half-plane associated with the edge of the plate. However if the source is allowed to approach this position in the same way all of the currents are finite and approach definite limits. Using these properties a simple example is given which shows that the solution is not reciprocal. A triangular flat plate, as shown in Figure 38, is illuminated by a source positioned above the plane of the plate in position one. The observation point is placed at position two in the plane of the plate such that it lies on the Keller cone for the points on edge one, as indicated in Figure 38. Both I_m^f and M^f are undefined for points along edge one which makes a nonzero

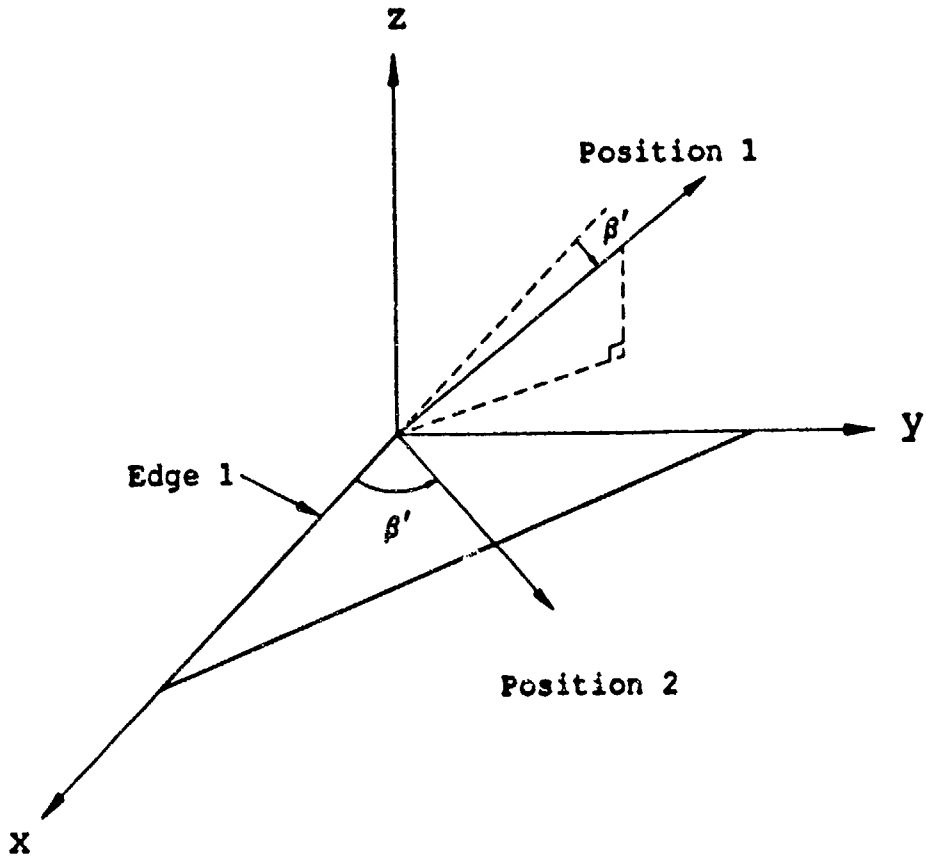

Figure 38: Reciprocity example.

contribution to the radiation integral. Therefore the scattered field is not defined here. However if the source and receiver are interchanged all of the currents are well defined and therefore the scattered field will be defined. It is not surprising that the new solution is not reciprocal since it contains PO terms which are not reciprocal themselves.

Several examples of bistatic scattering from a flat plate or a cube are given here to illustrate that the solution is essentially reciprocal in many instances. All of the examples are in terms of linearly polarized antennas in the far zone of the scatterer. First the RCS is calculated when the first antenna is receiving and the second antenna is transmitting. The RCS is then calculated for the reciprocal problem (antenna one transmitting and antenna two receiving). Both patterns are plotted on the same graph as a function of the position of antenna one, so that they may be easily compared.

The first set of examples show the scattering from a square plate two wavelengths on a side as shown Figure 39. In the first two examples both antennas are moved in the principle plane while they are offset by 90° in that plane, as shown in Figure 39. Figure 40 shows the results when both antennas are linearly polarized in the $\hat{\theta}$ direction, while Figure 41 shows the results when they are both linearly polarized in the $\hat{\phi}$ direction. The cross-polarized fields are zero in both cases. The results show that in this case the solution is reciprocal for practical purposes. This is not surprising since in this case the major contribution to the fields comes from the front and back edges. The receiving antenna lies on the Keller cone of the front and back edges for the entire pattern cut. The new solution is reciprocal for observation points on the Keller cone since, as is shown later in Section 4.6, it reduces to Keller's result there.

In the next two examples both antennas are moved in the $\phi = 45°$ plane offset

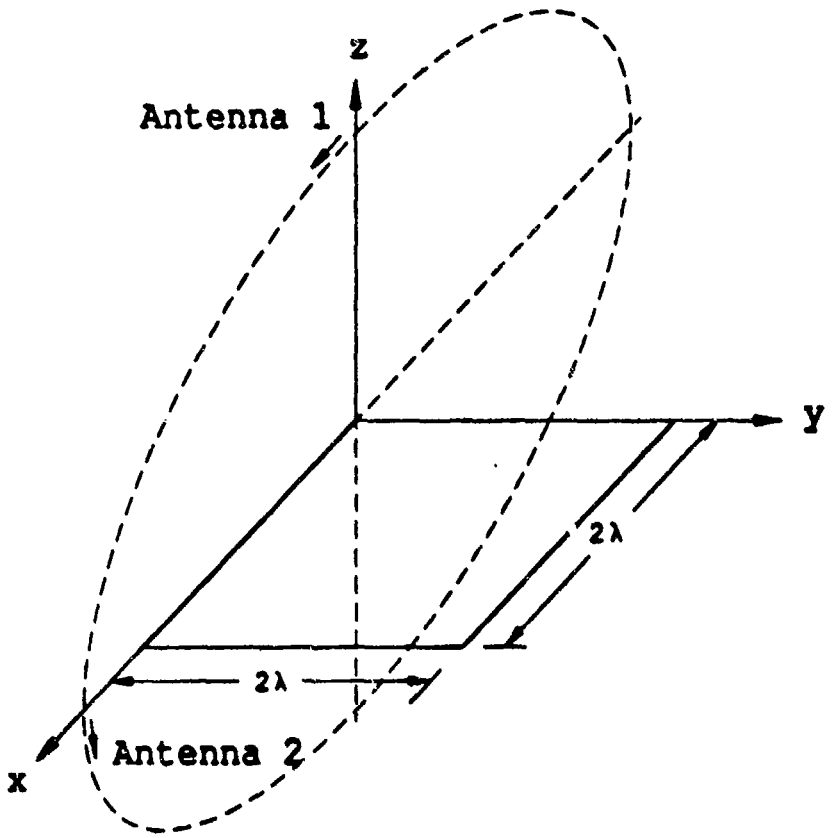

Figure 39: Relative positions of the two antennas for the first two patterns.

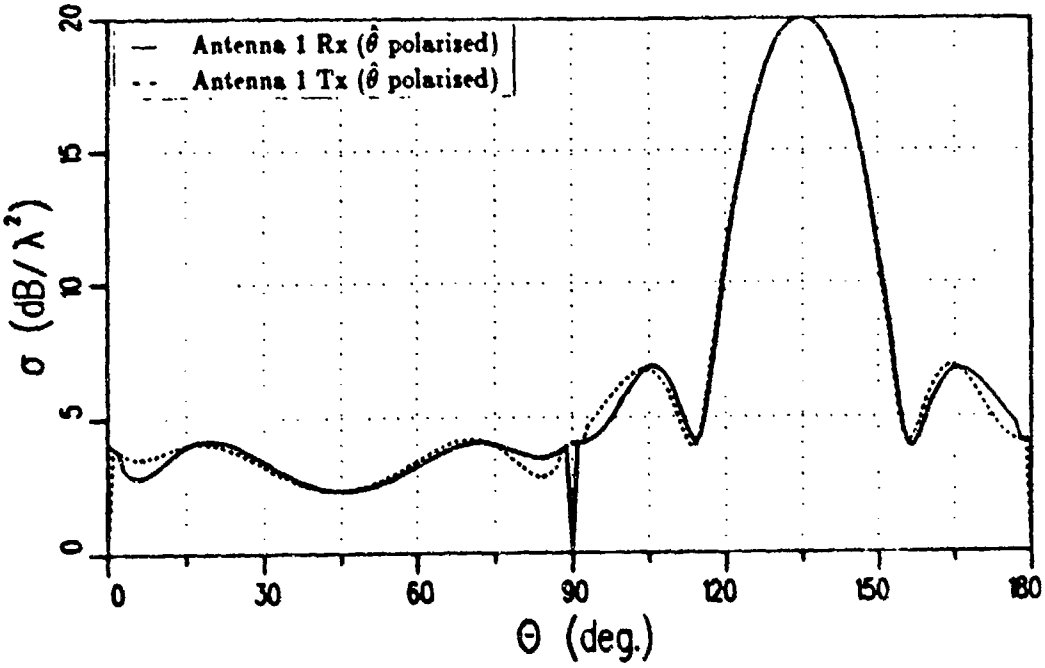

Figure 40: RCS of 2λ square plate for $\hat{\theta}$ polarized antennas (which are positioned as indicated in Figure 39) in the $\phi = 0°$ plane.

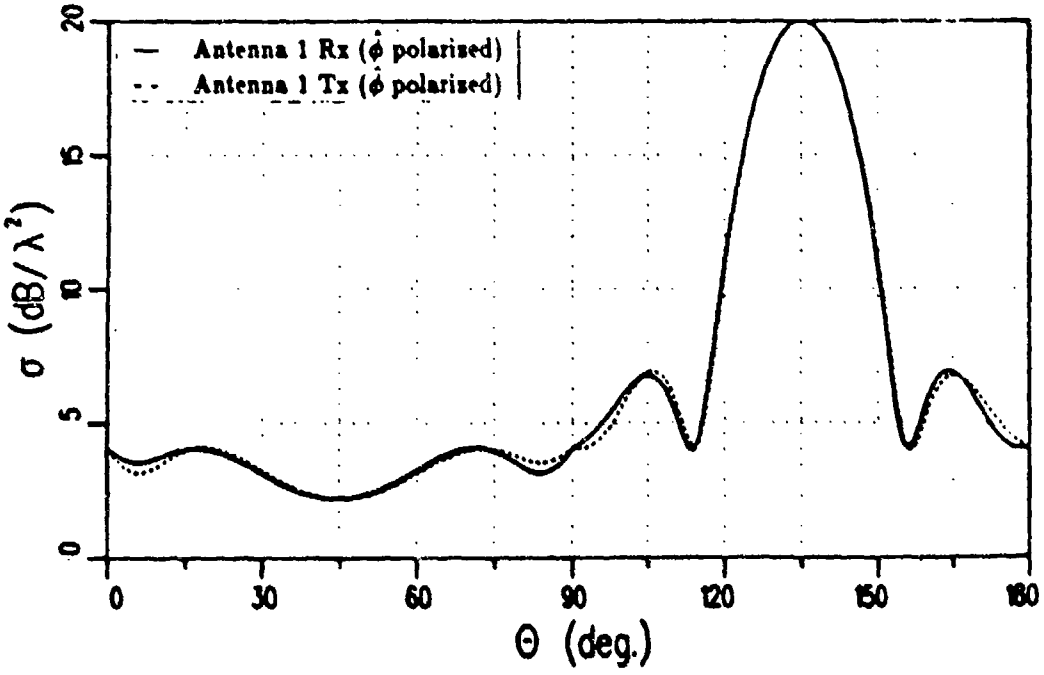

Figure 41: RCS of 2λ square plate for $\hat{\phi}$ polarized antennas (which are positioned as indicated in Figure 39) in the $\phi = 0°$ plane.

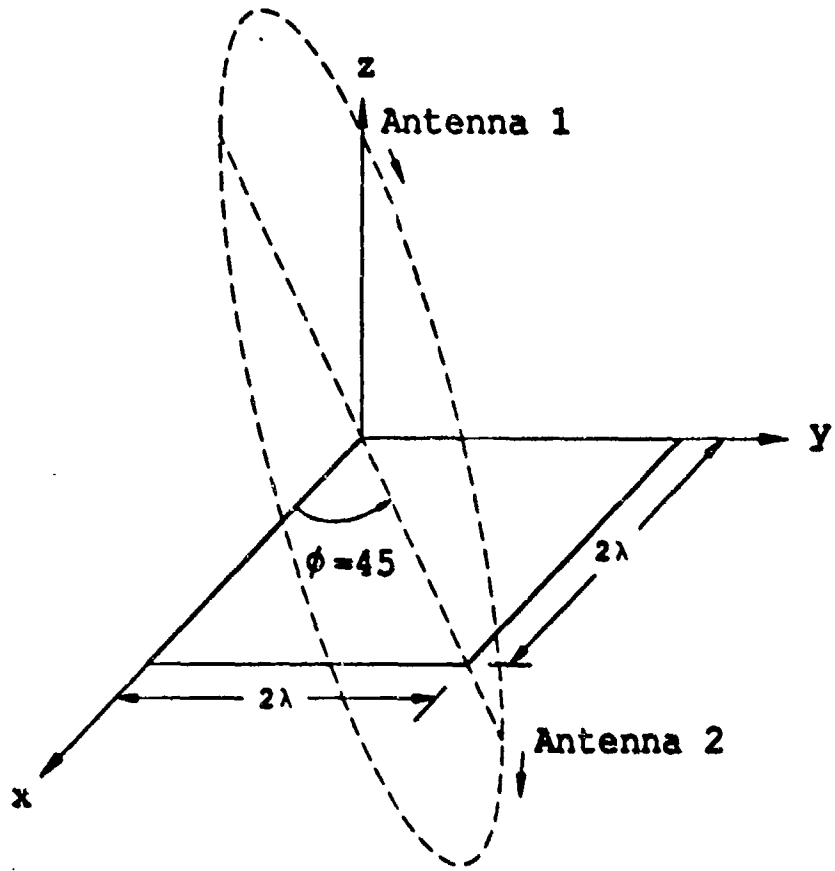

Figure 42: Relative positions of the two antennas for the next two patterns.

by 90° in that plane, as shown in Figure 42. Figure 43 shows the results when both antennas are linearly polarized in the $\hat{\theta}$ direction, while Figure 44 shows the results when they are both linearly polarized in the $\hat{\phi}$ direction. The cross-polarized fields are zero in both cases. Although the results are not nearly as close as in the previous patterns, the major differences occur when either the receiver or the source is near the plane of the plate where higher order terms may become important. The antennas are moved in the $\phi = 30°$ plane offset by 30° in that plane as shown in Figure 45 for the next three examples. Figure 46 shows the results when both antennas are linearly polarized in the $\hat{\theta}$ direction, while Figure 47 shows the results

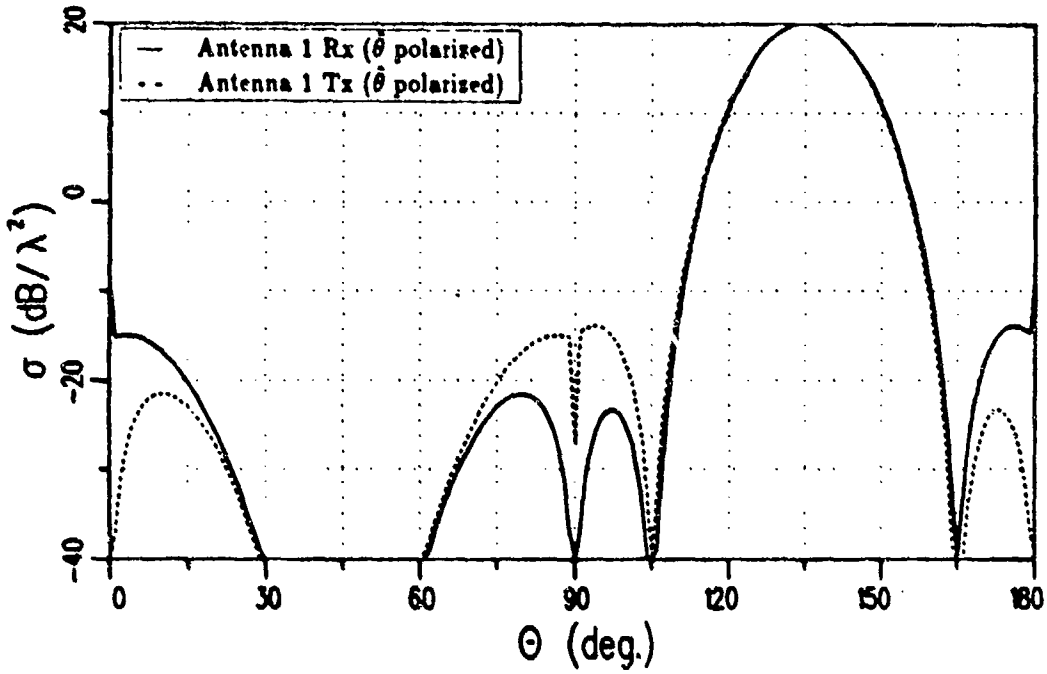

Figure 43: RCS of 2λ square plate for $\hat{\theta}$ polarized antennas (which are positioned as indicated in Figure 42) in the $\phi = 45°$ plane.

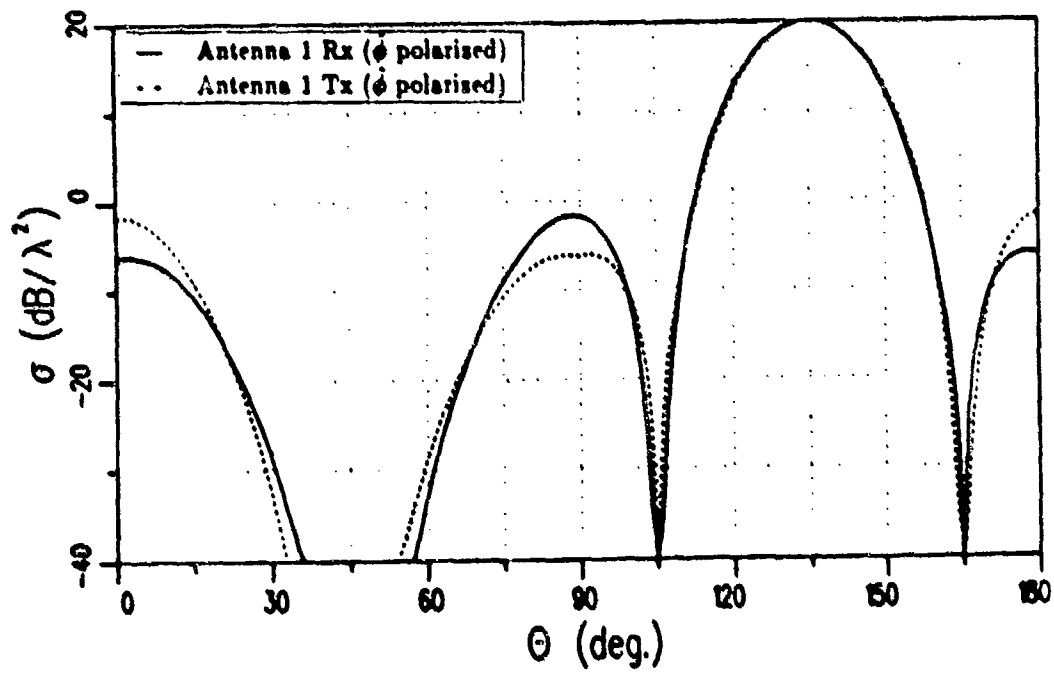

Figure 44: RCS of 2λ square plate for $\hat{\phi}$ polarized antennas (which are positioned as indicated in Figure 42) in the $\phi = 45°$ plane.

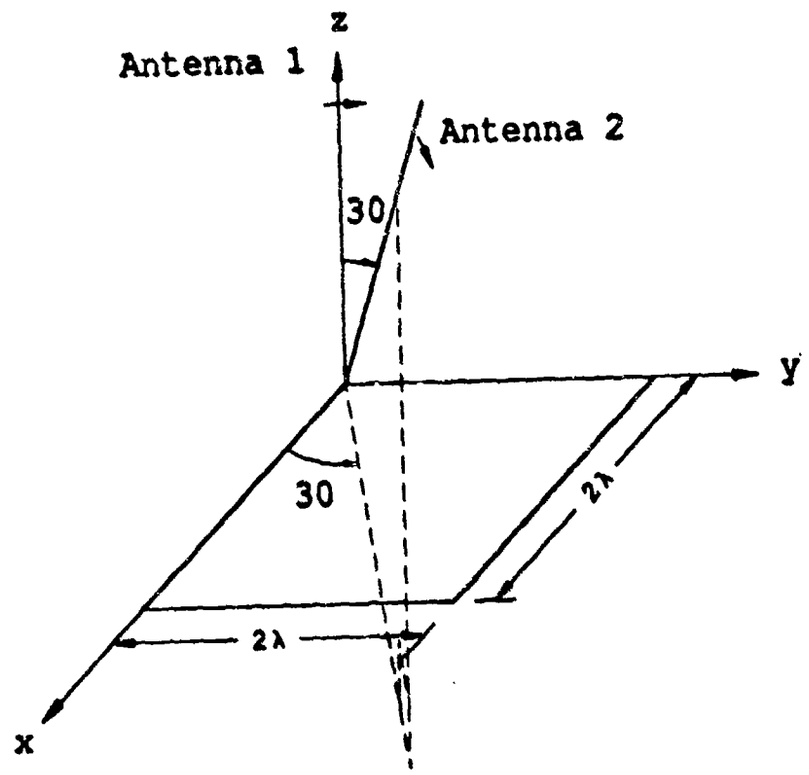

Figure 45: Relative positions of the two antennas for the next three patterns.

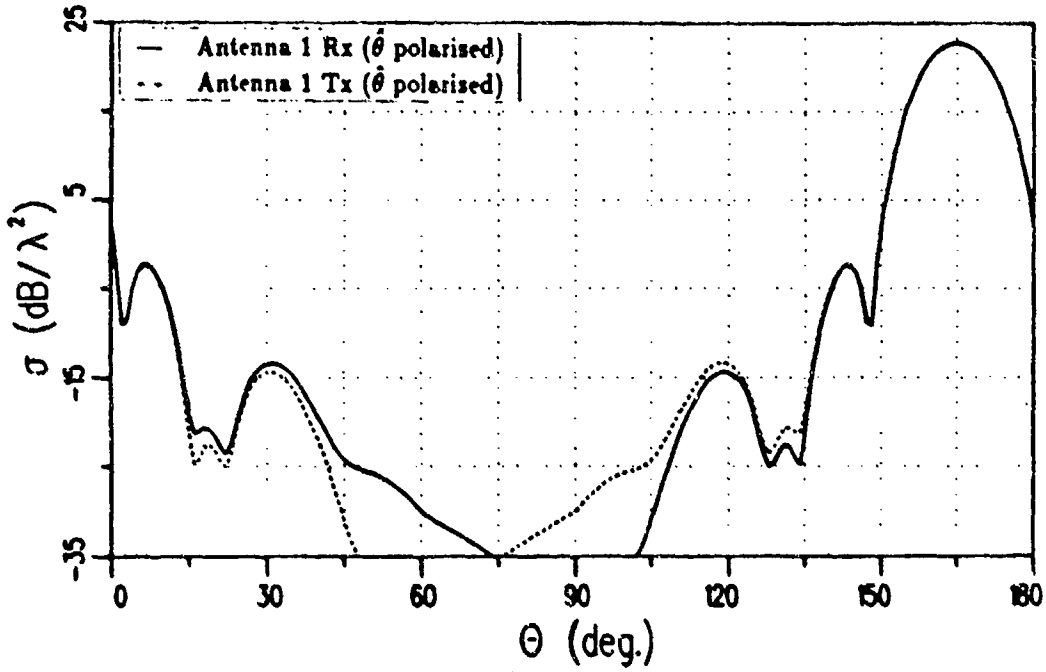

Figure 46: RCS of 2λ square plate for $\hat{\theta}$ polarized antennas (which are positioned as indicated in Figure 45) in the $\phi = 30°$ plane.

when they are both linearly polarized in the $\hat{\phi}$ direction. In this case, however, the cross-polarized fields are no longer zero. It should be noted that reciprocity does not imply that $\sigma_{\theta\phi} = \sigma_{\phi\theta}$ for bistatic scattering, and in general $\sigma_{\theta\phi} \neq \sigma_{\phi\theta}$ for bistatic scattering. Reciprocity implies that the pattern remains unchanged if the antenna originally transmitting receives while the antenna originally receiving transmits, but the positions of the two antennas remain unchanged (in the bistatic case, $\sigma_{\theta\phi}, \sigma_{\phi\theta}$ give the results when the positions of the antennas are interchanged). Figure 48 gives the cross-polarized results when antenna one is linearly polarized in the $\hat{\theta}$ direction and antenna two is linearly polarized in the $\hat{\phi}$ direction. If the polarizations are reversed, that is antenna one is linearly polarized in the $\hat{\phi}$ direction and antenna two is polarized in the $\hat{\theta}$ direction one simply obtains the mirror image of both curves due to the symmetry of the problem.

The co-polarized fields are close to being reciprocal in this case. The cross-polarized fields are reasonably reciprocal for regions away from the plane of the

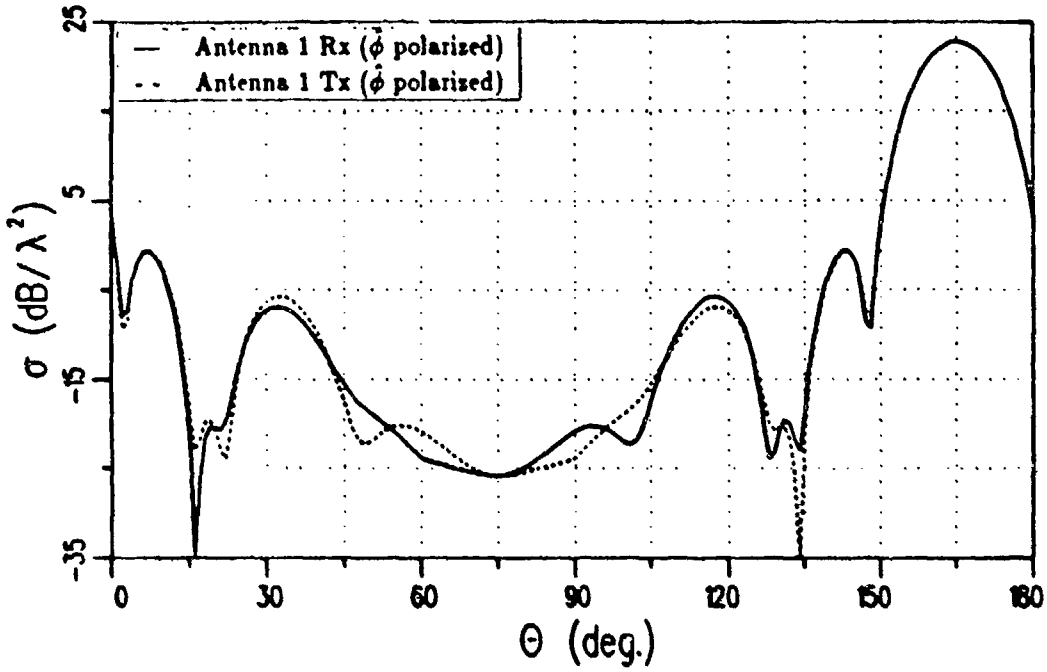

Figure 47: RCS of 2λ square plate for $\hat{\phi}$ polarized antennas (which are positioned as indicated in Figure 45) in the $\phi = 30°$ plane.

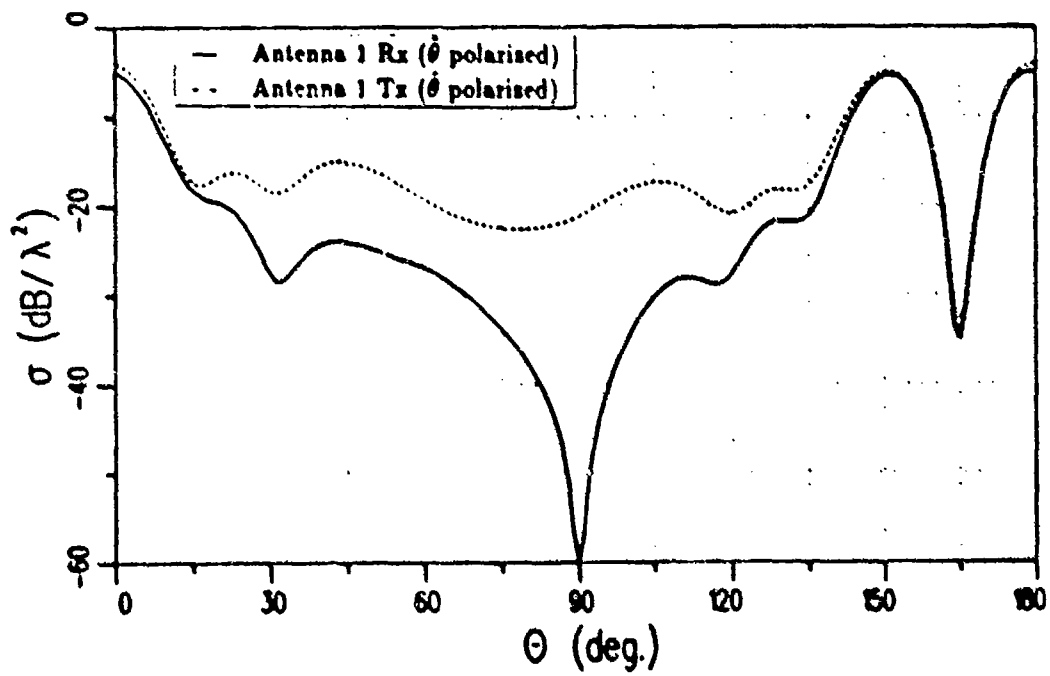

Figure 48: RCS of 2λ square plate for cross polarized antennas (which are positioned as indicated in Figure 45) in the $\phi = 30°$ plane.

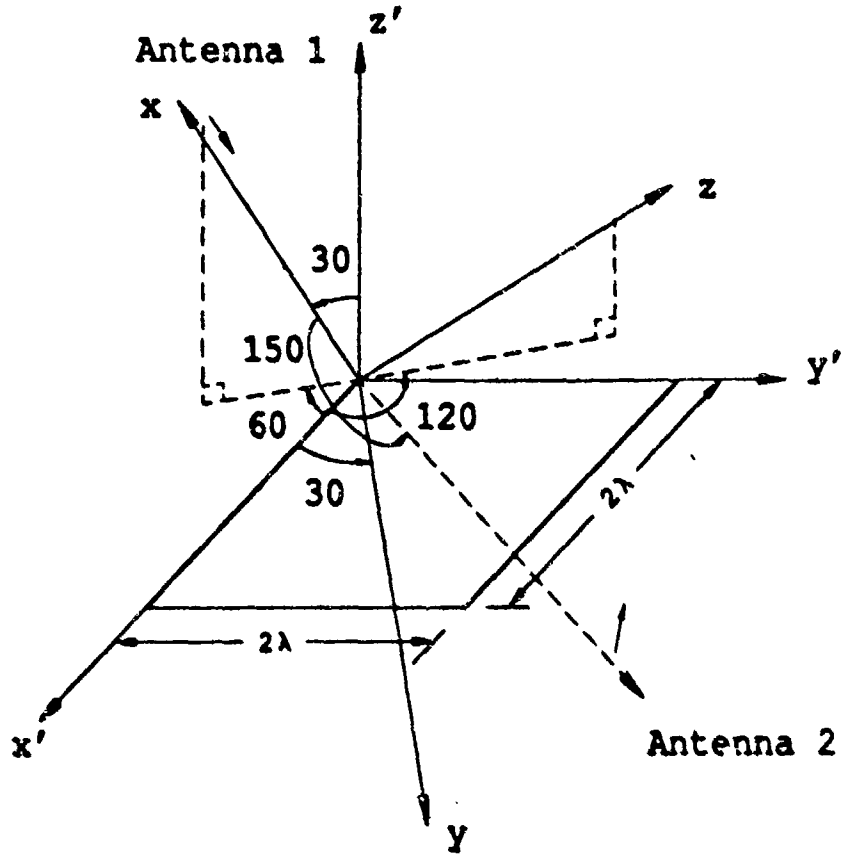

Figure 49: Relative positions of the two antennas for the next four patterns.

plate. In regions near the plane of the plate, the pattern with the null at $\theta = 90°$ is probably more accurate since the plate does not radiate any $\hat{\theta}$ polarized field in this plane. The lack of a null here in the other case may be explained by the fact that I_m (or D_2^c) does not meet the conditions in the plane of the face described in the previous section. Finally the antennas are moved in a plane found by rotating the x-z plane 120° in the $\hat{\phi}$ direction followed by tilting it 30° in the $\hat{\theta}$ direction, as shown in Figure 49. The two antennas are then offset by 150° in the x-y plane.

Figure 50 shows the results when both antennas are linearly polarized in the

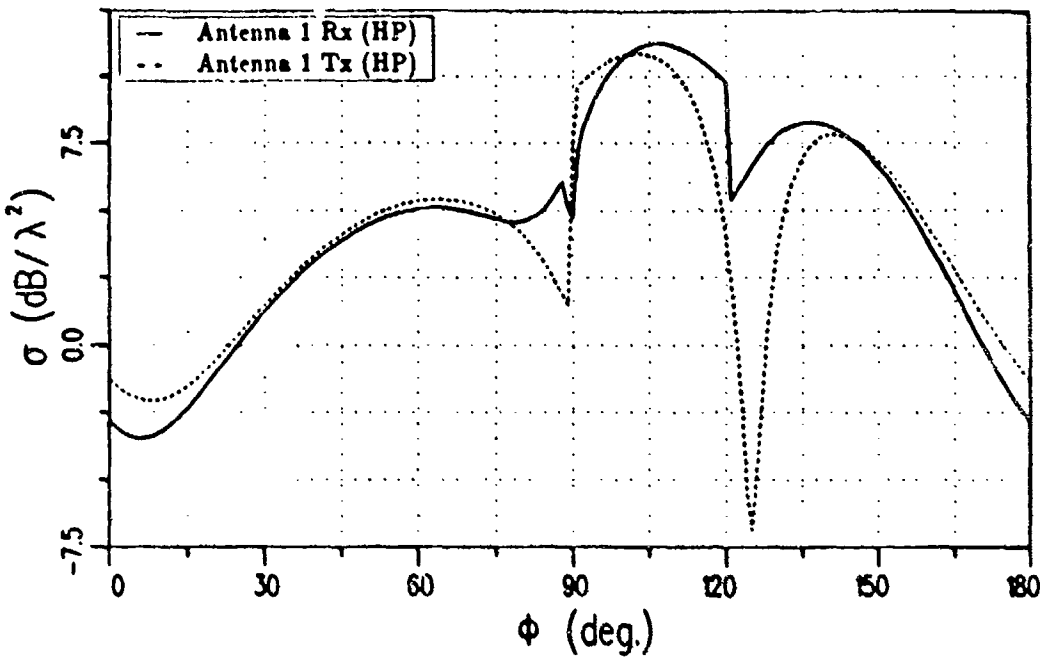

Figure 50: RCS of 2λ square plate for horizontally polarized antennas (which are positioned as indicated in Figure 49).

direction parallel to the plane the pattern is taken in and perpendicular to the incident ray (Horizontal Polarization), while Figure 51 shows the results when they are both linearly polarized in the direction perpendicular to the plane the pattern is taken in (Vertical Polarization). Once again the cross-polarized fields are not zero. Figure 52 gives the cross-polarized results when antenna one is horizontally polarized and antenna two is vertically polarized. Figure 53 gives the patterns for the opposite case where antenna one is vertically polarized and antenna two is horizontally polarized. The discontinuity in the four patterns which occurs when $\phi = 120°$ and antenna two is transmitting (solid curves in Figures 50, 51, 52, and 53) is due to the discontinuity in the PO components described in item 4 of Section 4.2. The discontinuity in the four patterns which occurs when $\phi = 90°$ and antenna two is transmitting is due to the discontinuity in the contribution from the edge along the x-axis. The direction $\phi = 90°$ corresponds to the intersection of the Keller cone and the infinite half plane associated with this edge ($\beta_1 \approx \beta_1' \approx 30°$

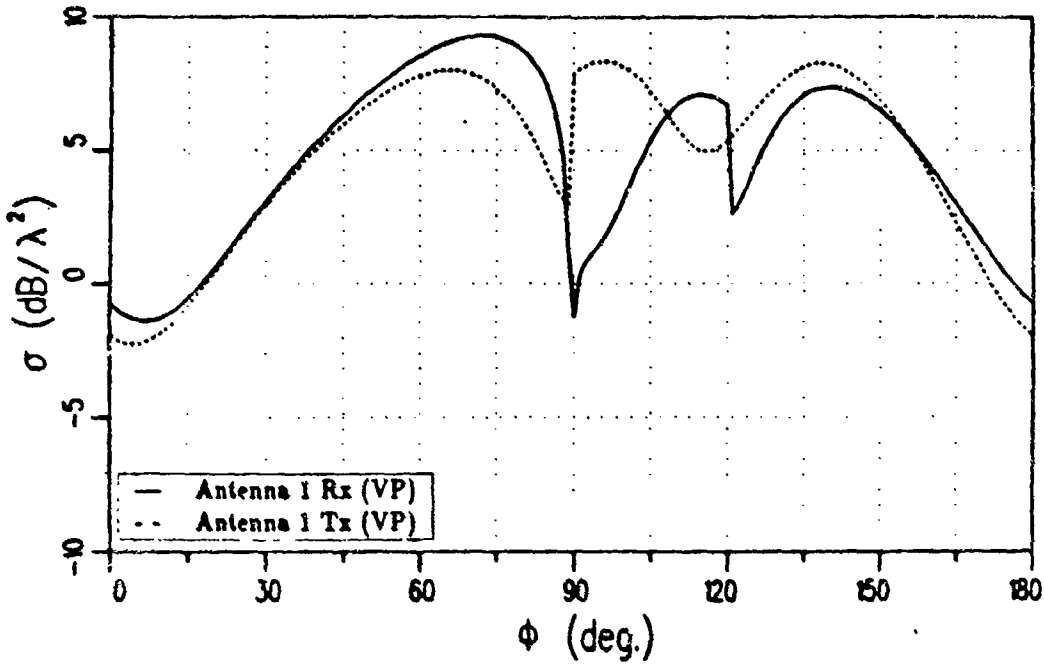

Figure 51: RCS of 2λ square plate for vertically polarized antennas (which are positioned as indicated in Figure 49).

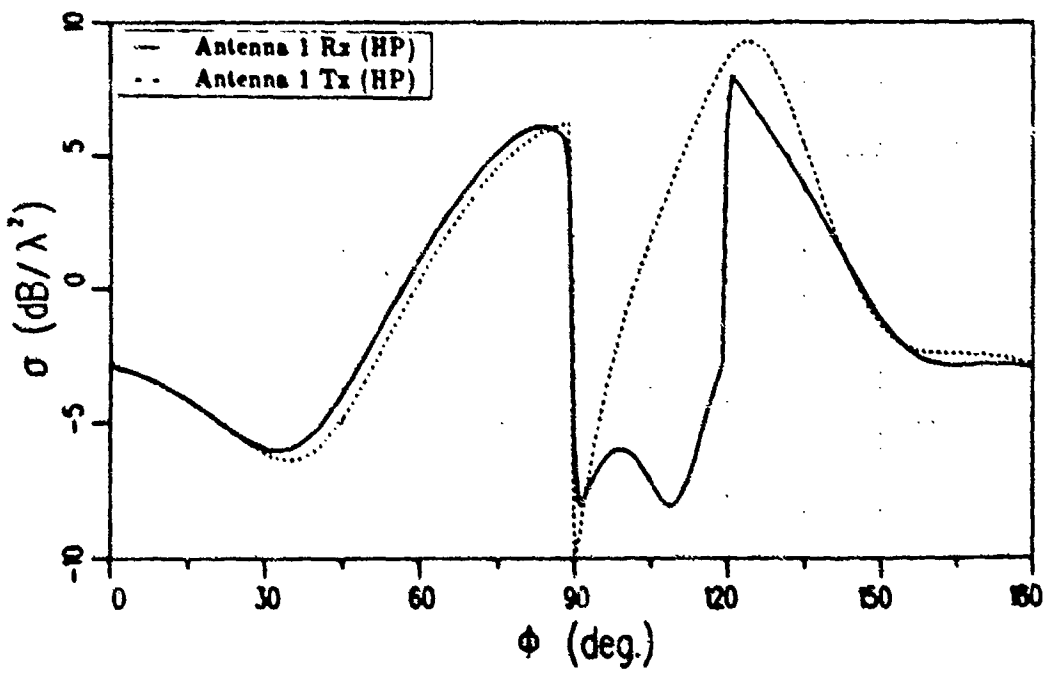

Figure 52: RCS of 2λ square plate for antenna one horizontally polarized and antenna two vertically polarized (which are positioned as indicated in Figure 49).

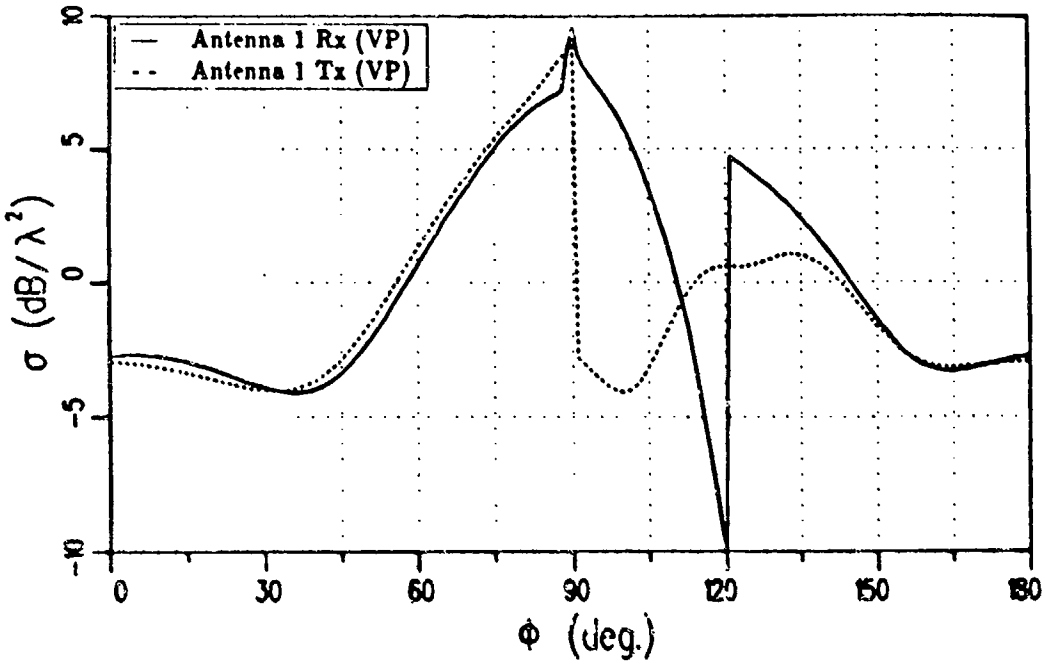

Figure 53: RCS of 2λ square plate for antenna one vertically polarized and antenna two horizontally polarized (which are positioned as indicated in Figure 49).

and $\phi_1 \approx 0°$) where the corner diffraction coefficient is discontinuous (see item 2 of Section 4.2). The discontinuity in the four patterns which occurs when $\phi = 90°$ and antenna one is transmitting (dashed line in Figures 50, 51, 52, and 53) is due to the discontinuity in the PO components described in item 4 of Section 4.2. For directions at least 15° to 20° away from these discontinuities the solution is close to being reciprocal.

To get some indication of the effect of wedge angle on these examples the same patterns are repeated for the case of a cube two wavelengths on a side. The cube is positioned in the usual way so that each edge is parallel to one of the three axes. The relative positions of the antennas for the first two patterns are given in Figure 39. Figure 54 shows the results when both antennas are linearly polarized in the $\hat{\theta}$ direction, while Figure 55 shows the results when they are both linearly polarized in the $\hat{\phi}$ direction. As in the case of the flat plate the co-polarized field

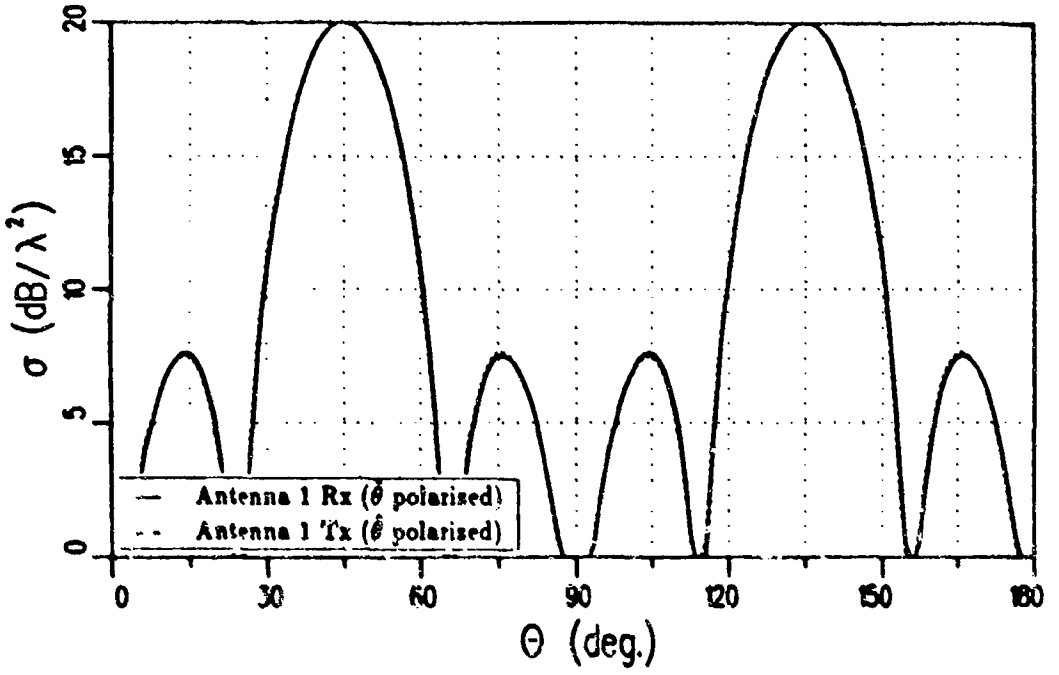

Figure 54: RCS of 2λ cube for $\hat{\theta}$ polarized antennas (which are positioned as indicated in Figure 39) in the $\phi = 0^{\circ}$ plane.

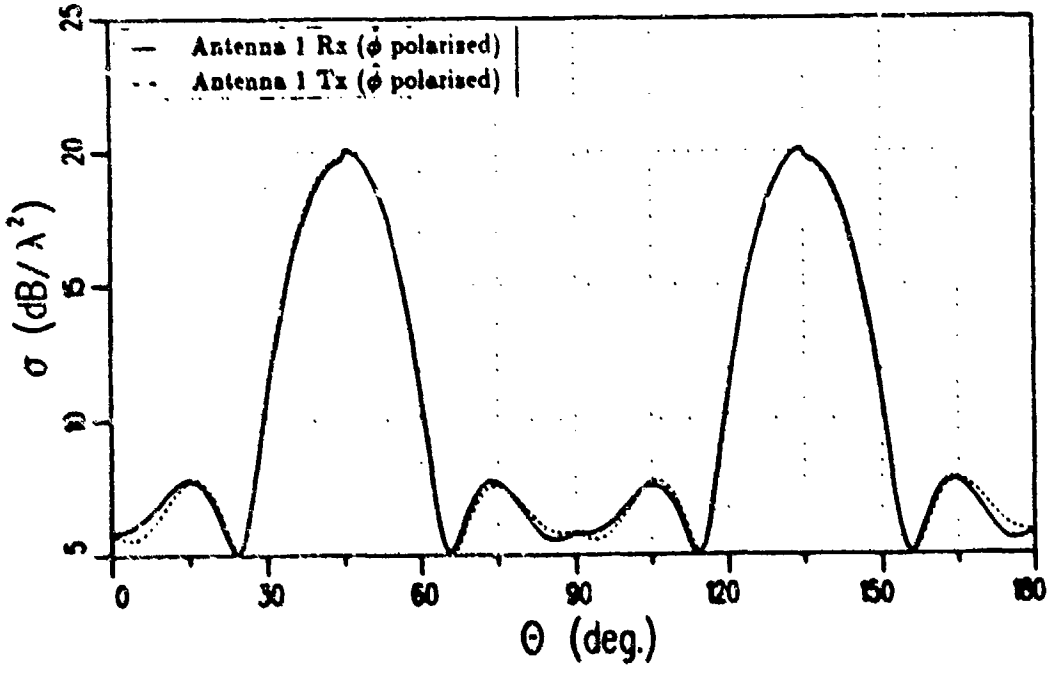

Figure 55: RCS of 2λ cube for $\hat{\phi}$ polarized antennas (which are positioned as indicated in Figure 39) in the $\phi = 0^{\circ}$ plane.

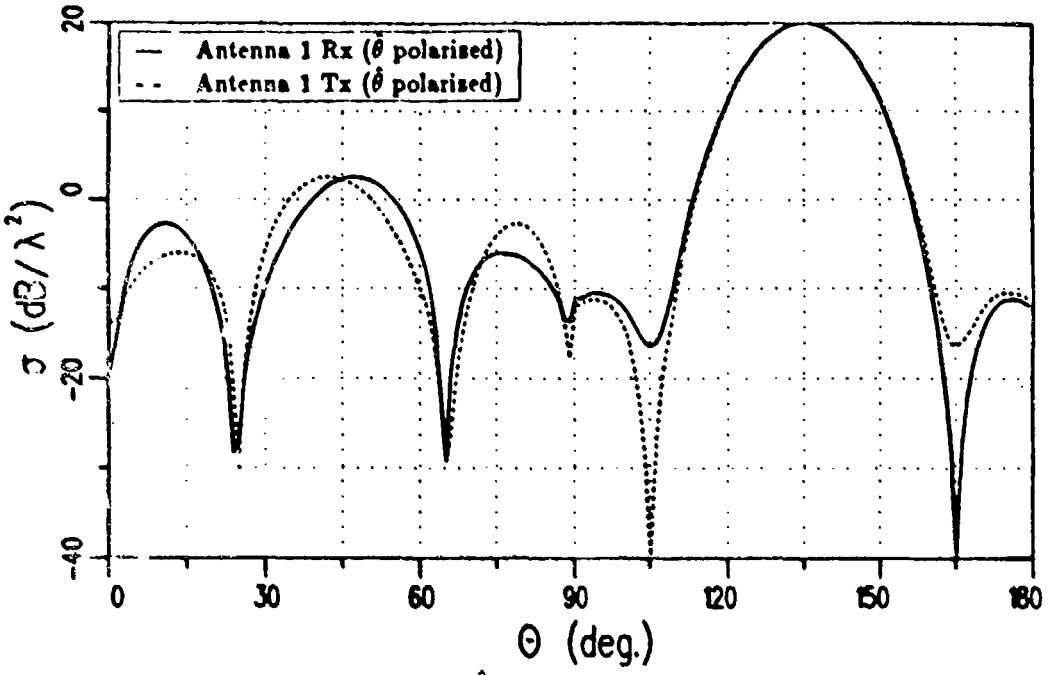

Figure 56: RCS of 2λ cube for $\hat{\theta}$ polarized antennas (which are positioned as indicated in Figure 42) in the $\phi = 45°$ plane.

in the principle plane is reciprocal for practical purposes. This is expected since the major contribution to the scattered field is from the edges perpendicular to the pattern plane. In both examples the receiving antenna lies on the Keller cone of these edges where the solution reduces to Keller's form as discussed in Section 4.6. The small discontinuity at the peaks of the $\hat{\phi}$ polarized pattern is due to the contribution from the two edges parallel to the pattern plane and farthest from the source and receiver. The contribution from these two edges is discontinuous in this case due to the discontinuity in D_h^c and D_2^c described earlier in item 2 of Section 4.2.

In the next two examples both antennas are moved in the $\phi = 45°$ plane offset by 90° in that plane, as shown in Figure 42. Figure 56 shows the results when both antennas are linearly polarized in the $\hat{\theta}$ direction, while Figure 57 shows the results when they are both linearly polarized in the $\hat{\phi}$ direction. The cross-polarized fields are zero in both cases. The results are fairly close to being reciprocal, although

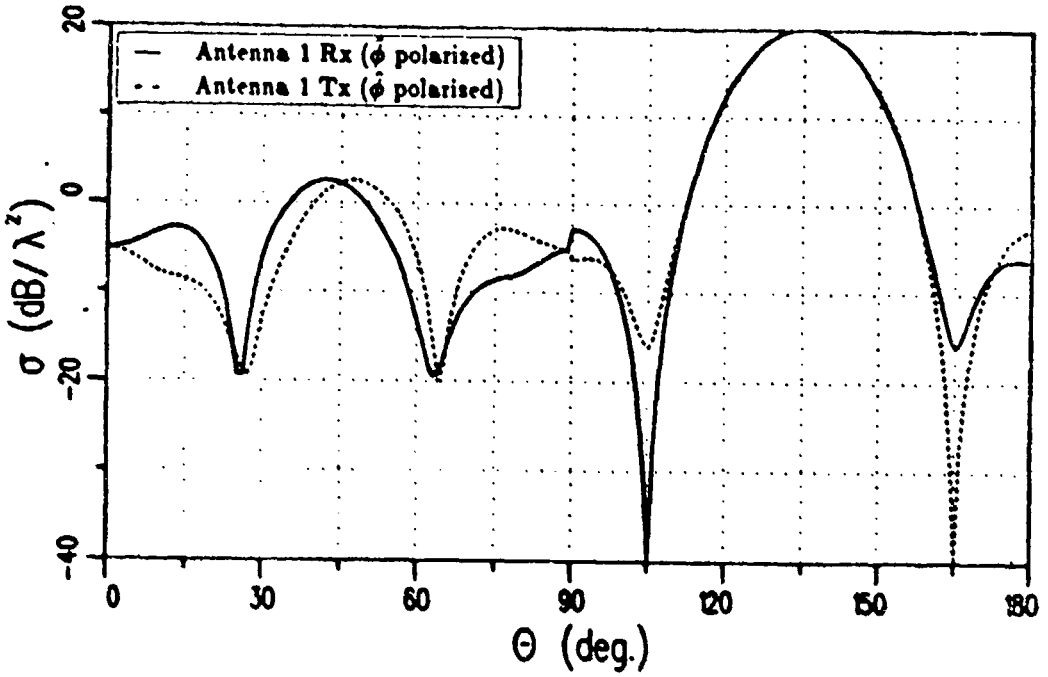

Figure 57: RCS of 2λ cube for $\hat{\phi}$ polarized antennas (which are positioned as indicated in Figure 42) in the $\phi = 45^\circ$ plane.

not as close as in the principle plane. All of the patterns are discontinuous at $\phi = 0^\circ, 90^\circ, 180^\circ$. This discontinuity is due to the discontinuity in the LPO and PO terms of D_h^c and D_2^c as described in item 4 of Section 4.2. The antennas are moved in the $\phi = 30^\circ$ plane offset by 30° in that plane as shown in Figure 45 for the next three examples. Figure 58 shows the results when both antennas are linearly polarized in the $\hat{\theta}$ direction, while Figure 59 shows the results when they are both linearly polarized in the $\hat{\phi}$ direction. In this case the cross-polarized fields are not zero. In order to avoid numerical problems associated with edge on incidence (see Appendix B) the cube was tilted 5° in the plane normal to the $\phi = 30^\circ$ plane for these calculations. Figure 48 gives the cross-polarized results when antenna one is linearly polarized in the $\hat{\theta}$ direction and antenna two is linearly polarized in the $\hat{\phi}$ direction. If the polarizations are reversed, that ie, if antenna one is linearly polarized in the $\hat{\phi}$ direction and antenna two is polarized in the $\hat{\theta}$ direction, one simply obtains the mirror image of both curves due to the symmetry of the problem.

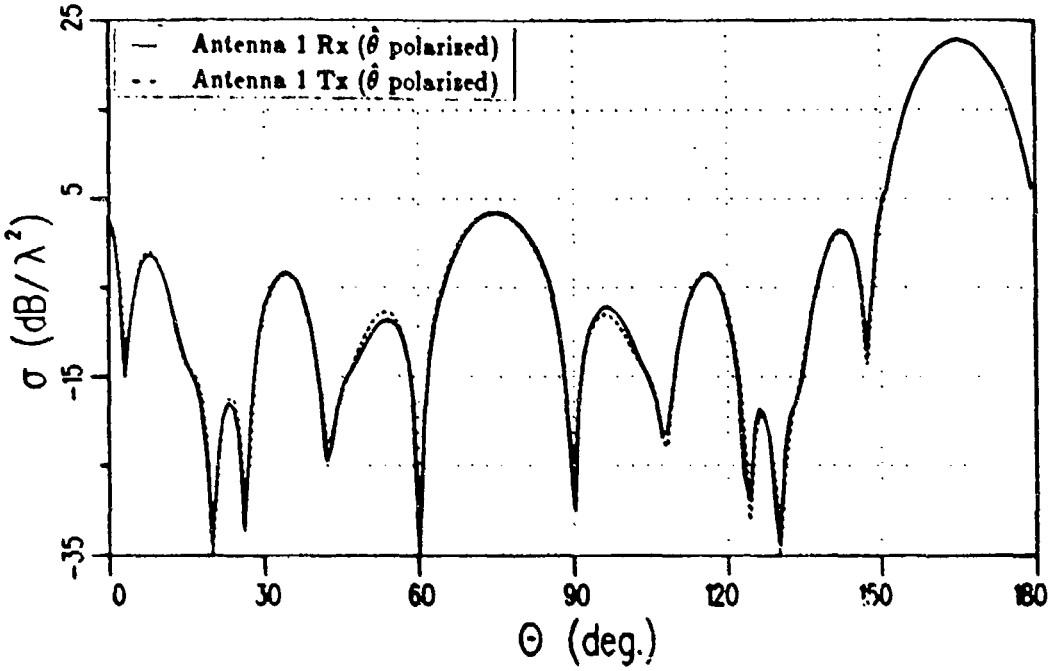

Figure 58: RCS of 2λ cube for $\hat{\theta}$ polarized antennas (which are positioned as indicated in Figure 45) in the $\phi = 30^\circ$ plane.

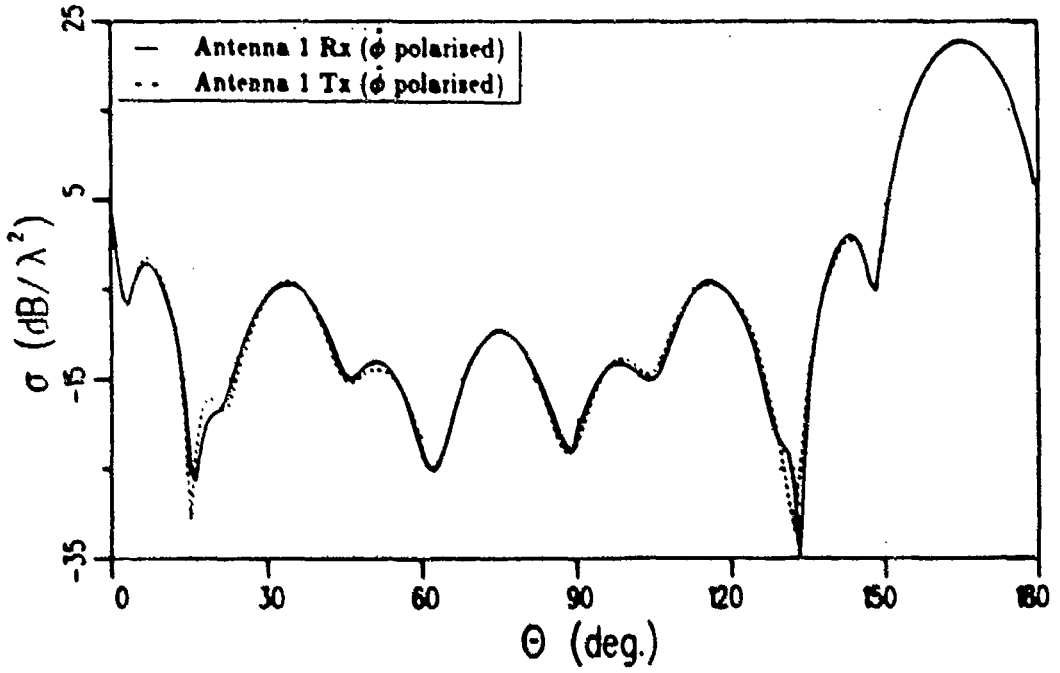

Figure 59: RCS of 2λ cube for $\hat{\phi}$ polarized antennas (which are positioned as indicated in Figure 45) in the $\phi = 30^\circ$ plane.

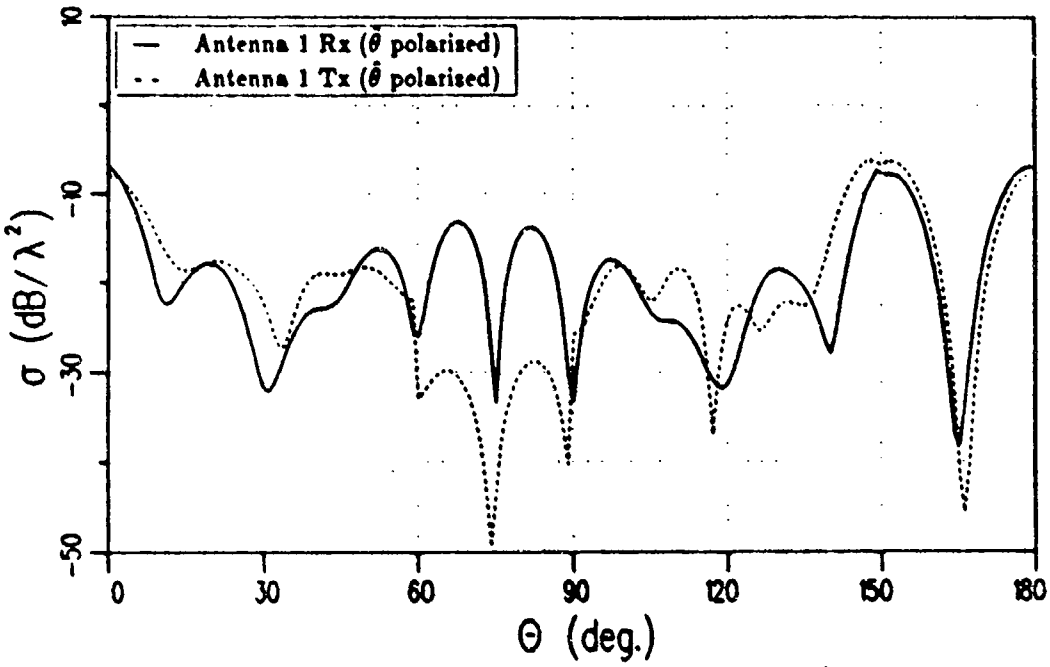

Figure 60: RCS of 2λ cube for cross polarized antennas (which are positioned as indicated in Figure 45) in the $\phi = 30°$ plane.

The co-polarized fields are essentially reciprocal in this case. The cross-polarized fields are close to being reciprocal, except in the region from $\theta = 60°$ to $90°$. All of the patterns for the case corresponding to the final example given for the plate have so many discontinuities that it is very difficult to get any information from them. For this reason they have been omitted here.

The major difference between the results for the flat plate and the results for the cube is the increase in the number of regions in space where the PO discontinuity (item 4 of Section 4.2) shows up in the patterns.

The examples given here illustrate that the solution is close to being reciprocal for the cases shown, except in regions of space where the patterns are discontinuous.

4.5 RCS of a Rectangular Plate at Broadside

As a check on the corner diffraction coefficient, the radar cross section of a flat rectangular plate (length ℓ, width w, and area A) at broadside was calculated

analytically (see Appendix C). The resulting co-polarized cross section, for either polarization, is given by

$$\sigma = \frac{4\pi A^2}{\lambda^2} . \tag{4.12}$$

This is the well known PO result, which is generally accepted as adequate for engineering purposes for sufficiently large plates. Therefore the new corner diffraction solution can be expected to give the correct value for backscatter from a general shape (consisting of flat plates) at broadside.

4.6 Equivalent Currents on the Keller Cone

The expressions for the equivalent currents on the Keller cone are easily obtained by letting $\beta = \beta'$ in Equations (3.38) and (3.40) combined with the fact that $\alpha = \gamma = \phi$ in this case. The resulting expressions for the equivalent currents with the contribution from both faces included is:

$$\begin{aligned} M &= -\frac{jH_t^i}{nY_0 k \sin^2\beta'} \left\{ \left[\cot\left(\frac{\pi - (\phi - \phi')}{2n}\right) + \cot\left(\frac{\pi + (\phi - \phi')}{2n}\right) \right] \right. \\ &\quad \left. + \left[\cot\left(\frac{\pi - (\phi + \phi')}{2n}\right) + \cot\left(\frac{\pi + (\phi + \phi')}{2n}\right) \right] \right\} \qquad (4.13) \\ I &= -\frac{jE_t^i}{nZ_0 k \sin^2\beta'} \left\{ \left[\cot\left(\frac{\pi - (\phi - \phi')}{2n}\right) + \cot\left(\frac{\pi + (\phi - \phi')}{2n}\right) \right] \right. \\ &\quad \left. - \left[\cot\left(\frac{\pi - (\phi + \phi')}{2n}\right) + \cot\left(\frac{\pi + (\phi + \phi')}{2n}\right) \right] \right\} \qquad (4.14) \end{aligned}$$

These are the same expressions for the equivalent currents as obtained by Ryan and Peters [1] given in Section 2.6. Ryan and Peters equivalent currents predict the same fields as Keller [10] obtained if the edges are straight and the observation point is on the Keller cone. Since the new equivalent currents and the new corner diffraction coefficient give the same result, the corner diffraction coefficient reduces to Keller's result for observation points on the Keller cone.

4.7 Physical Significance of Parameters α and γ

The two angles α and γ in the expressions for the equivalent currents obviously do not represent physical angles since they may become complex for several directions of incidence and observation. It is easily seen, however, that they are related to the directions along which the asymptotic endpoint contribution is taken in deriving the equivalent currents (described for the equivalent fringe currents in item 5 of Section 3.3). The first term, in Equations (3.44) and (3.45) is common to both α and γ along with the previous α parameter obtained by Michaeli [13] in his first paper on equivalent currents. The second term depends on the direction of integration used in finding the equivalent currents. Buyukdura [29] has shown that the equivalent currents associated with the PO surface integral (LPO terms) may also be obtained by making two simple changes to the procedure Michaeli used to find the fringe equivalent currents. The GO current is used on the infinite tangent wedge instead of the true current and the spatial integral is taken in the direction such that

$$\cot\theta_1 = \frac{\cos\beta - \cos\beta'}{\sin\beta\cos\phi + \sin\beta'\cos\phi'} \tag{4.15}$$

where θ_1 is the angle between the positive edge tangent and the direction of integration as shown in Figure 61. As explained in Chapter III the spatial integral used to evaluate the fringe equivalent currents was taken in a direction θ_2, where $\cot\theta_2 = \cot\beta'$, also shown in Figure 61.

Using the above angles it has been found that the new equivalent currents (and corner diffraction coefficients) may be written in a symmetric form for the special case of a flat plate. In this symmetric form, the arguments of the trigonometric functions are real valued for all angles of incidence and observation. It is also speculated that this may be done for a general wedge angle, although a method of

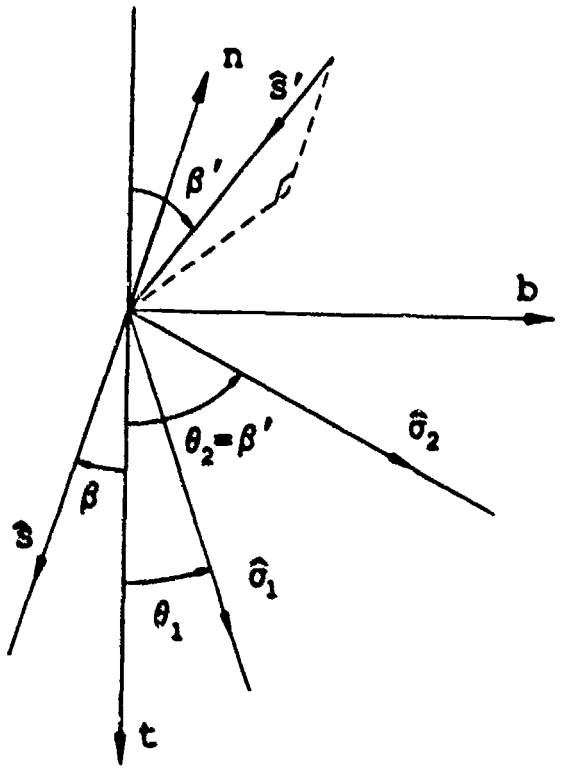

Figure 61: Integration direction (strip orientation) used to find the LPO components of the equivalent currents.

functions are real valued for all angles of incidence and observation. It is also speculated that this may be done for a general wedge angle, although a method of doing so has not been found. In the special case of a flat plate (n=2) the currents may be rewritten by properly using Equations (3.47) and (3.49) along with the trigonometric identities given in Section 3.4. The resulting expressions for the new equivalent currents are given by

$$M = M^{LPO} + M^{UTD} - M^{PO} \tag{4.16}$$

$$I = I_e + I_m \tag{4.17}$$

$$I_{e,m} = I_{e,m}^{LPO} + I_{e,m}^{UTD} - I_{e,m}^{PO} \tag{4.18}$$

where:

$$\begin{bmatrix} M^{LPO}, I_m^{LPO} \\ I_e^{LPO} \end{bmatrix} = \frac{1}{2} S^i \begin{bmatrix} a_{h,2}(1) \\ a_s(1) \end{bmatrix} \left\{ \left[\cot\left(\frac{\pi - (\psi_1 - \psi_1')}{4}\right) - \cot\left(\frac{\pi + (\psi_1 - \psi_1')}{4}\right) \right] \pm \left[\cot\left(\frac{\pi - (\psi_1 + \psi_1')}{4}\right) - \cot\left(\frac{\pi + (\psi_1 + \psi_1')}{4}\right) \right] \right\}$$

$$\begin{bmatrix} M^{UTD}, I_m^{UTD} \\ I_e^{UTD} \end{bmatrix} = \frac{1}{2} \begin{bmatrix} c_{h,2} \\ c_s \end{bmatrix} \left\{ \left[\cot\left(\frac{\pi - (\psi_2 - \psi_2')}{4}\right) - \cot\left(\frac{\pi + (\psi_2 - \psi_2')}{4}\right) \right] \pm \left[\cot\left(\frac{\pi - (\psi_2 + \psi_2')}{4}\right) - \cot\left(\frac{\pi + (\psi_2 + \psi_2')}{4}\right) \right] \right\}$$

$$\begin{bmatrix} M^{PO}, I_m^{PO} \\ I_e^{PO} \end{bmatrix} = \frac{1}{2} S^i \begin{bmatrix} a_{h,2}(2) \\ a_s(2) \end{bmatrix} \left\{ \left[\cot\left(\frac{\pi - (\psi_2 - \psi_2')}{4}\right) - \cot\left(\frac{\pi + (\psi_2 - \psi_2')}{4}\right) \right] \pm \left[\cot\left(\frac{\pi - (\psi_2 + \psi_2')}{4}\right) - \cot\left(\frac{\pi + (\psi_2 + \psi_2')}{4}\right) \right] \right\}$$

$$a_2(m) = \frac{jH_t^i}{k}\frac{\sin\theta_m}{\sin\psi_m}\left(\cot\beta\cos\phi + \cot\beta'\cos\phi'\right) \tag{4.20}$$

$$c_h = \frac{jH_t^i}{Y_0 k}\frac{\sin^2\beta'\sin\phi\cos\frac{\phi'}{2}}{\sin\beta\sin\psi_2\sin\frac{\psi_2}{2}} \tag{4.21}$$

$$c_s = \frac{jE_t^i}{Z_0 k}\frac{\sin\phi'\sin\frac{\psi_2}{2}}{\sin\beta'\sin\psi_2'\cos\frac{\phi'}{2}} \tag{4.22}$$

$$\begin{aligned} c_2 &= -\frac{jH_t^i}{k}\frac{\cos\frac{\phi'}{2}}{\sin\psi_2\sin\frac{\psi_2}{2}}\left[\cot\beta'\left(\cos\psi_2 - \cos^2\beta'\right)\right. \\ &- \left.\sin^2\beta'\cot\beta\cos\phi\right] \end{aligned} \tag{4.23}$$

$$\cos\psi_m = \sin\theta_m\sin\beta\cos\phi + \cos\theta_m\cos\beta \tag{4.24}$$

$$\cos\psi_m' = \sin\theta_m\sin\beta'\cos\phi' - \cos\theta_m\cos\beta' \tag{4.25}$$

$$\cot\theta_1 = \frac{\cos\beta - \cos\beta'}{\sin\beta\cos\phi + \sin\beta'\cos\phi'} \tag{4.26}$$

$$\cot\theta_2 = \cot\beta' \tag{4.27}$$

$$S^i = \begin{cases} -1 & ,\pi - \phi' < 0 \\ 1 & ,\pi - \phi' > 0 \end{cases} \tag{4.28}$$

The details are outlined in Appendix D. Notice that the arguments of the cotangent functions now correspond to physical angles and will always be real valued. The angles ψ_1, ψ_1', ψ_2, and ψ_2' are the angles between either the incident or the diffracted ray and either of the spatial integration directions, θ_1 or θ_2, used in finding the equivalent currents. The four new angles are defined by:

$$\cos\psi_1 = \hat{s}\cdot\hat{\sigma}_1 \tag{4.29}$$

$$\cos\psi_2 = \hat{s}\cdot\hat{\sigma}_2 \tag{4.30}$$

$$\cos\psi_1' = \hat{s}'\cdot\hat{\sigma}_1 \tag{4.31}$$

$$\cos\psi_2' = \hat{s}'\cdot\hat{\sigma}_2 \tag{4.32}$$

where:

$$\hat{\sigma}_1 = \hat{b}\sin\theta_1 + \hat{t}\cos\theta_1 \tag{4.33}$$

$$\hat{\sigma}_2 = \hat{b}\sin\theta_2 + \hat{t}\cos\theta_2 \tag{4.34}$$

and θ_1 and θ_2 are given in Equations (4.26) and (4.27), respectively. The first two angles, ψ_1 and ψ_2, are the angles between the observation direction and the direction that the asymptotic endpoint contribution was taken for the LPO and fringe components, respectively. Likewise the second two angles, ψ_1' and ψ_2', are the angles between the incident ray direction and the direction that the asymptotic endpoint contribution was taken for the LPO and fringe components, respectively. The LPO and PO components are easily written in this way. The UTD components look more complicated in this form, however it may be possible to write the UTD components in a form similar to the LPO and PO components if the endpoint contribution is done over entirely in a different coordinate system.

CHAPTER V

RESULTS

5.1 Introduction

The scattered fields predicted by the new corner diffraction coefficient derived in Chapter III are compared with previous high frequency solutions, measurements, and Moment Method solutions for some specific examples. The new solution is first compared with a few backscatter examples commonly found in the literature to show that in the principal planes it generally gives the same results as previous solutions. Then the new corner diffraction coefficient is compared with measurements for a swept frequency case which is described later. Finally the new corner diffraction solution is compared with Method of Moments and measurements for some new examples. Throughout this chapter the new corner diffraction solution and the new equivalent current solution will both be referred to as the new or new corner solution. Note that it was shown in Chapter III that both give the same results for first order scattering.

5.2 Brief Description of Program

A computer program written previously at OSU to calculate the RCS of a convex perfectly conducting body constructed from flat plates with straight edges was modified to calculate the RCS using the new solution. Since the program was written to handle objects with straight edges, the equivalent current form

of the solution, given in Equations (3.38) and (3.40), was used. The integration along the edge was done in closed form to give the contribution from each edge. For structures other than flat plates, it is also necessary to take shadowing into account. Since only concave structures are considered here this is fairly simple. The shadowing of the incident field is accounted for in the $\vec{E}_t^i$ and $\vec{H}_t^i$ terms in the equivalent currents and the unit step functions in the LPO and PO components of the equivalent currents. The shadowing of the diffracted ray is more complicated. The contribution from the LPO and PO components are present everywhere. They are treated as if they are radiating in free space, just like typical Physical Optics surface currents. The UTD components are shadowed like diffracted fields. They do not contribute if the observation point is inside the wedge ($\phi > n\pi$).

5.3 Examples

5.3.1 Ross

The backscatter at 9.227 GHz from a 4" × 4" plate in the y-z plane is shown next (see Figure 62) with the results for a pattern cut taken in the x-z plane are shown in Figure 63. Both the new corner and Sikta's results are basically the same near broadside, as expected. Sikta's results include double and triple diffraction, and thus are more accurate. In Figure 64 the new solution is compared with the equivalent currents of Ryan and Peters (the first order solution used by Sikta) and the previous corner solution. The three first order methods give essentially the same answer in this case.

5.3.2 Northrop Fin

The backscatter from the Northrop fin shape shown in Figure 65 is compared to measurements and calculations made by Sikta [26]. The E-plane pattern in the x-y plane is shown at 17.76 GHz in Figure 66. The new solution is compared

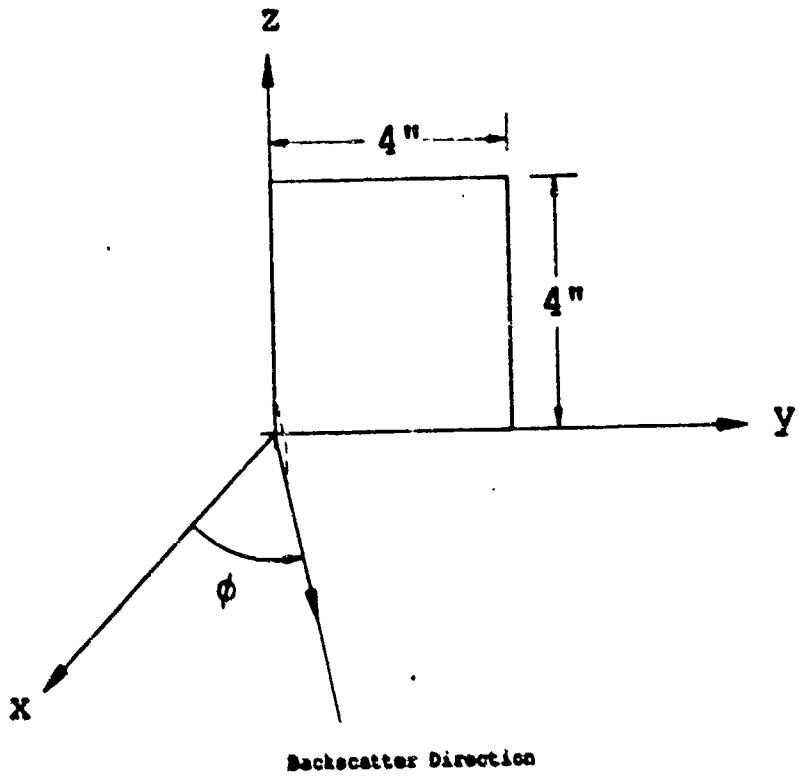

Figure 62: Ross 4" x 4" plate.

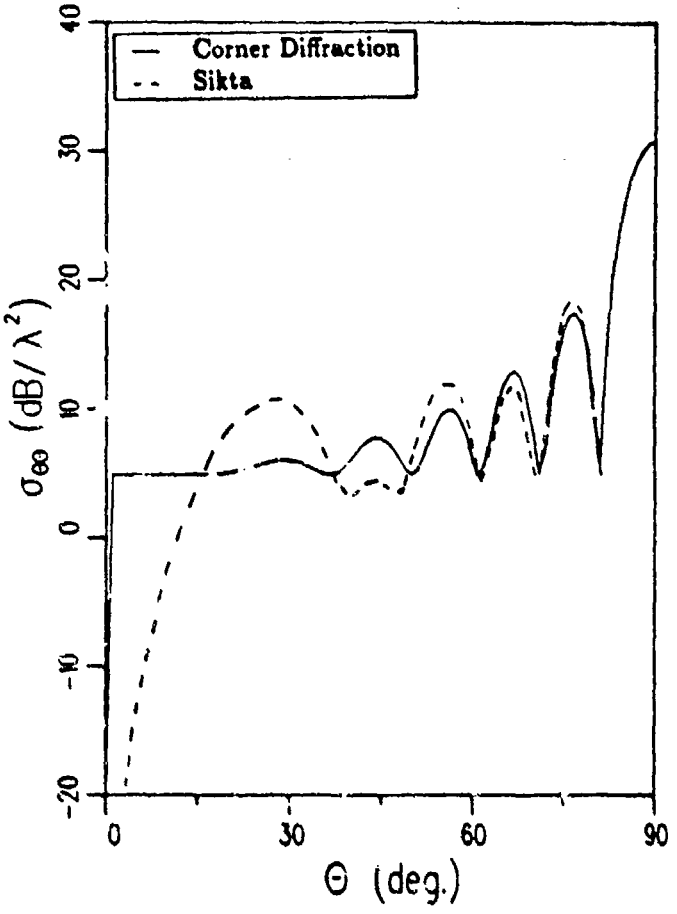

Figure 63: E-plane pattern in x-z plane of Ross plate.

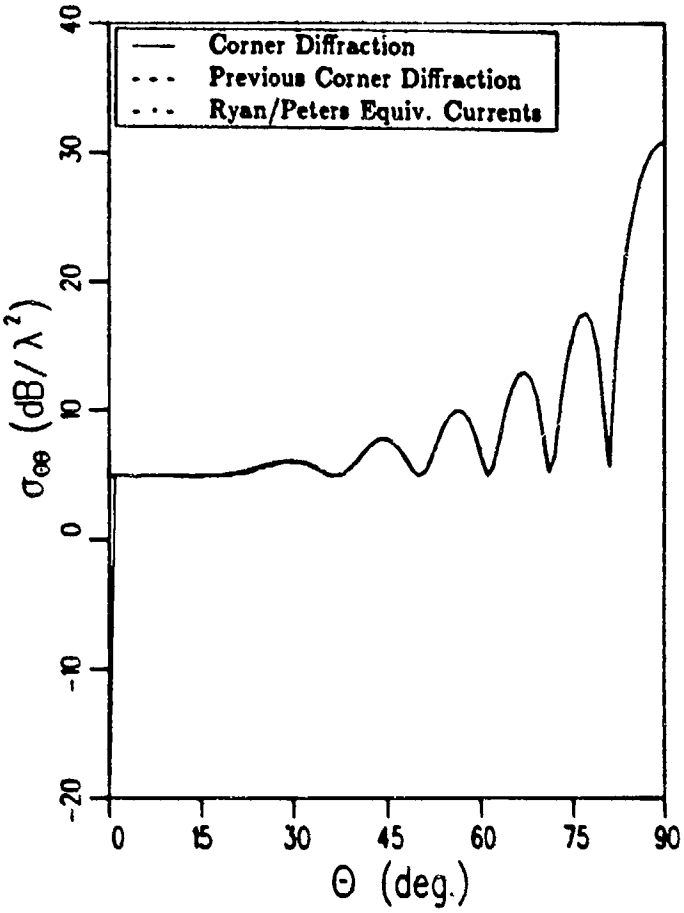

Figure 64: E-plane pattern in x-z plane of Ross plate.

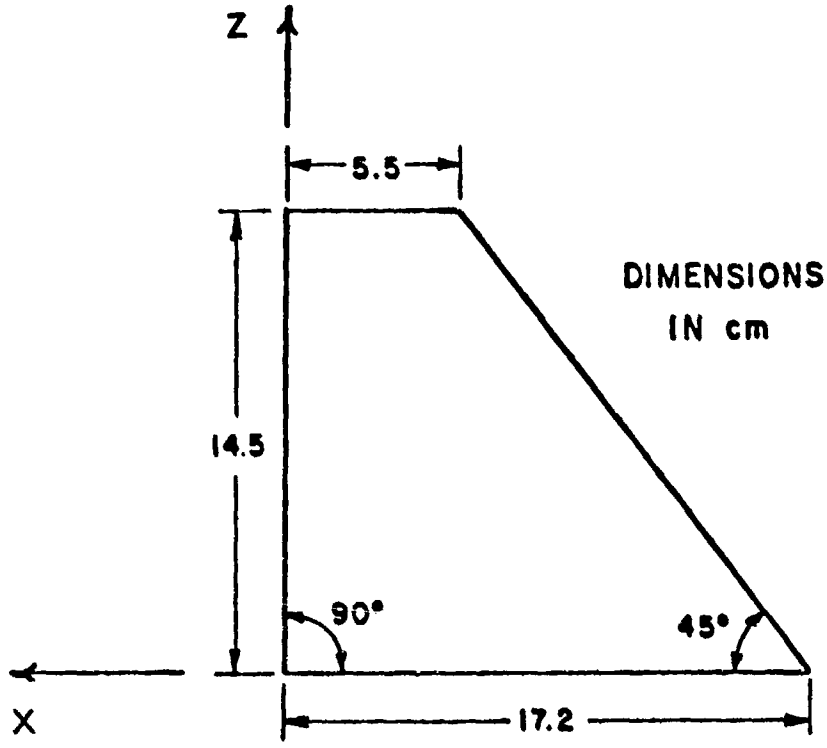

Figure 65: Northrop Fin.

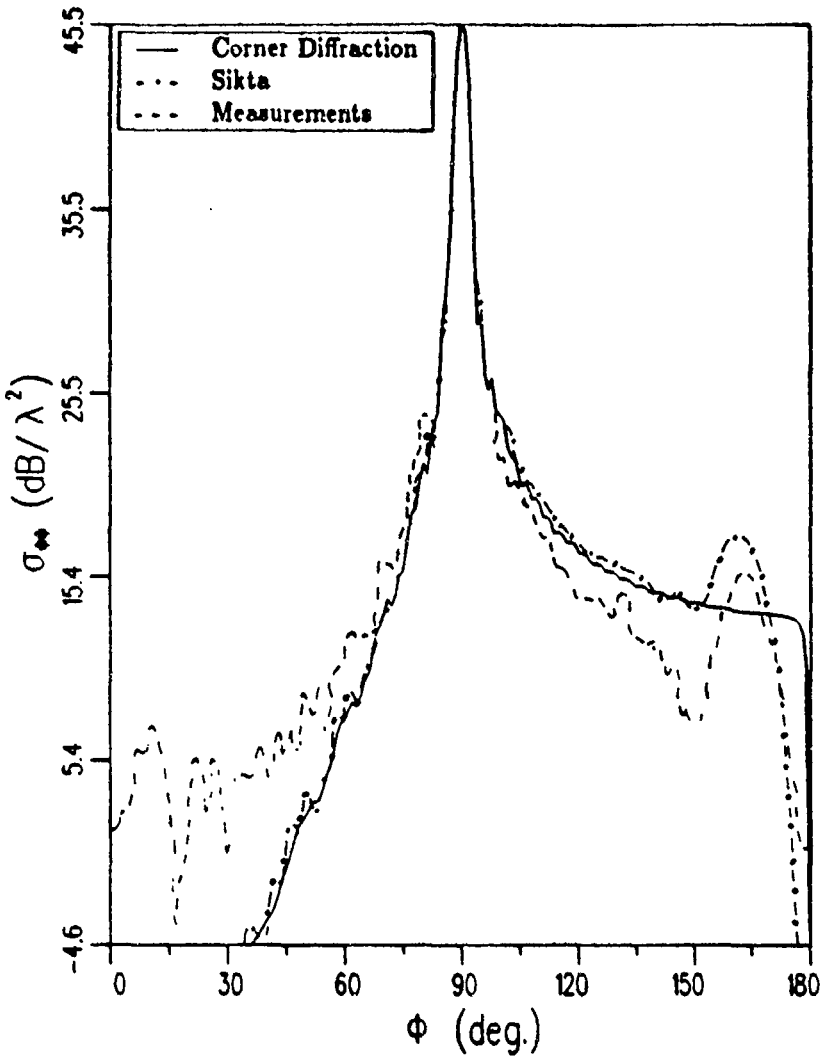

Figure 66: E-plane pattern in x-y plane at 17.76 GHz of Northrop Fin.

with measurements [30], Sikta's results, and results obtained by Northrop [19]. Sikta's results include higher order terms and are closer to the measured results than the new corner diffraction solution which includes only first order terms. The results obtained by Northrop [19], which are based on the exact solution of an infinite strip, are also close to the measured results and are essentially the same as Sikta's results. The new solution once again agrees well with the measurements in the region near broadside to the plate. The new solution is compared to first order results obtained by Sikta in Figure 67, to show that higher order terms are

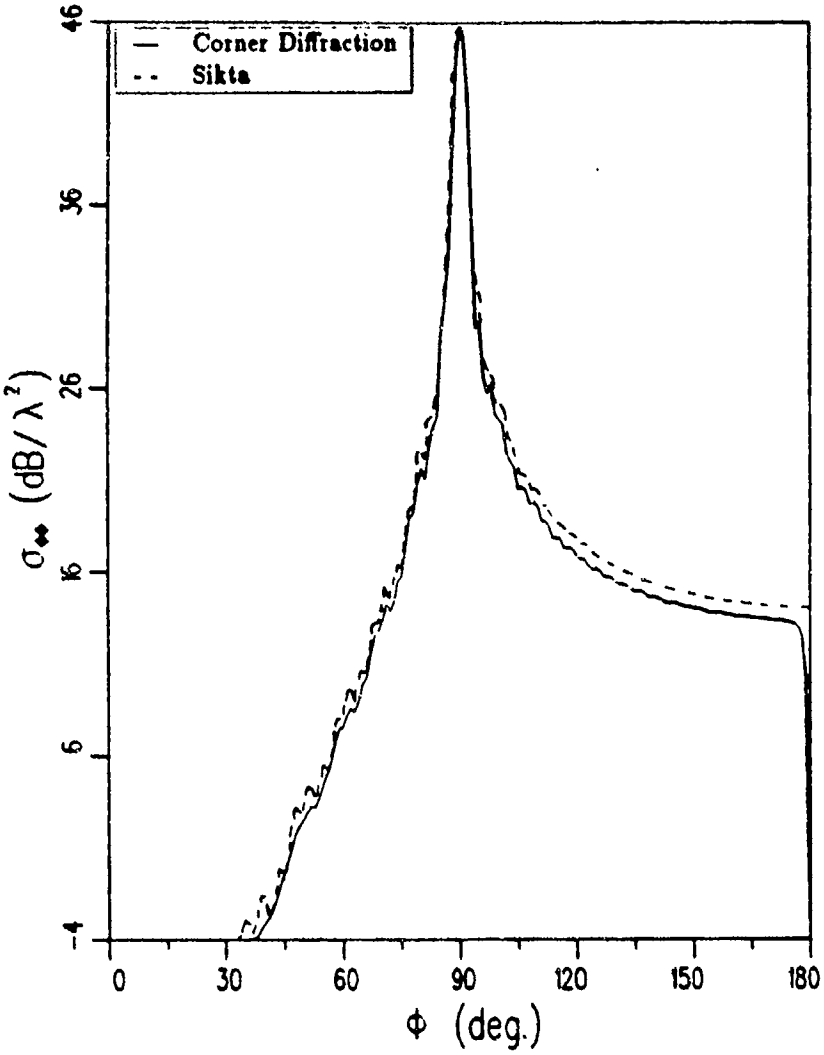

Figure 67: E-plane pattern in x-y plane at 17.76 GHz of Northrop Fin.

important in regions farther than 30° from broadside. Once again Sikta used the Ryan and Peters equivalent currents to obtain the first order contribution to the scattered field. The new solution and the first order solution obtained by Sikta are about the same as expected.

5.3.3 Sikta's triangle

The new solution is first compared with calculations and measurements obtained by Sikta [26]. The backscatter in the principal plane from the triangle shown

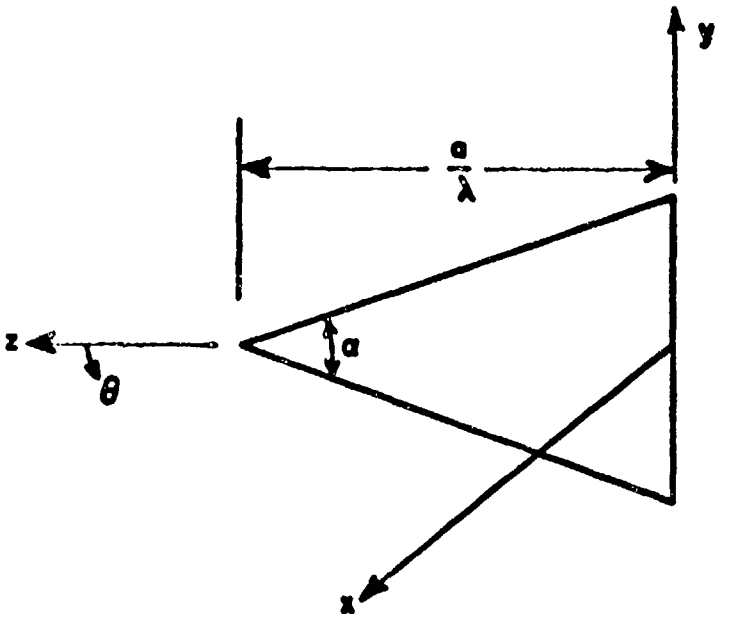

Figure 68: Sikta's Triangle.

in Figure 68 was calculated for different values of a/λ and α. The fields calculated using the new corner diffraction coefficients are compared with the results given by Sikta [26]. Sikta calculated the fields using Ryan and Peters equivalent currents to find the first order terms plus higher order terms (double and triple diffraction). The results are shown in Figures 69 to 92. Throughout these examples the two different polarizations are alternated, with the $\hat{\theta}$ polarized field being followed by the $\hat{\phi}$ polarized field. In Figures 69 to 74, the triangle length is varied ($a = 2\lambda$, 3λ, 9λ) while the vertex angle, α, is held constant at 30°.

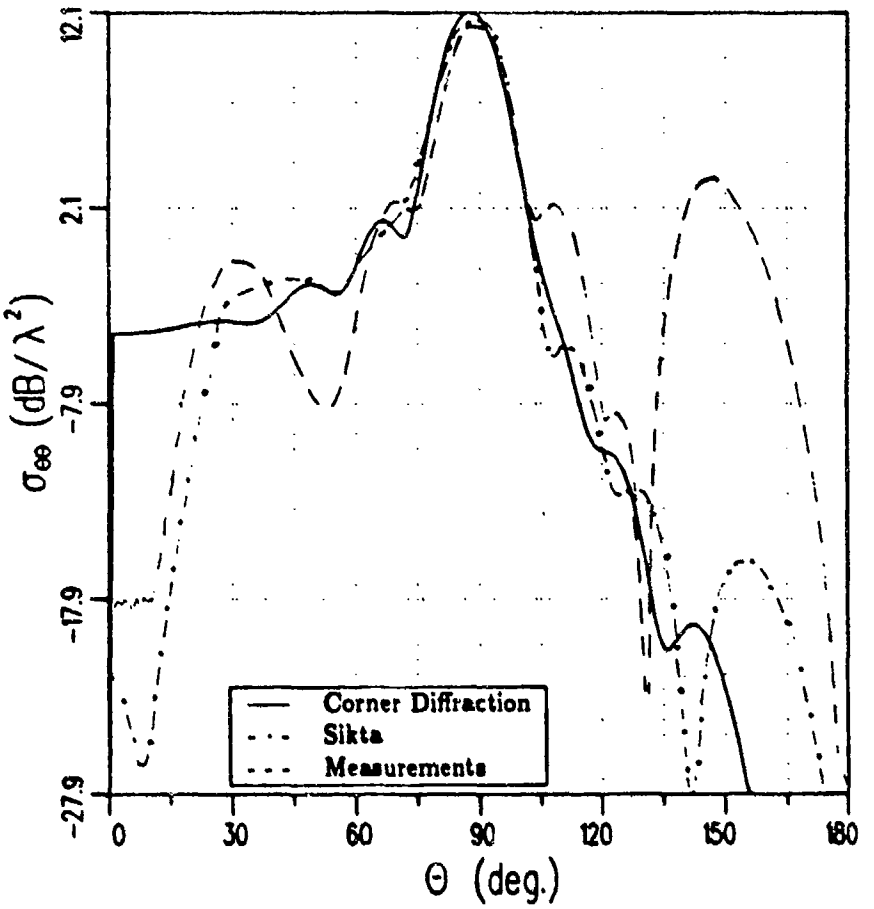

Figure 39: The E-plane pattern ($\phi = 0°$) for Sikta's triangle with $a = 2\lambda$ and $\alpha = 30°$.

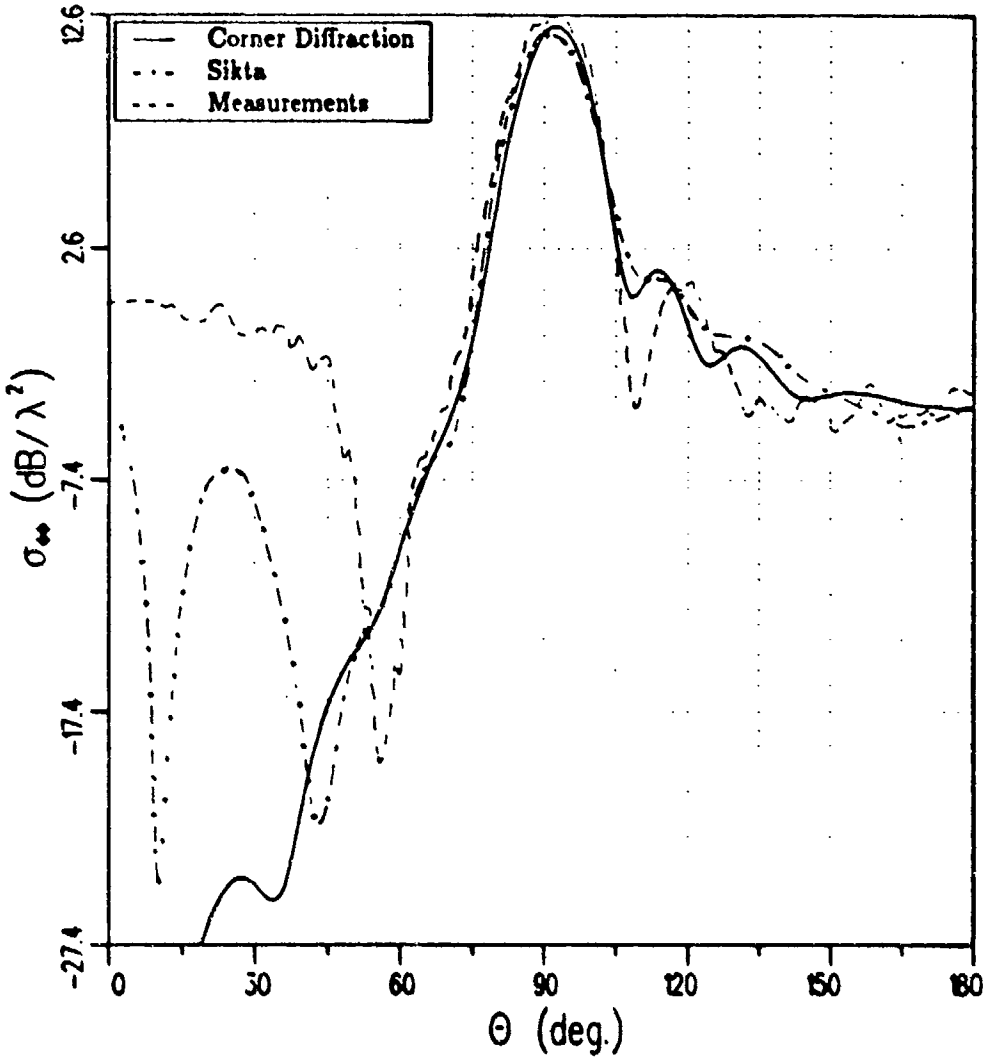

Figure 70: The H-plane pattern ($\phi = 0°$) for Sikta's triangle with $a = 2\lambda$ and $\alpha = 30°$.

In Figures 75 to 80 the results obtained using Ryan and Peters [1] equivalent edge currents (the first order solution used by Sikta) are compared with the results obtained using the new corner diffraction coefficient. The different polarizations and triangle sizes are given in the same order as that used previously in Figures 69 to 74. In Figures 81 to 86 the triangle length is held constant at $a = 4\lambda$ while the vertex angle α is varied ($\alpha = 45°, 60°, 90°$).

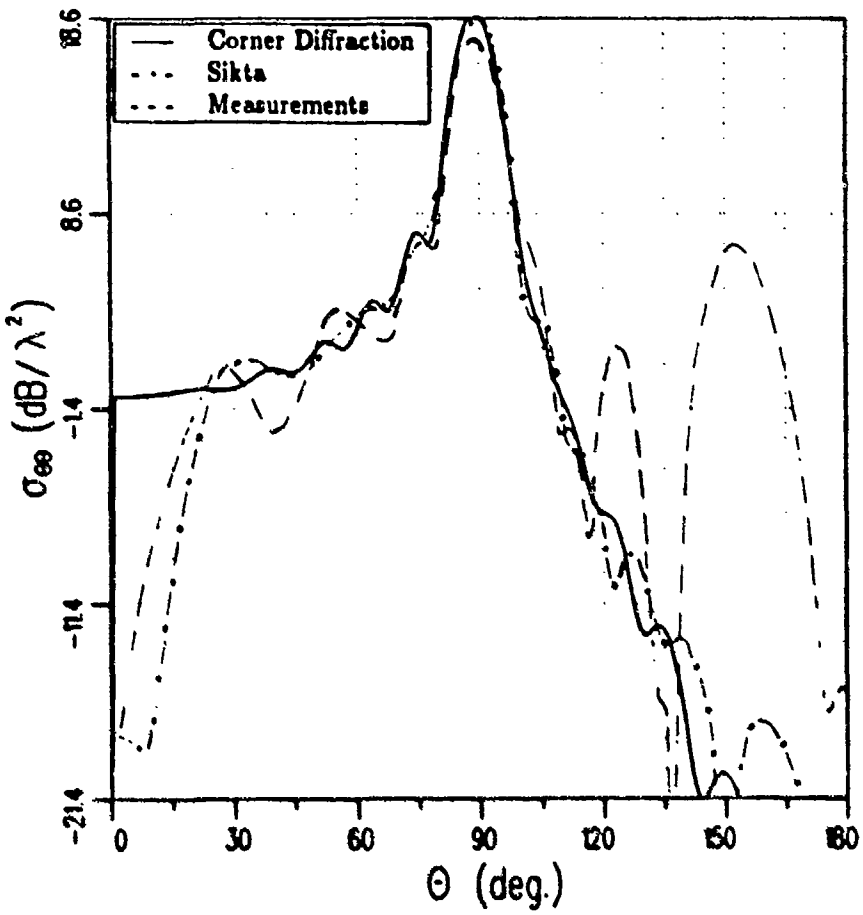

Figure 71: The E-plane pattern ($\phi = 0°$) for Sikta's triangle with $a = 3\lambda$ and $\alpha = 30°$.

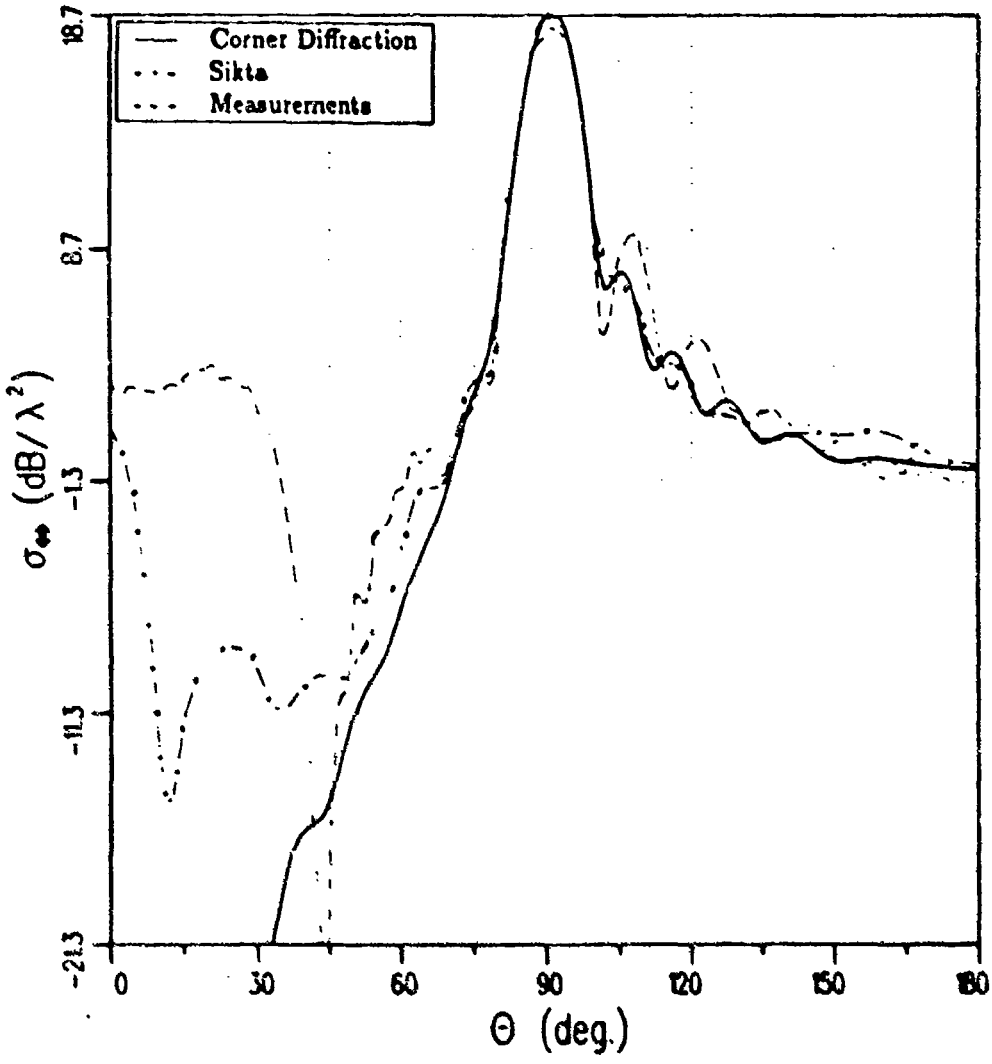

Figure 72: The H-plane pattern ($\phi = 0°$) for Sikta's triangle with $a = 3\lambda$ and $\alpha = 30°$.

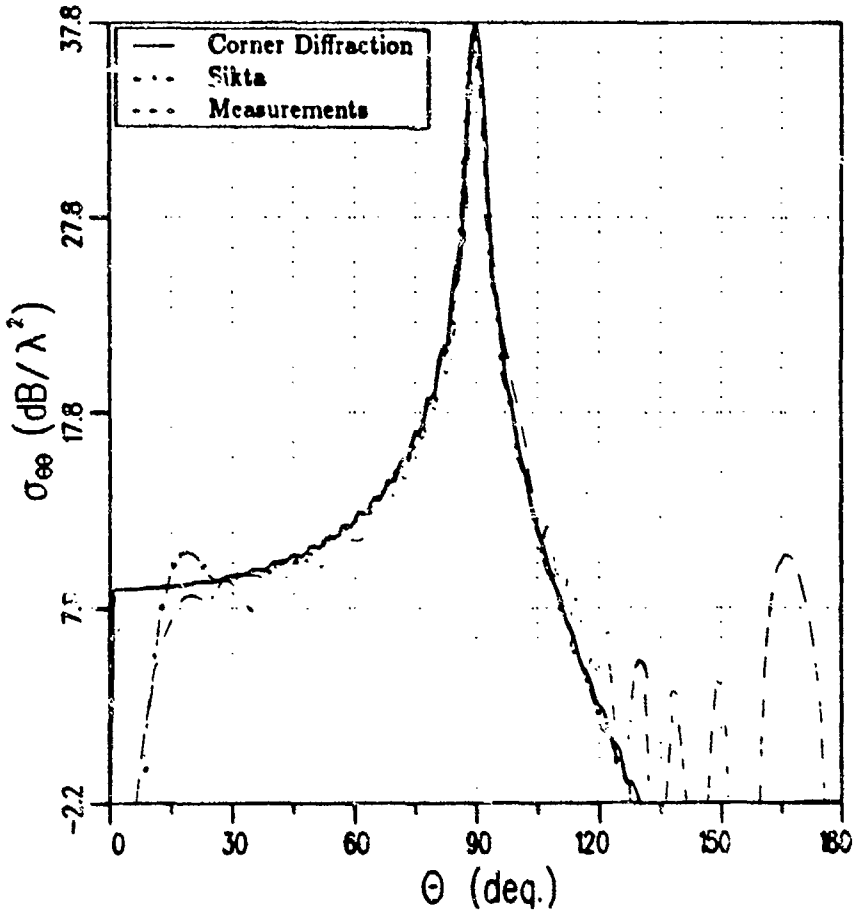

Figure 73: The E-plane pattern ($\phi = 0°$) for Sikta's triangle with $a = 9\lambda$ and $\alpha = 30°$.

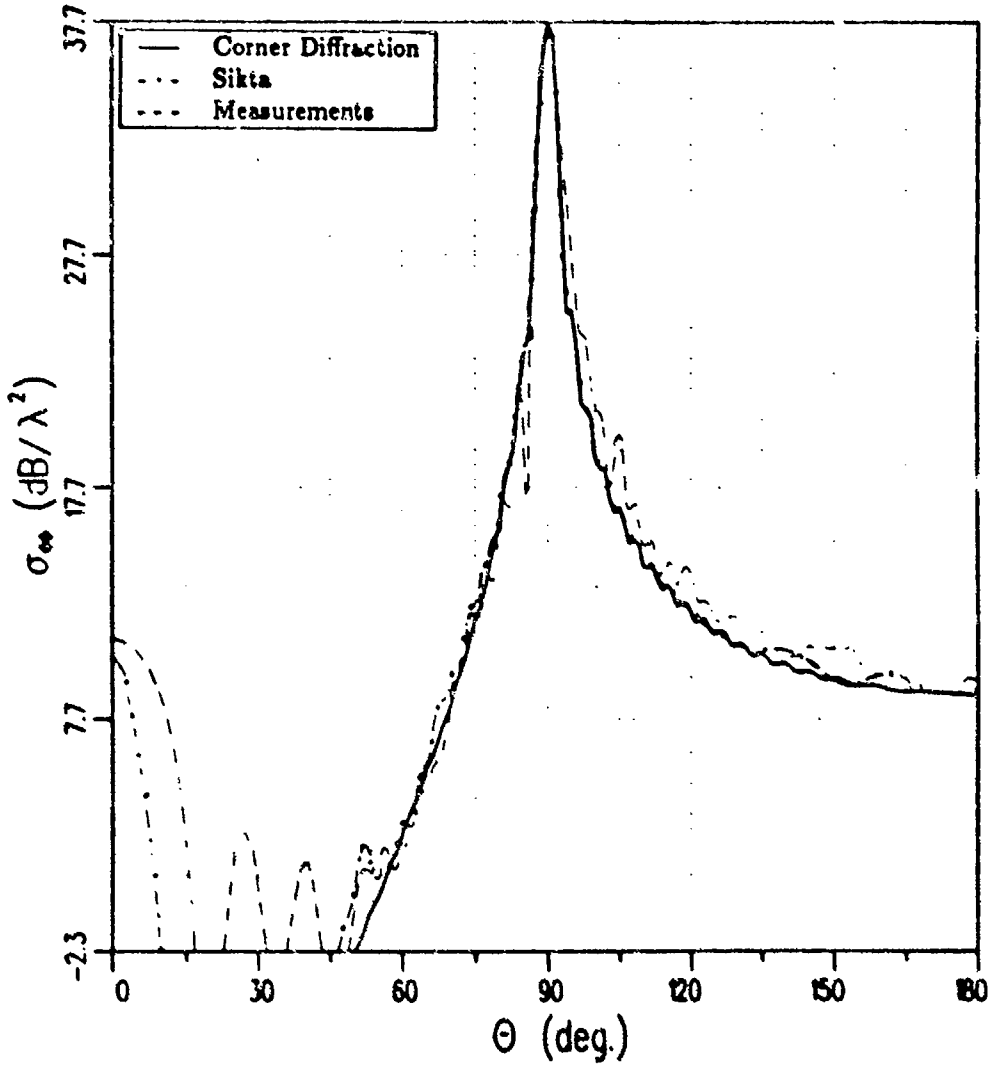

Figure 74: The H-plane pattern ($\phi = 0°$) for Sikta's triangle with $a = 9\lambda$ and $\alpha = 30°$.

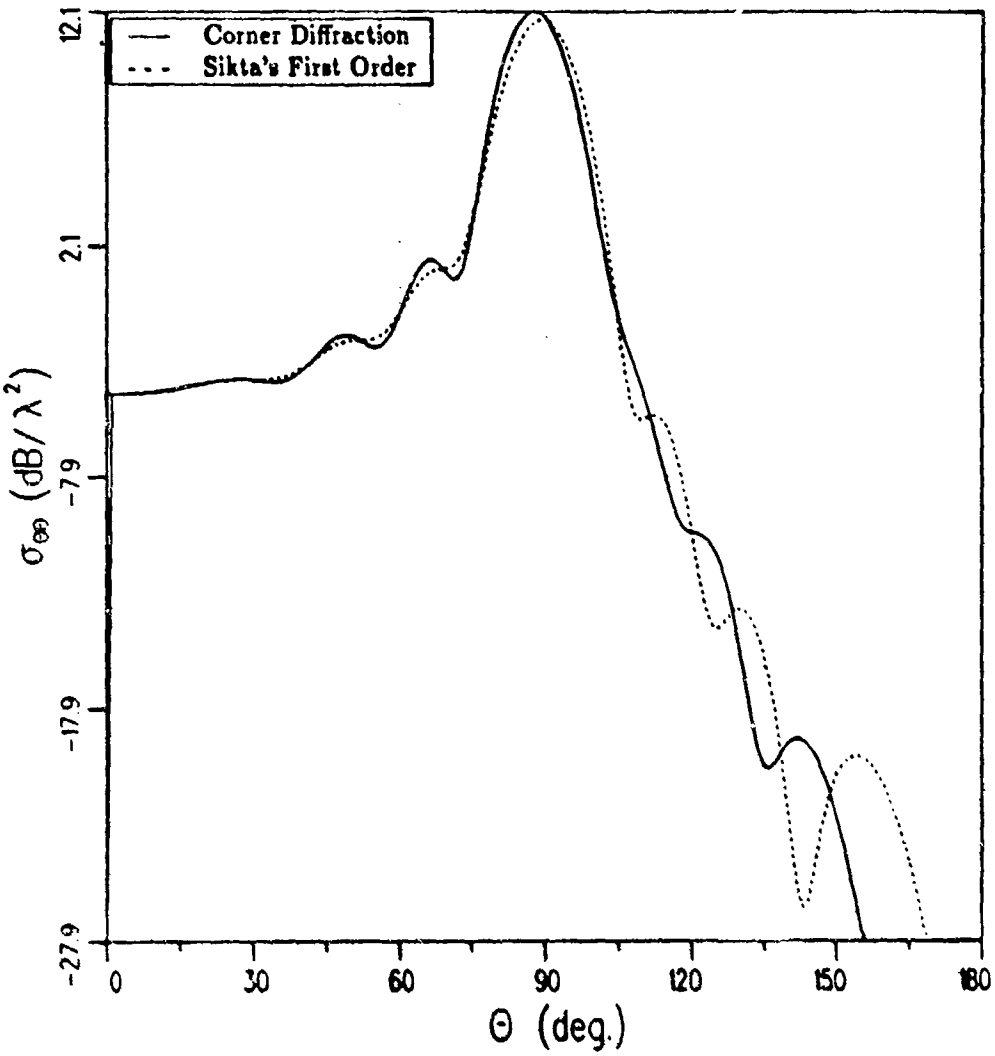

Figure 75: The E-plane pattern ($\phi = 0°$) for Sikta's triangle with $a = 2\lambda$ and $\alpha = 30°$.

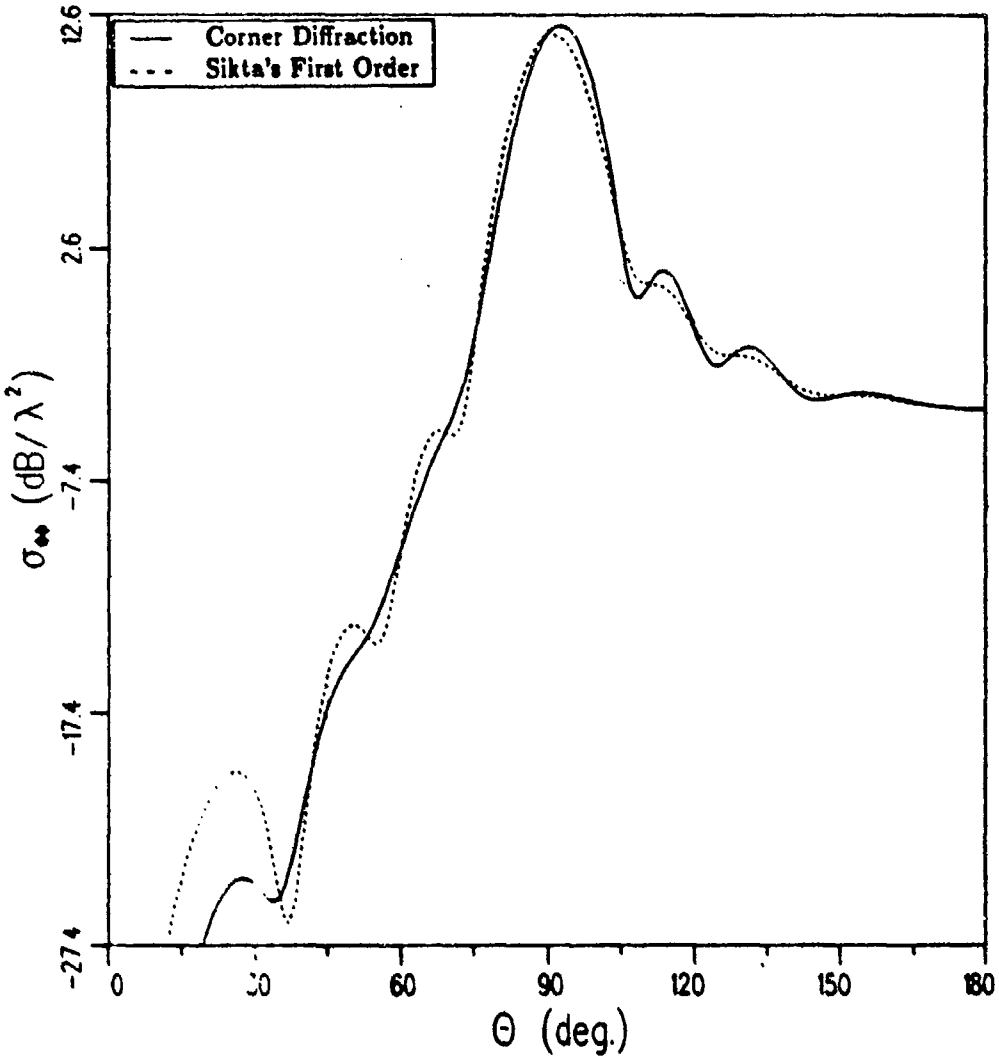

Figure 76: The H-plane pattern ($\phi = 0°$) for Sikta's triangle with $a = 2\lambda$ and $\alpha = 30°$.

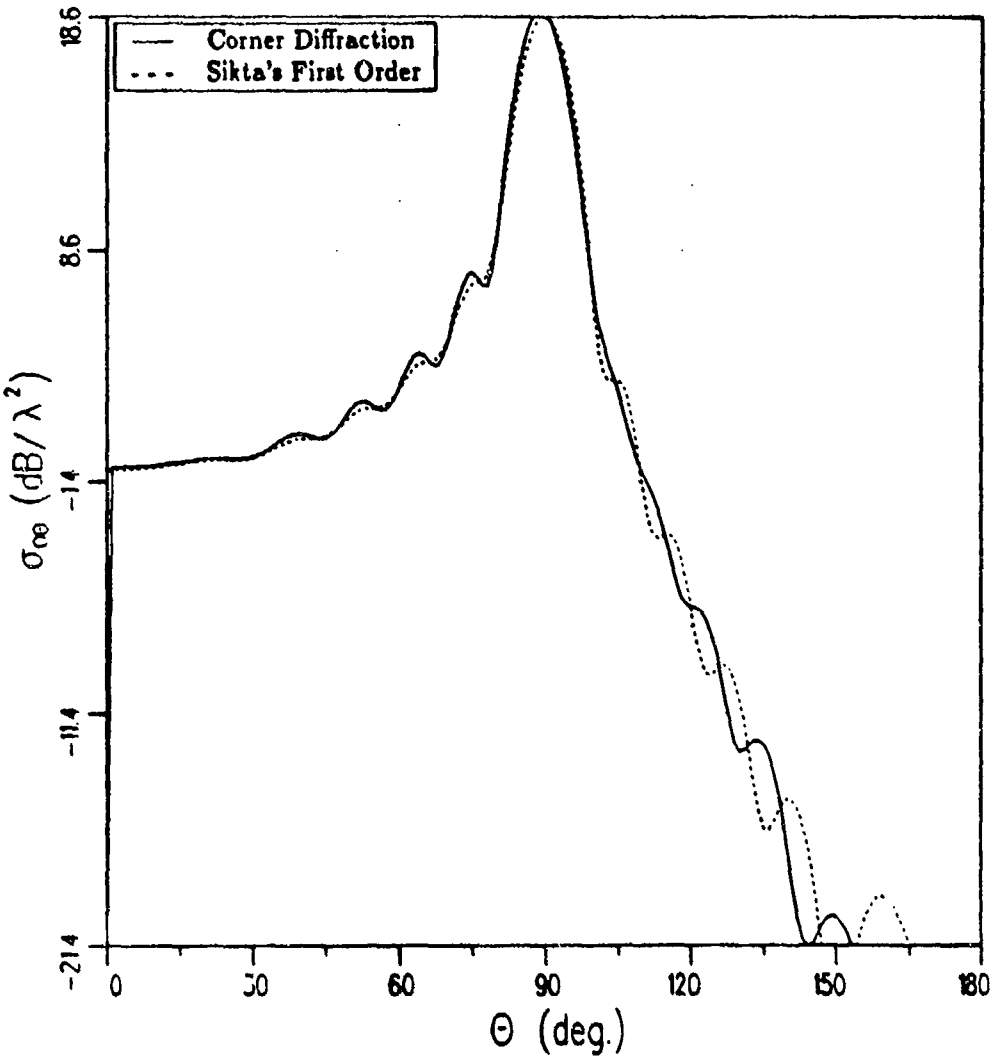

Figure 77: The E-plane pattern ($\phi = 0°$) for Sikta's triangle with $a = 3\lambda$ and $\alpha = 30°$.

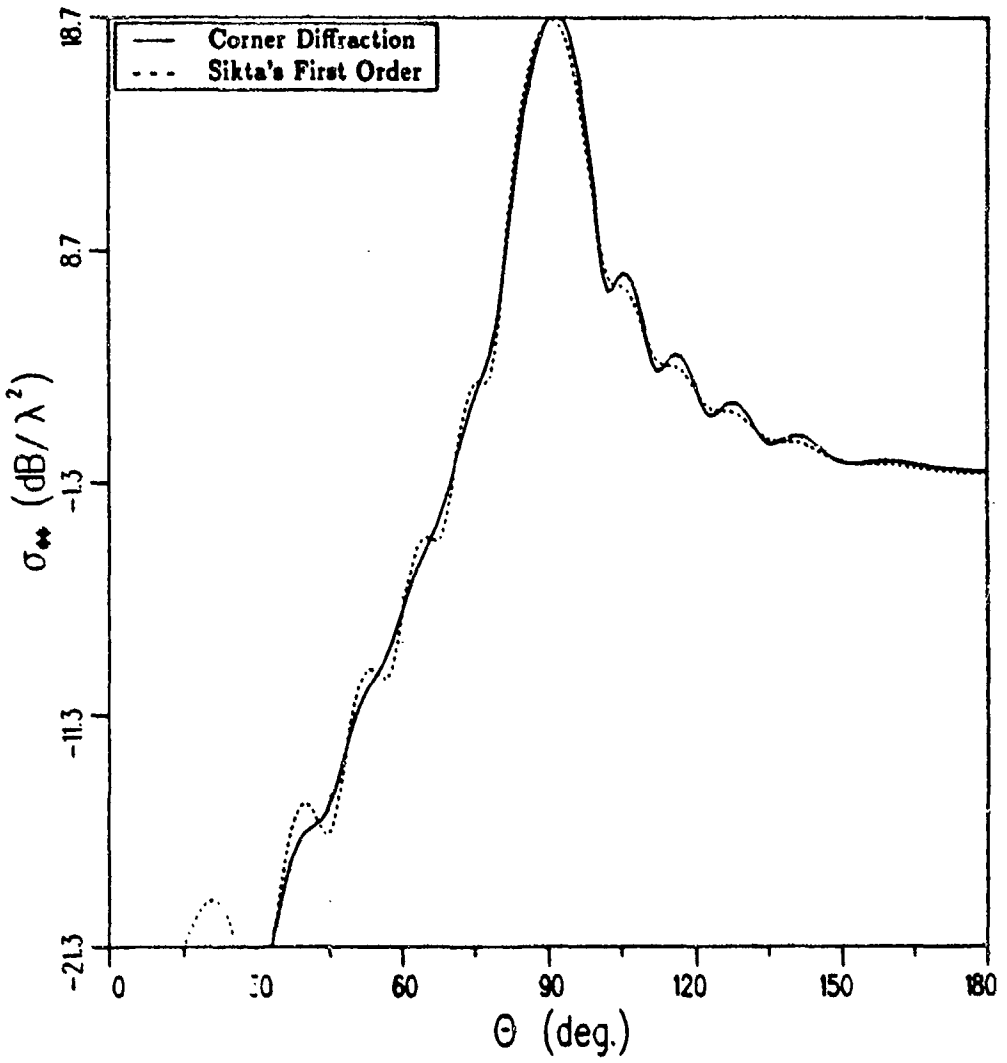

Figure 78: The H-plane pattern ($\phi = 0°$) for Sikta's triangle with $a = 3\lambda$ and $\alpha = 30°$.

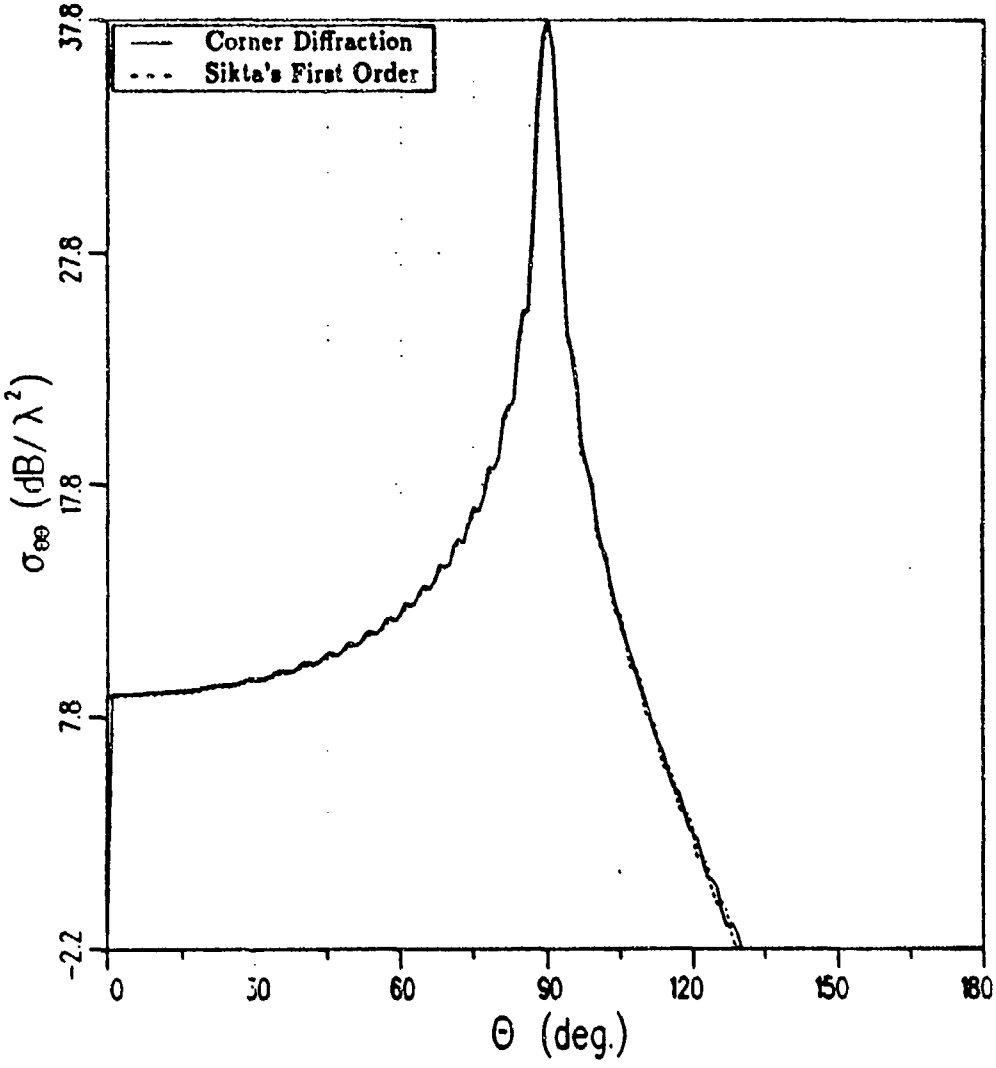

Figure 79: The E-plane pattern ($\phi = 0°$) for Sikta's triangle with $a = 9\lambda$ and $\alpha = 30°$.

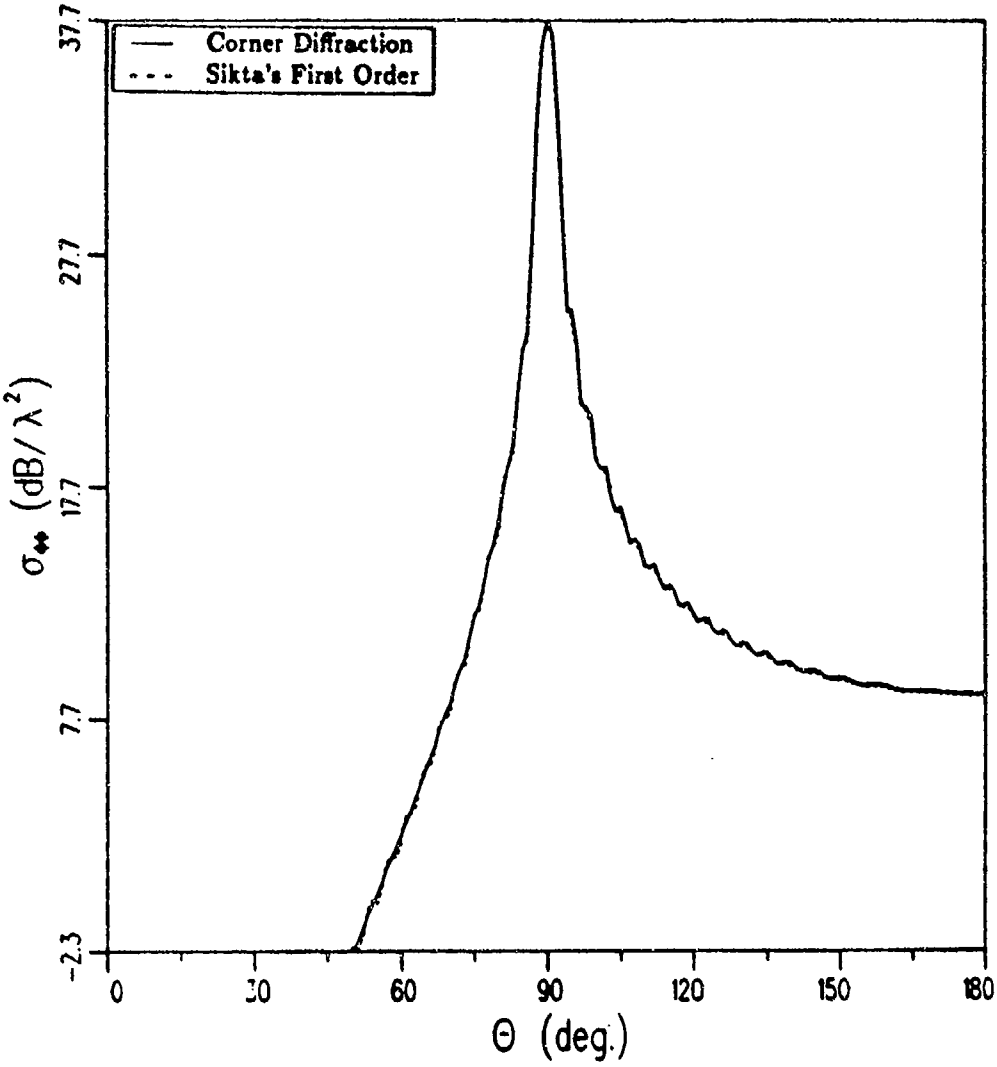

Figure 80: The H-plane pattern ($\phi = 0°$) for Sikta's triangle with $a = 9\lambda$ and $\alpha = 30°$.

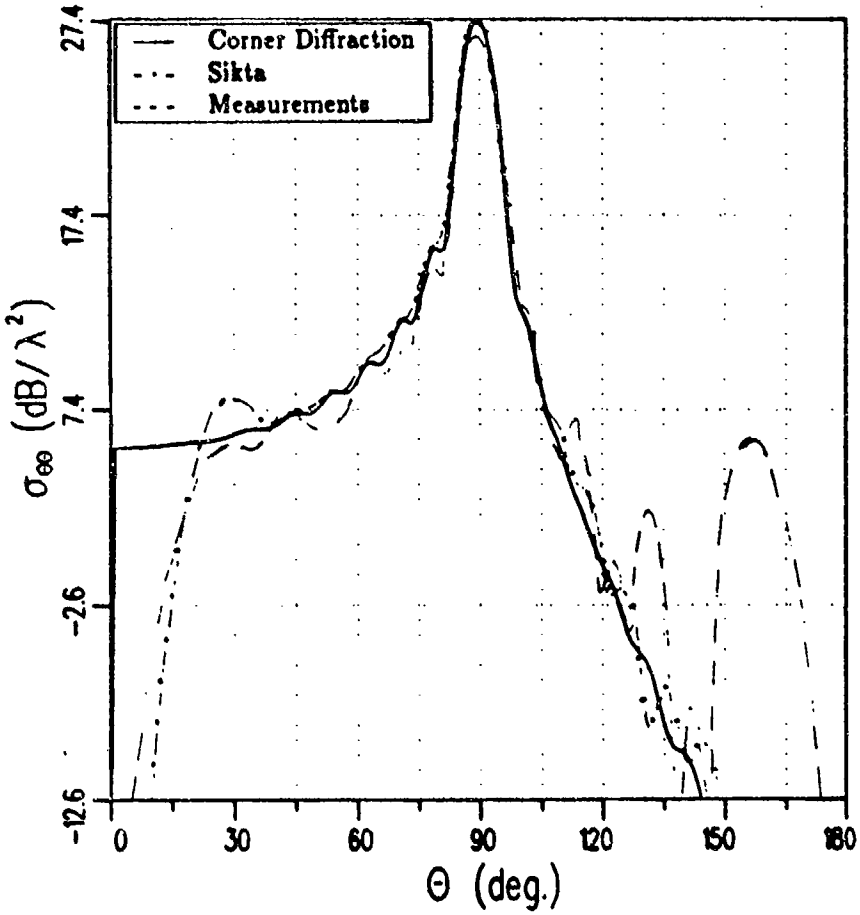

Figure 81: The E-plane pattern ($\phi = 0°$) for Sikta's triangle with $a = 4\lambda$ and $\alpha = 45°$.

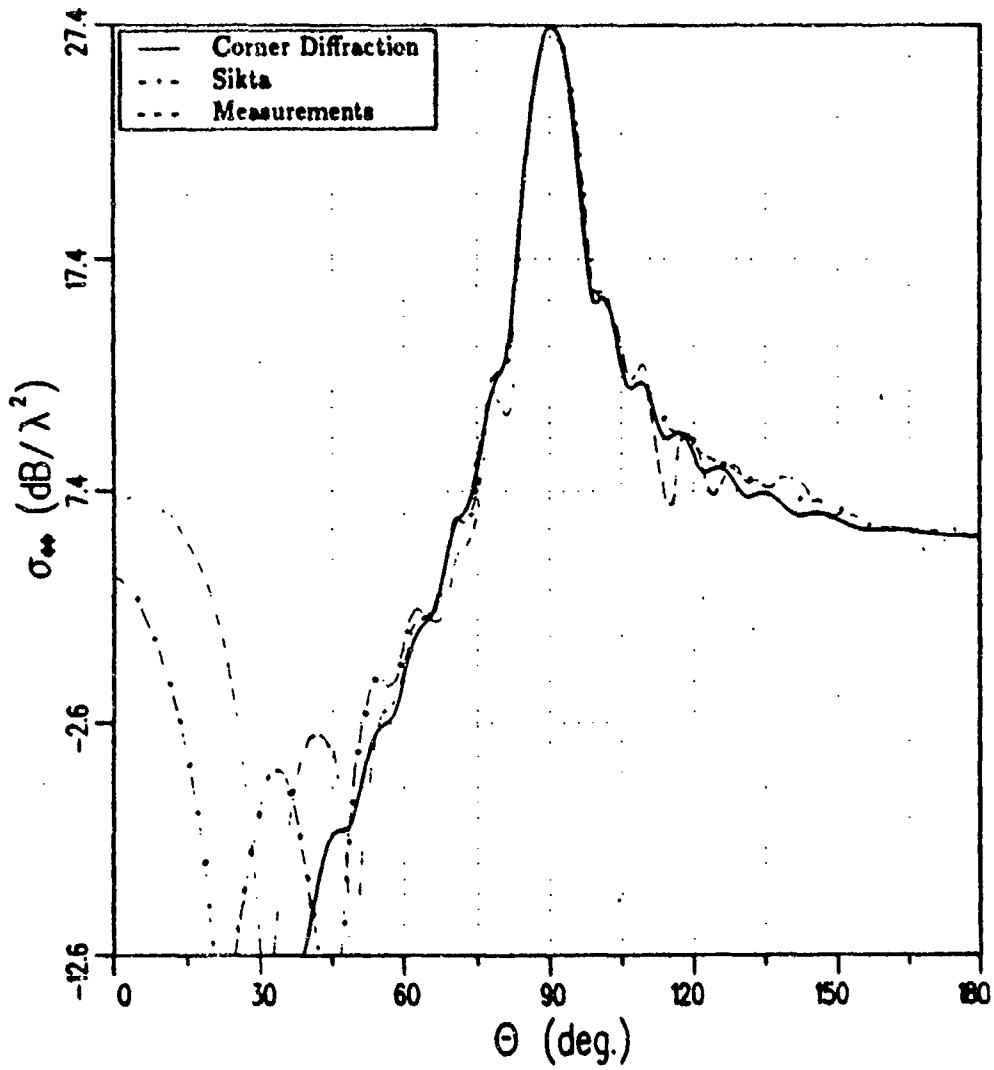

Figure 82: The H-plane pattern ($\phi = 0°$) for Sikta's triangle with $a = 4\lambda$ and $\alpha = 45°$.

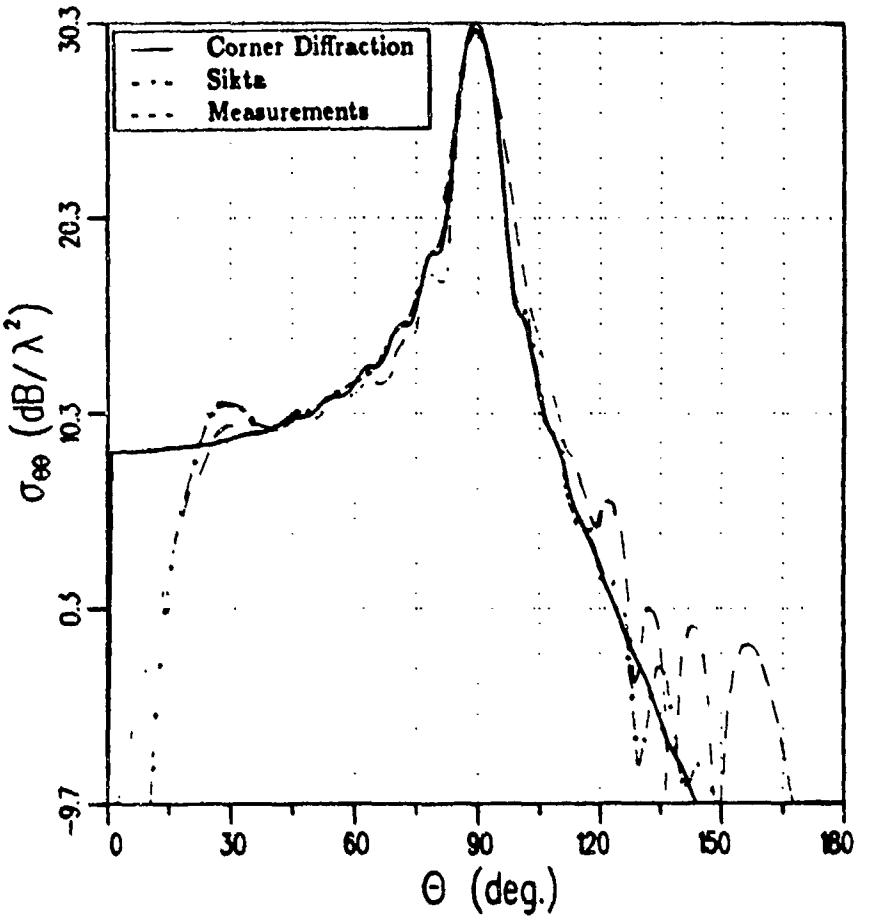

Figure 83: The E-plane pattern ($\phi = 0°$) for Sikta's triangle with $a = 4\lambda$ and $\alpha = 60°$.

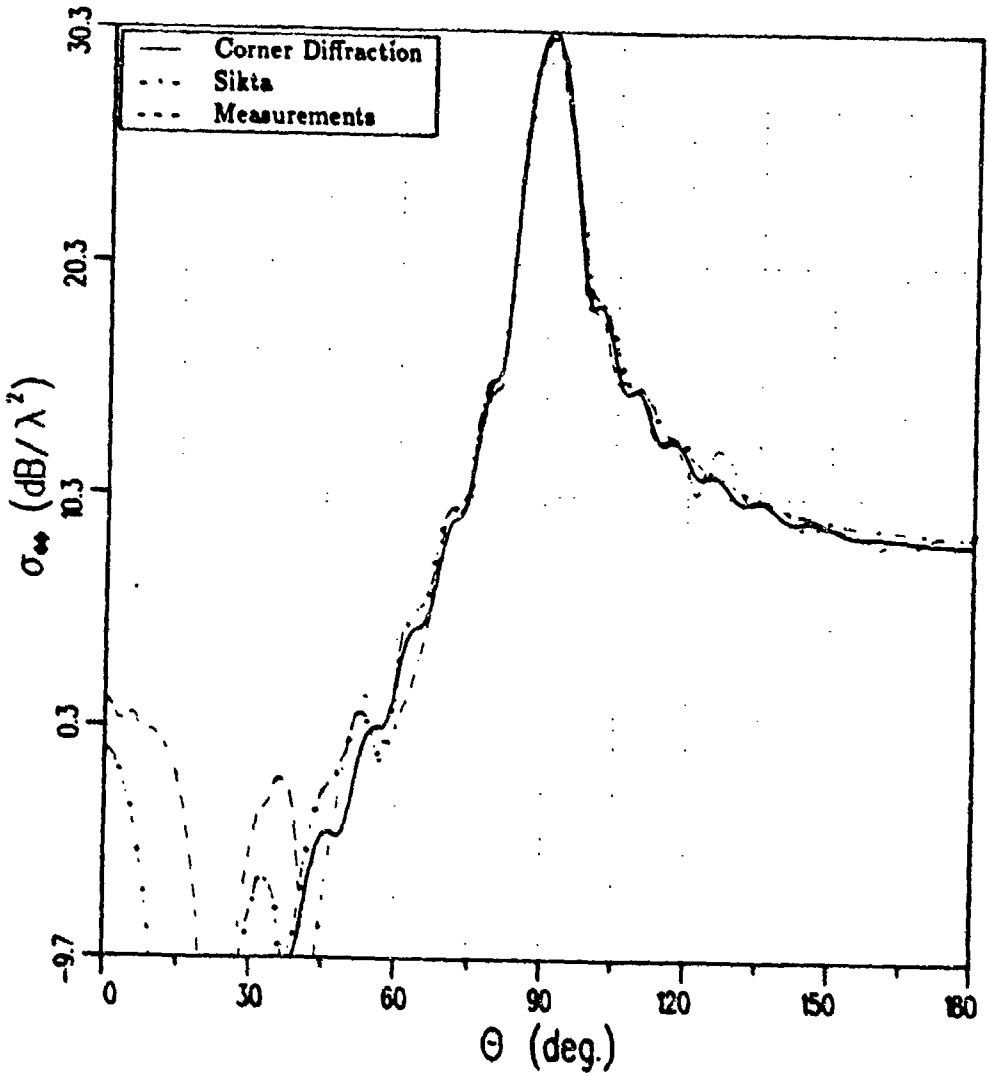

Figure 84: The H-plane pattern ($\phi = 0°$) for Sikta's triangle with $a = 4\lambda$ and $\alpha = 60°$.

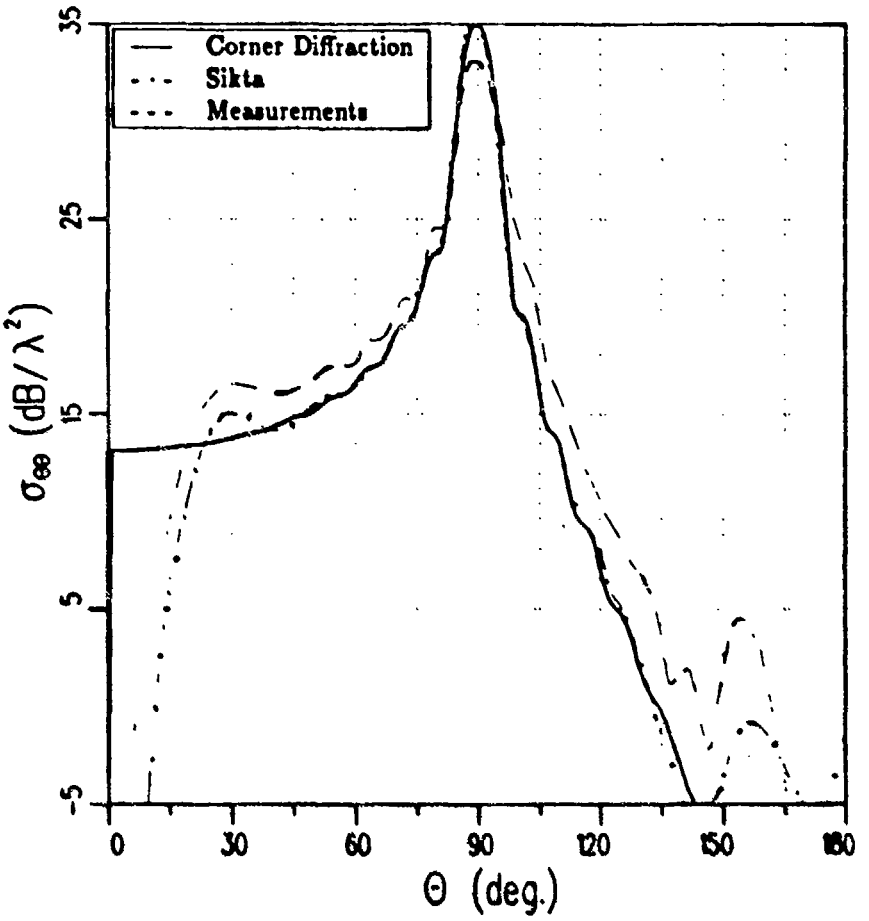

Figure 85: The E-plane pattern ($\phi = 0°$) for Sikta's triangle with $a = 4\lambda$ and $\alpha = 90°$.

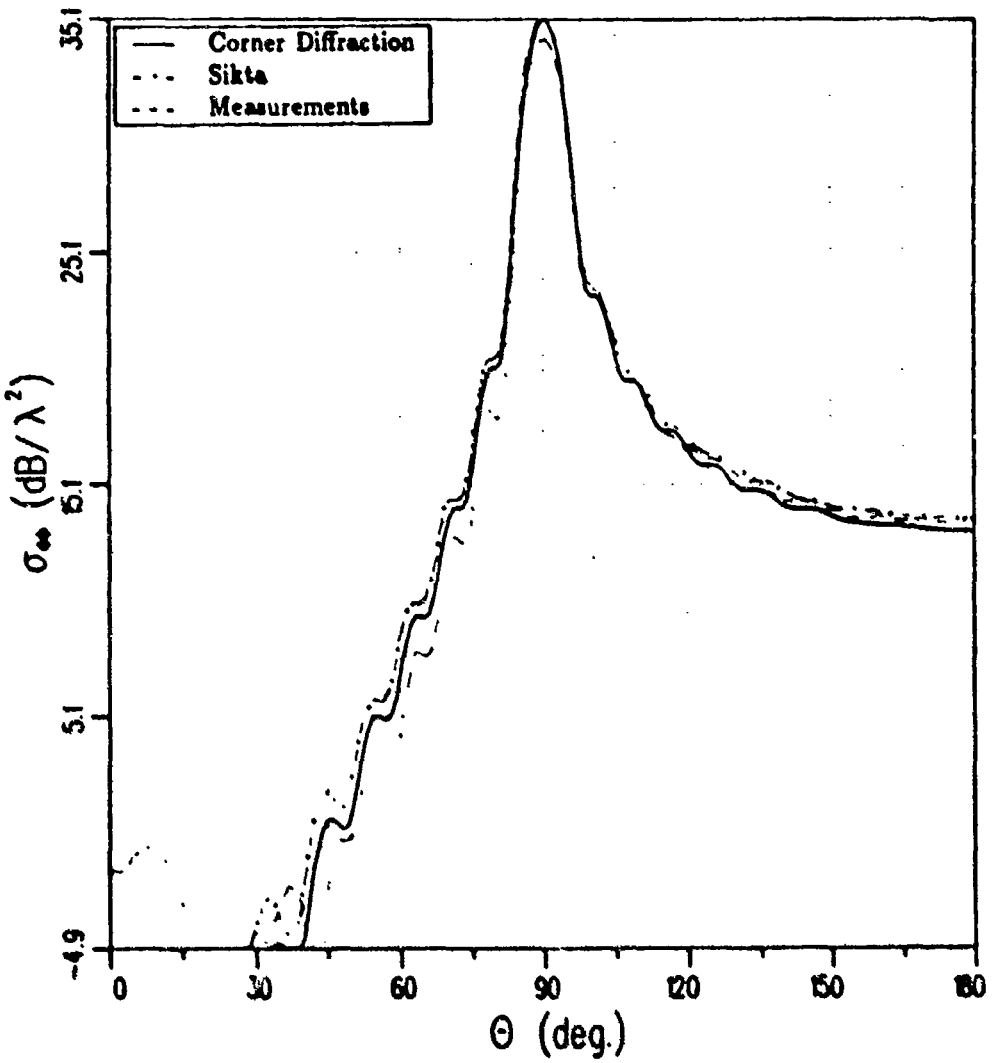

Figure 86: The H-plane pattern ($\phi = 0°$) for Sikta's triangle with $a = 4\lambda$ and $\alpha = 90°$.

As before, the results obtained using Ryan and Peters [1] equivalent edge currents (the first order solution used by Sikta) are compared with the results obtained using the new corner diffraction coefficient in Figures 87 to 92. The different polarizations and triangle sizes are given in the same order as that used previously in Figures 81 to 86.

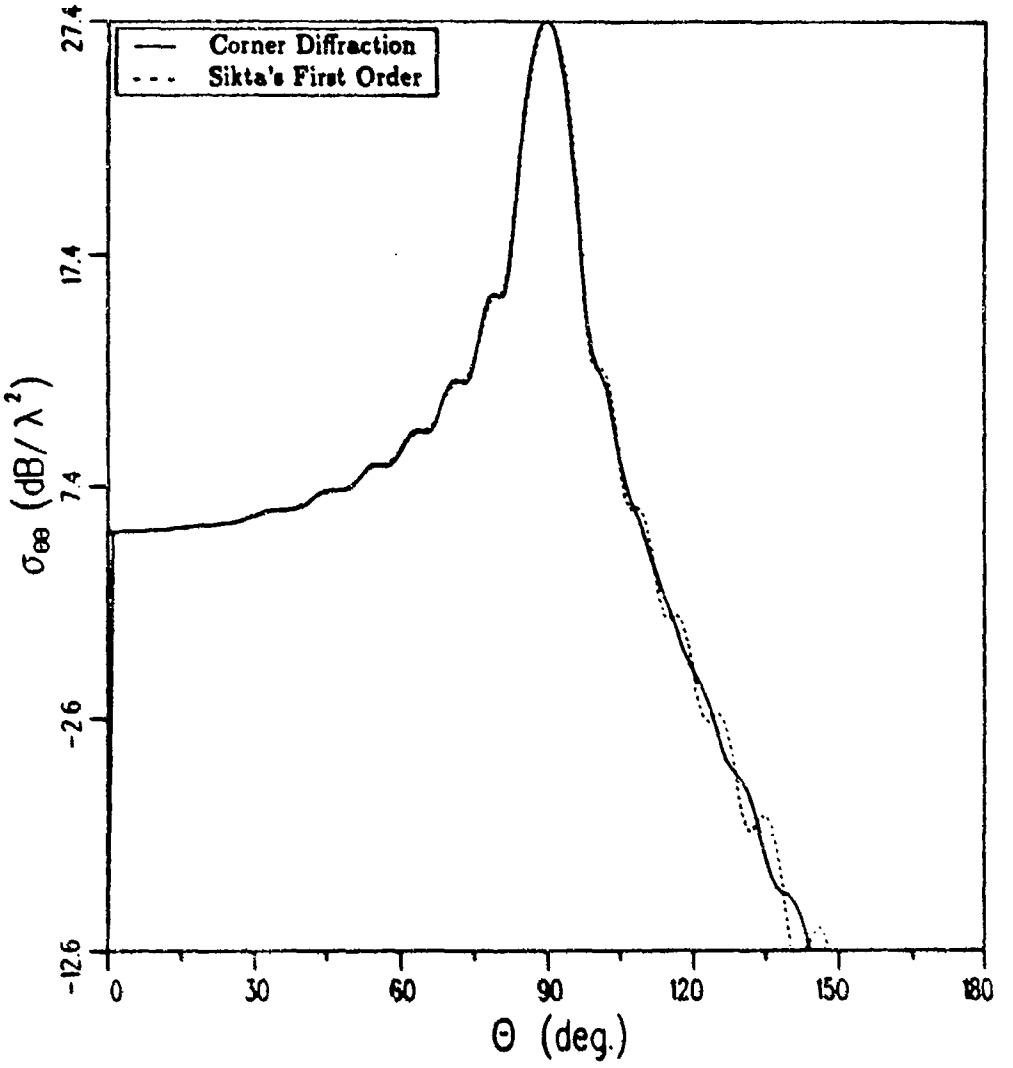

Figure 87: The E-plane pattern ($\phi = 0^\circ$) for Sikta's triangle with $a = 4\lambda$ and $\alpha = 45^\circ$.

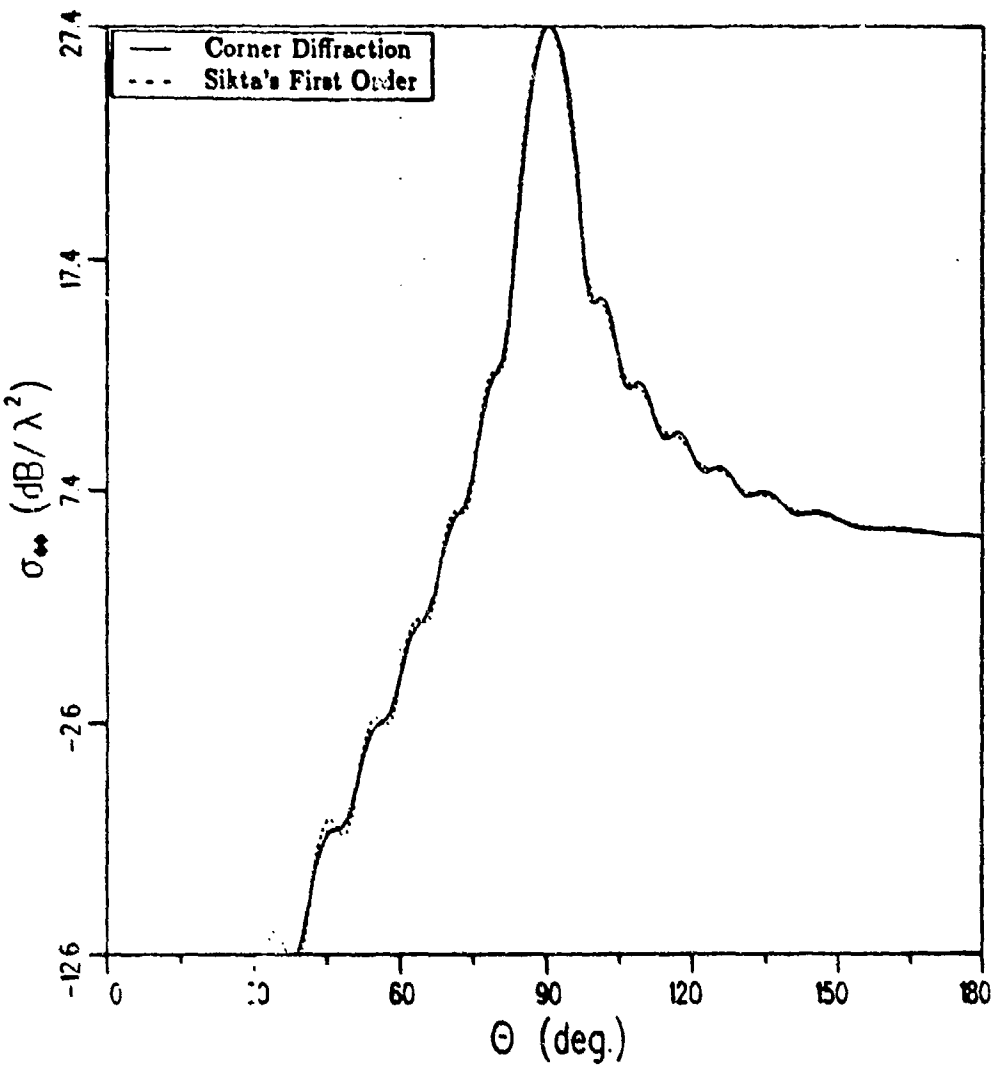

Figure 88: The H-plane pattern ($\phi = 0°$) for Sikta's triangle with $a = 4\lambda$ and $\alpha = 45°$.

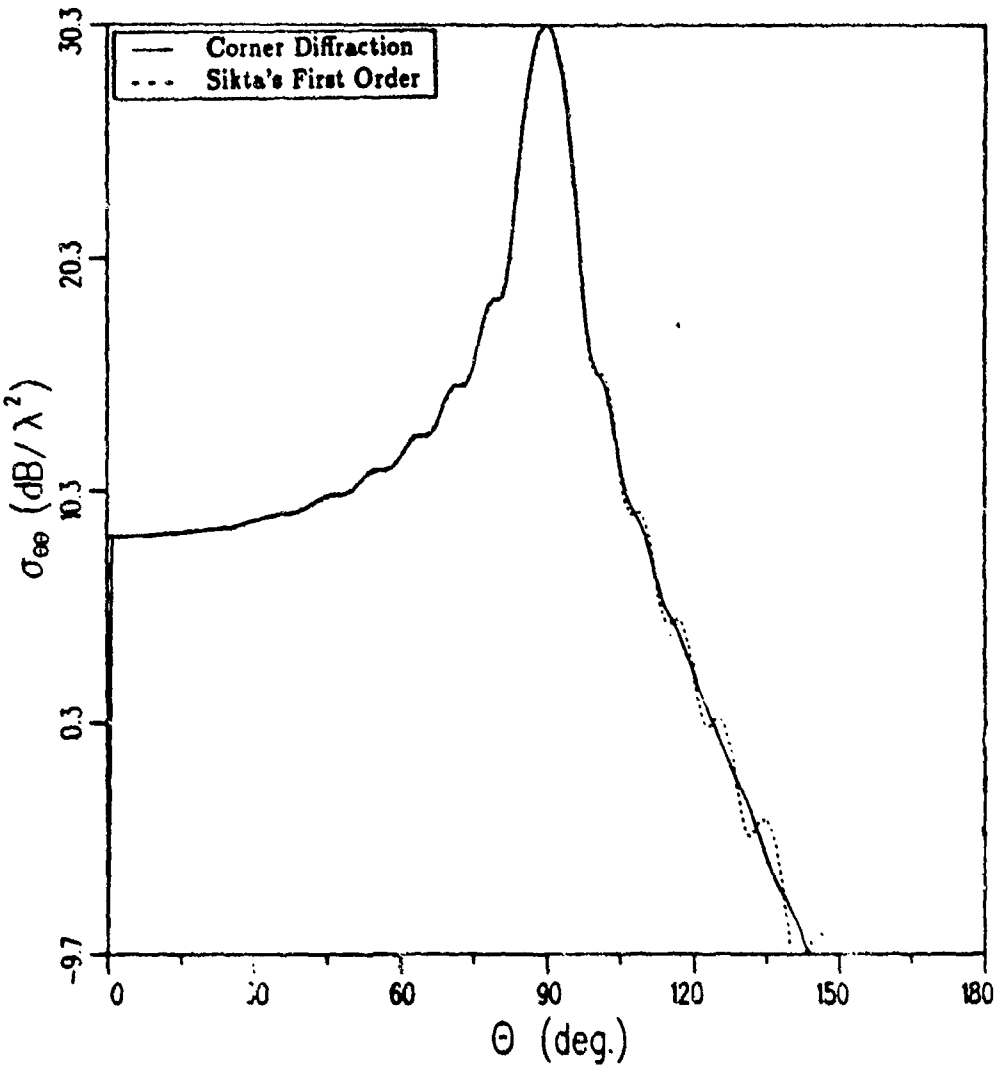

Figure 89: The E-plane pattern ($\phi = 0°$) for Sikta's triangle with $a = 4\lambda$ and $\alpha = 60°$.

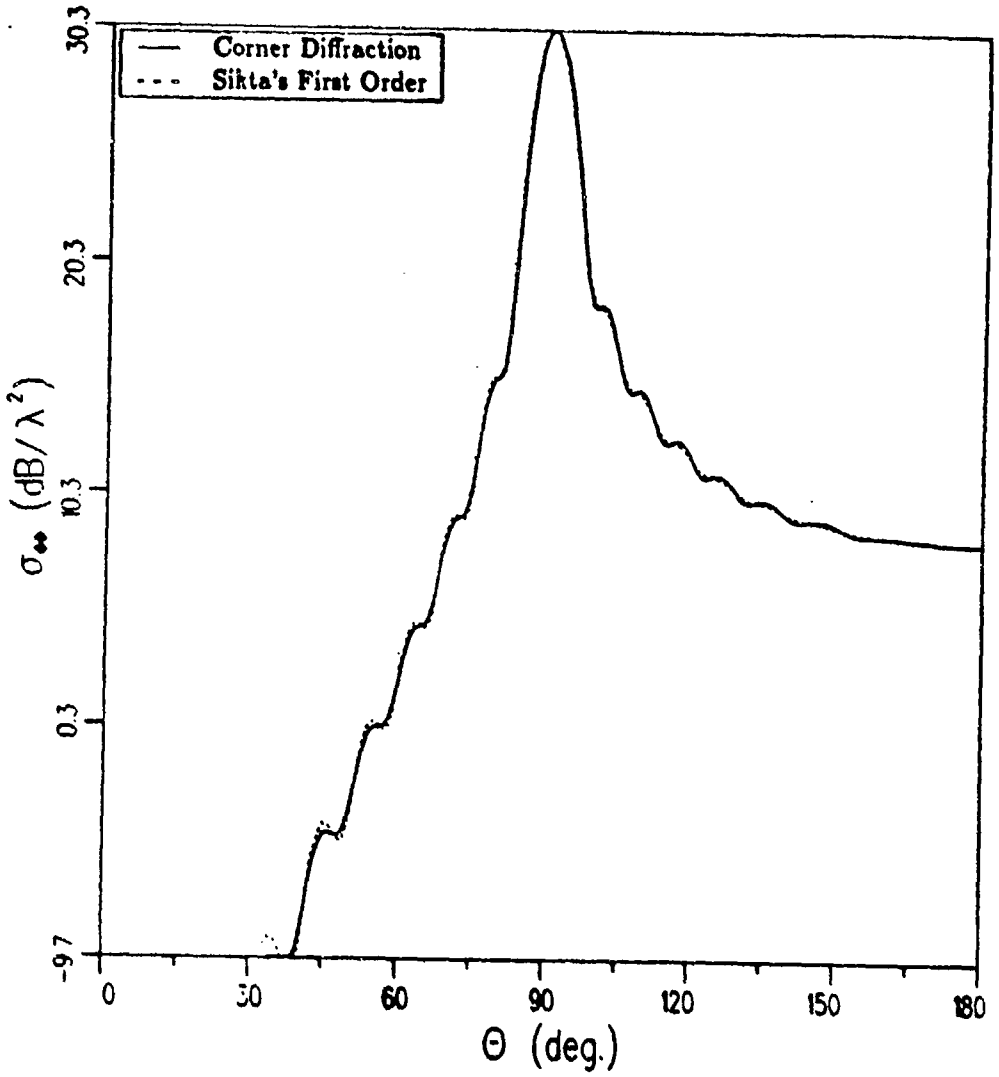

Figure 90: The H-plane pattern ($\phi = 0°$) for Sikta's triangle with $a = 4\lambda$ and $\alpha = 60°$.

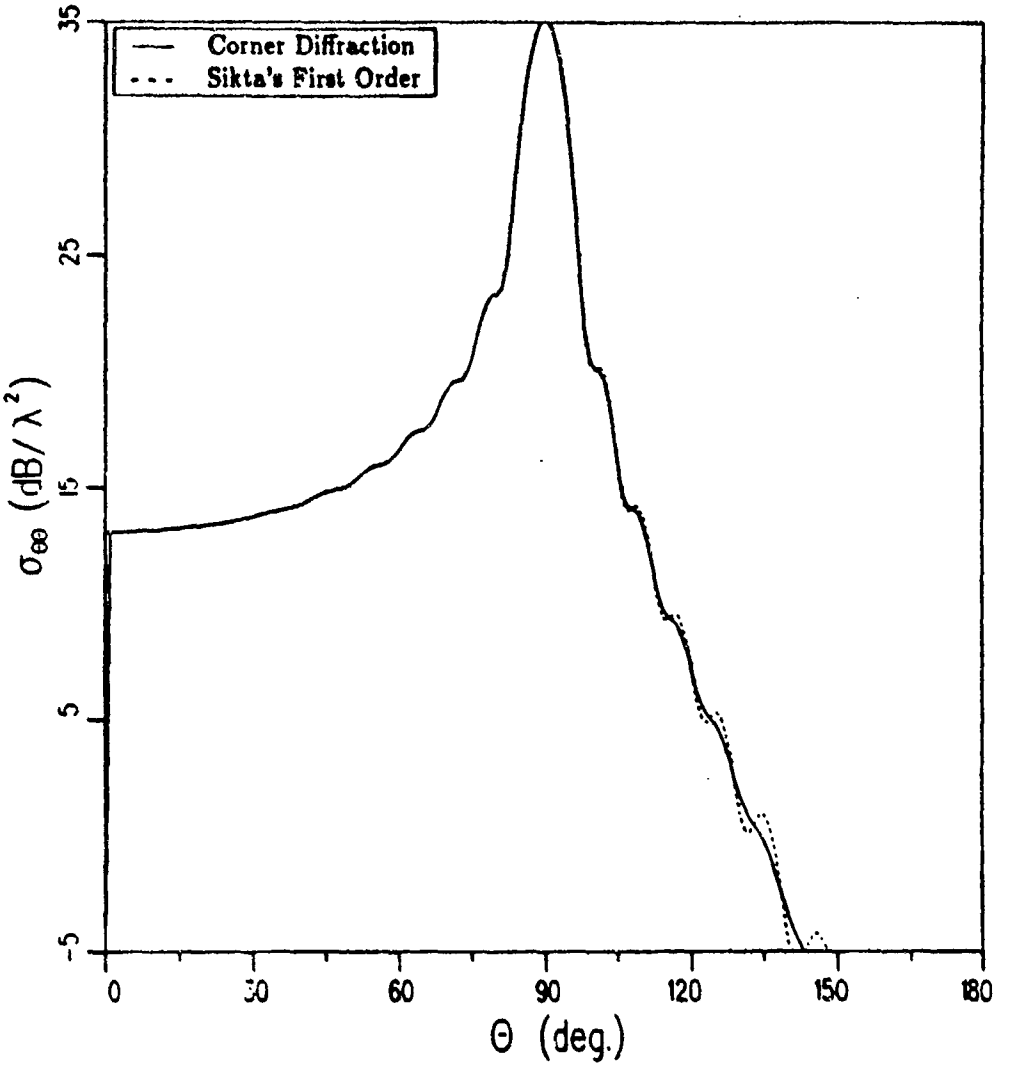

Figure 91: The E-plane pattern ($\phi = 0°$) for Sikta's triangle with $a = 4\lambda$ and $\alpha = 90°$.

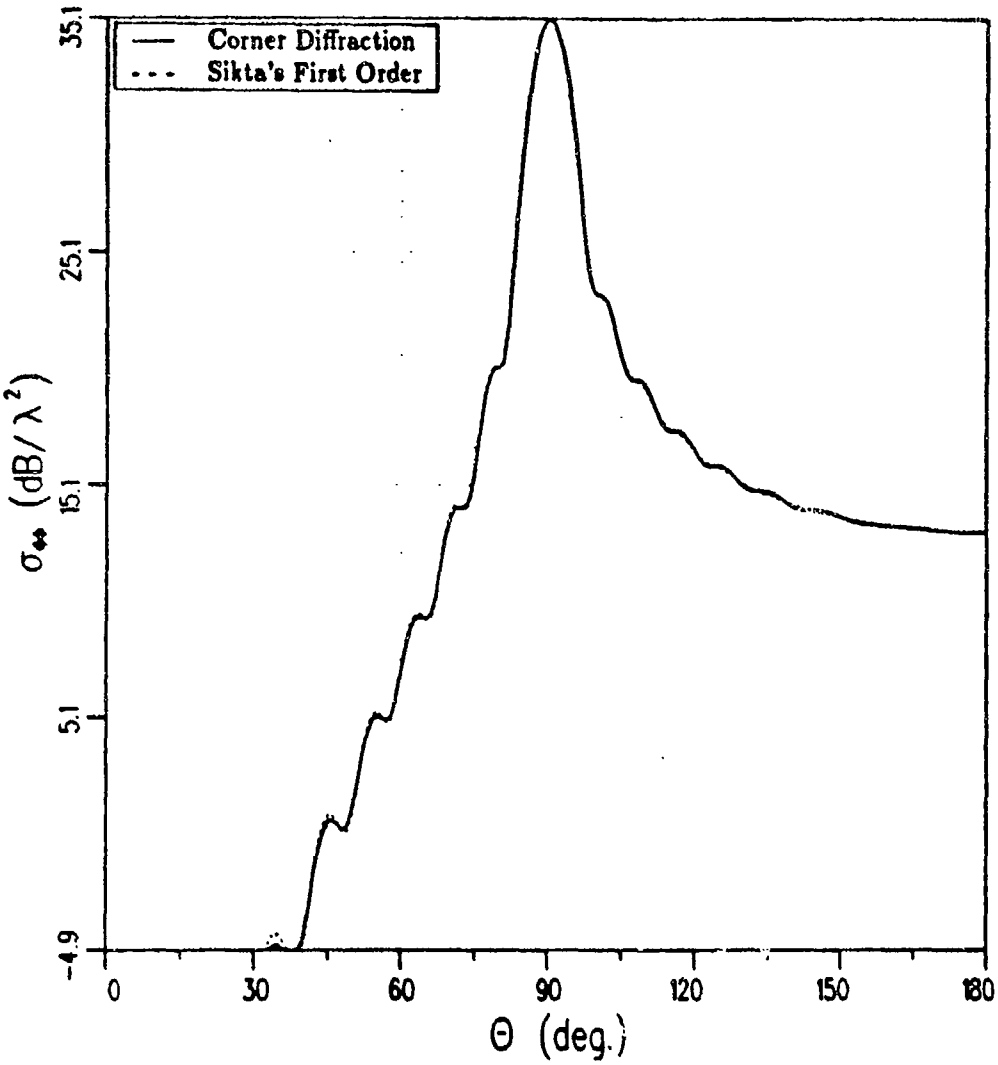

Figure 92: The H-plane pattern ($\phi = 0°$) for Sikta's triangle with $a = 4\lambda$ and $\alpha = 90°$.

In all cases the new solution and the measurements match well in the region within 50° of the broadside to the plate. In addition for the case of $\hat{\phi}$ polarization the new solution and the measurements are close enough for engineering purposes all the way to the plane of the plate in the region away from the tip of the triangle. For either polarization the new corner and the measurements differ significantly in the region of the tip of the triangle. Sikta shows that higher order terms are important in this region. The new solution and the first order terms obtained by Sikta using the equivalent currents of Ryan and Peters are approximately the same for all of the examples given here. There are only minor differences between the two different methods which become smaller as the size of the triangle is increased.

5.3.4 Cube

A few examples are illustrated here for the scattering from a cube with one wavelength long sides. The results are compared with those obtained using the Method of Moments. The cube is positioned relative to the axes in the usual way (each edge is parallel to one of the coordinate axes). The results for co-polarized backscatter in the principle plane are shown for the H-plane (with $\theta = 90°$) in Figure 93 and for the E-plane (with $\phi = 90°$) in Figure 94. The results obtained are very close to those obtained using the Method of Moments.

5.3.5 6" Cube

In this example the new solution is compared to backscatter measurements made on a 6" cube. All of the results are for co-polarized fields only. With the cube oriented so that each edge is parallel to one of the axes as shown in Figure 95, the pattern was taken in the x-y plane at 10 GHz. The results for a vertically polarized (or $\hat{\theta}$ polarized) incident field are shown in Figure 96, while the results for a horizontally polarized ($\hat{\phi}$ polarized) incident field are shown in

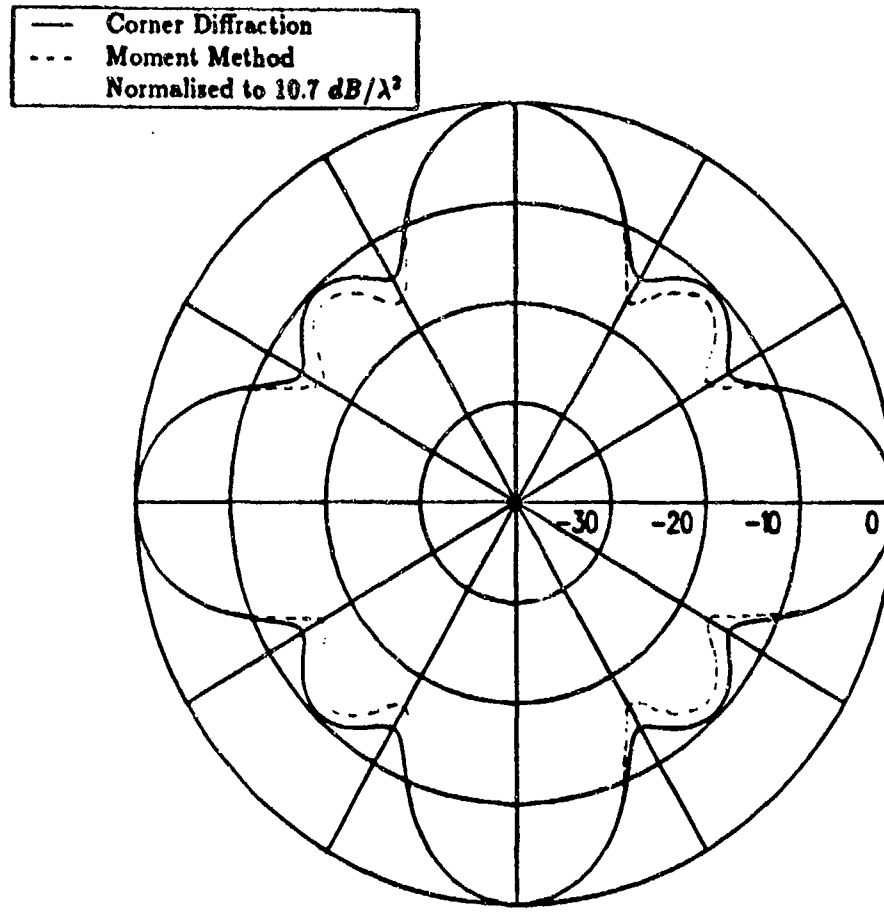

Figure 93: H-plane pattern for Cube (with $\theta = 90°$).

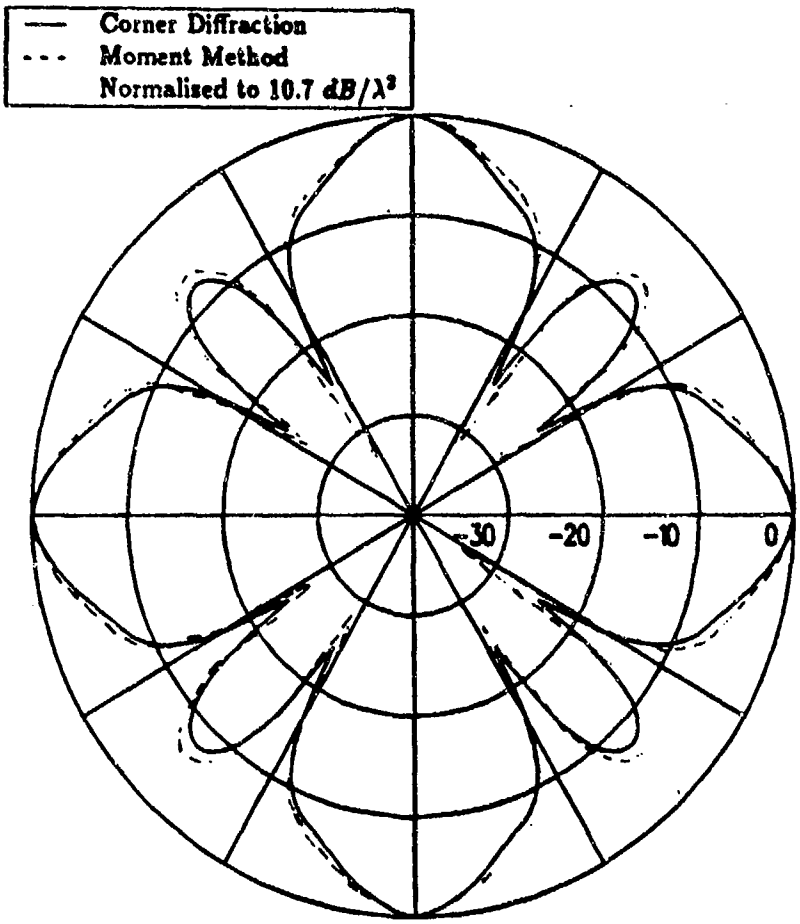

Figure 94: E-plane pattern for Cube (with $\phi = 90°$).

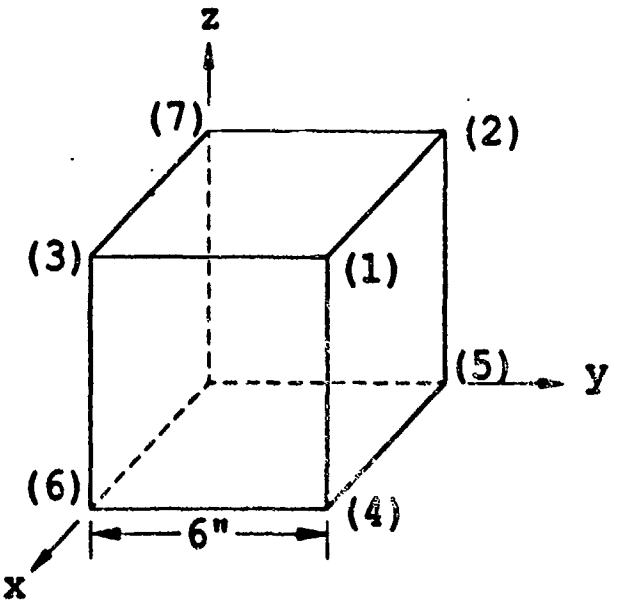

Figure 95: Cube geometry with the illuminated corners labeled.

Figure 97. The results agree fairly well everywhere, with differences of only a few *dB* throughout the patterns. The patterns are repeated for a cube tilted 45° in the x-z plane as illustrated in Figure 98. The results for the H-plane and E-plane patterns taken in the x-y plane are given in Figures 99 and 100, respectively. The results do not agree as well in this case. This is probably due to a combination of errors in the theory and in the measurements. The major error in the theory is the lack of higher order terms. The error in the measurements is likely two fold. First the faces of the cube were misaligned and so they did not form edges as sharp as may be required. Secondly it seems that there was some deviation from the desired pattern cuts as can be seen from the lack of symmetry in the measured patterns.

The final patterns are for a cube tilted 45° in the x-z plane followed by tilting it 35.2° in the y-z plane so that the z-axis coincides with one of the long diagonals passing through the center of the cube (as illustrated in Figure 101). The results

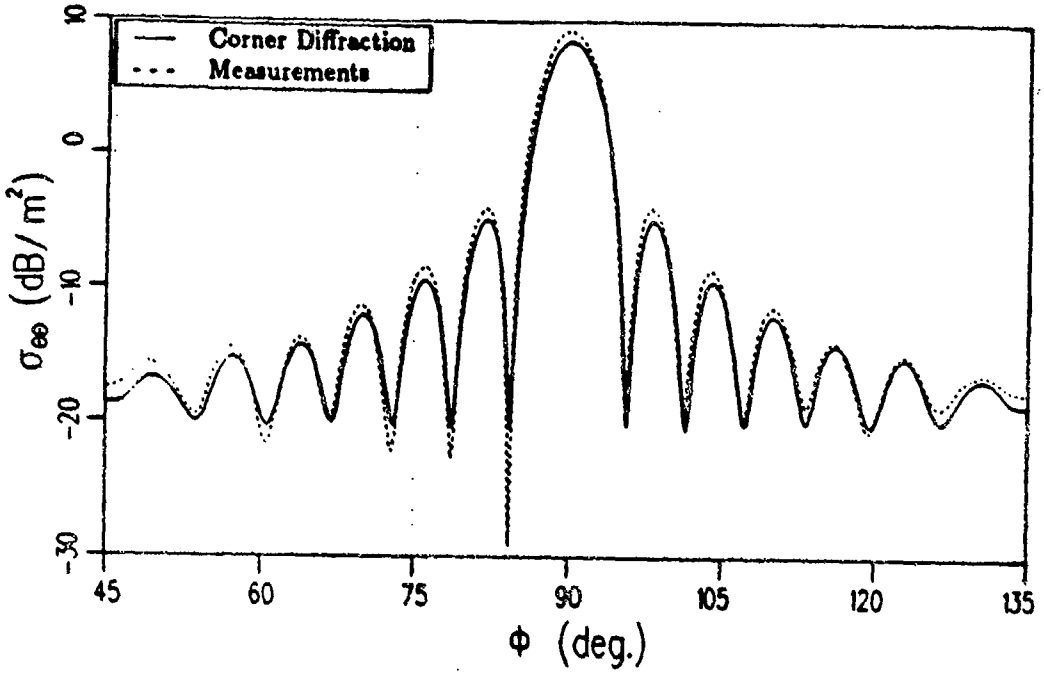

Figure 96: H-plane pattern for 6" cube.

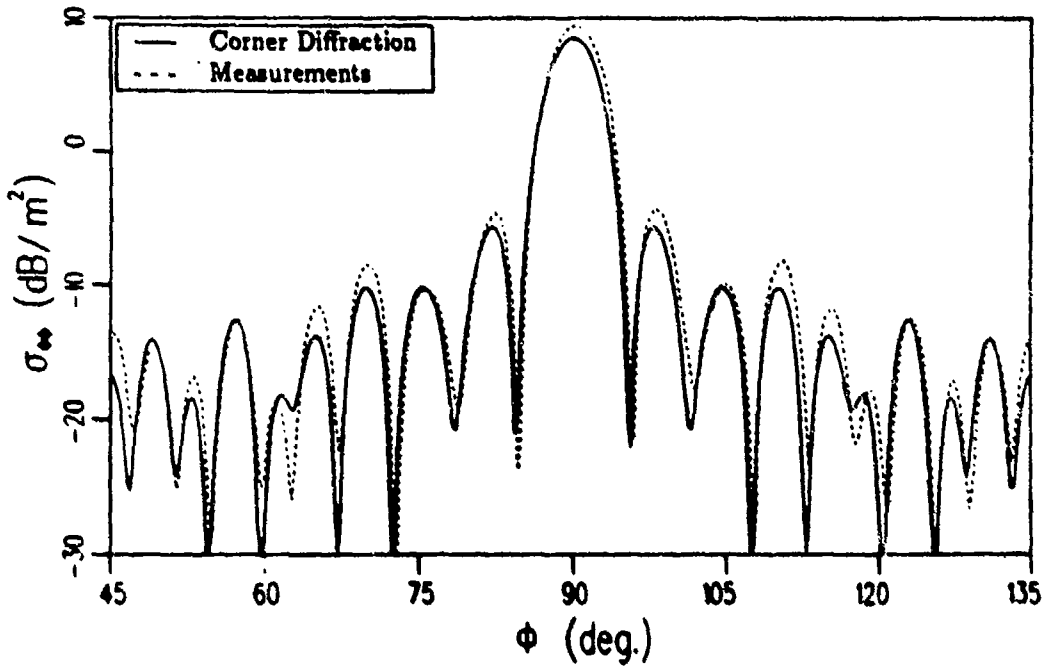

Figure 97: E-plane pattern for 6" cube.

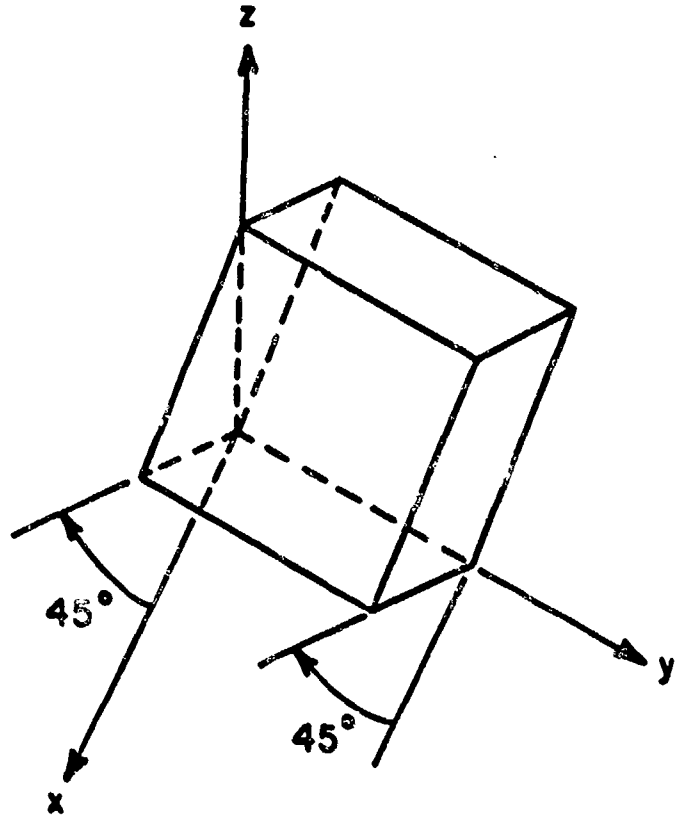

Figure 98: 6" Cube tilted 45° in the x-z plane.

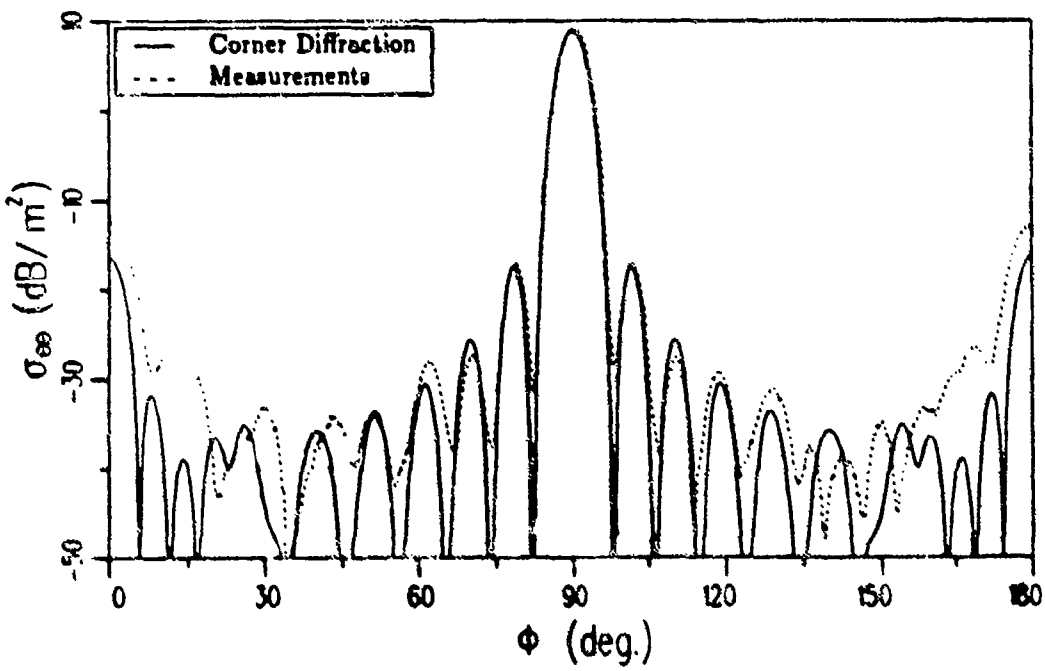

Figure 99: H-plane pattern for 6" cube tilted 45° in the x-z plane.

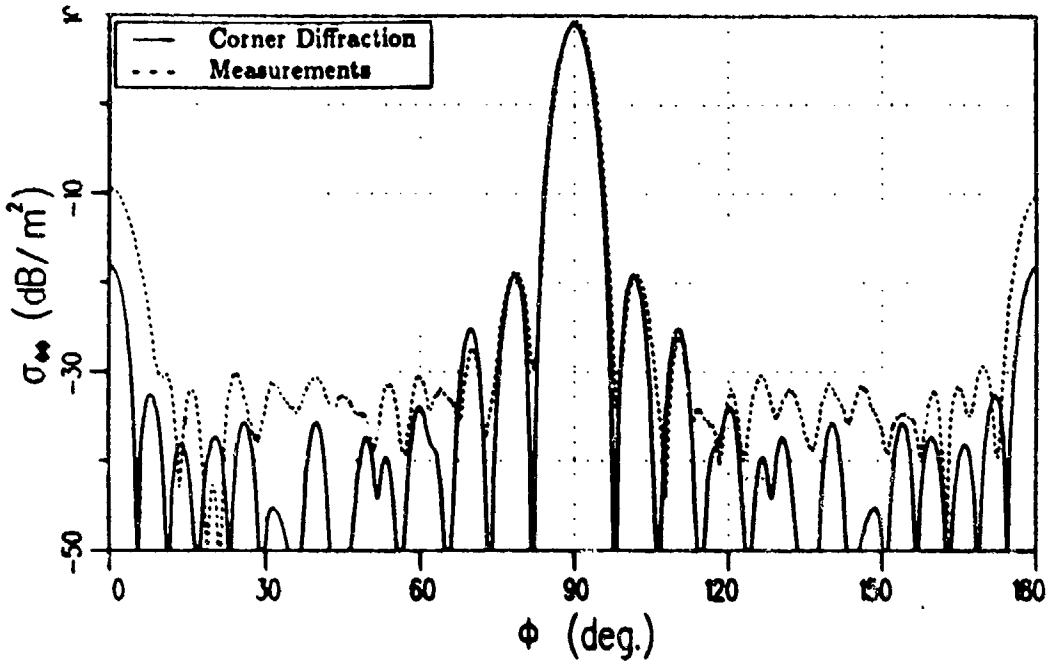

Figure 100: E-plane pattern for 6" cube tilted 45° in the x-z plane.

for the H-plane and E-plane patterns taken in the x-y plane are given in Figures 102 and 103, respectively. As with the previous patterns the higher level lobes agree fairly well, but the lower level lobes do not agree well. The reasons for this are the same as those stated previously.

5.3.6 Swept Frequency Results

In this section swept frequency measurements and calculations are transformed to the time domain as described by Dominek [31] and Leeper [32]. A brief description of the idea behind this is given here. While the target remains stationary the RCS is measured over a wide frequency range. An Inverse Fourier Transform is then preformed on the frequency domain data to give the "finite bandwidth impulse response" of the target as a function of time. In this manner the different scattering centers on a target may be resolved due to their different electrical lengths from the source. Obviously the closer the scattering center is to the source the earlier its contribution will appear in the time response. The

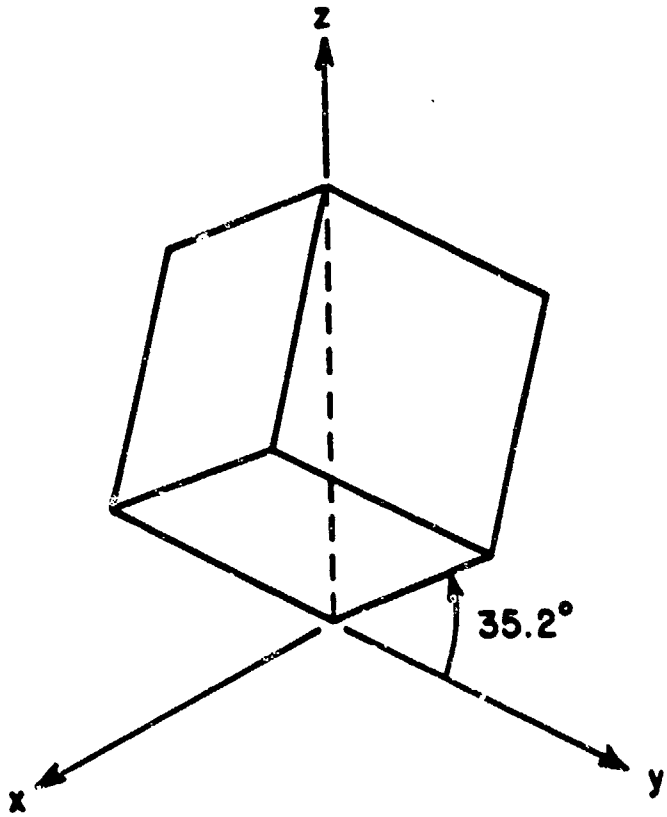

Figure 101: 6" Cube tilted 45° in the x-z plane, then 35.2° in the y-z plane.

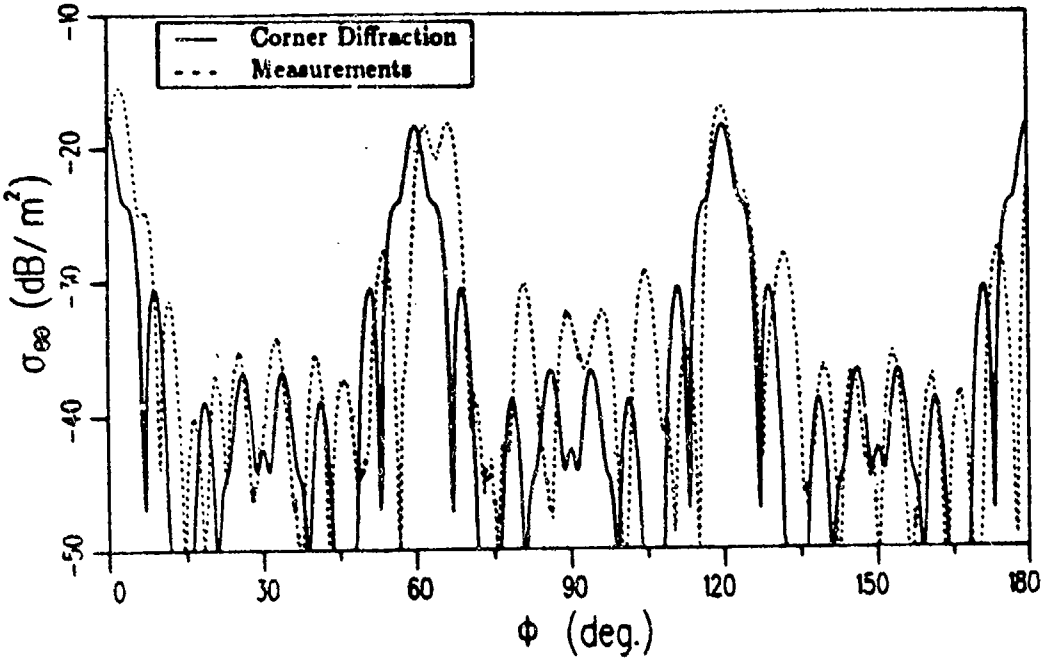

Figure 102: H-plane pattern for a 6" Cube tilted 45° in the x-z plane, then 35.2° in the y-z plane.

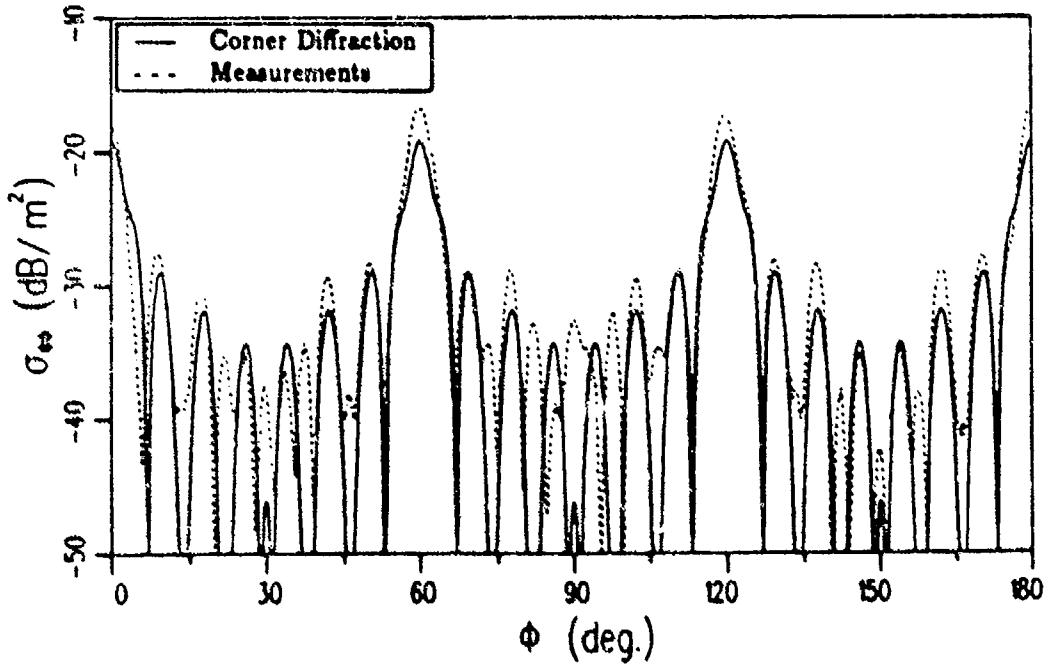

Figure 103: E-plane pattern for a 6" Cube tilted 45° in the x-z plane, then 35.2° in the y-z plane.

resolution of the scattering centers in the time domain is approximately equal to the reciprocal of the bandwidth of the measurements. Since actual distances on the target are related to the time delay by the speed of light, the resolution is approximately the speed of light divided by the bandwidth of the measurement. It should be noted that in practice the frequency data is usually passed through a linear phase filter before the Inverse Fourier Transform is taken. The filtering prevents the resulting time domain function from containing some unwanted ripples due to Gibb's phenomenon.

For this example a 6" cube was oriented as in Figure 95 and the RCS was measured for $\theta = 35.2°$, $\phi = 45°$ every 10 MHz while the frequency was swept from 2 GHz to 18 GHz. This data was passed through a Kaiser-Bessel bandpass filter with parameter $\alpha = 2$. The Inverse Fourier Transform was then performed. The co-polarized results for a vertically polarized incident field are shown in Figure 104, and the co-polarized results for a horizontally polarized incident field are given in Figure 105. The first pulse is due to the scattering from the corner closest to the source. In both cases the calculations match very closely with the measurements. The calculations match the second pulse well for the horizontally polarized case, while the measurements and calculations are significantly different for the vertically polarized case. A first order solution can only be expected to match the first two pulses though, since the measured time response includes higher order terms which have almost the same delays as contributions from the other corners making it difficult to separate out the contributions from individual corners. The contributions from each of the illuminated corners are still difficult to identify due to the limited bandwidth of the calculations. Since the bandwidth of the measurements was 6 GHz the resolution should be approximately 0.17 ns. The two way time delays for the illuminated corners are listed in Table 1. Obviously the returns

Table 1: Delay times from different corners of the 6" cube.

Corner No. (see Figure 95	Two Way Delay Time (nsec.)
1 (ref.)	0.00
2	0.41
3	0.41
4	0.83
5	0.83
6	1.24
7	1.24

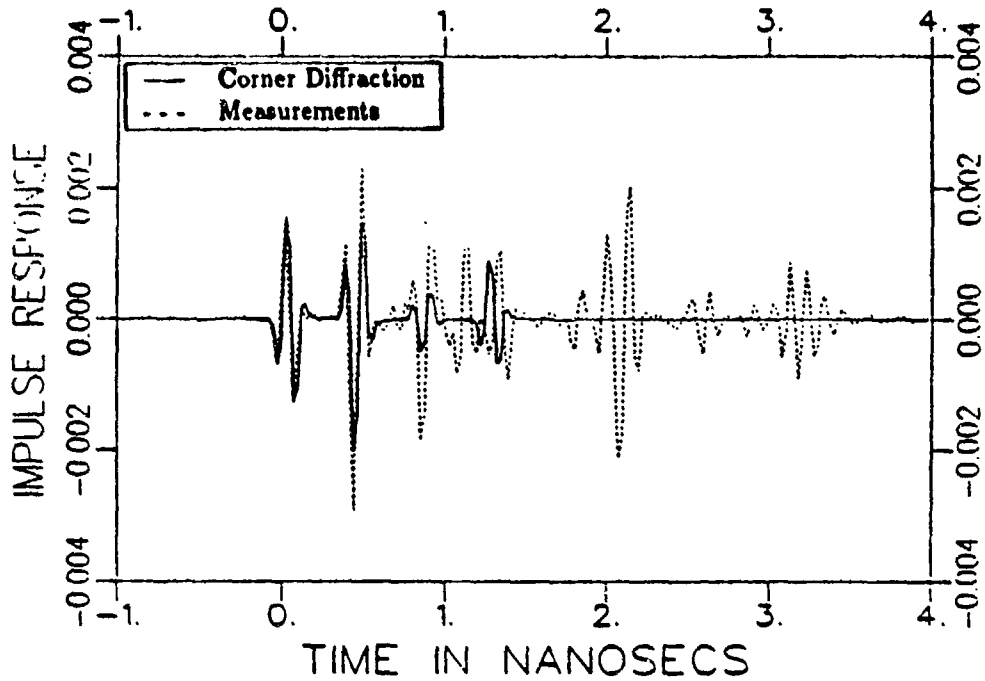

Figure 104: Impulse response for 6" cube and a $\hat{\theta}$ polarized source at $\theta = 35.2°$, $\phi = 45°$.

from many of the corners have essentially the same time delays so there is not a separate pulse corresponding to each corner.

5.3.7 Bistatic Scattering from a 2λ plate illuminated by a fixed source

The scattering from a square plate two wavelengths on a side is examined in detail next. The complete scattering matrix (all four values of σ) is found for the plate in the x-y plane with a fixed source at $\theta^i = 45°$ and $\phi^i = 0°$ (see Figure 106). Circular pattern cuts from $\phi = 0°$ to $\phi = 90°$ are taken every 30°. The results for the co-polarized fields and the $\phi = 0°$ pattern cut are compared with the previous equivalent currents and Method of Moment calculations in Figures 107 and 108 (the results for $\phi = 60°$ are given in Section 2.7 for the previous corner diffraction coefficients). The cross-polarized fields are zero for both a $\hat{\theta}$ polarized incident field and a $\hat{\phi}$ polarized incident field. The previous equivalent currents and the

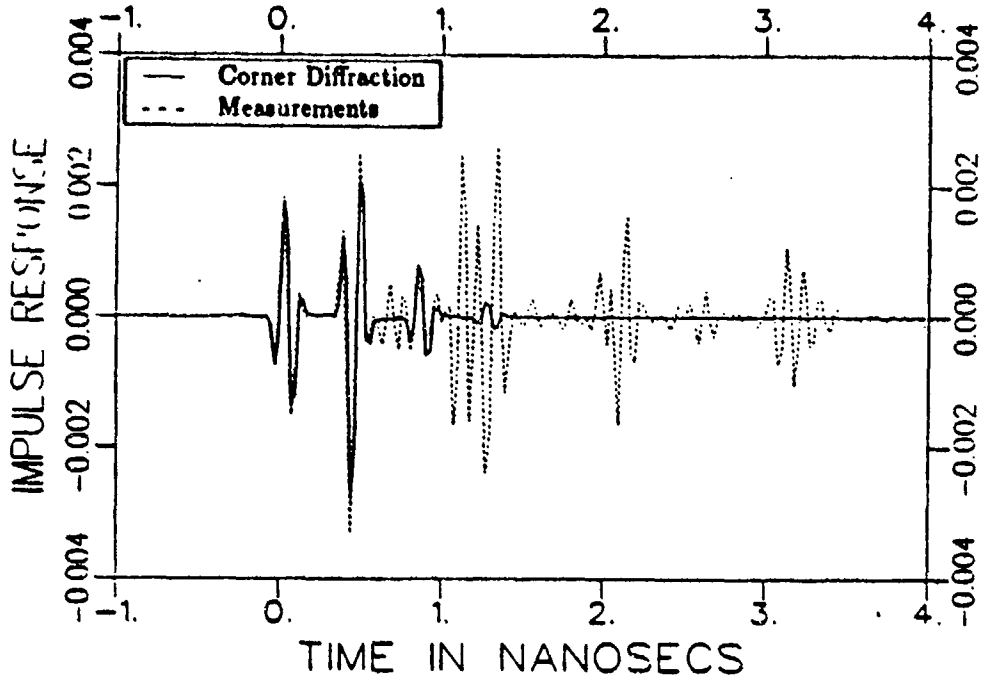

Figure 105: Impulse response for 6" cube and a $\hat{\phi}$ polarized source at $\theta = 35.2°$, $\phi = 45°$.

new corner diffraction coefficient agree so closely that they essentially lie on top of each other in this pattern. This is not unexpected since, in this pattern cut, the receiver is on the Keller cone for the front and back edges, which therefore give the major contribution to the scattered field. The new solution reduces to previous solutions on the Keller cone (see Section 4.6), which do not radiate any cross polarized field for incidence normal to the edge. The results for the $\phi = 30°$ pattern cut are compared with the previous equivalent currents and Method of Moment calculations for the co-polarized fields in Figures 109 and 110. Similarly the results for the cross-polarized fields are given in Figures 111 and 112. The results for the $\phi = 60°$ pattern cut are compared with the previous equivalent currents and Method of Moment calculations for co-polarized fields in Figures 113 and 114. Similarly the results for the cross-polarized fields are given in Figure 115 and

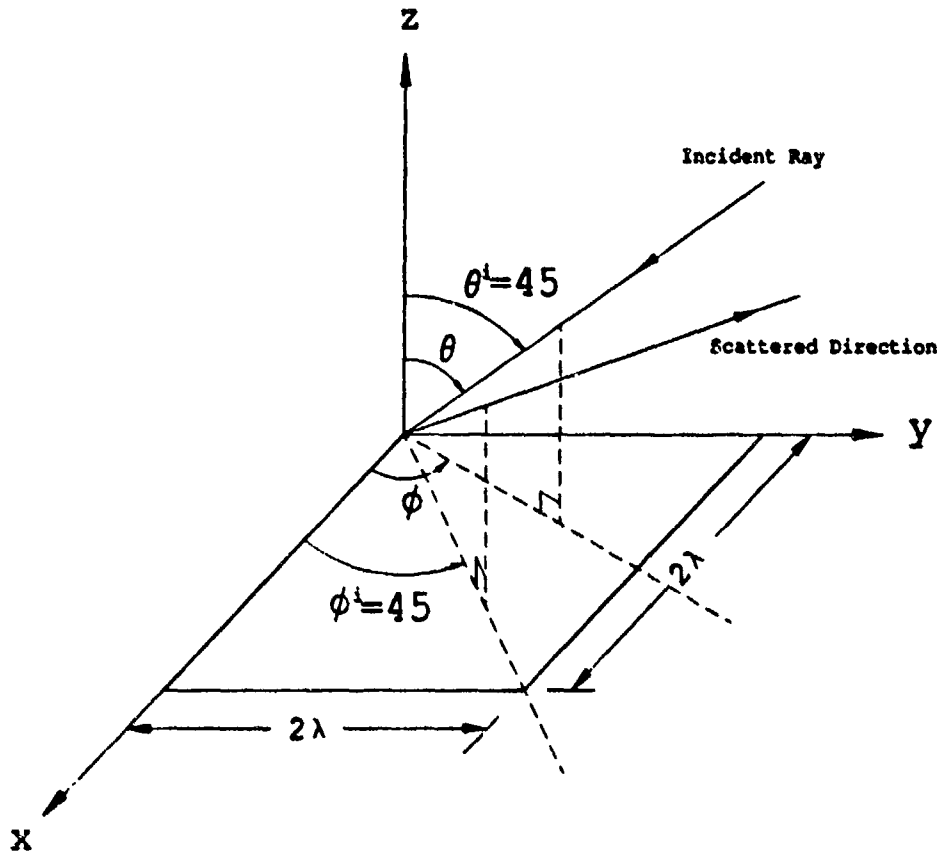

Figure 106: 2λ square plate in the x-y plane with a fixed source at $\theta^i = 45°$ and $\phi^i = 0$.

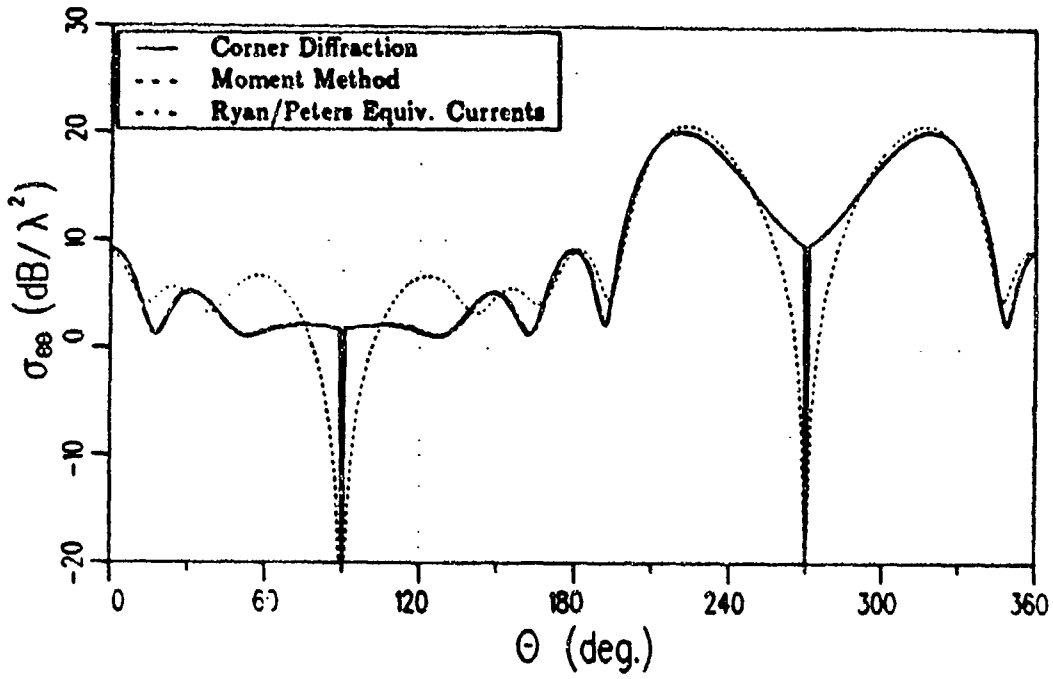

Figure 107: Co-polarized RCS in the $\phi = 0°$ plane of a 2λ square plate with a $\hat{\theta}^i$ polarized fixed source at $\theta^i = 45°$, $\phi^i = 0°$.

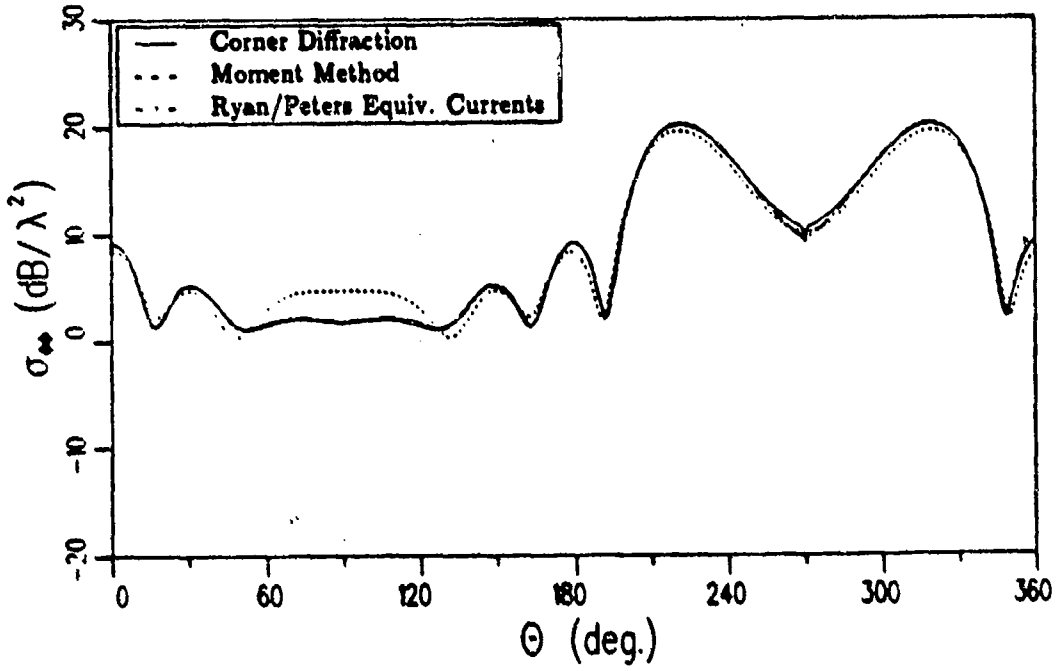

Figure 108: Co-polarized RCS in the $\phi = 0°$ plane of a 2λ square plate with a $\hat{\phi}^i$ polarized fixed source at $\theta^i = 45°$, $\phi^i = 0°$.

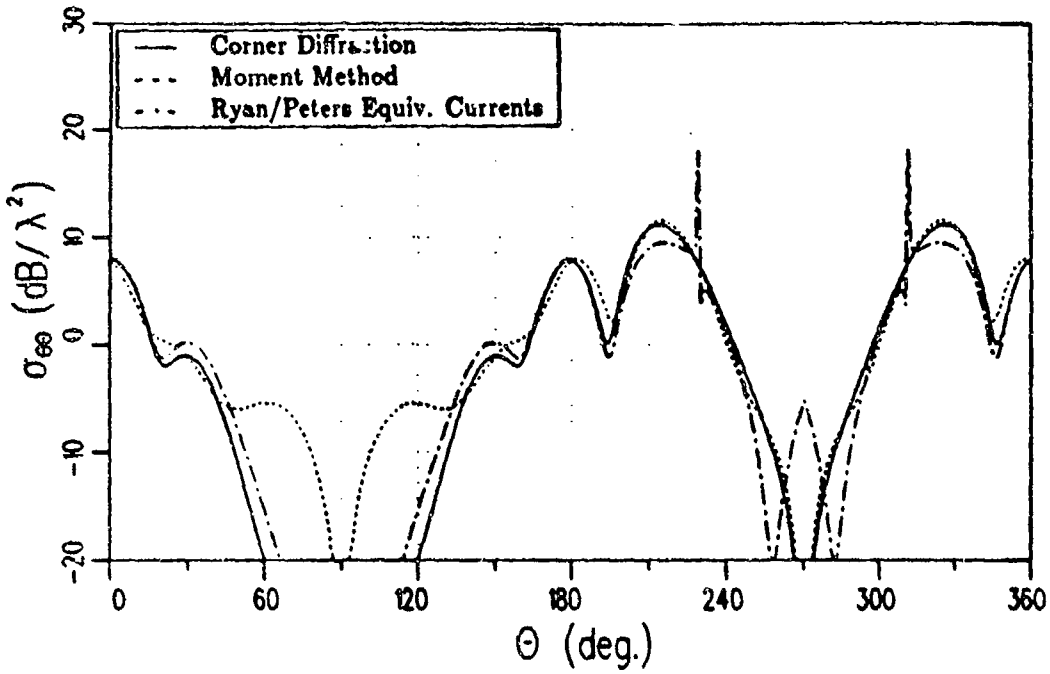

Figure 109: Co-polarized RCS in the $\phi = 30°$ plane of a 2λ square plate with a $\hat{\theta}^i$ polarized fixed source at $\theta^i = 45°$, $\phi^i = 0°$.

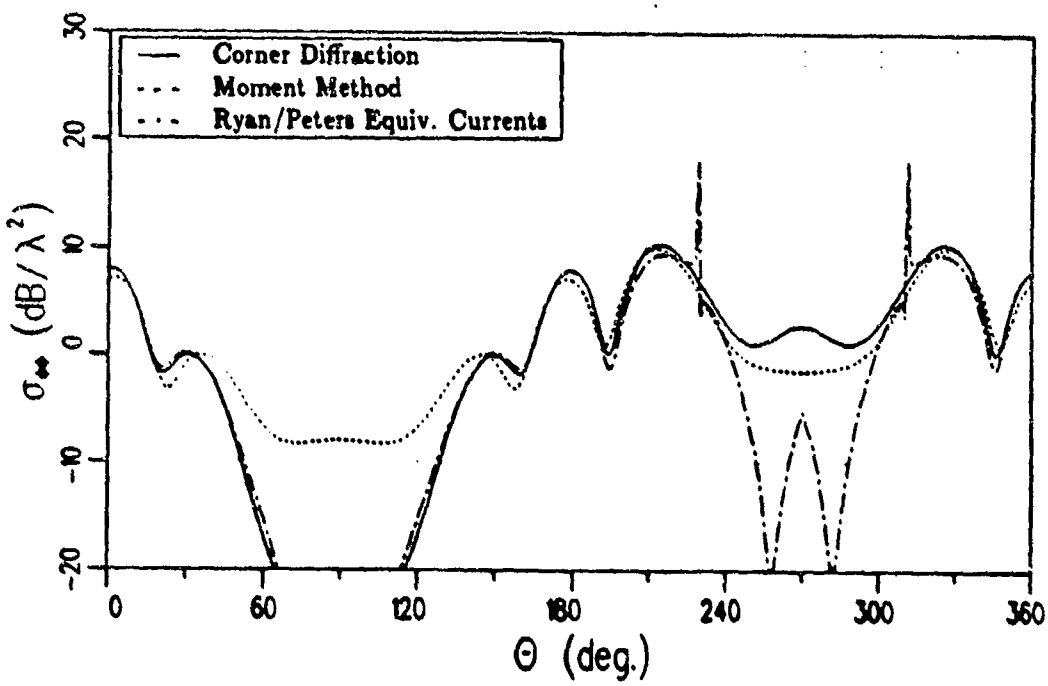

Figure 110: Co-polarized RCS in the $\phi = 30°$ plane of a 2λ square plate with a $\hat{\phi}^i$ polarized fixed source at $\theta^i = 45°$, $\phi^i = 0°$.

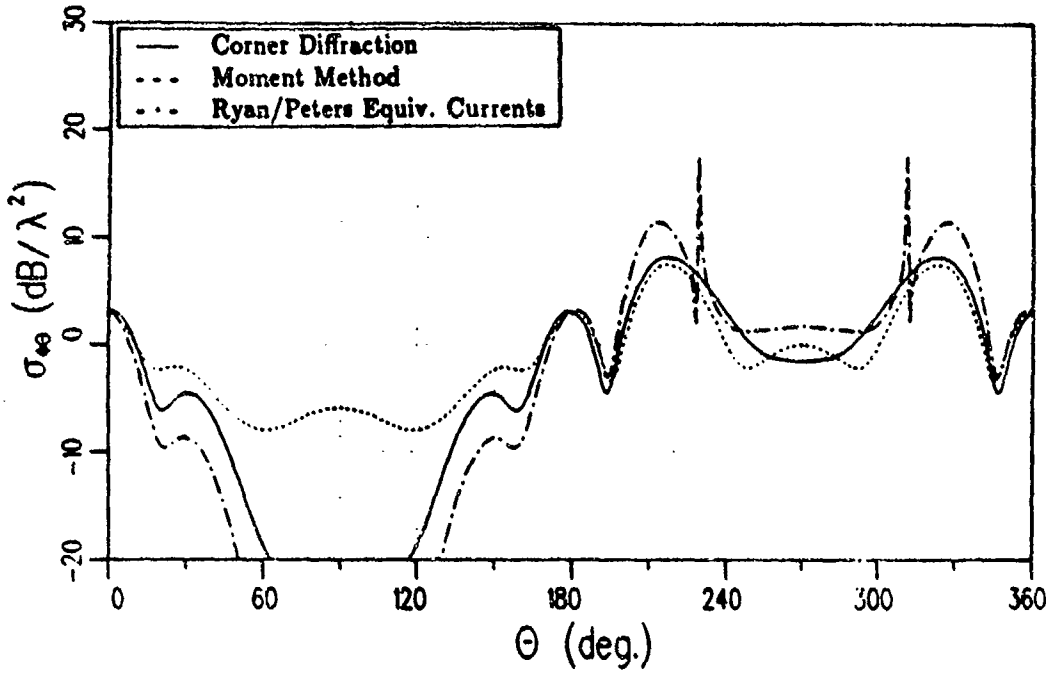

Figure 111: Cross-polarized RCS in the $\phi = 30°$ plane of a 2λ square plate with a $\hat{\theta}^i$ polarized fixed source at $\theta^i = 45°$, $\phi^i = 0°$.

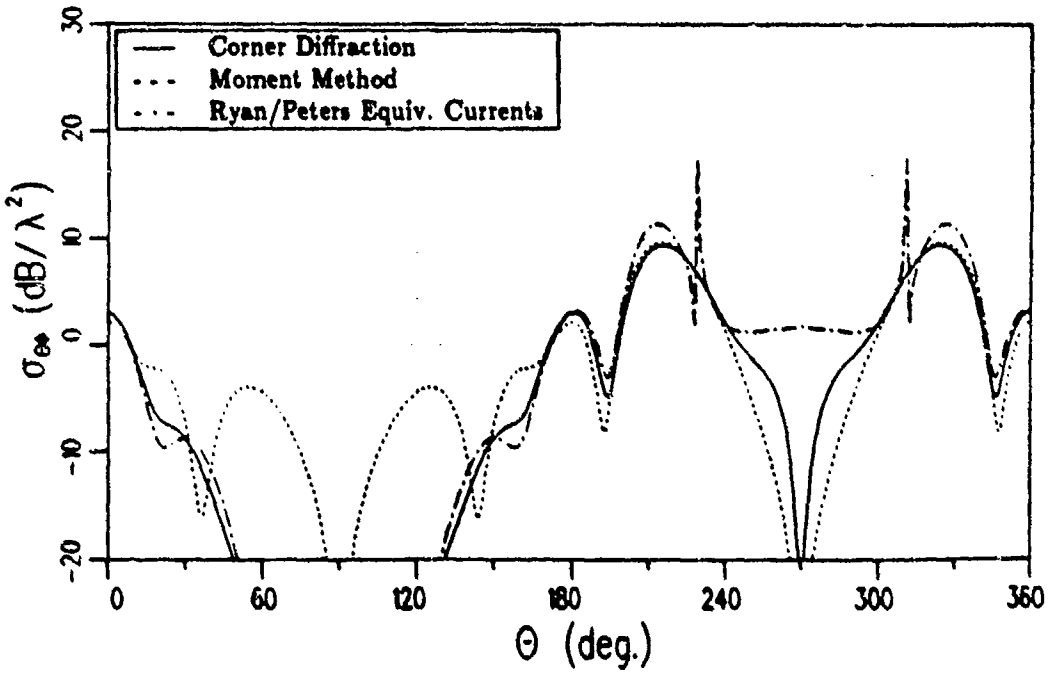

Figure 112: Cross-polarized RCS in the $\phi = 30°$ plane of a 2λ square plate with a $\hat{\phi}^i$ polarized fixed source at $\theta^i = 45°$, $\phi^i = 0°$.

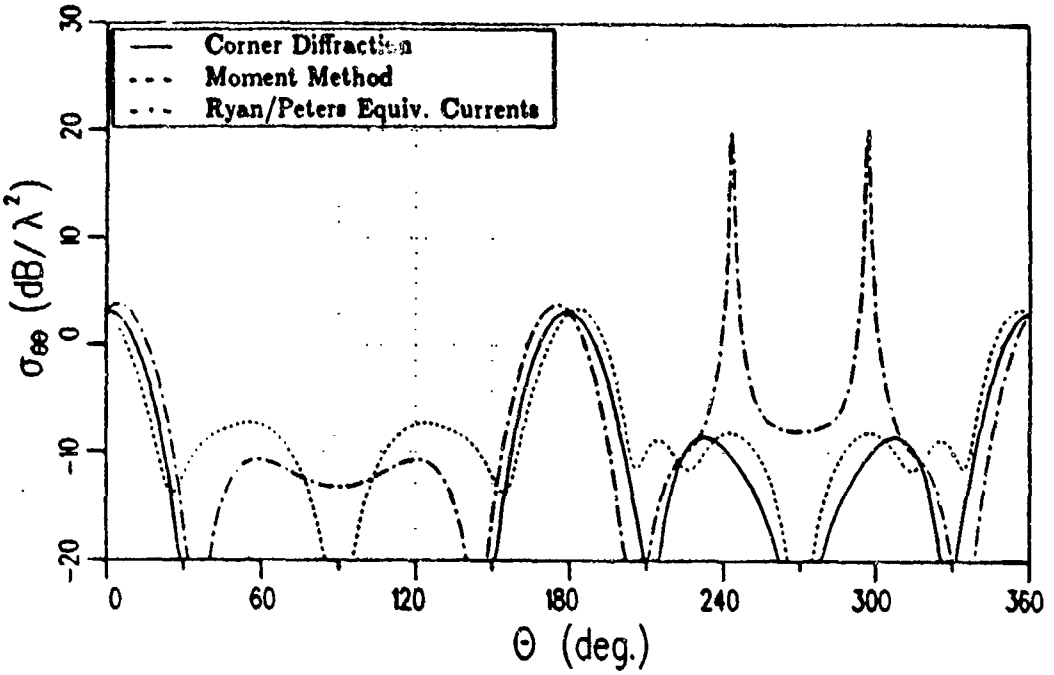

Figure 113: Co-polarized RCS in the $\phi = 60°$ plane of a 2λ square plate with a $\hat{\theta}^i$ polarized fixed source at $\theta^i = 45°$, $\phi^i = 0°$.

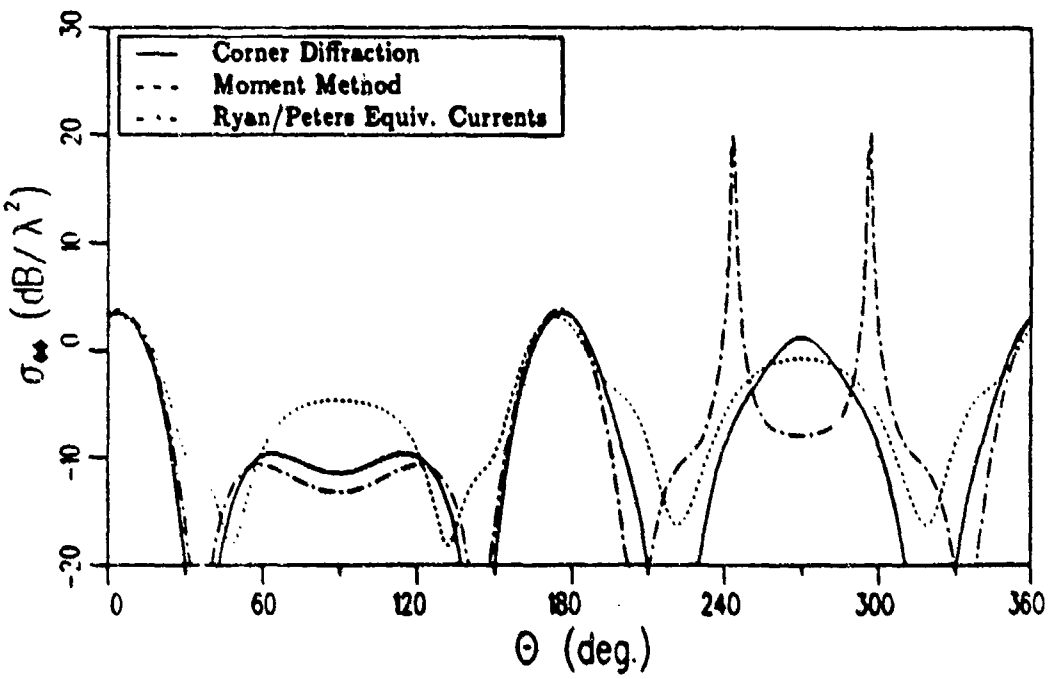

Figure 114: Co-polarized RCS in the $\phi = 60°$ plane of a 2λ square plate with a $\hat{\phi}^i$ polarized fixed source at $\theta^i = 45°$, $\phi^i = 0°$.

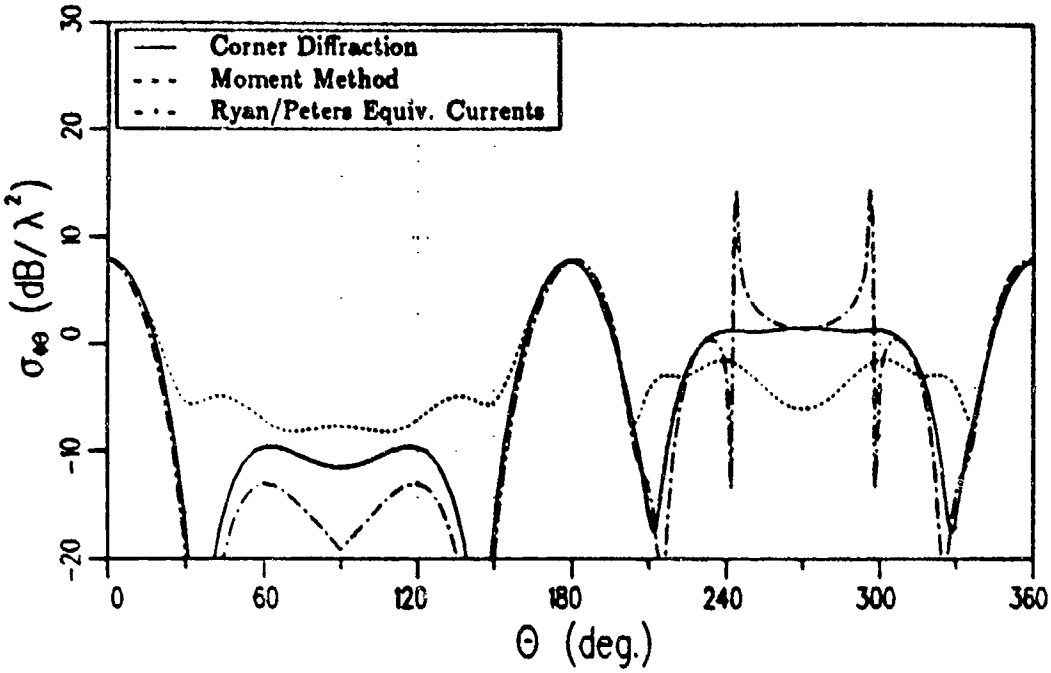

Figure 115: Cross-polarized RCS in the $\phi = 60°$ plane of a 2λ square plate with a $\hat{\theta}^i$ polarized fixed source at $\theta^i = 45°$, $\phi^i = 0°$.

Figure 116. The results for the $\phi = 90°$ pattern cut are compared with the previous equivalent currents and Method of Moment calculations for co-polarized fields in Figures 117 and 118. Similarly the results for the cross-polarized fields are given in Figures 119 and 120. Buyukdura [22] also gives results using the new solution for the case of a $\hat{\theta}$ polarized incident field (the slight differences between his results and those given here are suspected to be due to a sign error in his program). Overall the new solution agrees well with the Method of Moment calculations and does not exhibit the false shadow boundaries mentioned in Sections 2.6 and 2.7. The previous equivalent current solutions exhibit spikes at the false shadow boundaries which occur near $\theta = 130°$ and $\theta = 310°$ for the $\phi = 30°$ pattern cut and near $\theta = 240°$ and $\theta = 300°$ for the $\phi = 60°$ pattern cut. In the region from $\theta \approx 60°$ to $120°$ (i.e. near the plane of the plate) for both the $\phi = 30°$ and $\phi = 60°$ the new solution and the Method of Moments solution differ by more than 20 dB. It is suspected that most of these differences are due to the effects of higher order

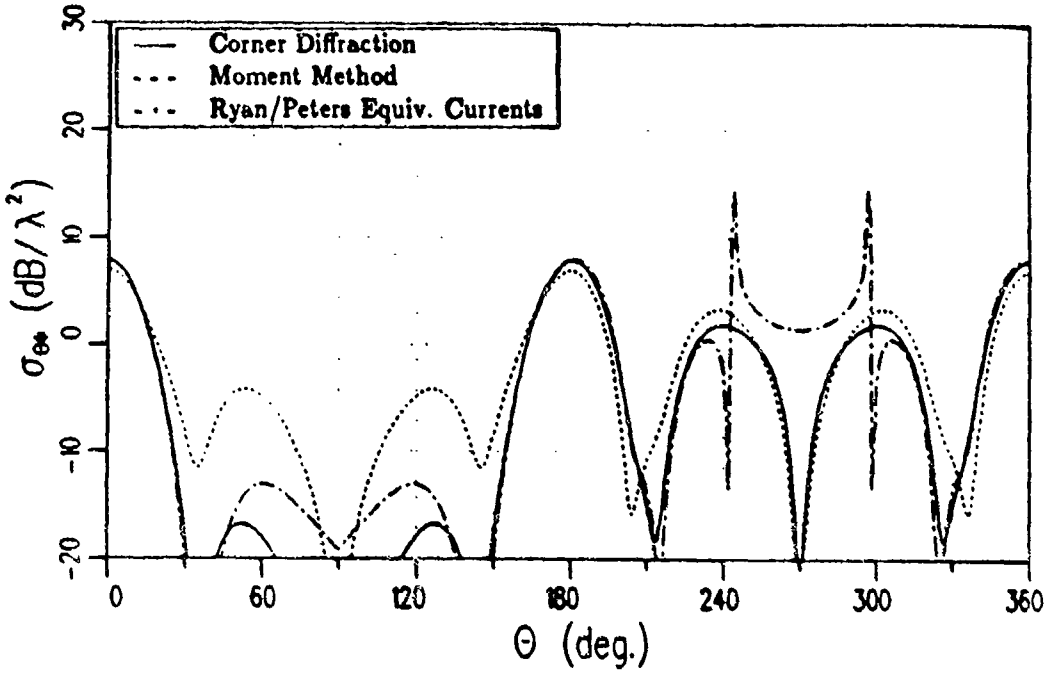

Figure 116: Cross-polarized RCS in the $\phi = 60°$ plane of a 2λ square plate with a $\hat{\phi}^i$ polarized fixed source at $\theta^i = 45°$, $\phi^i = 0°$.

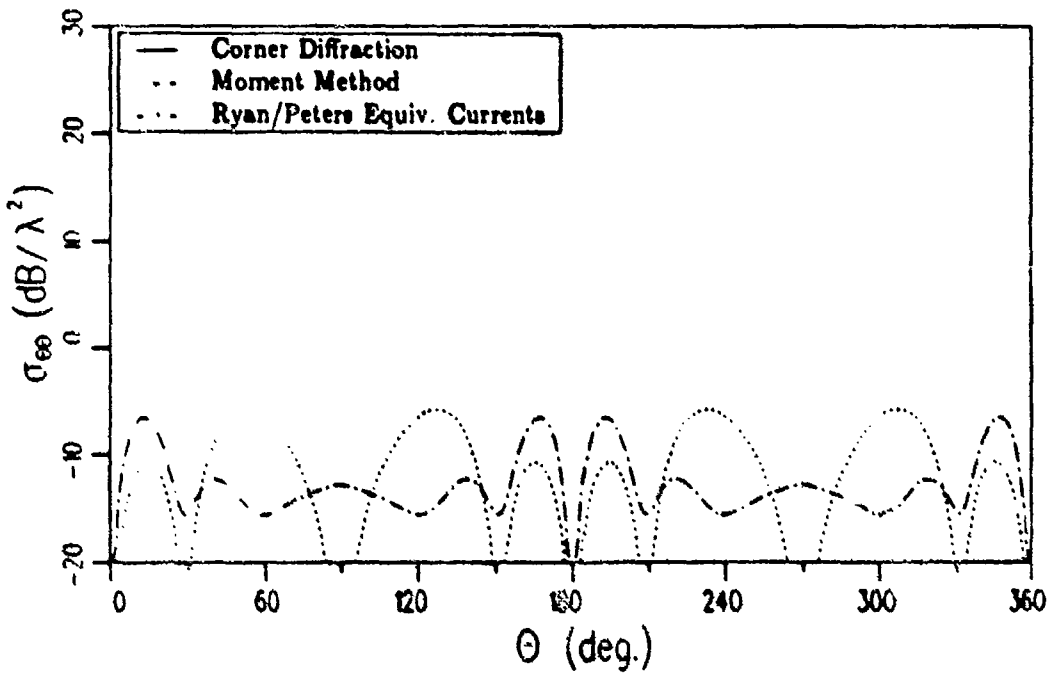

Figure 117: Co-polarized RCS in the $\phi = 90°$ plane of a 2λ square plate with a $\hat{\theta}^i$ polarized fixed source at $\theta^i = 45°$, $\phi^i = 0°$.

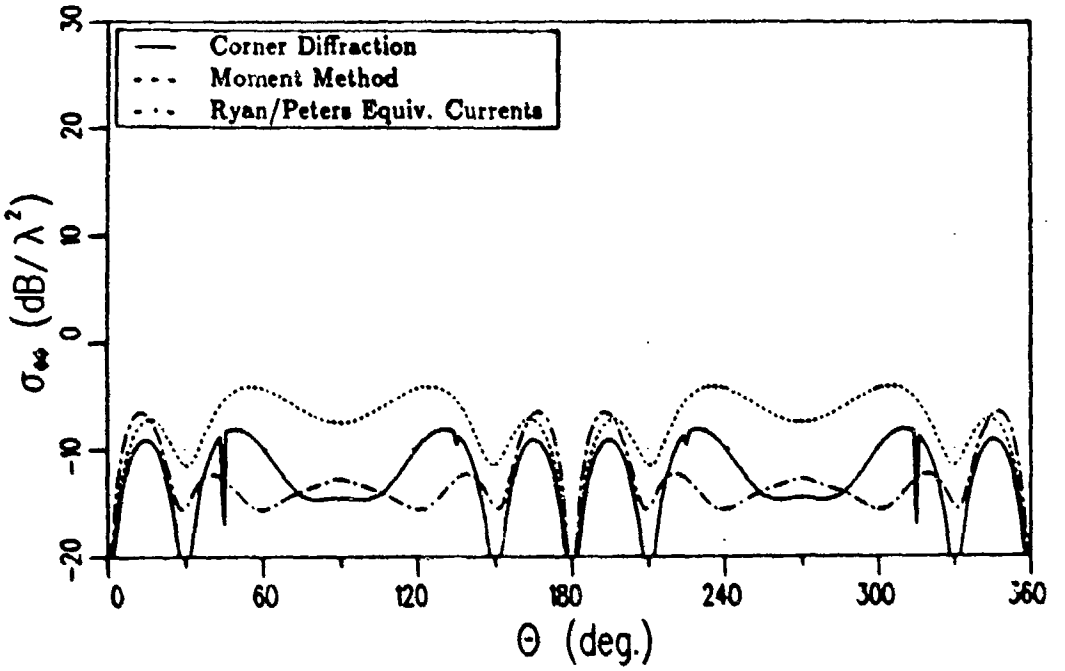

Figure 118: Co-polarized RCS in the $\phi = 90°$ plane of a 2λ square plate with a $\hat{\phi}^i$ polarized fixed source at $\theta^i = 45°$, $\phi^i = 0°$.

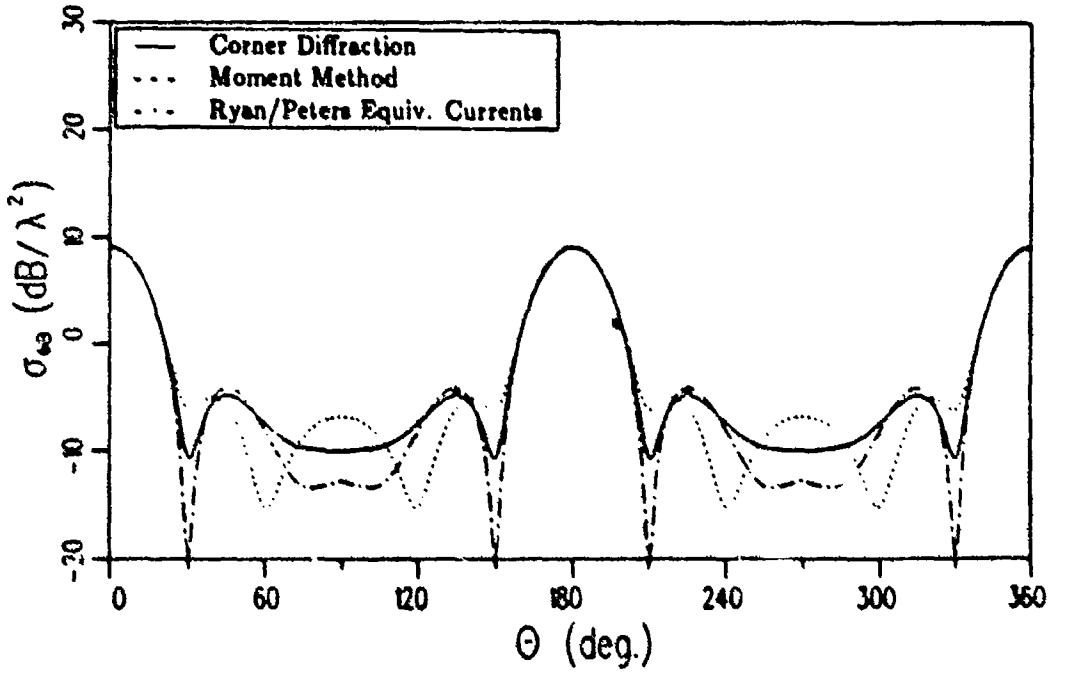

Figure 119: Cross-polarized RCS in the $\phi = 90°$ plane of a 2λ square plate with a $\hat{\theta}^i$ polarized fixed source at $\theta^i = 45°$, $\phi^i = 0°$.

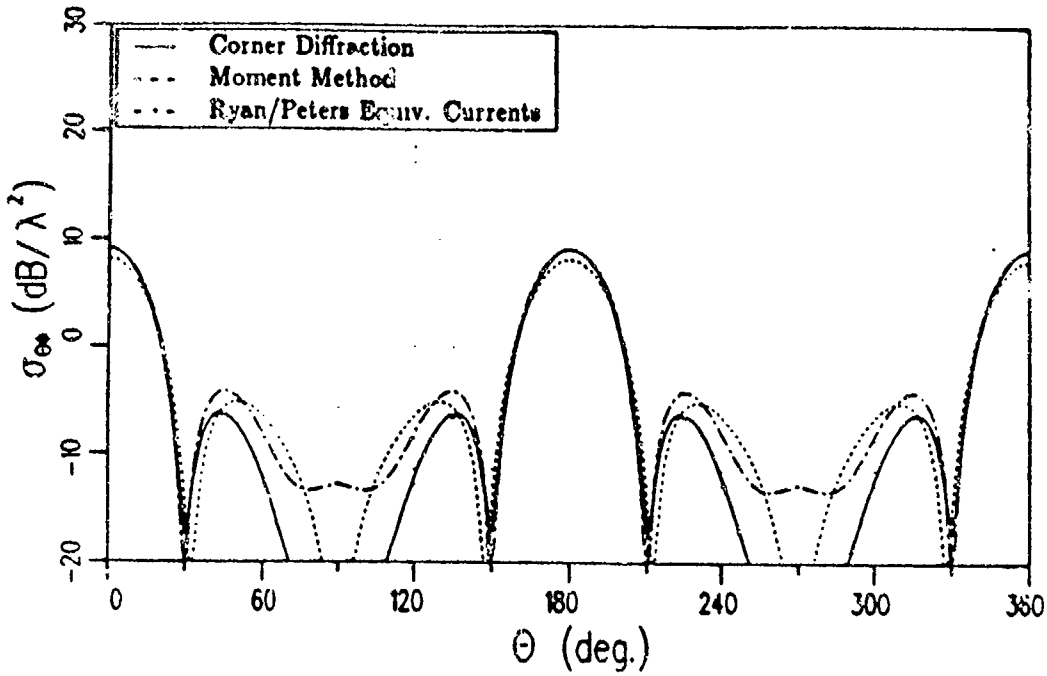

Figure 120: Cross-polarized RCS in the $\phi = 90°$ plane of a 2λ square plate with a $\hat{\phi}^i$ polarized fixed source at $\theta^i = 45°$, $\phi^i = 0°$.

terms (double and triple diffraction, edge waves) which are not included in the new solution. This may also be the case for $\sigma_{\theta\theta}$ in the $\phi = 90°$ pattern, although this also indicates that the higher order terms for the new solution and the previous solution must differ for points off of the Keller cone. The results for a pattern cut near the plane of the plate ($\theta = 39°$) have been given in Section 4.2.

5.3.8 Bistatic scattering from a 2λ plate illuminated by a fixed source in a second position

In the previous example the scattered field depended on only one or two currents along each edge instead of all three. This may be easily seen from the geometry. For a $\hat{\theta}$ polarized incident field the incident electric field tangent to the front and back edges is zero and the incident magnetic field tangent to the two sides is zero. Therefore only I_m (D_2^c) and M (D_h^c) along the front and back edges and I_e (D_s^c) along the right and left edges contribute to the scattered field. If the incident field is $\hat{\phi}$ polarized instead, the currents contributing from each edge are

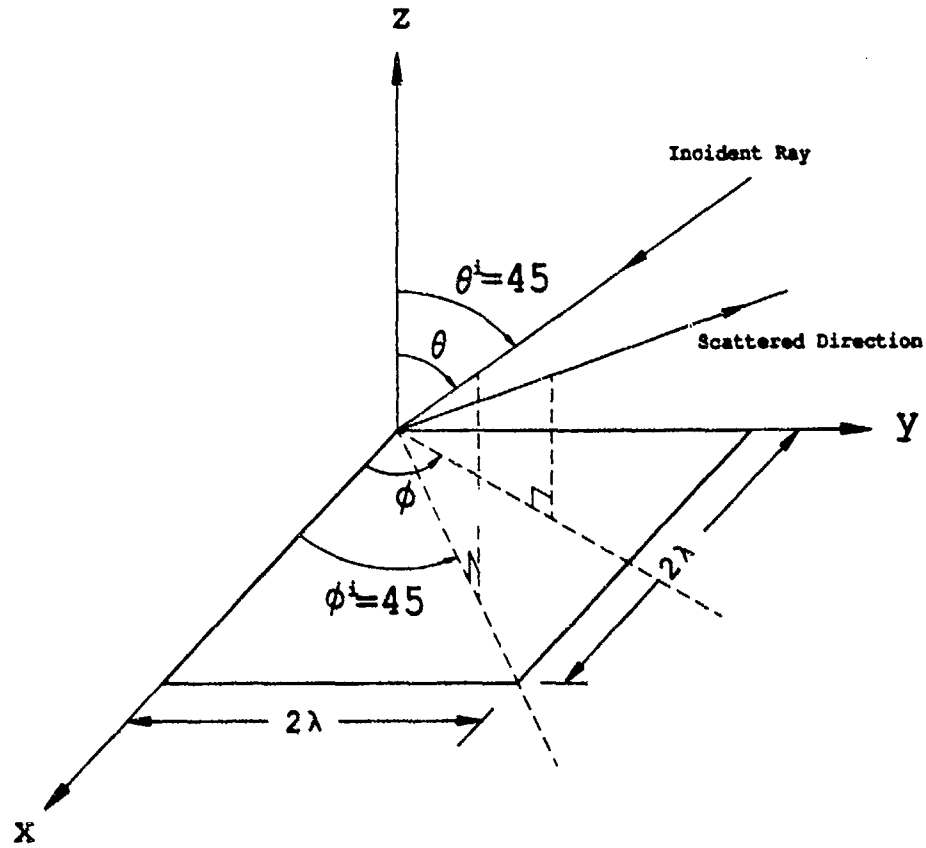

Figure 121: 2λ square plate in the x-y plane with a fixed source located at $\theta^i = 45°$, $\phi^i = 45°$.

the opposite of those for the $\hat{\theta}$ polarized incident field.

In order that all three currents along each edge will contribute to the scattered field the source is moved to a new location. Retaining the square plate from the above example and moving the source to $\theta^i = 45°$ and $\phi^i = 45°$ (see Figure 121) circular pattern cuts were once again taken every 30° from $\phi = 45°$ to $\phi = 135°$. The results for the co-polarized fields and the $\phi = 45°$ pattern cut are compared with Method of Moment calculations in Figures 122 and 123. The cross-polarized fields are zero for both a $\hat{\theta}$ polarized incident field and a $\hat{\phi}$ polarized incident field. The results for the $\phi = 75°$ pattern cut are compared with Method of Moment

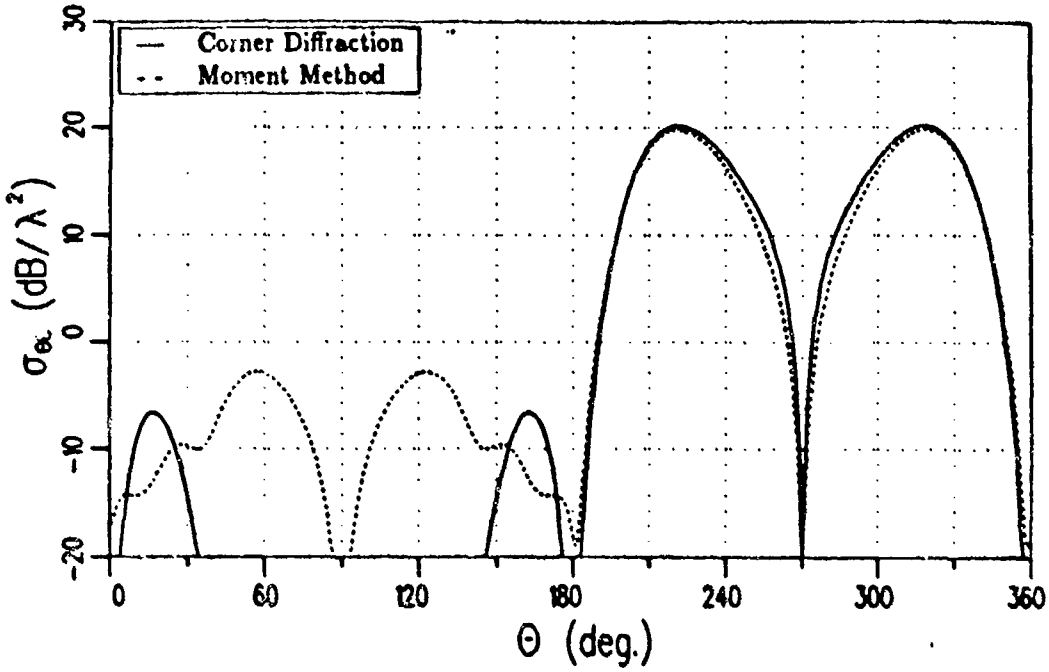

Figure 122: Co-polarized RCS in the $\phi = 45°$ plane of a 2λ square plate with a $\hat{\theta}^i$ polarized fixed source at $\theta^i = 45°$, $\phi^i = 45°$.

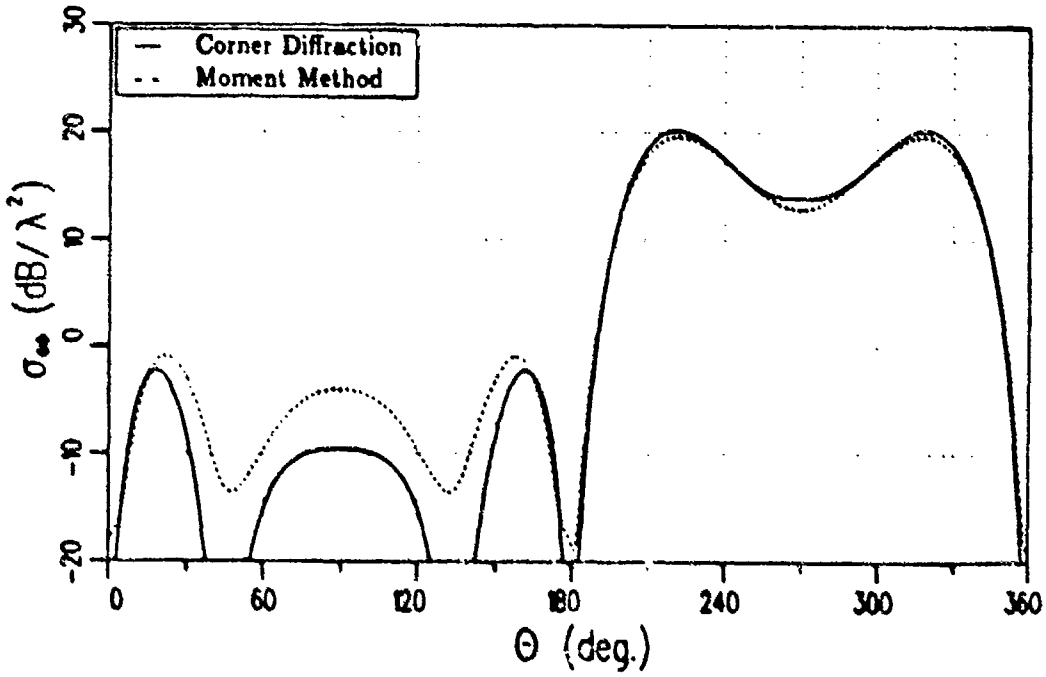

Figure 123: Co-polarized RCS in the $\phi = 45°$ plane of a 2λ square plate with a $\hat{\phi}^i$ polarized fixed source at $\theta^i = 45°$, $\phi^i = 45°$.

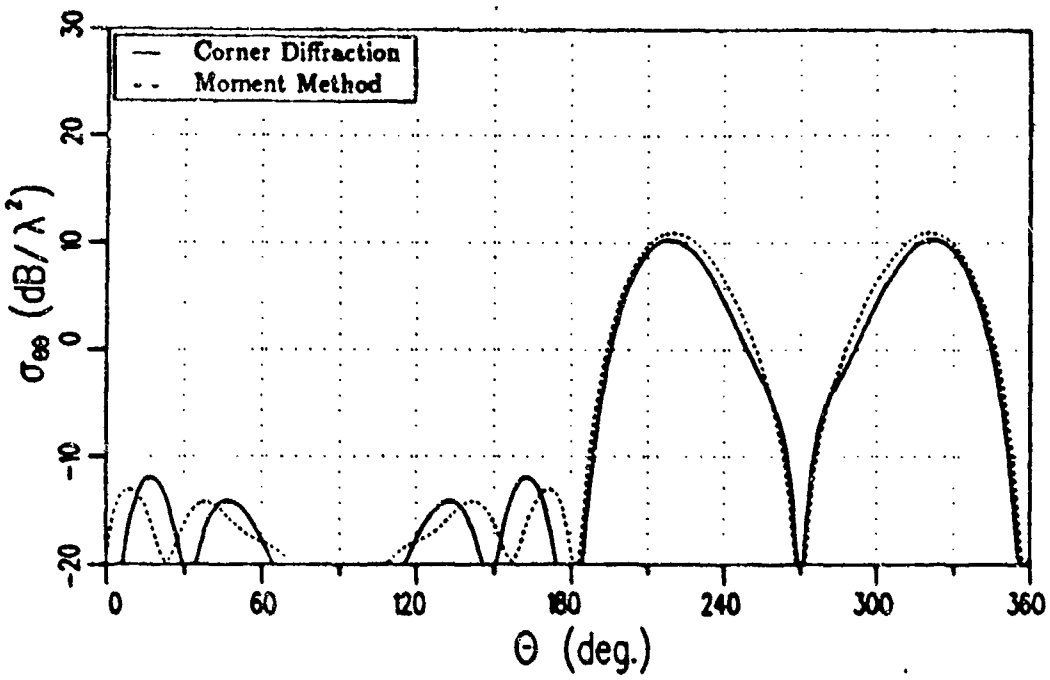

Figure 124: Co-polarized RCS in the $\phi = 75°$ plane of a 2λ square plate with a $\hat{\theta}^i$ polarized fixed source at $\theta^i = 45°$, $\phi^i = 45°$.

calculations for the co-polarized fields in Figures 124 and 125. Similarly the results for the cross-polarized fields are given in Figures 126 and 127. The results for the $\phi = 105°$ pattern cut are compared with Method of Moment calculations for the co-polarized fields in Figures 128 and 129. Similarly the results for the cross-polarized fields are given in Figures 130 and 131. The results for the $\phi = 135°$ pattern cut are compared with Method of Moment calculations for co-polarized fields in Figures 132 and 133. Similarly the results for the cross-polarized fields are given in Figures 134 and 135. The conclusions which may be drawn from this example are generally the same as those of the previous example. The new solution and the Method of Moments agree well overall. The region of space where the results are not in good agreement is close to the plane of the plate as in the previous example. Once again, it is speculated that these differences are due to higher order terms (double or triple diffraction).

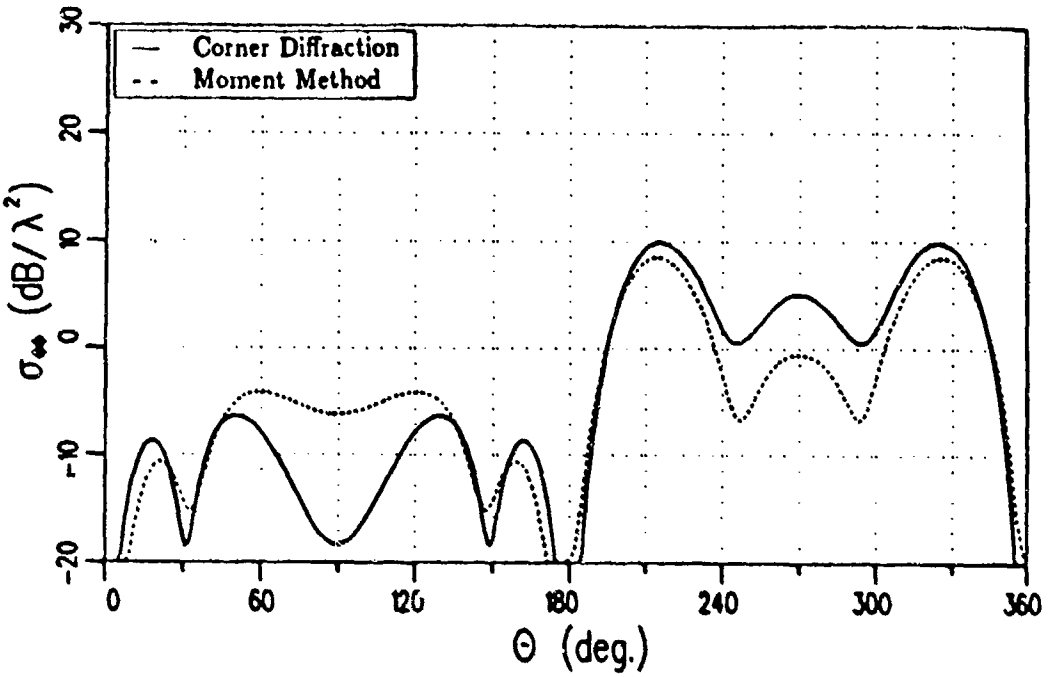

Figure 125: Co-polarized RCS in the $\phi = 75°$ plane of a 2λ square plate with a $\hat{\phi}^i$ polarized fixed source at $\theta^i = 45°$, $\phi^i = 45°$.

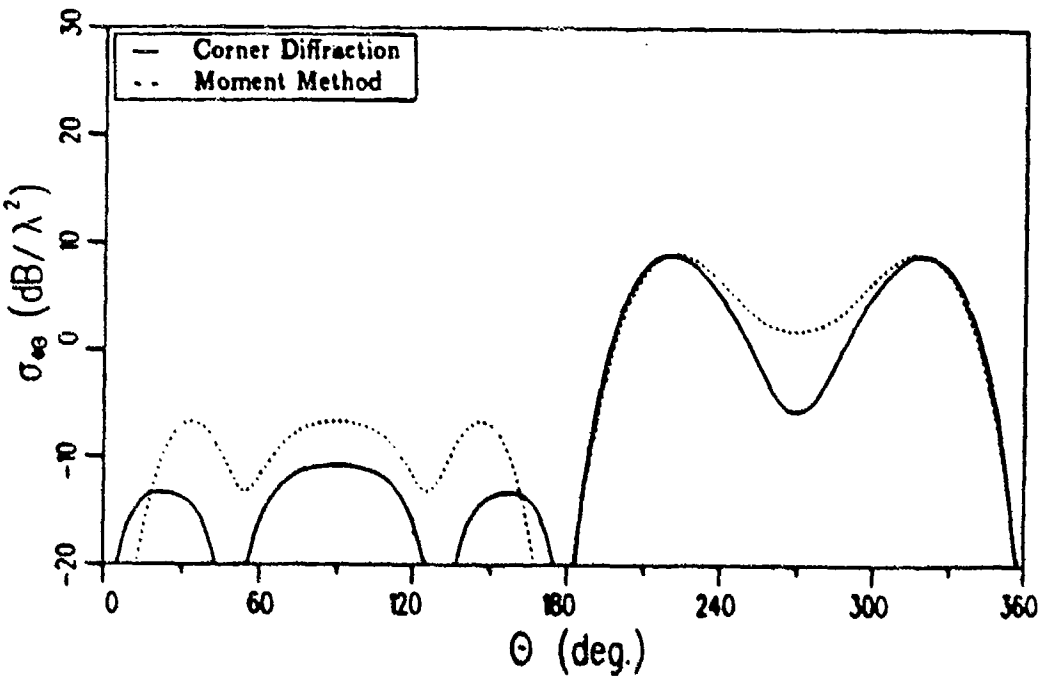

Figure 126: Cross-polarized RCS in the $\phi = 75°$ plane of a 2λ square plate with a $\hat{\theta}^i$ polarized fixed source at $\theta^i = 45°$, $\phi^i = 45°$.

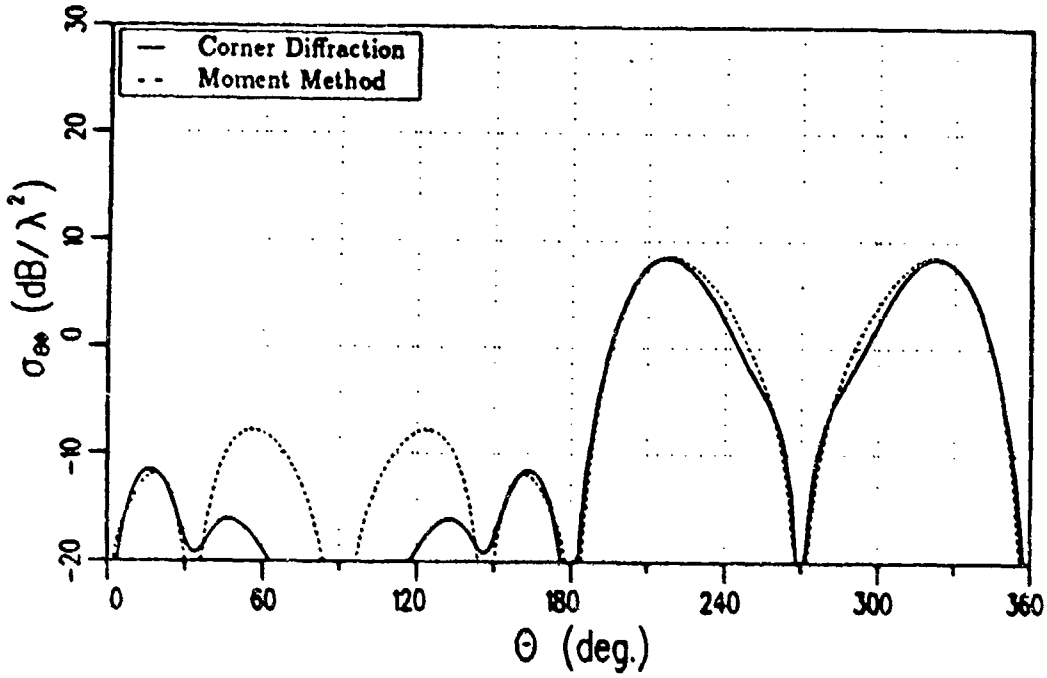

Figure 127: Cross-polarized RCS in the $\phi = 75°$ plane of a 2λ square plate with a $\hat{\phi}^i$ polarized fixed source at $\theta^i = 45°$, $\phi^i = 45°$.

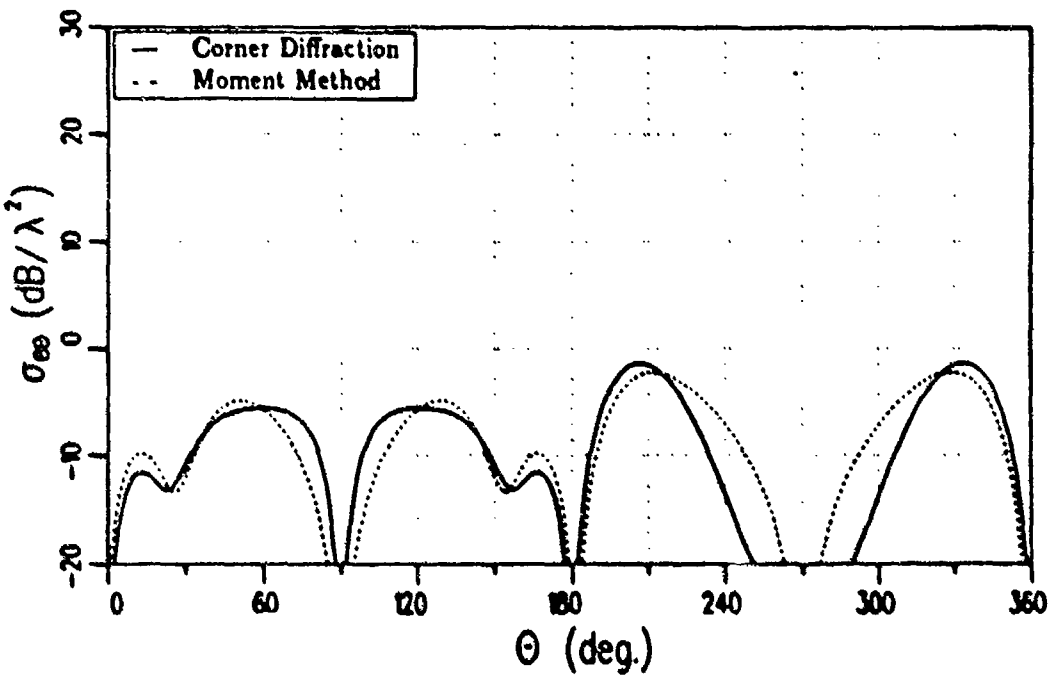

Figure 128: Co-polarized RCS in the $\phi = 105°$ plane of a 2λ square plate with a $\hat{\theta}^i$ polarized fixed source at $\theta^i = 45°$, $\phi^i = 45°$.

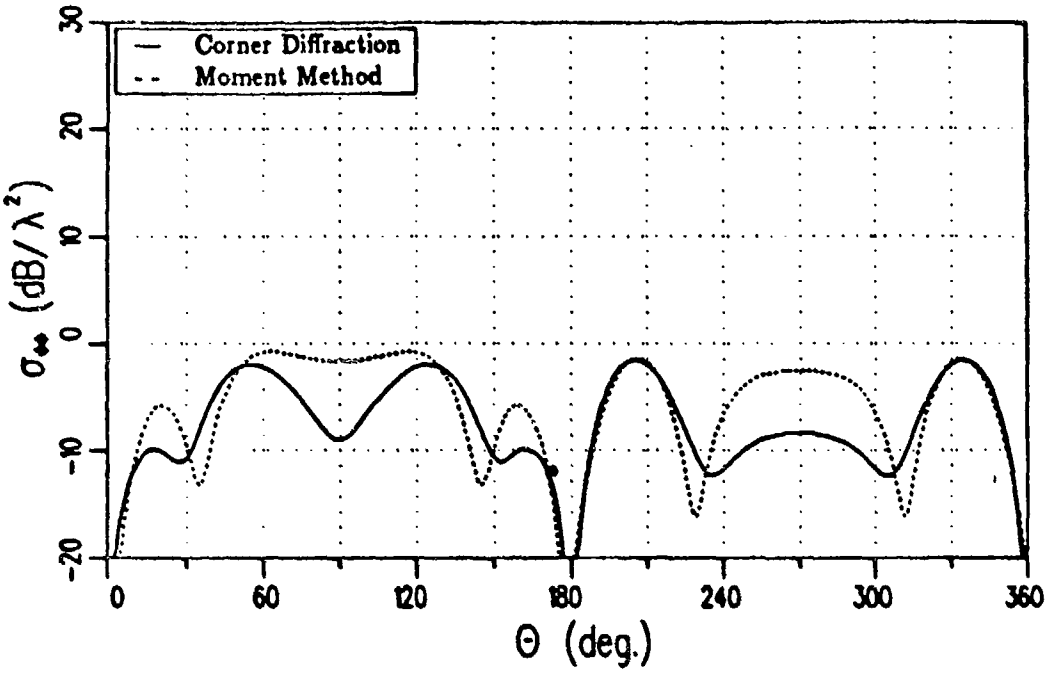

Figure 129: Co-polarized RCS in the $\phi = 105°$ plane of a 2λ square plate with a $\hat{\phi}^i$ polarized fixed source at $\theta^i = 45°$, $\phi^i = 45°$.

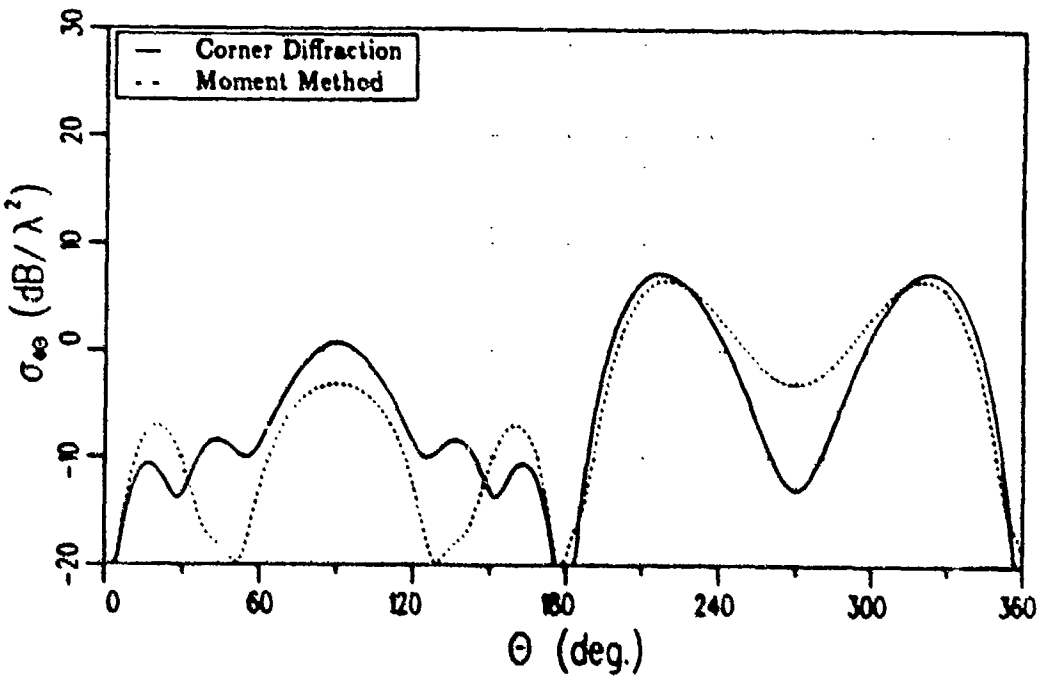

Figure 130: Cross-polarized RCS in the $\phi = 105°$ plane of a 2λ square plate with a $\hat{\theta}^i$ polarized fixed source at $\theta^i = 45°$, $\phi^i = 45°$.

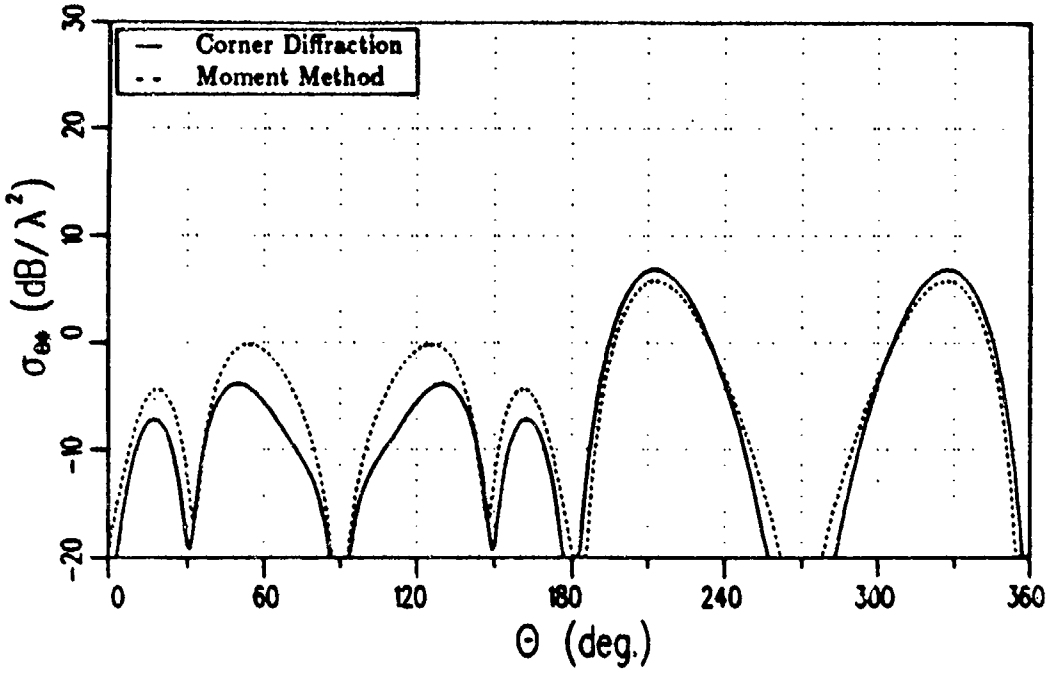

Figure 131: Cross-polarized RCS in the $\phi = 105°$ plane of a 2λ square plate with a $\hat{\phi}^i$ polarized fixed source at $\theta^i = 45°$, $\phi^i = 45°$.

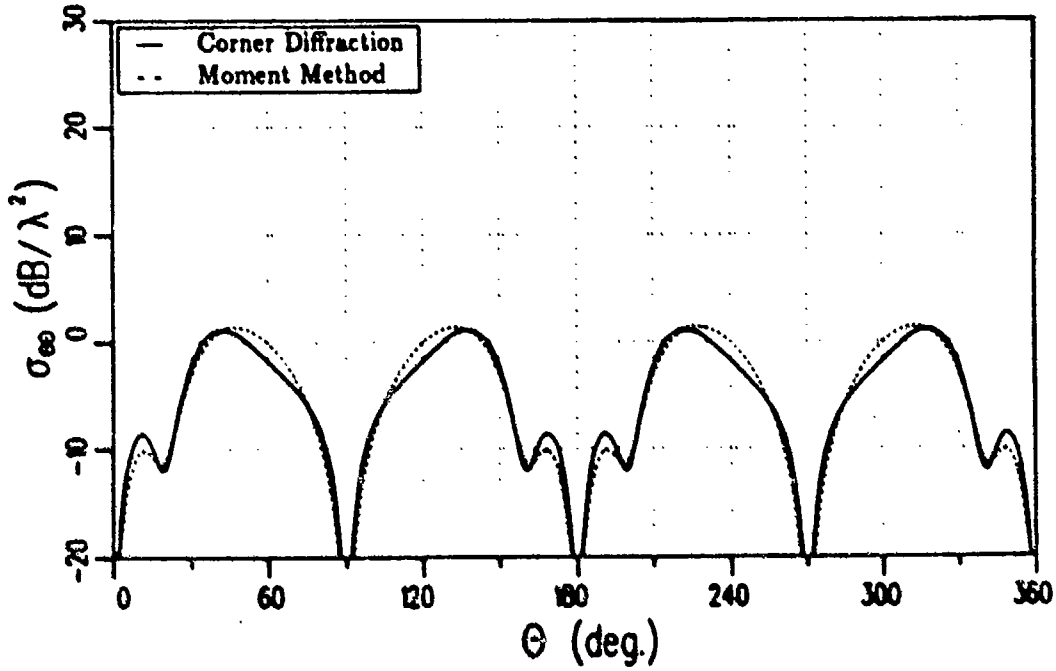

Figure 132: Co-polarized RCS in the $\phi = 135°$ plane of a 2λ square plate with a $\hat{\theta}^i$ polarized fixed source at $\theta^i = 45°$, $\phi^i = 45°$.

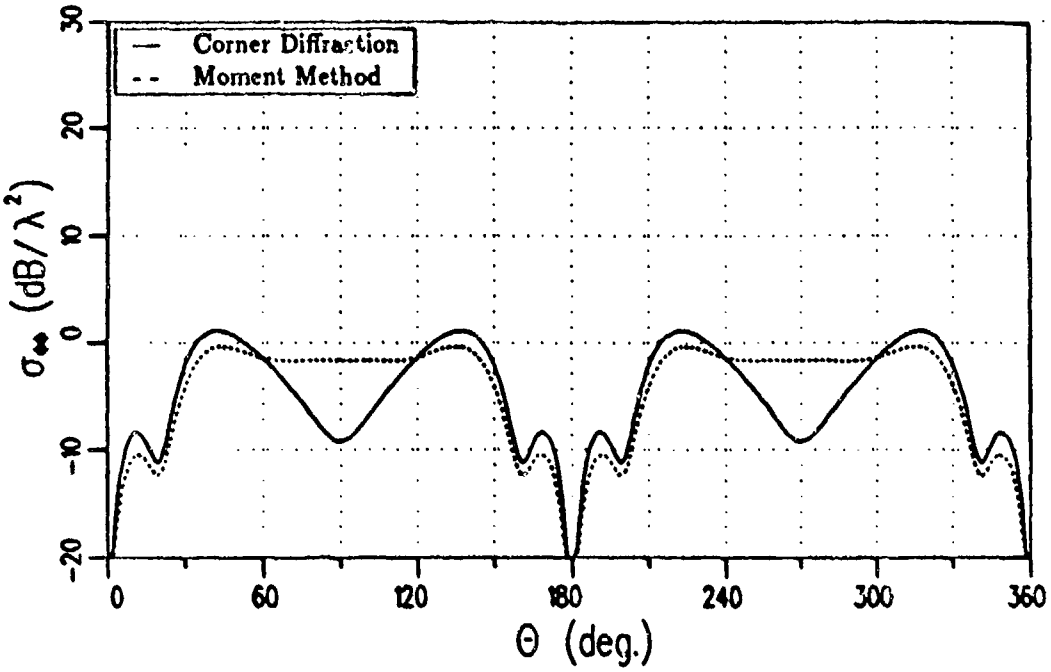

Figure 133: Co-polarized RCS in the $\phi = 135°$ plane of a 2λ square plate with a $\hat{\phi}^i$ polarized fixed source at $\theta^i = 45°$, $\phi^i = 45°$.

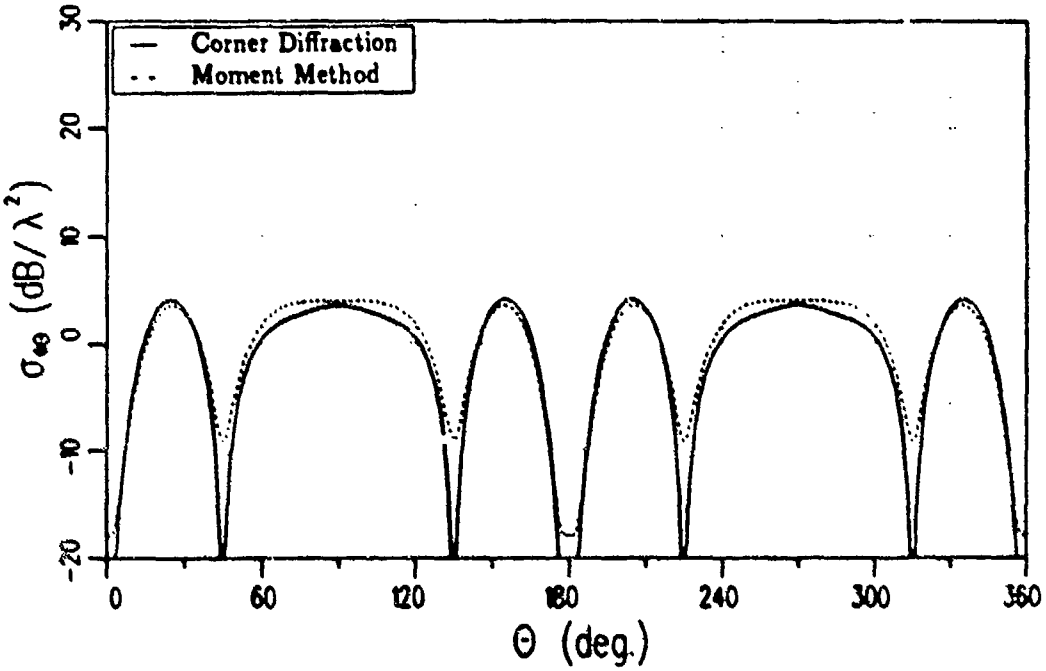

Figure 134: Cross-polarized RCS in the $\phi = 135°$ plane of a 2λ square plate with a $\hat{\theta}^i$ polarized fixed source at $\theta^i = 45°$, $\phi^i = 45°$.

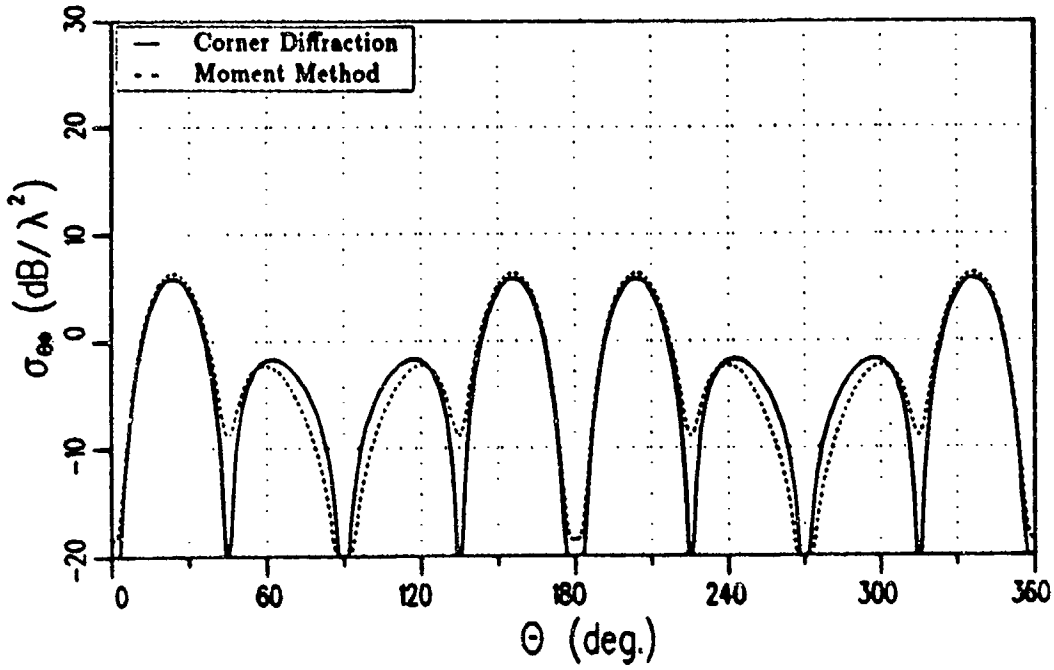

Figure 135: Cross-polarized RCS in the $\phi = 135°$ plane of a 2λ square plate with a $\hat{\phi}^i$ polarized fixed source at $\theta^i = 45°$, $\phi^i = 45°$.

5.4 Conclusion

Several examples have been given in this chapter comparing the new corner diffraction solution with previous high frequency solutions, Method of Moments solutions, and measurements. The first set of examples (Sections 5.3.1, 5.3.2, and 5.3.3) illustrate that the new solution gives essentially the same results as the previous equivalent currents for patterns in the principle plane of flat plates. The next set of examples for bistatic scattering (Sections 5.3.7 and 5.3.8) illustrate that the new solution agrees very well with Method of Moments results for a wide range of bistatic angles. Further most of the differences between the two are probably due to higher order terms.

CHAPTER VI

CONCLUSION

The new equivalent currents are valid for perfectly conducting structures with straight edges and flat faces. The contribution to the equivalent edge currents due to each face of the edge is given in Equations (3.38) and (3.40) where the angles are the edge fixed angles described in Figure 1 of Section 1.5.3. The total equivalent edge currents for the special case of a flat plate are given in Equations (3.47) and (3.49). The equivalent currents may be used to find the scattered field in the far zone when the object is illuminated by a plane wave.

A new corner diffraction coefficient for finite closed structures made up of perfectly conducting flat plates has been derived from the new equivalent currents. It has been demonstrated in Chapter V to agree reasonably well with both method of moments calculations and measurements, especially in regions of space where higher order diffracted fields are negligible. The contribution to the corner diffracted field from one face and one edge is given in Equation (A.2). For the special case of a flat plate the contribution due to each edge is given by Equation (A.3). The important properties of the solution are described in Chapter IV. The new corner diffraction coefficient may be used to calculate the far zone scattered field, to first order, from an object illuminated by a plane wave.

The new corner diffraction coefficients and equivalent currents have some disadvantages and some advantages over previous high frequency solutions. The main

disadvantages of the new solutions are that they are not valid in the near zone and some of the terms must be shadowed in a PO way. Since parts of the new solutions must be shadowed in a PO way it is unclear whether they can be combined with other UTD solutions to find the RCS of a general three-dimensional object. On the other hand it has been shown that the new corner diffraction coefficients and the new equivalent currents give the same results for first order diffraction. The new solution approaches a definite limit normal to the plate, reducing to the well known PO result in this direction. The new solution also agrees closely with Method of Moments solutions for bistatic scattering from a flat plate.

APPENDIX A

NEW CORNER DIFFRACTION COEFFICIENTS

The new corner diffraction coefficients are given in a form similar to previous expressions for diffraction coefficients:

$$\begin{bmatrix} E^c_\beta \\ E^c_\phi \end{bmatrix} = \begin{bmatrix} D^c_s & D^c_2 \\ 0 & D^c_h \end{bmatrix} \begin{bmatrix} E^i_{\beta'} \\ E^i_{\phi'} \end{bmatrix} \frac{e^{-jks}}{s} \tag{A.1}$$

$$D^c_{s,h,2} = \pm \frac{j}{4\pi k} \frac{1}{\cos\beta - \cos\beta'} \left[d^{LPO}_{s,h,2} + d^{UTD}_{s,h,2} - d^{PO}_{s,h,2} \right] \tag{A.2}$$

where the plus or minus sign is chosen depending on which endpoint contribution is being calculated. Section 3.5 discusses choosing the correct sign. The expressions for $d^{LPO}_{s,h,2}$, $d^{UTD}_{s,h,2}$, and $d^{PO}_{s,h,2}$ are given by(O-face contribution only)

$$\begin{aligned}
d^{LPO}_{\substack{s \\ h,2}} &= \frac{1}{2} U^i c_{\substack{s \\ h,2}}(\gamma, \phi') \left\{ \left[\cot\left(\frac{\pi - (\gamma - \phi')}{4} \right) - \cot\left(\frac{\pi + (\gamma - \phi')}{4} \right) \right] \right. \\
&\mp \left. \left[\cot\left(\frac{\pi - (\gamma + \phi')}{4} \right) - \cot\left(\frac{\pi + (\gamma + \phi')}{4} \right) \right] \right\} \\
d^{UTD}_{\substack{s \\ h,2}} &= \frac{1}{n} c_{\substack{s \\ h,2}}(\alpha, \pi - \alpha) \left[\cot\left(\frac{\pi - (\alpha - \phi')}{2n} \right) \right. \\
&\mp \left. \cot\left(\frac{\pi - (\alpha + \phi')}{2n} \right) \right] \\
d^{PO}_{\substack{s \\ h,2}} &= \frac{1}{2} U^i c_{\substack{s \\ h,2}}(\alpha, \phi') \left\{ \left[\cot\left(\frac{\pi - (\alpha - \phi')}{4} \right) - \cot\left(\frac{\pi + (\alpha - \phi')}{4} \right) \right] \right. \\
&\mp \left. \left[\cot\left(\frac{\pi - (\alpha + \phi')}{4} \right) - \cot\left(\frac{\pi + (\alpha + \phi')}{4} \right) \right] \right\}
\end{aligned}$$

$$
\begin{aligned}
c_s(\delta,\epsilon) &= -\frac{\sin\beta}{\sin\beta'} \\
c_h(\delta,\epsilon) &= \frac{\sin\phi}{\sin\delta} \\
c_2(\delta,\epsilon) &= -\frac{\sin\beta}{\sin\delta}\left(\cot\beta\cos\phi + \cot\beta'\cos\epsilon\right) \\
\cos\gamma &= \frac{\sin\beta\cos\phi}{\sin\beta'} + \frac{(\cos\beta-\cos\beta')^2}{\sin\beta'(\sin\beta\cos\phi+\sin\beta'\cos\phi')} \\
\cos\alpha &= \frac{\sin\beta\cos\phi}{\sin\beta'} + \frac{(\cos\beta-\cos\beta')\cos\beta'}{\sin^2\beta'} \\
\cos^{-1}\mu &= -j\ln\left(\mu+\sqrt{\mu^2-1}\right) \\
\sqrt{\mu^2-1} &= \begin{cases} -\left|\sqrt{\mu^2-1}\right| & \mu<-1 \\ j\left|\sqrt{1-\mu^2}\right| & -1\le\mu\le 1 \\ \left|\sqrt{\mu^2-1}\right| & \mu>1 \end{cases} \\
U^i &= \begin{cases} 0 & ,\pi-\phi'<0 \\ 1 & ,\pi-\phi'>0 \end{cases}
\end{aligned}
$$

where the + sign is associated with d_h^{LPO}, d_2^{LPO}, d_h^{UTD}, d_2^{UTD}, d_h^{PO}, and d_2^{PO} while the − sign is associated with the d_s^{LPO}, d_s^{UTD}, and d_s^{PO} terms. For the special case of a flat plate ($n=2$) the contribution from both faces may be found using

$$
\begin{aligned}
d_{\substack{s\\h,2}}^{LPO} &= \frac{1}{2}S^i c_{\substack{s\\h,2}}(\gamma,\phi')\left\{\left[\cot\left(\frac{\pi-(\gamma-\phi')}{4}\right)-\cot\left(\frac{\pi+(\gamma-\phi')}{4}\right)\right]\right. \qquad \text{(A.3)} \\
&\mp \left.\left[\cot\left(\frac{\pi-(\gamma+\phi')}{4}\right)-\cot\left(\frac{\pi+(\gamma+\phi')}{4}\right)\right]\right\} \\
d_{\substack{s\\h,2}}^{UTD} &= \frac{1}{n}c_{\substack{s\\h,2}}(\alpha,\pi-\alpha)\left\{\left[\cot\left(\frac{\pi-(\alpha-\phi')}{4}\right)+\cot\left(\frac{\pi+(\alpha-\phi')}{4}\right)\right]\right. \\
&\mp \left.\left[\cot\left(\frac{\pi-(\alpha+\phi')}{4}\right)+\cot\left(\frac{\pi+(\alpha+\phi')}{4}\right)\right]\right\} \\
d_{\substack{s\\h,2}}^{PO} &= \frac{1}{2}S^i c_{\substack{s\\h,2}}(\alpha,\phi')\left\{\left[\cot\left(\frac{\pi-(\alpha-\phi')}{4}\right)-\cot\left(\frac{\pi+(\alpha-\phi')}{4}\right)\right]\right.
\end{aligned}
$$

$$\mp \left[\cot\left(\frac{\pi-(\alpha+\phi')}{4}\right) - \cot\left(\frac{\pi+(\alpha+\phi')}{4}\right)\right]\Bigg\}$$

$$S^i = \begin{cases} -1 & ,\pi-\phi' < 0 \\ 1 & ,\pi-\phi' > 0 \end{cases} \tag{A.4}$$

where γ, α, and the other variables have been defined previously.

APPENDIX B

EQUIVALENT CURRENTS FOR EDGE ON INCIDENCE

The steps required to show that the new equivalent currents are finite for edge on incidence ($\beta' \to 0$ or $\beta' \to \pi$) are outlined in this appendix. Michaeli [14] gives a very brief outline of the procedure required to find the fringe equivalent currents as edge on incidence is approached in the limit.

Showing that the LPO and PO components of the equivalent currents are finite for edge on incidence is fairly trivial, and is only briefly described here. Using the form of the LPO components given in Equations (3.23) and (3.24) and the form of the PO components given in Equations (3.29) and (3.30), along with the relations

$$E_t^i \propto E_o^i \sin\beta' \tag{B.1}$$

$$H_t^i \propto H_o^i \sin\beta' \tag{B.2}$$

where E_o^i and H_o^i are the magnitude of the incident electric and magnetic fields respectively, it may be easily shown that both equivalent currents approach finite limits as $\beta' \to 0$ or $\beta' \to \pi$. It has been assumed that the face under consideration is being illuminated by the incident field, otherwise the LPO and PO components of the equivalent currents are identically zero.

Finding the UTD components of the equivalent currents as edge on incidence is approached is more complicated. First an appoximation to the parameter α must be found for $\sin\beta' \to 0$. Using Equation (3.45) and the assumption $\sin\beta' \ll \cos\beta'$

results in

$$\alpha \approx \pi + j2\ln\left(\sin\beta'\right) \tag{B.3}$$

which leads to

$$\sin\alpha \approx \frac{j}{2}\frac{1}{\sin^2\beta'} \tag{B.4}$$

$$\sin\left(\frac{\pi-\alpha}{n}\right) \approx \frac{j}{2}\sin^{-\frac{2}{n}}\beta' \tag{B.5}$$

$$\cos\left(\frac{\pi-\alpha}{n}\right) \approx \frac{1}{2}\sin^{-\frac{2}{n}}\beta' \tag{B.6}$$

Using Equations (B.1), (B.2), (B.4), (B.5), and (B.6) in Equations (3.27) and (3.28) and then letting $\beta' \to 0$ or letting $\beta' \to \pi$ shows that M^{UTD} and I_e^{UTD} are finite for edge on incidence. The contribution from both faces must be included to show that the other component of the electric equivalent current (I_m^{UTD}) is finite for edge on incidence. The contribution to the equivalent currents from the N-face is found by replacing $\hat{t}$ with $-\hat{t}$, β' with $\pi-\beta'$, ϕ' with $n\pi-\phi'$, β with $\pi-\beta$, and ϕ with $n\pi-\phi$ in the expressions for the contribution to the equivalent currents from the O-face. For I_m^{UTD} the resulting expression for the contribution from both faces is given by

$$\begin{aligned} I_m^{UTD} &= \frac{2j}{k\sin\beta'} \\ &\times \left\{\frac{1/n(\cos\alpha_o\cot\beta' - \cot\beta\cos\phi)}{\cos(\phi'/n) - \cos[(\pi-\alpha_o)/n]}\frac{\sin[(\pi-\alpha_o)/n]}{\sin\alpha_o}H_t^i\right. \\ &- \left.\frac{1/n(-\cos\alpha_n\cot\beta' - \cot\beta\cos(n\pi-\phi))}{\cos[(n\pi-\phi')/n] - \cos[(\pi-\alpha_n)/n]}\frac{\sin[(\pi-\alpha_n)/n]}{\sin\alpha_n}\left(-H_t^i\right)\right\} \end{aligned} \tag{B.7}$$

where all of the angles are measured with respect to the edge fixed coordinate system associated with the O-face. For $\sin\beta' \to 0$ it is easily shown that $\alpha_n \approx \alpha_o$ and the expressions for both α_n and α_o are the same as the expression for α given in Equation (B.3). Therefore combining the above with Equations (B.2), (B.4),

(B.5), and (B.6) in Equation (B.7) one obtains an expression for I_m^{UTD} which is valid for regions of space where $\sin\beta'$ is small. After placing the entire expression over a common denominator, the limit taken as edge on incidence is approached is finite.

All of the equivalent currents are finite in the limit as edge on incidence is approached (except for the forward scatter direction). In practice this means that as long as the source is kept reasonably far away from edge on incidence the computer should be able to take the limit numerically. The distance from edge on incidence that must be maintained depends on the precision of the computer and which form of the equivalent currents are used. In this regard considerable errors may accur in finding I_m^{UTD} if each face is considered separately, since the contribution to I_m^{UTD} from each face becomes infinte as edge on incidence is approached (although the sum of the contributions from the two faces remains finite).

APPENDIX C

RCS FOR NORMAL INCIDENCE ON A RECTANGULAR FLAT PLATE

The RCS of a rectangular flat plate shown in Figure 136 is found using the new equivalent currents. The field radiated by the equivalent currents on an arbitrarily oriented finite straight edge is found first to simplify later calculations. The finite straight edge is shown in Figure 137 along with the edge fixed coordinates required to define the equivalent currents. The currents are substituted into the far zone radiation integral

$$\begin{aligned}\vec{E}^s &= \frac{jk}{4\pi}\left\{Z_0\,\hat{s}\times\hat{s}\times\int_{-\frac{a}{2}}^{\frac{a}{2}}\left[\hat{z}I(z')\frac{e^{-jkR}}{R}\right]dz'\right.\\ &+ \left.\hat{s}\times\int_{-\frac{a}{2}}^{\frac{a}{2}}\left[\hat{z}M\frac{e^{-jkR}}{R}\right]dz'\right\} \qquad \text{(C.1)}\end{aligned}$$

Doing the integration in closed form (only the phase of E_t^i and H_t^i are functions of z') results in

$$\begin{aligned}\vec{E}^s &= -\frac{1}{\pi}\frac{\sin\left[k\frac{a}{2}\left(\cos\beta-\cos\beta'\right)\right]}{k\sin\beta\sin\beta'\left(\cos\beta-\cos\beta'\right)}\\ &\times\left\{\hat{\beta}\left(G_{ie}E_{t0}^i+G_{im}Z_0H_{t0}^i\right)-\hat{\phi}G_mZ_0H_{t0}^i\right\} \qquad \text{(C.2)}\end{aligned}$$

where the relations between the equivalent currents and the functions G_{ie}, G_{im}, and G_m are given in Equation (3.53) and Equation (3.54), while E_{t0}^i and H_{t0}^i are the complex components of the incident electric and magnetic fields tangent to the edge with the phase reference taken to be at the midpoint of the edge.

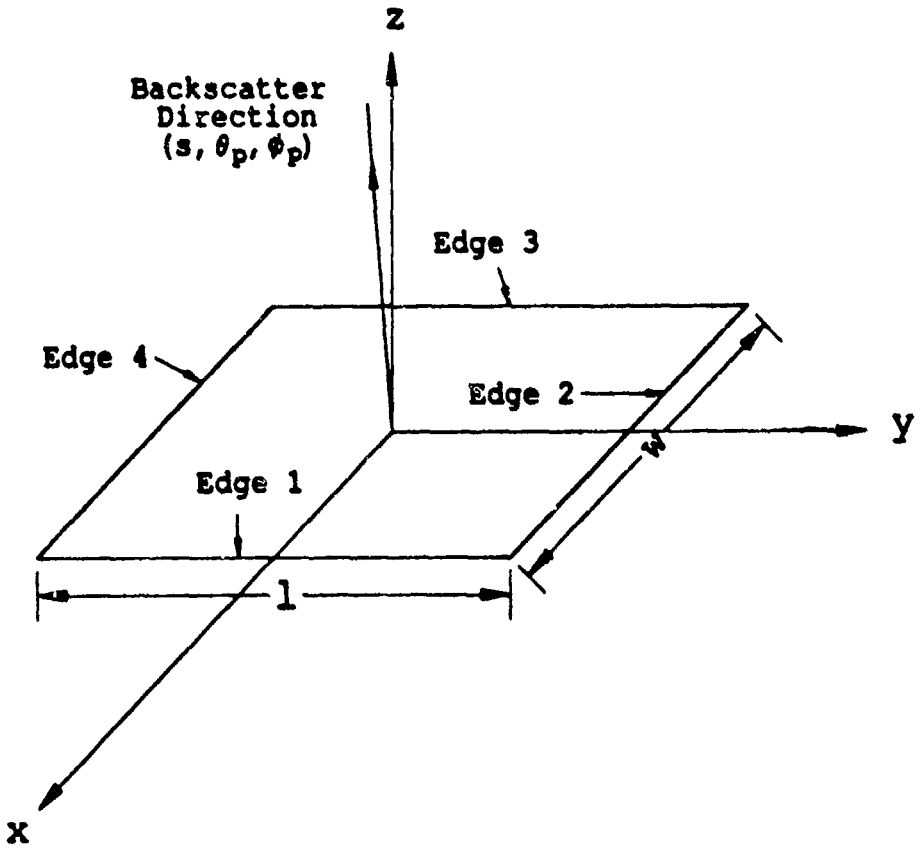

Figure 136: Flat plate for RCS calculation with normal incidence.

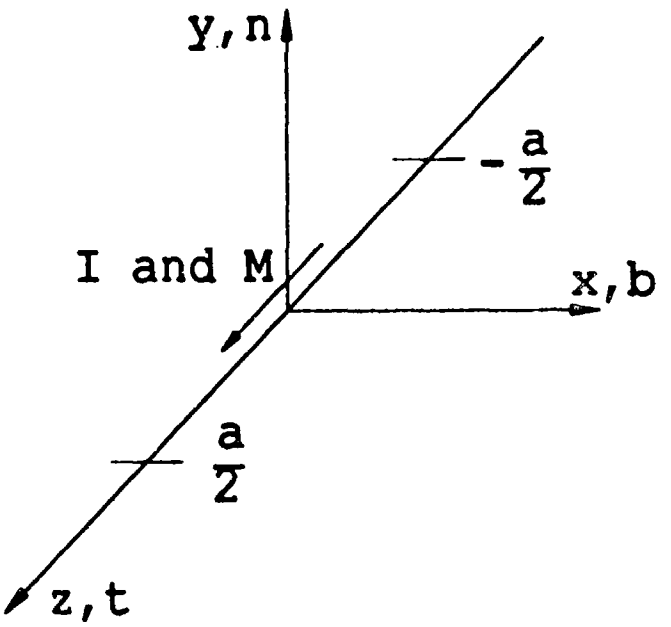

Figure 137: Equivalent currents on a finite straight edge.

Using the above results carefully will allow the RCS of the plate to be found for normal incidence. The edge fixed coordinates for each edge of the rectangular plate are shown in Figure 138 along with their relationship to the pattern coordinates. The relationships between the pattern coordinates and the edge fixed coordinates that will be used later are

$$\begin{aligned}
\cos\beta_1 &= \sin\theta_p \sin\phi_p \\
\sin\beta_1 \cos\phi_1 &= -\sin\theta_p \cos\phi_p \\
\sin\beta_1 \sin\phi_1 &= \cos\theta_p \\
\cos\beta_2 &= -\sin\theta_p \cos\phi_p \\
\sin\beta_2 \cos\phi_2 &= -\sin\theta_p \sin\phi_p \\
\sin\beta_2 \sin\phi_2 &= \cos\theta_p
\end{aligned}$$

The expression for the total scattered field may be obtained from a superposition

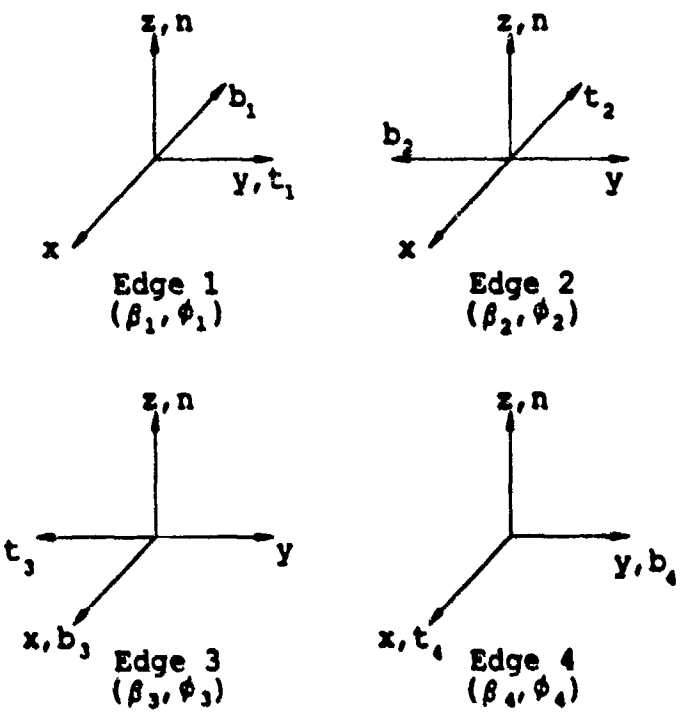

Figure 138: Relationship between the edge fixed coordinates and the pattern coordinates.

of the scattered field due to each edge. The phase reference is placed at the origin of the pattern coordinate system. Using the expression from Equation (C.2) for the scattered field from each edge (in the case of backscatter, $\beta' = \pi - \beta$) results in

$$\begin{aligned}
\vec{E}^s &= -\frac{1}{\pi}\frac{e^{-jks}}{s}\Sigma_{n=1,3}\frac{\sin(kw\cos\beta_n)}{2k\sin^2\beta_n\cos\beta_n} \\
&\times \left\{\hat{\beta}_n\left(G_{ie}(\beta_n,\phi_n)E^i_{tn0} + G_{im}(\beta_n,\phi_n)Z_0H^i_{tn0}\right)\right. \\
&- \left.\hat{\phi}_nG_m(\beta_n,\phi_n)Z_0H^i_{tn0}\right\}e^{i_1jk\frac{\ell}{2}\sin\theta_p\cos\phi_p} \\
&- \frac{1}{\pi}\frac{e^{-jks}}{s}\Sigma_{n=2,4}\frac{\sin(k\ell\cos\beta_n)}{2k\sin^2\beta_n\cos\beta_n} \\
&\times \left\{\hat{\beta}_n\left(G_{ie}(\beta_n,\phi_n)E^i_{tn0} + G_{im}(\beta_n,\phi_n)Z_0H^i_{tn0}\right)\right. \\
&- \left.\hat{\phi}_nG_m(\beta_n,\phi_n)Z_0H^i_{tn0}\right\}e^{i_2jk\frac{w}{2}\sin\theta_p\cos\phi_p} \qquad \text{(C.3)}
\end{aligned}$$

where

$$\begin{aligned}
i_1 &= (-1)^{\frac{1}{2}(n-1)} \\
i_2 &= (-1)^{\frac{1}{2}(n-2)}
\end{aligned}$$

where the exponential factors that have been added shift the phase references from the center of each edge to the center of the plate and E^i_{tn0} (H^i_{tn0}) is the component of the incident electric (magnetic) field tangent to edge n at the center of the edge.

Simply plugging $\theta_p = 0$ ($\beta_n, \phi_n = \pi/2$, $n = 1,2,3,4$) in Equation (C.3) will not work since some of the terms become infinite here. However if the limit is taken as θ_p approaches zero, a finite result may be obtained. The algebra required in taking the limit is fairly complicated, so to simplify the calculations the contribution from each component of the current (LPO, UTD, and PO) is calculated separately, and then the contributions are summed to give the total scattered field.

$$\vec{E}^s = \vec{E}^{LPO} + \vec{E}^{UTD} - \vec{E}^{PO} \qquad (C.4)$$

The contribution from the LPO terms is found first. Letting

$$\vec{E}^i = \hat{x}E^i_{x0} + \hat{y}E^i_{y0} \quad \vec{H}^i = \hat{x}H^i_{x0} + \hat{y}H^i_{y0} \tag{C.5}$$

be the incident field at the origin (the center of the plate). Using

$$G^{LPO}_{ie}(\beta,\phi) = \frac{1}{2}\frac{\sin^2\beta\sin\phi\cos\phi}{(\sin^2\beta\cos^2\phi+\cos^2\beta)} \tag{C.6}$$

$$G^{LPO}_{im}(\beta,\phi) = 0 \tag{C.7}$$

$$G^{LPO}_{m}(\beta,\phi) = -G^{LPO}_{ie}(\beta,\phi) \tag{C.8}$$

along with

$$E^i_{t10} = E_{y0}e^{jk\frac{\ell}{2}\sin\theta_p\cos\phi_p} \tag{C.9}$$

$$H^i_{t10} = H_{y0}e^{jk\frac{\ell}{2}\sin\theta_p\cos\phi_p} \tag{C.10}$$

$$E^i_{t30} = -E_{y0}e^{-jk\frac{\ell}{2}\sin\theta_p\cos\phi_p} \tag{C.11}$$

$$H^i_{t30} = -H_{y0}e^{-jk\frac{\ell}{2}\sin\theta_p\cos\phi_p} \tag{C.12}$$

$$H^i_{t20} = -H_{x0}e^{jk\frac{w}{2}\sin\theta_p\cos\phi_p} \tag{C.13}$$

$$E^i_{t40} = E_{x0}e^{-jk\frac{w}{2}\sin\theta_p\cos\phi_p} \tag{C.14}$$

$$H^i_{t40} = H_{x0}e^{-jk\frac{w}{2}\sin\theta_p\cos\phi_p} \tag{C.15}$$

$$\begin{aligned}
\hat{\beta}_3 &= -\hat{\beta}_1 \quad \hat{\beta}_4 = -\hat{\beta}_2 \\
\beta_3 &= \pi - \beta_1 \quad \phi_3 = \pi - \phi_1 \; ; \; (\phi_1 \approx \frac{\pi}{2}) \\
\beta_4 &= \pi - \beta_2 \quad \phi_4 = \pi - \phi_2 \; ; \; (\phi_2 \approx \frac{\pi}{2})
\end{aligned}$$

(skipping the details) results in

$$\vec{E}^{LPO} = -\frac{jk}{2\pi}(w\ell)\frac{e^{-jks}}{s}\vec{E}^i \tag{C.16}$$

As should be expected, the same result would be obtained using the PO currents in the surface integral.

Using the same procedure for the UTD components of the currents, which are written in the same form as in Section 4.7,

$$G_{ie}^{UTD}(\beta,\phi) = \frac{1}{2}\frac{\sqrt{2}\sin\beta\sin\frac{\phi}{2}\sqrt{\sin^2\beta(1-\cos\phi)+2\cos^2\beta}}{(\sin^2\beta\cos\phi-\cos^2\beta)} \tag{C.17}$$

$$G_{im}^{UTD}(\beta,\phi) = -\sin\beta\cos\beta\cos\frac{\phi}{2}\sqrt{\frac{2}{\sin^2\beta(1-\cos\phi)+2\cos^2\beta}} \tag{C.18}$$

$$G_{m}^{UTD}(\beta,\phi) = -\frac{1}{2}\frac{\sin^3\beta\cos\frac{\phi}{2}}{(\sin^2\beta\cos\phi-\cos^2\beta)} \times \sqrt{\frac{2}{\sin^2\beta(1-\cos\phi)+2\cos^2\beta}}. \tag{C.19}$$

Plugging Equations (C.9) through (C.15) and Equations (C.17) through (C.19) in Equation (C.3) and taking the limit as $\theta_p \to 0$ results in

$$\vec{E}^{UTD} = -\frac{jk}{\pi}(w\ell)\frac{e^{-jks}}{s}\vec{E}^i + \frac{1}{2\pi}(w\tan^2\phi_p + \ell\cot^2\phi_p)\frac{e^{-jks}}{s}\vec{E}^i \tag{C.20}$$

Finally the contribution from the PO components of the currents is found. Using the form of the currents given in Section 4.7

$$G_{ie}^{PO}(\beta,\phi) = \frac{1}{2}\frac{\sin^2\beta\sin\phi}{(\sin^2\beta\cos\phi-\cos^2\beta)} \tag{C.21}$$

$$G_{im}^{PO}(\beta,\phi) = 0 \tag{C.22}$$

$$G_{m}^{PO}(\beta,\phi) = -G_{ie}^{PO}(\beta,\phi) \tag{C.23}$$

Plugging Equations (C.9) through (C.15) and Equations (C.21) through (C.23) into Equation (C.3) results in

$$\vec{E}^{PO} = -\frac{jk}{\pi}(w\ell)\frac{e^{-jks}}{s}\vec{E}^i + \frac{1}{2\pi}(w\tan^2\phi_p + \ell\cot^2\phi_p)\frac{e^{-jks}}{s}\vec{E}^i \tag{C.24}$$

which is the same as $\vec{E}^{UTD}$.

Combining the results of Equations (C.16), (C.20), and (C.24) gives the total scattered field

$$\vec{E}^s = -\frac{jk}{2\pi}(w\ell)\frac{e^{-jks}}{s}\vec{E}^i \tag{C.25}$$

or converting it to RCS

$$\begin{aligned}
\sigma_{co-pol} &= 4\pi\frac{(w\ell)^2}{\lambda^2} \\
\sigma_{co-pol} &= 4\pi\frac{A^2}{\lambda^2} \\
\sigma_{x-pol} &= 0
\end{aligned}$$

Notice that the fringe components (UTD-PO) cancel for backscatter at normal incidence, and the field is determined by the LPO component of the currents (which predict the same fields as the PO surface integral).

APPENDIX D

AN EQUIVALENT EXPRESSION FOR THE EQUIVALENT CURRENTS

The expressions for the equivalent currents in Equations (4.16) and (4.18) are derived here from previous expressions in Buyukdura [22] and Michaeli [13]. Since the expressions are quite complicated each of the three components (LPO, UTD, and PO) will be derived separately.

Starting with the LPO components of the currents from Buyukdura [22].

$$I^{LPO} = -\frac{2Y_0}{jk}E_t^i\frac{\sin\phi'}{\sin\beta'}C + \frac{2}{jk}H_t^i(\cot\beta\cos\phi + \cot\beta'\cos\phi')C \qquad \text{(D.1)}$$

$$M^{LPO} = \frac{2Z_0}{jk}H_t^i\frac{\sin\phi}{\sin\beta}C \qquad \text{(D.2)}$$

where

$$C = \frac{\sin\beta\cos\phi + \sin\beta'\cos\phi'}{\left[(\cos\beta - \cos\beta')^2 + (\sin\beta\cos\phi + \sin\beta'\cos\phi')^2\right]} \qquad (D.3)$$

Further separating the equivalent electric current into I_e^{LPO} and I_m^{LPO} components results in

$$I_e^{LPO} = -\frac{2Y_0}{jk}E_t^i\frac{\sin\phi'}{\sin\beta'}\frac{1}{\left[\frac{(\cos\beta-\cos\beta')^2}{\sin\beta\cos\phi+\sin\beta'\cos\phi'} + (\sin\beta\cos\phi + \sin\beta'\cos\phi')\right]} \qquad (D.4)$$

combining with

$$\cos\psi_1 = \sin\theta_1\sin\beta\cos\phi + \cos\theta_1\cos\beta \qquad \text{(D.5)}$$

$$\cos\psi_1' = \sin\theta_1 \sin\beta' \cos\phi' + \cos\theta_1 \cos\beta' \tag{D.6}$$

$$\cot\theta_1 = \frac{\cos\beta - \cos\beta'}{\sin\beta\cos\phi + \sin\beta'\cos\phi'} \tag{D.7}$$

results in

$$I_e^{LPO} = -\frac{2Y_0}{jk} E_t^i \frac{\sin\phi' \sin\theta_1}{\sin\beta'} \frac{1}{\cos\psi_1 + \cos\psi_1'} \tag{D.8}$$

Using a trigonometric identity from Section 3.4 results in

$$\begin{aligned} I_e^{LPO} &= \frac{jY_0}{2k} E_t^i \frac{\sin\phi' \sin\theta_1}{\sin\beta' \sin\psi_1'} \\ &\left\{ \left[\cot\left(\frac{\pi - (\psi_1 - \psi_1')}{4}\right) - \cot\left(\frac{\pi + (\psi_1 - \psi_1')}{4}\right) \right] \right. \\ &- \left. \left[\cot\left(\frac{\pi - (\psi_1 + \psi_1')}{4}\right) - \cot\left(\frac{\pi + (\psi_1 + \psi_1')}{4}\right) \right] \right\} \end{aligned}$$

The expression here is the same as that given in Section 4.7 except for the step function which is implied in this expression since Buyukdura assumes O-face incidence. Using a similar procedure the expressions in Section 4.7 for I_m^{LPO} and M^{LPO} may be derived.

Next the expression for I_m^{UTD} is developed. Starting with the expression for I_m^{UTD} derived by Buyukdura [22].

$$\begin{aligned} I_m^{UTD} &= \frac{2j}{k} H_t^i \frac{\sin\beta' \cos\frac{\phi'}{2}}{\sin\beta'(\sin\beta\cos\phi + \sin\beta'\cos\phi') + (\cos\beta - \cos\beta')\cos\beta'} \\ &\times \left[\cot\beta' \left(\sin\beta\cos\phi + (\cos\beta - \cos\beta')\cot\beta'\right) - \sin\beta'\cot\beta\cos\phi\right] \\ &\times \sqrt{\frac{2}{\sin\beta'(\sin\beta\cos\phi + \sin\beta'\cos\phi') - (\cos\beta - \cos\beta')\cos\beta'}} \end{aligned} \tag{D.9}$$

(although the terms are not separated in this way by Buyukdura [22], it can be shown that the part of I given here corresponds to I_m^{UTD})

Using

$$\cos\psi_2 = \cos\beta' \tag{D.10}$$

$$\cos\psi_2 = \sin\theta_2 \sin\beta \cos\phi + \cos\theta_2 \cos\beta \tag{D.11}$$

$$\cos\psi_2' = \sin\theta_2 \sin\beta' \cos\phi' + \cos\theta_2 \cos\beta' \tag{D.12}$$

results in

$$I_m^{UTD} = -\frac{2}{jk} H_t^i \frac{\sin\beta' \cos\frac{\phi'}{2}}{\cos\psi_2 + \cos\psi_2'} i_m \sqrt{\frac{2}{1-\cos\psi_2}} \qquad (D.13)$$

where

$$i_m = \frac{\cot\beta'}{\sin\beta'}\left[\cos\psi_2 - \cos^2\beta'\right] - \frac{\sin\beta'\cos\beta\cos\phi}{\sin\beta} \qquad (D.14)$$

Using the trigonometric identity as before results in

$$\begin{aligned} I_m^{UTD} &= -\frac{jH_t^i}{2k}\frac{\sin\beta'\cos\frac{\phi'}{2}}{\sin\frac{\psi_2}{2}\sin\psi_2} i_m \\ &\times \left\{\left[\cot\left(\frac{\pi-(\psi_2-\psi_2')}{4}\right) - \cot\left(\frac{\pi+(\psi_2-\psi_2')}{4}\right)\right]\right. \\ &+ \left.\left[\cot\left(\frac{\pi-(\psi_2+\psi_2')}{4}\right) - \cot\left(\frac{\pi+(\psi_2+\psi_2')}{4}\right)\right]\right\} \qquad (D.15) \end{aligned}$$

which is the same as the expression given in Section 4.7. The results for I_e^{UTD} and M^{UTD} are obtained in a similar manner.

Finally the expression for M^{PO} of Section 4.7 is found. Starting with the expression given by Michaeli [14]

$$M^{PO} = \frac{2Z_0}{jk} H_t^i U(\pi-\phi') \frac{\sin\phi}{\sin\beta\sin\beta'(\cos\phi+\cos\alpha)} \qquad (D.16)$$

$$\cos\alpha = \frac{\sin\beta\cos\phi}{\sin\beta'} + \frac{(\cos\beta-\cos\beta')\cos\beta'}{\sin^2\beta'} \qquad (D.17)$$

Substituting the expression for $\cos\alpha$ into the expression for M^{PO} results in

$$\begin{aligned} M^{PO} &= \frac{2Z_0}{jk} H_t^i U(\pi-\phi') \frac{\sin\phi\sin\beta'}{\sin\beta} \\ &\times \frac{1}{\sin^2\beta'\cos\phi + \sin\beta'\sin\beta\cos\phi + (\cos\beta-\cos\beta')\cos\beta'} \qquad (D.18) \end{aligned}$$

Using ψ_2, ψ_2', and θ_2 defined previously.

$$M^{PO} = \frac{2Z_0}{jk} H_t^i U(\pi-\phi') \frac{\sin\phi\sin\beta'}{\sin\beta} \frac{1}{\cos\psi_2 + \cos\psi_2'} \qquad (D.19)$$

Using the trigonometric identity from Section 3.4 as before results in

$$
\begin{aligned}
M^{PO} &= \frac{jZ_0}{2k} H_t^i U(\pi - \phi') \frac{\sin\phi \sin\theta_2}{\sin\beta \sin\psi_2} \\
&\times \left\{ \left[\cot\left(\frac{\pi - (\psi_2 - \psi_2')}{4} \right) - \cot\left(\frac{\pi + (\psi_2 - \psi_2')}{4} \right) \right] \right. \\
&+ \left. \left[\cot\left(\frac{\pi - (\psi_2 + \psi_2')}{4} \right) - \cot\left(\frac{\pi + (\psi_2 + \psi_2')}{4} \right) \right] \right\} \qquad \text{(D.20)}
\end{aligned}
$$

which is the same as the expression given in Section 4.7. The apparent difference due to the replacement of the S^i function by the step function $U(\pi - \phi')$ is only a technicality since the expression given here gives the contribution from both faces, but is valid only for O-face incidence while the expression in Section 4.7 gives the contribution from both faces for either O-face or N-face incidence. The other two terms I_e^{PO} and I_m^{PO} may be found similarly.

REFERENCES

[1] Ryan, C.E., Jr., and L. Peters, Jr., "Evaluation of Edge Diffracted Fields Including Equivalent Currents for the Caustic Regions," *IEEE Trans. on Antennas and Propagation*, Vol. AP-17, pp. 292-299, May 1969.

[2] Sikta, F.A., W.D. Burnside, T.T. Chu, and L. Peters, Jr., "First-Order Equivalent Current and Corner Diffraction Scattering from Flat Plate Structures," *IEEE Trans. on Antennas and Propagation*, Vol. AP-31, No. 4, pp. 584-589, July 1983.

[3] Kouyoumjian, R.G., and P.H. Pathak, "A Uniform Geometrical Theory of Diffraction for an Edge in a Perfectly Conducting Surface," *Proc. IEEE*, Vol. 62, pp. 1448-1461, Nov. 1974.

[4] Ufimtsev, P.Ya., "Method of Edge Waves in the Physical Theory of Diffraction," Air Force Systems Command, Foreign Tech. Div., Document ID No. FTD-HC-23-259-71, 1971 (Translation from the Russian "Method Krayevykh voin v fizicheskoy teorii difraktsi," Soviet Radio Publication House, Moscow, 1962).

[5] Luneberg, R.K., *Mathematical Theory of Optics*, University of California Press, 1964.

[6] Kline, M., "An Asymptotic Solution of Maxwell's Equations," *The Theory of Electromagnetic Waves*, Interscience Publishers, Inc., 1951.

[7] Kline, M., *Electromanetic Theory and Geometrical Optics*, edited by L.E. Langer, University of Wisconsin Press, 1962.

[8] Kline, M., and I.W. Kay, *Electromagnetic Theory and Geometrical Optics*, Interscience Publishers, Inc., 1965.

[9] Balanis, C.A., *Antenna Theory: Analysis and Design*, New York: Harper and Row Publishers, Inc., 1982.

[10] Keller, J.B., "Geometrical Theory of Diffraction," *J. Opt. Soc. of America*, Vol. 52, No. 2, pp. 116-130, Feb. 1962.

[11] Harrington, R.F., *Time-Harmonic Electromagnetic Fields*, New York, McGraw-Hill Book Company, pg. 127, 1961.

[12] Ufimtsev, P.Ya., "A New Mathematical Formulation of the Physical Theory of Diffraction," submitted to *IEEE Proc.* for publication.

[13] Michaeli, A., "Equivalent Edge Currents for Arbitrary Aspects of Observation," *IEEE Trans. on Antennas and Propagation*, Vol. AP-32, No. 3, pp. 252-258, March 1984.

[14] Michaeli, A., "Elimination of Infinities In Equivalent Edge Currents, Part I: Fringe Current Components," *IEEE Trans. on Antennas and Propagation*, Vol. AP-34, No. 7, pp. 912-918, July 1986.

[15] Ufimtsev, P.Ya., and D.I. Butorin, "Explicit Expressions for an Acoustic Edge Wave Scattered by an Infinitesimal Edge Element," *Sov. Phys. Acous.*, Vol. 34, No. 4, pp. 283-287, July-August 1986.

[16] Millar, R.F., "An Approximate Theory of the Diffraction of an Electromagnetic Wave by an Aperture in a Plane Screen," *IEE Monograph*, No. 152 R, Oct. 1955.

[17] Millar, R.F., "The Diffraction of an Electromagnetic Wave by a Circular Aperture," *IEE Monograph*, No. 196, Sept. 1956.

[18] Millar, R.F., "The Diffraction of an Electromagnetic Wave by a Large Aperture," *IEE Monograph*, No. 213 R, Dec. 1956.

[19] S.S. Locus, H.C. Heath, F.K. Oshiro, and J.R. Coleman, "Radar Cross Section Studies," Northrop Corp. final rep. NOR-74-83, April 1974.

[20] Marhefka, R.J., personal communication.

[21] Jones, D.S., and M. Kline,"Asymptotic Expansion of Multiple Integrals and the Method of Stationary Phase," *J. Math. Phys.*, 37, pp. 1-28, 1958.

[22] Buyukdura, O.M., R.J. Marhefka, and W. Ebihara, "Radar Cross Section Studies, Phase III," Technical Report 716622-1, The Ohio State University, ElectroScience Laboratory, April 1986.

[23] Gordon, Willliam B., "Far-Field Approximations to the Kirchoff-Helmholtz Representations of Scattered Fields," *IEEE Trans. on Antennas and Propagation*, pp. 590-592, July 1975.

[24] Mitzner, K.M., "Incremental Length Diffraction Coefficients," Northrop Corp., Aircraft Division, Tech. Rep. No. AFAL-TR-73-296, April 1974.

[25] Knott, E.F., "The Relationship Between Mitzner's ILDC and Michaeli's Equivalent Currents," *IEEE Trans. on Antennas and Propagation*, Vol. AP-33, No. 1, pp. 112-114, January 1985.

[26] Sikta, F.A., "UTD Analysis of Electromagnetic Scattering by Flat Plate Structures," Ph.D. dissertation, The Ohio State University, Department of Electrical Engineering, Columbus, Ohio, 1981.

[27] Tiberio, R., M. Giuliano, G. Pelosi, and R.G. Kouyoumjian, "High-Frequency Electromagnetic Scattering of Plane Waves From Double Wedges," to be published.

[28] Michaeli, A., "Equivalent Currents for Second-Order Diffraction by the Edges of Perfectly Conducting Polygonal Surfaces," *IEEE Trans. on Antennas and Propagation*, Vol. AP-35, No.2, pp. 183-190, February 1987.

[29] Buyukdura, O.M., personal communication.

[30] Chu, T.,"Plate Measurements," The Ohio State University, ElectroScience Laboratory Measurements Facilities, Department of Electrical Engineering.

[31] Dominek, A.K., "A Uniform Electromagnetic Reflection Ansatz for Surfaces with Small Radii of Curvature," Ph.D. dissertation, The Ohio State University, Department of Electrical Engineering, Columbus, Ohio, 1984.

[32] Leeper, W.J., "Identification of Scattering Mechanisms from Measured Impulse Response Signatures of Several Conducting Objects," Thesis (M.S.), The Ohio State University, Department of Electrical Engineering, Columbus, Ohio, 1983.

[33] Ross, R.A., "Radar Cross Section of Rectangular Flat Plates as a Function of Aspect Angle," *IEEE Trans. on Antennas and Propagation*, Vol. AP-14, pp. 329-335, May 1966.

U.S. Government Printing Office 548-076